The University Of Sheffield.

Roller Compaction: Mechanistic understanding of ribbon splitting and sticking

Osama Mahmah

A thesis submitted in partial fulfilment of the requirements for the degree of Doctor of Philosophy

The University of Sheffield
Faculty of Engineering
Department of Chemical and Biological Engineering

August 2019

Abstract

Roller compaction is a dry granulation technique in which the feed powder is subjected to different types of stresses, which are applied between two counter-rotating rollers. The stress applied during this process mediates both desired (intact ribbon) and undesired (ribbon splitting/sticking) bond formation. The phenomenon of ribbon splitting/sticking could originate from either process or formulation related causes; due to the imbalanced combination of material mechanical properties and stress application which has the potential to result in different types of ribbon failures i.e. cohesion and/or adhesion-related ribbon failure. Despite current research work conducted in the field of roller compaction, there remains a lack of comprehensive understanding in relation to the development of ribbon failure during roller compaction which can hinder the use of roller compaction with many formulations. Therefore, an in-depth understanding of the causes of ribbon failure during roller compaction is required to design better formulations and incorporate steps which will mitigate/stop the occurrence of ribbon splitting/sticking.

The aim of this work is to build a mechanistic understanding of ribbon splitting/sticking phenomenon in terms of the ribbon-roller interactions in both the bulk and at the roller walls.

A range of materials was selected to cover a wide range of powder deformability, the minimum gap between the two smooth rollers was fixed and the maximum roll stress was varied. Ribbon splitting was observed to occur either transversally (through the ribbon thickness) or longitudinally (through the ribbon width). It was observed that transverse splitting is commonly associated with sticking of the split ribbons to the rollers. Longitudinal splitting is associated with an across-width distribution of the ribbon density which may cause an adverse effect on the mechanical strength and dissolution properties of the tablets formed from the milled granules. The observed trends of ribbon splitting were rationalised in terms of a splitting index which is a measure of the residual stresses driving crack growth relative to the tensile strength of the ribbons.

Furthermore, knurled rollers with higher roller/powder contact surface area have been investigated in terms of the occurrence of ribbon splitting/sticking. The predictability of the splitting index was improved by incorporating the ribbon solid fraction difference across the ribbon width. Using knurled rollers extends the range of transversal

splitting/roller sticking when compared with the smooth rollers and reduces the extent of longitudinal splitting.

Attempts have been conducted to correlate powder and metal thermodynamic work of adhesion with its sticking tendency during roller compaction. The technology of inverse gas chromatography was utilised to characterise both powder and metal in terms of their surface energy. No clear correlation between the work of adhesion/cohesion and sticking probability was found which suggests that particle deformation is the dominant factor of sticking during compaction. However, the result could contribute to the elaboration of the lubrication mechanism of MgSt during powder compaction.

Finally, a data-driven model was developed to predict the ribbon porosity distribution using the artificial neural network approach (ANN). Various process-related parameters and material properties considered as the inputs of the ANN. While the outputs of the network were the porosity which was experimentally measured by X-ray tomography across the ribbon width, powder and ribbon porosity distribution have linked together using ANN approach as a novel approach to predict the heterogeneity of ribbon in terms of its porosity distribution. Results showed that the ANN was able to successfully map various material and process parameters to the ribbon porosity distribution across the ribbon width, which is considered to be one of the most important quality attributes in the roller compaction process. Due to its short processing time This is particularly useful as it allows potentially for future powders and formulations to be modelled to understand the propensity of undesired ribbon properties to occur.

Acknowledgements

I would like to express my sincere appreciation and thanks to my supervisor Prof. Agba D. Salman, you have been a tremendous mentor for me. The completion of this work could not have been possible without your support. I would like to thank you for your critical comments. Thanks to the particle product group (PPG) for being my family for the whole of the PhD period. I am extremely grateful for The University of Sheffield for funding my PhD study.

Special thanks to Prof. Mike Adams for his valuable contributions. It was an honour to work with such a knowledgeable and experienced scientist with tens of years of experience in the field of particle science and technology. Great thanks to Dr Bindhu Gururajan, Dr Syed Islam, and Dr Chalak Omar for their continuous help and support.

No words can be strong enough to express my gratitude and appreciation for my parents, sisters, brothers, and wife for always being here for me, adding love to everything you do. One day, I will join you back in Syria when the war hopefully stops.

On top of all, I will give thanks to you GOD for everything I have and for everything I have been blessed with. Praise be to GOD, Lord of the worlds.

LIST OF PUBLICATIONS AND PRESENTATIONS

- O. Mahmah, M.J. Adams, C.S. Omar, B. Gururajan, A.D. Salman, Roller compaction: Ribbon splitting and sticking, International Journal of Pharmaceutics. 559 (2019) 156–172.
- O. Mahmah, M.J, B. Gururajan, A.D. Salman, Roller compaction: ribbon splitting and sticking. Conference paper at 8th International Granulation Workshop. Sheffield, UK. 26th-28th June 2017. Paper No. 86.
- O. Mahmah, B. Gururajan, A.D. Salman, Roller compaction: ribbon splitting and sticking. Poster presentation at 8th International Granulation Workshop. Sheffield, UK. 26th-28th June 2017.

TABLE OF CONTENTS

LIST OF FIGURES

List of Tables

Nomenclature

A	Parameter described in Equation 2-7
b	Width of ribbon (mm)
C	The BET or sorption constant related to the heat of adsorption and condensation
C_h	A constant related to the volume reduction of the powder (Equation 3-1)
d	Average thickness of the briquette rolled when the roll gap is zero (mm)
dps	Travelling distance per lubricant shot (mm)
d_r	Roll diameter (mm)
E_p	Young's modulus (Pa)
E^*	Reduced effective young's modulus (GPa)
f	The activation function (ANN)
F	Force applied during compaction test (N)
F_{ad}	Adhesion forces (N)
F_{co}	Cohesion forces (N)
F_c	Carrier gas flow rate (ml/min)
F_{det}	Detachment force (N)
f_{fac}	Force factor
F_{max}	Force required to break the ribbon (N)
F_{vdW}	Lifshitz-van der waal force (N)
h	Displacement during single particle test (mm)
h_c	Current powder bed height (mm)
h_d	Distance separation between the contiguous bodies (m)
h_i	Initial height of powder (mm)
h_m	Displacement of the moving platen (single particle test) (mm)
I_S	Splitting index
J	James-Martin correction factor
K	Compressibility factor
L_s	Distance between the supporters in the three point bend test (mm)
m	Ribbon thickness (mm)
M	The molar mass (g mol^{-1})
m_{ads}	The mass of the adsorbent (g)
N_A	The Avogadro number ($6.022 \times 1023\ mol^{-1}$)
n	The amount of gas adsorbed at equilibrium pressure
n_m	The amount of gas adsorbed in a monolayer

p	Pressure (MPa)
P_0	Outlet pressure of IGC (mmHg)
P_D	The molar deformation polarisation of the gaseous probe ($cm^3\ mol^{-1}$)
P_{eq}	Equilibrium pressure (BET specific surface area)
P_i	Inlet pressure of IGC (mmHg)
p_{max}	The maximum stress applied on the material (Johason's theory) (MPa)
p_r	Poisson's ratio of the powder particle
P_{sat}	Saturation pressure (BET specific surface area)
Py	Particle yield strength (single particle test) (MPa)
Q	Contact angle between a droplet and a surface (º)
r	Particle radius (m)
R	Coefficient of correlation
R^2	Coefficient of determination
Rf	Roller separation force (kN)
R_g	Ideal gas constant ($8.314\ J.mol^{-1}$)
Rz	Peak to trough surface roughness (µm)
S	Roll gap (mm)
s_{BET}	BET specific surface area (m^2g^{-1})
Spm	Number of shots per minute
SR	Stress ratio
T	The threshold value (Equation 7-1)
t_r	Retention time (min)
t_0	Dead time (min)
V	The molar volume of the adsorbed gas
V_N	Retention volume (ml)
v_r	Roll speed (rpm)
W	Roller width (mm)
Wad	Work of adhesion ($mJ.m^{-2}$)
Wco	Work of cohesion ($mJ.m^{-2}$)
w_i	The weight of x_i input (Equation 7-1)
w_{ri}	Refractive index
X	Material related constant (Heckel analysis-Equation 3-1)
x_i	Input (i) to the node
$\overline{x}_i$	The average of all of the actual values
x_n	The normalised value of the input x

Y	Tablet relative density (Heckel analysis-Equation 3-1)
y_{prd}	The predicted output of the node

Greek alphabet

α	Nip angle (º)
α_{ads}	The cross sectional area of the adsorbing gas molecule (m^2)
α_{CH2}	The cross sectional area of a methylene molecule (6 $Å^2$)
β	True nip angle (Adam's equation) (º)
β_C	Solid fraction at ribbon centre
β_E	Solid fraction at ribbon edge
γ	Surface free energy ($mJ.m^{-2}$)
γ_{ab}	Polar surface energy for acid-base interaction ($mJ.m^{-2}$)
γ_a^+	Acidic surface energy ($mJ.m_{-2}$)
γ_b^-	Basic surface energy ($mJ.m^{-2}$)
γ_{CH2}	The surface free energy of a solid contains methylene groups ($mJ.m^{-2}$)
γ^d	Dispersive surface energy ($mJ.m^{-2}$)
γ_{sl}	The interfacial energies between solid and liquid ($mJ.m^{-2}$)
γ_{sv}	The interfacial energies between solid and vapour ($mJ.m^{-2}$)
γ_{lv}	The interfacial energies between liquid and vapour ($mJ.m^{-2}$)
$\Delta\beta$	Solid fraction difference
ΔG_a^{sp}	The specific component of the free energy of adsorption
δ_E	Effective angle of the internal friction (º)
ε	Compressive natural strain
ε_R	Elastic recovery
ε_L	Energy of loading (N.mm)
ε_U	Energy of unloading (N.mm)
θ	Angular position in roll bite (º)
κ	Modified compressibility factor (Adam's equation)
μ	Parameter in Johanson's theory (Equation 2-9)
ν	Acute angle between the direction of the principle stress and the tangent to the roll surface (Equation 2-8)
ρ	Density (g/mm3)
σ	Stress (MPa)
σ_θ	Mean normal stress at position θ (MPa)
σ_{max}	Maximum normal stress applied in roller compaction (Johanson's theory) (MPa)
σ_t	Tensile strength (MPa)

σ_Y	Powder yield strength (MPa)
τ_0	Constant related to mechanical strength of particles “Adams equation”
$\emptyset_w$	Angel of wall friction (º)
$\hbar\bar{\omega}$	Lifshitz-van der waal constant (J)

Abbreviations

ANN	Artificial neural network
APAP	Acetaminophen (Paracetamol)
API	Active pharmaceutical ingredients
CP	Capping propensity
DBC	Drucker-Prager cap model
DOF	Depth of field of the lens
FEM	Finite elements modelling
IER	In-die elastic recovery
IGC	Inverse gas chromatography
L	Longitudinal splitting
MCC	Microcrystalline cellulose
MDP	Maximum die wall pressure
MgSt	Magnesium stearate
MISO	Multiple inputs single output structure
MPC	Model predictive control
NIR-CI	Near-infrared chemical imaging
RDP	Residual die wall pressure
SCR	Scraper force
T	Transversal splitting

CHAPTER 1 INTRODUCTION

1.1 Granulation in general

As a result of increasing diversity and competition between the pharmaceutical companies, most of the globally working pharmaceutical companies attempt to maximize the efficiency of the manufacturing processes. Direct tabletting is the most preferred formulation technique for the solid dosage forms. However, all ingredients in the case of direct tabletting have to be homogenous in terms of physical and chemical properties. Otherwise, a negative variation in segregation behaviour might occur, and this may result in tablets with poor mass and content uniformity. Moreover, in addition to the need for sufficient flowability and compressibility behaviour, the need for specially produced direct compressible excipients could affect its cost-effectiveness [1].

To overcome such problems and to mask the poor flow properties exhibited by many drug compounds, granulation by incorporation into an excipient's matrix is used to modify the properties of the raw powder in order to obtain a final dosage form with the desired stability, disintegration and integrity profile. Granulation can be defined as a size enlargement process in which particles are physically grouped into strong agglomerates in which the original raw particles can be distinguished [2].

1.2 Why dry granulation

Granulation processes are mainly classified into two main categories: wet and dry processes. In wet granulation, an external liquid is used in conjunction with agitation to achieve particle agglomeration. Wet granulation process can be subdivided into three main approaches: low shear, high shear, and fluid bed granulation. Each of these processes has its own merits and demerits. Nevertheless, all of the wet granulation processes exploit the principle of forming cohesive forces between the moist particles with the added granulation liquid in the form of liquid bridges; these are converted into more permanent forces during the subsequent drying stage.

Use of wet granulation improves the flow, compression, and density of the powder particles, as well as, ensuring better distribution of the colouring agent or the active

ingredient if it was solubilized in the granulation liquid. Furthermore, the use of this technique reduces the amount of segregation and dust formation during powder processing.

Wet granulation processes still suffer from a few disadvantages that might affect its effectiveness such as the need for huge amounts of energy and processed air for the subsequent drying stage. This is in addition to the stability issues when heat and moisture sensitive compounds are processed. Moreover, the use of organic solvent as a granulation liquid can result in hard restrictions on the residual solvent in the end product. All of these limitations encourage researchers to adopt dry granulation as an alternative solution that is more cost-effective and capable of forming good quality granules without the need of adding liquid during granulation or removing it during drying stage [3].

Dry granulation can be defined as a pressure mediated agglomeration process where the materials are agglomerated without using any moisture or heat. Initially, the process started by compressing the powder blend into a large tablet (2.5 cm. diameter, 0.6 cm. thickness) in a process called slugging where the slugs are milled into smaller particles known as granules [4]. This method has multiple limitations. It results in a considerable amount of dust that could lead to cross-contamination issues. Since it is a single batch process, slugging has very poor process control and poor manufacturing throughput per hour. Consequently, roller compactor has been introduced to the market to deal with such limitations. It is a continuous technique, which is the key for more advanced dry granulation.

It has considerable production capacity, more control over the processing variables, which is accompanied by the ability of processing material having inconsistent density, flowability, or compactibility. Thus this technique satisfies the need for the high processing rate, together with a competitive cost and quality efficiency [5].

Conventional roller compactors usually consist of three systems; the feed system, roll system, and granulation system. The process starts with the feeding system that delivers the powder by gravity or by a screw feeder into the compaction area, which is theoretically divided into three zones (Figure 1-1), while the boundaries between these zones are defined by their angular positions. The powder within the slip zone moves at speed slower than the rolls speed by the effect of gravity, friction, or force feeder, which

push and rearrange the powder particles to fill the interstitial spaces and expel the air inside. Both of the particle shape and size are the key factors in this zone [2,5,6].

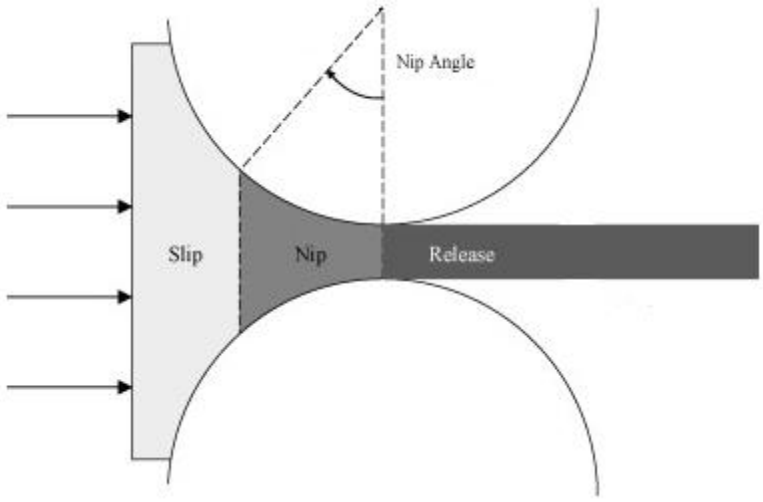

Figure 1-1: Schematic diagram of the roller compaction process showing the different compaction zones– Adapted [7].

In the nip zone, the particles now move at a speed equal to that of the rolls and the pressure applied to the powder increases as the gap distance between the rolls decreases. As the particles become closer to each other, plastic deformation and/or particle fragmentation increases the contact surface area between them and create new bonds by various mechanisms [8].

In the release zone, the applied compaction pressure begins to decrease as the gap distance starts to expand. Once the pressure is relieved, the compacted material may have tendency to retain its original shape due to its elastic potential properties. Therefore, the resulting ribbon shape and thickness depends on the predomination of the plasticity and/or elasticity responses upon decompression. The quality of the final products depends on powder responses to compression and decompression processes. The mechanical properties of the powder's components and their interactions with each other and with the equipment in addition to the processing parameters and equipment design significantly affect the powder's response, and thus the quality of the final product.

1.3 Roller compaction challenges

Roller compaction like any other process has its own drawbacks that have to be taken into account before starting any production process. Firstly, the loss of workability on

recompaction which was referred by many authors as being due to work hardening effect of the feed materials [9] or to the enlargement in particle size [10]. Secondly, the heterogeneity of the ribbon in terms of its density distribution, which is usually periodical in nature and synchronized with the screw feeder period. Heterogeneity is mainly governed by two main factors, which are the design of the powder feed system [11] and the powder flow behaviour in the compaction zone [12,13]. Moreover, the leakage of high amount of uncompacted powder between the roller seals could greatly affect the efficiency of the process, the main cause of this phenomenon is the weak bonding of ribbons at its edges as a result of non-homogenous feeding or air entrapment [2].

In addition, splitting and sticking of the compacted ribbons on the roller surface is one of the main limitations that could hinder the use of roller compactor with many formulations. It is a complex phenomenon that takes place in the release region; such that the ribbon might split in different ways and in some cases stick to roller surface [14]. Ribbon splitting could take place across different ribbon dimensions but does not prevent the ribbons from being milled into granules, however similar to the defects encountered during a tabletting process; this phenomenon could be a signature of more serious processing defects such as the heterogeneity of density across compact dimensions [15–17]. Additionally, ribbon splitting could be related/associated with powder sticking, which is one of the most important problems encountered during powder compaction processes in general. It could have various deleterious consequences that range from losing control over process parameters such as the gap distance in roller compaction [18] or the force applied in a tabletting process [19], tool wearing, material wasting [20]. Also, sticking could lead to problems related to product uniformity if one or more of the formulation components shows a preferential sticking to the tooling surfaces or even batch failure in case of severe powder sticking to tooling surfaces [19].

Splitting/sticking as one of the compact defects that occur during powder compaction has been investigated in the field of tabletting but to a very limited extent in the field of roller compaction where a different combination of shear and normal stresses are applied.

1.4 Mechanism of bonding

Understanding of inter-particular bonding mechanisms could assist in mitigating many problems such as the stickiness on the roller surface or the amount of fines produced during compaction; this could be implemented by modifying the formulation components or adjusting the processing parameters and/or design in order to have the optimal bonding mechanism for the intended product quality. For example, changing design of the feeding system by adding feeding guiders could significantly improve the quality of the produced ribbons [13]. The bonding adjustment depends on the bonding mechanism and the limit of the adjustment should fulfil the intended quality of the final products, i.e., porosity, strength, and dissolution profile.

The particle bonding via roller compaction is mainly controlled by the applied forces since it is a dry process. Moreover, material properties such as deformability could also affect bonding strength and subsequently the properties of the final dosage form.

The pressure applied during roller compaction enforces particles to rearrange their positions to tightly pack by reducing the air voids, this stage is mainly controlled by both particle shape and size distribution. At a certain limit of the applied force, the free volumes of particles are minimized and thus prevent particle movement, and so the particles start to fragment or deform as a response to the applied pressure, and consequently their contact areas increase. The compacted powder is initially subjected to elastic deformation according to its Young's modulus, and at its yield point of pressure, it deforms plastically. The contact area between powder particles could also be increased by fragmentation where particles break down to smaller fragments when the applied stress is greater than their tensile strength, and then they might undergo subsequent stages of rearrangements, elastic and plastic deformation [2,8]. The mechanical properties of the powder components control their ability to form permanent bonds due to plastic deformation (irreversible) or temporary bonds due to elastic deformation (reversible). Also, the tendency to fracture is responsible for creating a new contact area and modifying the size distribution to fit the voidage. Generally, the fragmentation phenomenon predominates over the deformation when the materials are hard and brittle [4]. Bond formations can be called an agglomeration process because particles agglomerate tightly

together to form a larger entity. The stages of bonding and compression mechanism during roller compaction are illustrated in (Figure 1-2).

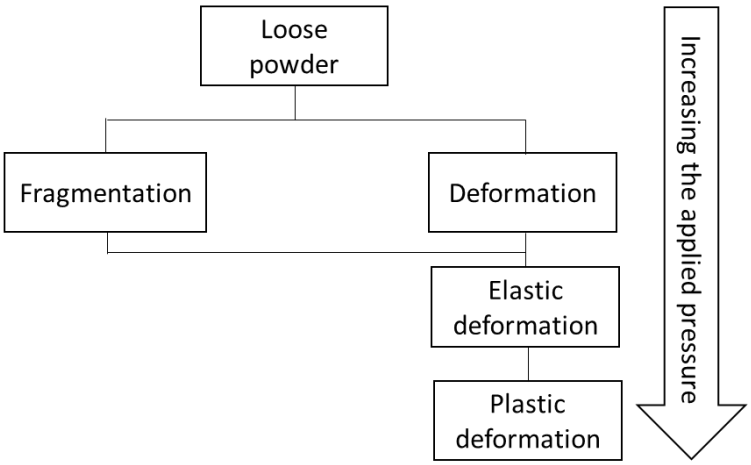

Figure 1-2: Possible events during particle compaction cycle–Adapted [21].

The interparticular forces generated during an agglomeration process are due to mechanical interlocking, intermolecular forces and the solid bridges [22]. Mechanical interlocking occurs between adjacent particles, and it is mainly controlled by the shape, regularity and the surface properties of the particles [8,23]. The intermolecular forces, i.e., adsorption bonding, is mainly governed by the van der Waals forces and more precisely to the London dispersion forces which are believed to be the most important bonding mechanism [24]. These types of forces maintain the attractive forces in gases and liquids within distances of 10-100 nm. The solid bridges are usually considered as the strongest interparticulate bond. They occur when the degree of mixing between the interfaces is high. This happens when the movement and/or diffusion of the particles induce sufficient molecular mobility. The diffusion can be mediated either by contact melting due to highly localized stress during compaction, or by a glass-rubbery transition of an amorphous material. Figure 1-3 shows different types of bonds and their theoretical strengths in relation to particle size.

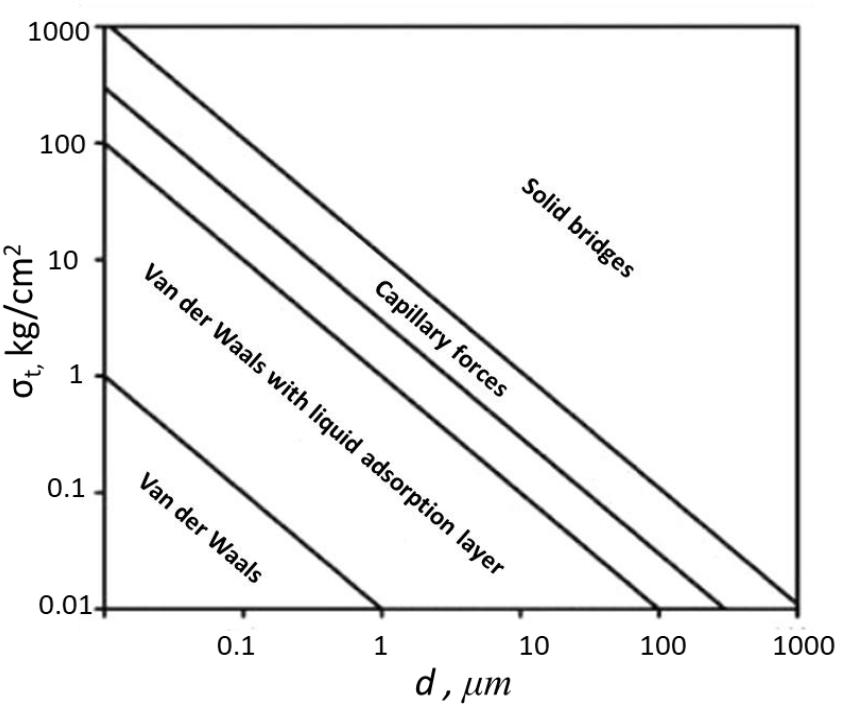

Figure 1-3: Suggested bond types and their theoretical strengths in relation to particle size [22,24].

1.5 Thesis overview

The outline of the thesis is as follows:

Chapter 2 presents a review of the existed literature efforts conducted in the field of powder compact integrity. The chapter will focus on the factors that could affect the integrity of a compact during and after stress application in roller compaction and other stress-mediated processes such as tabletting. In addition, the chapter includes a comprehensive review of the work related to the area of this thesis.

Chapter 3 describe the main types of equipment, methods, and materials used to characterise both the feed powders and compacts.

Chapter 4 corresponds to the main results and discussion of this research work.

In this chapter, a comprehensive study was conducted in an attempt to build a mechanistic understanding of the splitting phenomenon. The observed trends of ribbon splitting were rationalised in terms of a splitting index.

Chapter 5 investigated the effect of knurled rollers which have a higher roller/powder contact surface area on the occurrence of ribbon splitting/sticking. The predictability of the splitting index was applied to the new data.

Chapter 6 focuses on the effect of the intermolecular interactions between feed powder and metal surface on the occurrence of ribbon sticking. Energies of interaction have been examined for any correlation with the trend of ribbon sticking.

Chapter 7 looked at the development of a data-driven model to predict the ribbon porosity distribution using the artificial neural network approach (ANN). The chapter presents a practical approach that could be implemented in the control system across the manufacturing line.

Chapter 8 presents the overall conclusion of the thesis and recommends some future studies.

CHAPTER 2 LITERATURE REVIEW

In an attempt to build a mechanistic understanding to the phenomena of ribbon spitting/sticking, there is a need first to review the existed research efforts conducted in the field of powder compact integrity during stress-mediated processes. The current chapter focuses on the work reported in the literature about the factors that could affect the integrity of a compact during and after stress application in roller compaction and other stress-mediated processes such as tabletting. Compact integrity could be disrupted externally by improper bond formation with the tooling surfaces or internally by un-designed responses of the compact to the stress applied. Figure 2-1 summaries the factors affecting compact integrity, which will be discussed from the literature point of view in the following section. Additionally, the chapter highlights some physical and data-driven model used to enhance our understanding of the roller compaction process.

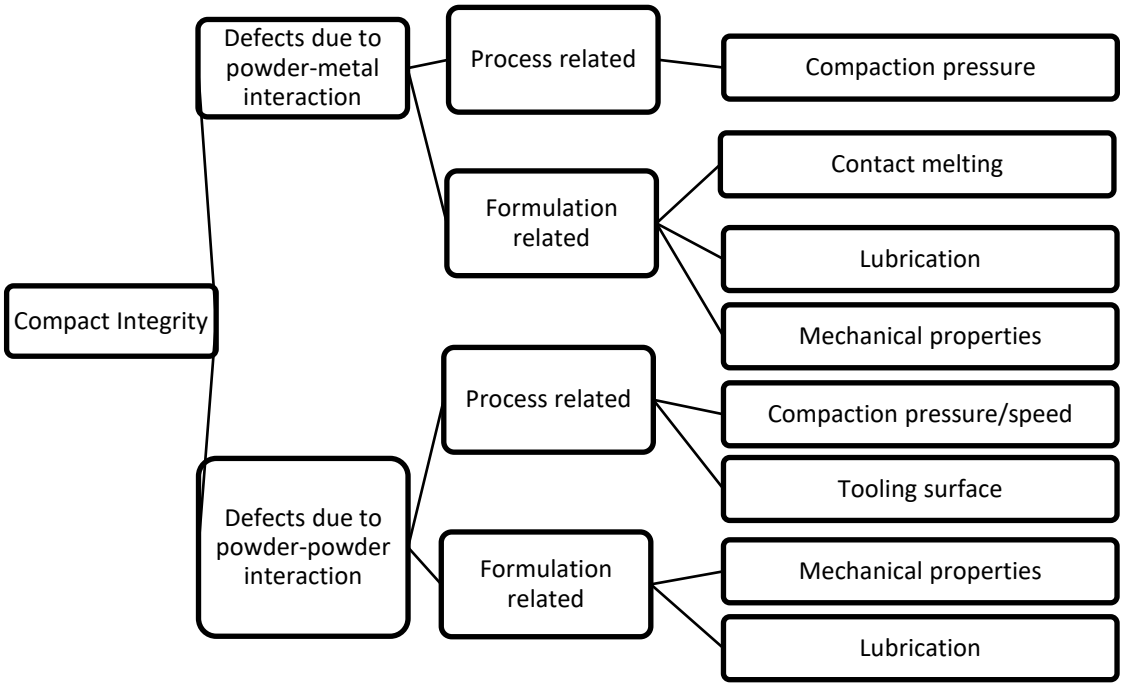

Figure 2-1: Main points discussed in this chapter.

2.1 Compact defects due to sticking (powder-metal interaction)

Stickiness or adhesion of powder formulations during compaction is one of the most common problems that are usually referred to the tablet stickiness. Materials adhere onto the compression tooling, such as the roller surface, punch surface or the die wall, and undergo multiple compaction cycles with the new materials being compacted; this may result in an unacceptable, poor quality condition of the compact and might cause serious damage to the press machine [19].

At the molecular scale, as hypothesized by Wang et al. [25], the potential of adhesion during powder compaction is mainly determined by the intermolecular interaction between the powder molecules and the tooling surface. In other words, the energies of interaction on the molecular level between the powder and metal surface will determine the primary adhesion process, and the subsequent mechanical events will affect the extent of adhesion.

At a higher scale, Waimer et al. [26] explained sticking phenomenon during a tabletting process; the study mentioned that tablet sticking occurred when there is an imbalance in the relationship between the detachment force (F_{det}), which is applied perpendicularly to remove the tablet from the punch surface in comparison to the adhesion forces between surfaces F_{ad} and the cohesion forces inside the tablet (F_{co}). Thus, if the applied perpendicular detachment force was higher than the adhesion force but not as high as the cohesion forces within the tablet, the tablet will be removed freely from the punch surface with no sticking. The measured detachment force in this case represents the real adhesion forces between the tablet and the punch surface. However, if the applied detachment force was lower than the adhesion forces, but higher than the cohesion inside the tablet, the separation will take place within the tablet and stickiness will happen. In this case, the measured detachment forces will represent the cohesion within the tablet. Moreover, if the adhesion and cohesion forces are similar in their extent, separation takes place at the surface as well as within the tablet and powder sticks partially to the punch face (Figure 2-2).

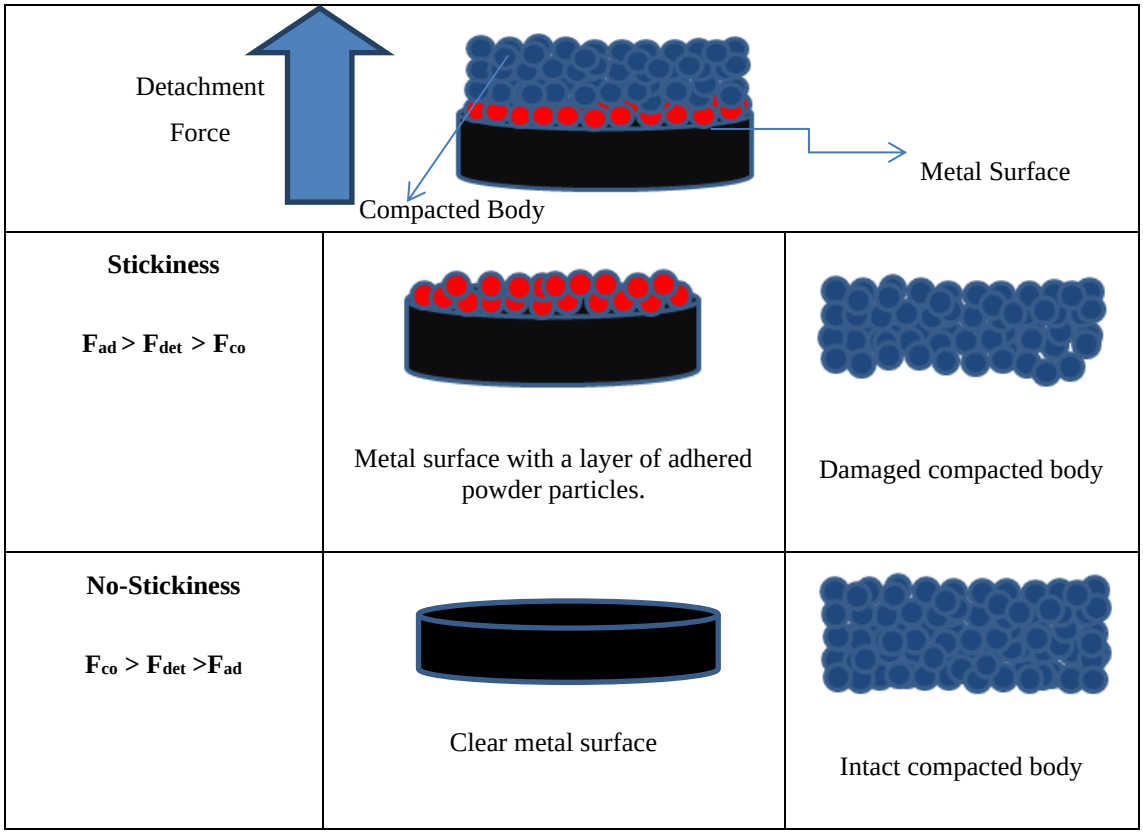

Figure 2-2: Possible cases during detachment of an adhered compacted powder; particles are detached by perpendicular forces–Adapted [26].

Limited research efforts have been made to study the sticking phenomena during roller compaction; the research has mainly focused on the consequences of this phenomenon and highlighted some mitigation strategies. The effect of powder stickiness in roller compaction depends on the extent of stickiness, which can range from improper ribbon quality to batch failure where the process has to be stopped in order to clean the surfaces of the rollers [27].

Using the gap controlling system during roller compaction is more likely to cause a problem in the case of roller sticking. This system uses a set point for the minimum roll separation distance, and any deviation from this point will be corrected by an automated adjustment of the auger feed rotational speed. If the powder sticks to the roller surface, it will cause the gap distance to open wider which activates the gap controlling system to decrease the speed of the feeding screw to return the gap to its original set point. The extent of the screw speed reduction will depend on the thickness of the adhered layer, which will consequently affect the mass throughput of the process. Moreover, the adhered layer on the roller surface will undergo multiple compaction cycles that might affect the properties of the final granules [28].

The effects of powder sticking on a roller surface were investigated by a recent study conducted by Hamdan et al. [27]; a thin layer of Instant-mix Epoxy (3 cm in length and covering the entire roller width) was attached to roller surface to mimic the occurrence of roller sticking. The treated roller was used for MCC roller compaction. For comparison purposes, the process response to this event was compared with the same experiment without the epoxy layer being fixed to the roller surface. The process response to this event was analysed and showed that the adhered layer caused a periodic oscillation in roller gap, leading to ribbon density variation while both of the feed screw speed, hydraulic pressure and roll speed remained unaffected (Figure 2-3).

This oscillation in the roller gap is usually compensated by adjusting the feed screw speed by the roller gap controlling system; however, if the oscillation is large enough to affect the ribbon quality and consequently the tablet quality, the process has to be shut down in order to remove the powder from the roll, this can consequently affect the continuity of the process and affect its cost-effectiveness [27].

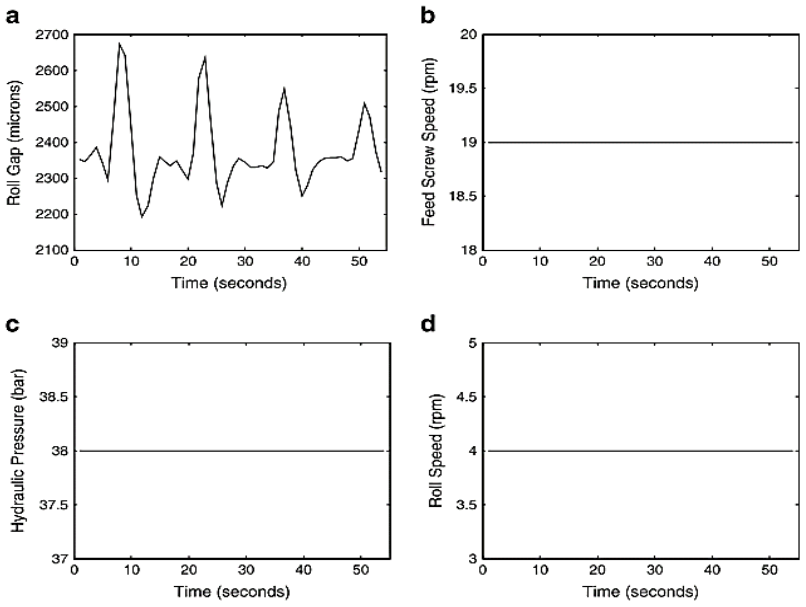

Figure 2-3: Oscillation in roller compactor process parameters as a result of roller stickiness [20].

This problem usually occurs when a significant number of particles adhere to the roller surface and disturb the integrity of the ribbon and affect the continuity of the process. In a tabletting process and similarly in other compaction mediated processes sticking of powder to the metal surfaces is mainly attributed to either a formulation or process causes (Table 2-1). Whereas, hygroscopicity, cohesiveness, low melting point, insufficient

lubrication and poor powder characteristics; such as particle size and polymorphism are the main formulation related causes. Using inappropriate scraper adjustment, or surface configuration, too low compaction pressure, and rough surfaces are the main process-based causes (Table 2-1).

Table 2-1: The main causes of powder stickiness during the tabletting process [19].

Formulation-related causes	**Process-related causes**
Insufficient lubrication [29]	Rough punch surface [19]
Poor powder characteristics [30] (particle size, crystal structure or crystal habit)	Insufficient compaction force [31]
Contact melting [32]	Improper surface engraving [19]
High moisture content [33]	Improper compaction speed [31]

It is worth mentioning that both of the cohesion and adhesion are mediated by the same mechanisms discussed before, but the term adhesion is usually referred to the interaction between particles of different chemical nature [34].

In the literature, adhesion mechanisms are generally classified according to the presence or absence of material bridges between the contacted surfaces (Figure 2-4).

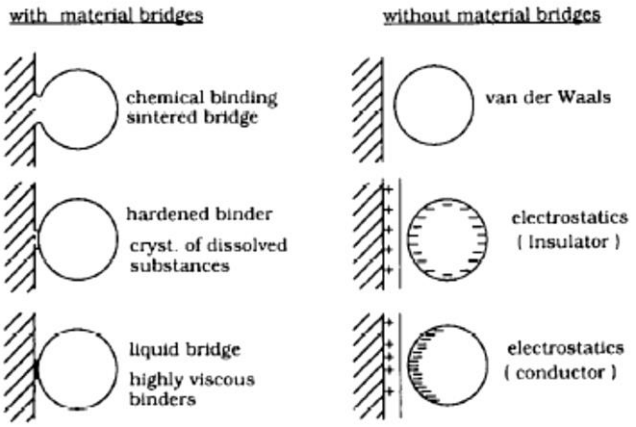

Figure 2-4: classification of the bonding mechanisms according to the presence or absence of material bridges between the contacted surfaces [35].

However, other studies find it more useful to rank the adhesion forces according to their strength in the following order (from weakest to strongest); electrostatic forces, van der Waals, liquid bridges, and solid bridges respectively [35].

During processing, the different types of adhesion mechanisms could be prompted by discrete mechanisms that could be a formulation or process-related.

2.1.1 Factors affecting sticking (powder-metal interaction)

2.1.1.1 Process-related factors

2.1.1.1.1 Effect of compaction pressure

The main function of the applied force during compaction is to create more contact area, which will be provided either by the deformation or the breakage in order to increase the probability of bond formation. Thus the higher the applied pressure, the more the cohesive forces between the particles will be. However, the same applied force can mediate the formation of unwanted bonding with the metal surface that can cause the problem of sticking.

Kakimi et al. [31] investigated the effects of compaction pressure and speed on the tablet sticking during compaction; a rotatory tabletting machine was used to compact wet extruded granules made with a formulation of n-Butyl *p*-hydroxybenzoate, lactose, anhydrous silicic acid and a binder of hydroxypropyl cellulose. The study showed that sticking occurs when the adhesive forces between the tablet surface and the metal plate are stronger than the cohesion forces inside the tablet. This outcome was confirmed by measuring the scraper force (SCR), which is the shear force between the lower punch surface and the surface of the tablet. As expected, increasing the compaction pressure leads to stronger tablets that will result in a lower scraper force (Figure 2-5). At the same time, the study showed the effects of the compaction speed on the sticking behaviour, where high compaction speeds led to inadequate time to achieve relaxation within the tablet and consequently a higher amount of residual pressure imparted to the lower the punch, which is related to a higher adhesion force between the surfaces of the lower punch and the tablet.

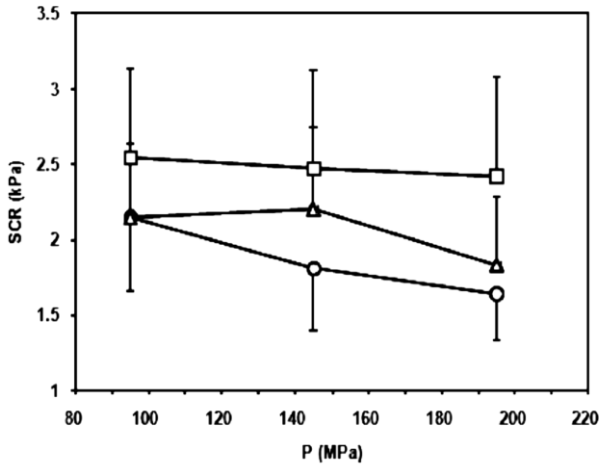

Figure 2-5: The relationship between the compression pressure and the scraper force at different compression speed, where; ○10 rpm; Δ 15 rpm; □ 20 rpm [31].

The effects of compaction pressure on compact sticking were further investigated by Waimer et al. [26] using a specially instrumented upper punch designed to measure the adhesion force that occurs when the punch detaches itself from the tablet surface after compaction. In the case of sorbitol tablets, increasing the compaction pressure resulted in higher adhesion forces with no sticking observed (Figure 2-6); this was claimed to be a result of increasing cohesion inside the tablet (no experimental proof was provided), so the tablet can detach itself completely from the punch surface with no sticking. Also, the force recorded in this case will be a true measurement of the adhesion on the tablet surface. Unlike Sorbitol, sticking was observed as a thin film of aggregated particles when microencapsulated acetylsalicylic acid (ASA) was used. Smaller adhesion forces were observed which indicate a lower degree of adhesion and cohesion inside the tablets (Figure 2-7). Increasing the compaction forces led to lower adhesion forces and less sticking occurrence (Figure 2-7); this was attributed to the higher level of cohesion inside the tablet at higher compaction forces. In all cases, adding magnesium stearate (MgSt) to sorbitol or microencapsulated ASA always led to a decrease in the measured adhesion forces.

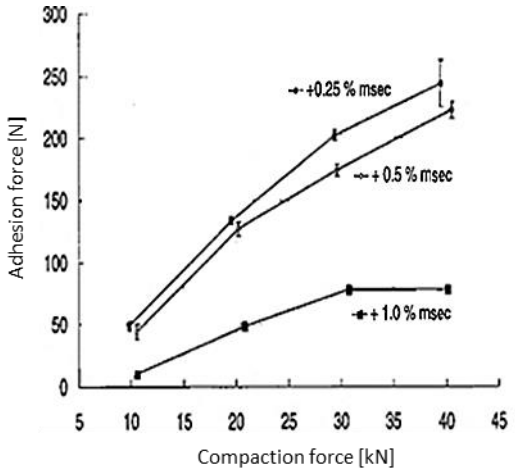

Figure 2-6: Adhesion force versus compression force profiles of sorbitol at three different magnesium stearate levels (0.25, 0.5, and 1.0%) [26].

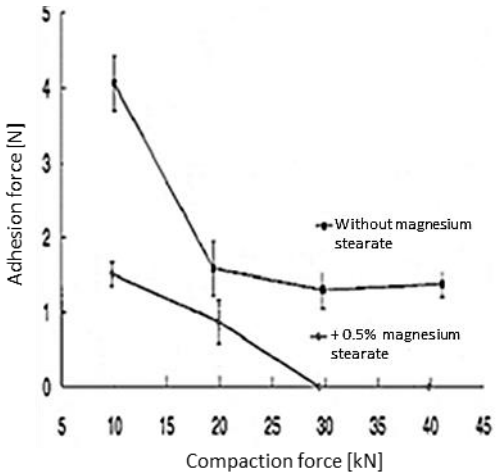

Figure 2-7: Adhesion force versus compression force profiles of microencapsulated ASA with and without 0.5% magnesium stearate [26].

A similar finding was reported by Toyoshima et al. [36] who used surface roughness measurements to evaluate the stickiness of lactose formulations. Tablets were compacted using a single-punch tabletting machine equipped with a concave punch and at a rate of 15 tablets per minute. Tablets were then measured for their surface roughness and the values of surface roughness were plotted against the number of compression cycle; the slope of the resulted regression line was used to evaluate tablet sticking so that higher slope values is an indication of higher sticking tendency. The study showed that the log of the sticking parameter for the different lactose formulation decreased as the compression pressure increases from 0.4 to 0.8 ton.

In another study, Paul et al. [37] studied the effects of compaction pressure on tablet sticking propensities of 5 active pharmaceutical compounds that were mixed with MCC and MgSt in the following percentages respectively 10%/89.75%/0.25%. Sticking was assessed by measuring the weight of the adhered mass on a removable punch tip. The tip was attached to the face of the upper punch. Unlike the studies mentioned above, it was shown that increasing compaction pressure from 50 to 200 MPa tends to make tablet sticking more problematic. This behaviour was attributed to the greater contact surface area between the active pharmaceutical ingredient (API) particles and punch tip achieved at a higher compaction pressure. However, the study did not take the role of the thermal sensitivity of the studied material into the account. For example, the relatively low melting point of ibuprofen ($T_m \simeq 76$ °C) could lead to contact melting and change the involved sticking mechanism [38].

Although extensive research has been conducted on the effect of compaction pressure on the occurrence of sticking during the tabletting process, no attempt has been made to investigate the effects of the applied stress on the development of sticking in the roller compaction process in which different combinations of normal and shear stresses are applied. This creates a research gap that will be addressed in more details in the coming chapters.

2.1.1.1.2 Effect of tooling surface engravings

Fitting imposing or engravings onto the compaction-tooling surface could be essential for identification purposes or to enhance the efficiency of the process; in the case of tabletting processes, engravings are applied to the surfaces of the tablets for identification purposes as ruled by the FDA for all solid oral dosage forms [39,40]. In the case of the roller compaction process, knurled rollers are usually used to overcome problems associated with insufficient gripping of feed powder into the gap between rollers. However, such modifications could deteriorate the sticking problems encountered during powder compaction [7,14,18,41,42].

Waimer et al. [43] used a specially designed upper punch to investigate the influence of engraving on the extent of tablet sticking by measuring the tablet pull off force; the punch was equipped with a small cone that could have different angles between the punch face and the cones lateral face (Figure 2-8). During unloading, the measured adhesion signal could either represents a separation at the punch surface (adhesion) or inside the tablet (cohesion).

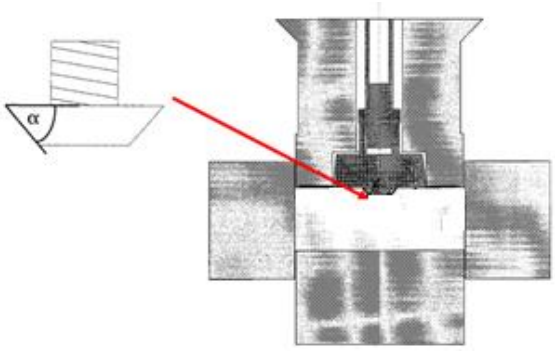

Figure 2-8: The instrumented compaction tooling used by Waimer et al. [43]. The figure also shows a schematic drawing to the shear cone that is fixed to the upper punch surface. α is the angle between the punch plain surface and the cone lateral surface.

The study concluded that the shape of the shear cones is an important factor for the occurrence of punch sticking; the two formulations explored in this study showed more

tablet sticking when the cone angle increased from 45º to 60 º. The study also mentioned that the cones create a stress and strength distribution at the tablet surface that could consequently affect the behaviour of sticking at the engravings of the punch surface.

Similarly, Roberts et al. [44] investigated the effect of punch tip embossments on tablet stickiness of an ibuprofen formulation. Tablet sticking was quantified by measuring the weight of the adhered powder on the upper punch tip. The presence of engravings on the punch faces significantly increased tablet sticking comparing with the non-embossed punches. This was attributed to the high shear stresses at the lateral faces of the engravings that enhance the occurrence of sticking during punch retraction. The authors stated that sticking to embossed punches was less dependent on compaction pressure compared with the non-embossed punches. The study also showed that sticking to the punch face was reduced by increasing punch tip curvature but was independent on punch diameter.

In the case of the roller compaction process, using knurled rollers could be advantageous in terms of increasing friction at powder/roller interface. This could be mandatory for some lubricated formulation. Otherwise, the powder will build up in the pre-nip area and block the feeding system [28]. However, the use of knurled rollers was observed by many researchers to deteriorate the occurrence of roller sticking and affect the efficiency of the process [7,14,18,28,41,42]. Alternatively, a pair of smooth rollers or a combination of knurled and smooth rollers are used to reduce roller sticking.

On the basis of the existing literature and experimental observations, further work is required to understand the impact of using knurled rollers in terms of its influence on the occurrence of sticking and the properties of the compacted ribbons.

2.1.1.2 Formulation related factors

2.1.1.2.1 Effect of particle mechanical properties

Particle adhesion to a surface can vary according to the mechanical properties of the contacting materials such as hardness, elasticity and viscoelasticity. These properties control the response of powder particles to the applied stress and can consequently influence powder sticking by changing both of bonding area and bonding strength either between powder particles (cohesion) or between powder particles and the metal surface (adhesion).

Hardness can be defined as the resistance of the solid material against the indentation caused by a second solid body [45]. On the other hand, elasticity is the ability of the

material to recover its shape and size upon load release and it is usually characterised by Young's modulus E_p [Pa] which is the constant of linear proportionality between the extensional stress σ [Nm^{-2}] and the extensional strain ε:

$$\sigma = E_p \varepsilon \quad \textbf{(}\text{Equation 2-1}\textbf{)}$$

However, during stress application, the nature of particle deformation changes from elastic to plastic at a certain applied stress called the yield stress (P_y). Additionally, if the mechanical properties of the material such as Young's modulus of elasticity changed with time, then the material is referred to as viscoelastic.

Paul et al. [37] studied the sticking propensities of five different APIs to the punch during tabletting; the API was mixed with MCC at 9.75 w/w%. Sticking was evaluated by the weight of the adhered powder to a removable punch tip after 25 compactions for a total of 100 compactions. They investigated tablet sticking at a range of powder deformability and compaction forces. The powders deformability was assessed by macro-indentation method using a spherical indenter on tablets made from 1:1 mixture of MCC and API; tablets have been compacted at a range of pressures, indentation hardness of the compacted tablets at zero porosity that is obtained by extrapolation was then used to order materials according to their plasticity. The study showed that the sticking tendency increases with increasing powder deformability in the moderate to high pressure range (100-200 MPa), the authors mainly attributed this to the higher contact surface area with the punch and the higher cohesion of the API to the sticking layer on the punch. However, it was difficult to show a clear relationship between particle deformability and punch sticking at lower compaction pressures. Nevertheless, the study neglected the effects of powder thermal properties, which could affect particle adhesion behaviour during compaction, for example, the relatively low melting point of ibuprofen (Tm ≃ 76 ℃) could lead to contact melting and change the sticking mechanism [38].

On the contrary, Chattoraj et al. [39] reported that a large number of compounds that show a tendency to stick during compaction are among those with the highest yield point in pharmaceutical formulations. For example, the authors mentioned both α-lactose monohydrate and mannitol as sticky materials with a relatively high yield-values in comparison with plastic materials. In another study, Abdel-Hamid and Betz [46] used the radial die wall pressure as a criterion to evaluate punch sticking; this includes SR (the stress ratio which is axial to radial stress transmission) and RDP (the residual die pressure

measured just after removing the normal stress). Different amounts of a highly sticking drug (Mefenamic acid) were mixed with various types of fillers that are either brittle (lactose or mannitol) or elastic-plastic (MCC or starch) in nature. The mixtures were then compacted using a compaction simulator at a range of compaction pressures. The study showed that formulations made with brittle fillers showed higher tendencies for punch sticking than viscoelastic fillers, which showed higher sticking to the die-walls. The authors ascribed sticking observations to the higher SR in the case of brittle fillers; they claimed that brittle fillers undergo higher axial to radial stress transmission which offers a higher chance for this formulations to interact with the punch surface and enhance punch sticking. This is unlike formulations made with viscoelastic fillers which exhibited higher tendencies for die wall sticking associated with higher values RDP; this was further confirmed by the higher ejection forces observed with these formulations.

So far, there are no available studies to investigate the effects of material mechanical properties on the sticking during roller compaction processes. However, some efforts were made to correlate powder mechanical properties to the cohesion properties of the compacted ribbons, which could be helpful to understand the sticking that could take place during roller compaction. Al-Asady et al. [45] successfully correlated the Nano-Indentation hardness for six different types of materials to their workability during roller compaction. The investigated materials ranged from very hard material calcium carbonate to a very ductile material MCC. Materials were characterised for their flow properties and compressibility and the maximum stress applied during roller compaction was estimated using Johanson's theory [47]. The authors found that if the measured particle hardness was lower than the maximum stress applied during roller compaction then stronger ribbon are expected as a result of more plastic deformation (Figure 2-9). Higher particle deformability was also associated with higher ribbon width and lower ribbon porosity. This was believed to be due to the higher contact area as a result of more plastic deformation that provided a higher probability for bonds formation.

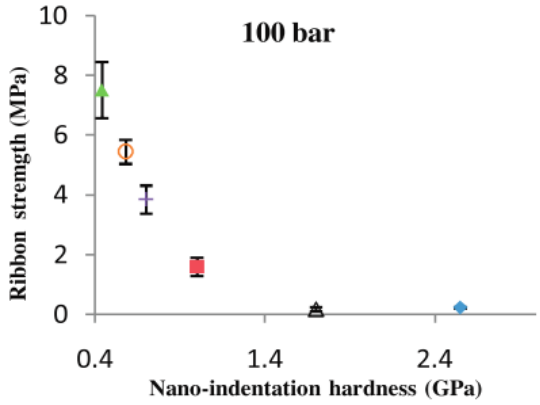

Figure 2-9: The effect of materials hardness value on its ribbon tensile strength that was produced using roller compactor at 100 bar hydraulic pressure. (▲Avicel PH 101, ○ Glucidex16, + Tylpor 604, ■ pharmatose 200 M, Δ sodium carbonate, ◆ calcium carbonate) [45].

2.1.1.2.2 Effect of Lubrication

One of the most obvious causes of sticking during compaction is insufficient lubrication of the formulation. In the pharmaceutical industry, the most common lubrication mechanism is boundary lubrication in which the lubricant particles form layers between the surfaces or at interfaces to reduce the direct contact between the intended surfaces. Lubricant concentration/mixing time in the formulation has to be optimized so that it can reduce unnecessary friction/adhesion to the tool surfaces at the minimal adverse effect on the particle-particle interaction inside the formulation, which could consequently influence the performance of the lubricated compact in terms of strength and dissolution [48].

Lubrication has been extensively studied in the field of tabletting processes; most of the research conducted in this field showed a significant reduction in the occurrence of sticking as the lubricant content was increased in the formulation [36,49,50]. However, not all materials show the same effect. Roberts et al. [51] used two different types of lubricant, namely magnesium stearate and stearic acid to evaluate the sticking tendency of an ibuprofen/lactose formulation on the punch tips during tabletting. Sticking was assessed by quantifying the amount of ibuprofen adhered to the upper punch using diode array spectroscopy. Unexpectedly, the study showed that increasing lubricant content does not reduce the sticking occurrence. Adding magnesium stearate to the formulation led to higher punch sticking, the authors attributed this to the lowering of ibuprofen melting point by magnesium stearate combined with the negative effect of the lubricant

on the cohesive forces within the tablet. The authors also mentioned that the presence of glidant (Aerosil) in the formulation alleviated the deleterious effect of magnesium stearate on the tablet strength. However this comes at the cost of reducing the lubricating efficiency and lead to capping problems.

Limited studies were conducted to understand the effect of lubrication on the performance of roller compaction processes; a study carried out by Dawes et al. [18] investigated the effect external lubrication on the adhesion behaviour of a pharmaceutical formulation containing adhesive API. A novel system was designed to spray a controlled quantity of magnesium stearate on the roller surface; the travel roll distance per shot (d_{ps}), which is the distance the circumference of the roll travels between lubricant shots has been used as a scalable parameter to ensure consistent lubrication during roller rotation (Equation 2-2).

$$d_{ps} = \frac{\pi . d_r . v_r}{S_{pm}} \qquad \text{(Equation 2-2)}$$

where, d_r is the roll diameter, v_r is the roll speed (rpm), and S_{pm} is the number of shots per minute (min^{-1}).

A placebo formulation of microcrystalline cellulose, anhydrous β-lactose and croscarmellose sodium were used in this study. It showed that reducing the d_{ps} from 3 to 1 cm led to four different scenarios of roller sticking that ranged from (a) the best case to (d) the worst case (Figure 2-10). Working with an unlubricated formulation led to the worst case in which the formulation adhered to the roller surfaces and formed a complete surface coverage (Figure 2-10-d). The application of external lubricant using a d_{ps} of 3 cm decreased the severity of the roller sticking so that the ribbons split in half after leaving the minimum gap and incompletely removed by the scraper (Figure 2-10-c). A further decrease of the d_{ps} to 2 cm leads to the compacted ribbon appearing to completely adhere to the roller surface, but it was entirely removed by the scraper and the roll surface remained clean during its rotation (Figure 2-10-b). At a roller travelling distance of 1 cm, the ribbon was observed to leave the roller surface immediately after release from the minimum gap with no splitting and again resulting in a clean roll surface (Figure 2-10-a).

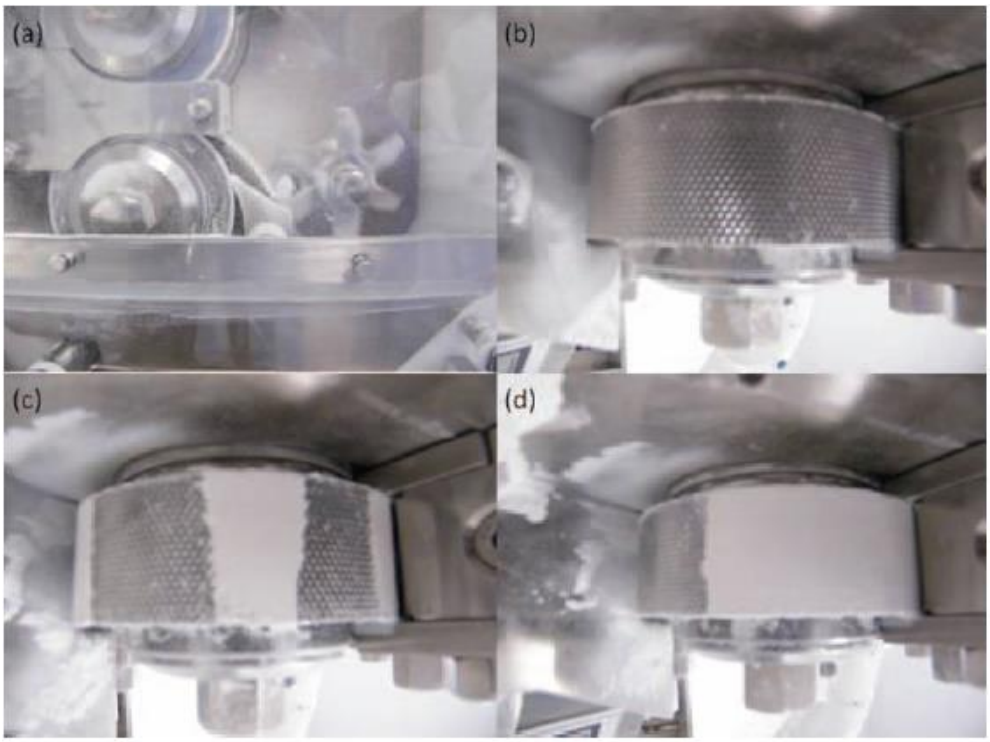

Figure 2-10: Suggested scenarios of the roller stickiness ranging from the best case (a) to worst case with complete roller coverage (d) [18].

The study also reported that sticking to the roller surfaces was associated with variation in the measured roller gap with time. The use of external lubrication kept the roller gap relatively constant. However, cessation of external lubrication resulted in a significant increase in the roller gap that started to fluctuate between 1.6 and 2.2 mm (Figure 2-11).

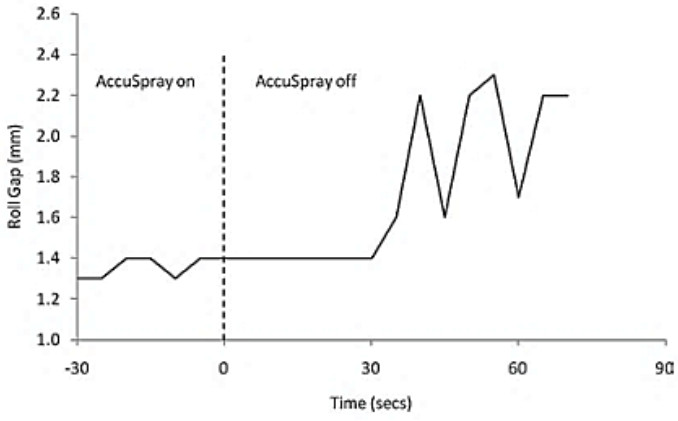

Figure 2-11: Change in roll gap distance as a response to external lubrication application.

A similar study conducted by the same researchers [28] in which a similar formulation of anhydrous β-lactose, microcrystalline cellulose and sodium croscarmellose sodium was used to investigate the effect internal lubrication (magnesium stearate) on the powder

feeding during roller compaction. It was shown that roller sticking of the unlubricated formulation occurred in about 30-60 sec from the start up. However, adding magnesium stearate to the formulations (from 0.05 to 0.5% w/w) completely impeded roller sticking during compaction. The authors reported that compared to the un-lubricated formulation, a lubricated formulation showed a higher mass throughput when a pair of knurled rollers were used. Nevertheless, this effect was remarkably lowered if one or both rollers were replaced with smooth rollers.

2.1.1.2.3 Contact melting

During compression, particles are subjected to high levels of localized stress that could create points of high temperature. The generated heat might exceed the melting/glass transition temperature of the compressed material and subsequently enhance its adhesion to the roller surface [52]. At relatively low temperatures, and excluding the effects of moisture, adhesion is dominated by London Lifshitz-van der Waals forces which are described by the following equation [34]:

$$F_{vdW} = \frac{\hbar\bar{\omega} r}{8\pi {h_d}^2} \qquad \text{(Equation 2-3)}$$

where F_{vdW} is the Lifshitz-van der Waal force [N], $\hbar\bar{\omega}$ is the Lifshitz-vand der Waal constant, [J], r is the particle radius [m], and h_d is the distance of separation between the contiguous bodies [m]. Temperature can affect the interaction constant $\hbar\bar{\omega}$, as it is a measure of the energy of the Lifshitz-van der Waal interaction between two bodies of similar or different geometry. This value may be measured using dielectric spectroscopy or can be derived from the properties of the materials in contact and can change according to the medium temperature [34].

At higher temperatures, closer to the thermal transition of the material that could be a glass transition in the case of amorphous material or melting in the case of crystalline materials, the heating will excite the molecules to higher vibration energies and consequently increase the mobility and its plastic deformability [53].

In the case of tabletting processes, the high compaction speed and the build-up of temperature during long operation times can increase the temperature by 20-30 $^{\circ}$C beyond the ambient temperature [52,54]. This could have an influence on a lower melting point

component of the formulation such as ibuprofen (T_m 75-78 °C) and affect both of the mechanical properties and the sticking behaviour of the compacted materials [19,51].

Danjo et al. [32] studied the effects of operating temperature on the sticking of butyl *p*-hydroxybenzoate during tabletting. Punch sticking was evaluated by measuring the pressure applied by the scraper to detach the tablet from the lower punch. Punch temperature was controlled using thermocouples that were placed at different parts of the tabletting machine and then connected to an air dryer. The study showed that the scrapper pressure indicates a maximum value when the ratio of the lower punch temperature to the API melting point becomes about 0.9 for every sample. This thermal ratio was accompanied by a remarkable punch sticking, which was attributed to the occurrence of sintering between the tablet and punch surfaces. The scraper pressure findings were further confirmed by conducting a shear test between the tablet and a metal plate surface at a range of temperatures using specially designed equipment. It showed that both scrapper pressure and shear strength were maximal at the same thermal ratio.

In another study, Cespi et al. [55] investigated the effect of processing temperature on the cohesion of tablets, which as explained previously could affect the sticking tendencies during tabletting. Four different types of pharmaceutical excipients that have different mechanical behaviours and distinct thermal sensitivities were investigated; this included both of microcrystalline cellulose (MCC) and dicalcium phosphate dehydrate (PDC) which do not have any thermal change in the range of 20-150 °C, polyethene oxide (PEO) which has a melting point between 50-75 °C, and Eudragit RS (EURS) with a glass transition transformation at 50-60 °C. Tabletting was conducted using a rotary tabletting machine that was equipped with special sensors and devices to control temperature and humidity in the compaction area. The authors reported that only materials which have a thermal change at relatively a low range of temperatures showed a changed in the compact properties. Yet, this change was less significance for less ductile and negligible for brittle materials. As shown in Figure 2-12, both PEO and EURS have a significant increase in the deformability (lower yield strength (P_y) values-determined by Heckel analysis) at lower temperatures. On the other hand, both MCC and PDC were less affected. The effect of temperature was reflected as a change in tablet tensile strength; an analysis showed a remarkable increase in tablet strength for materials characterized by a thermal transition at low temperatures.

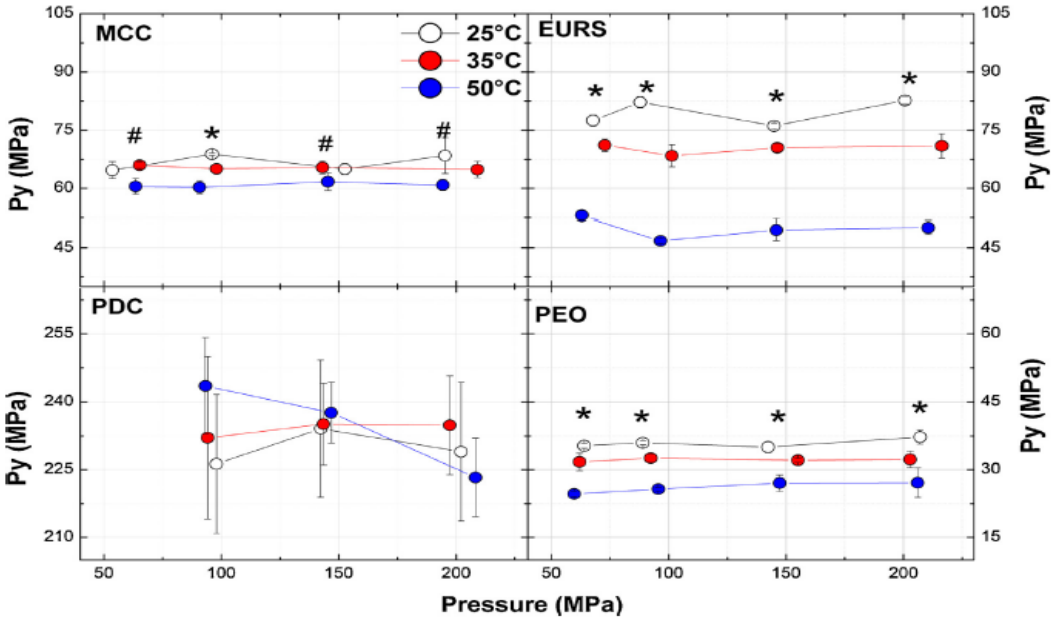

Figure 2-12: Effect of the temperature and compression pressure on the yield pressure (P_y) values derived from Heckel analysis for all the different materials tested. To easily compare materials with different ductility and consequently P_y, the y-axis is set to show a Py range of 60 MPa. Symbols * and # refer to statistical significance [55]

In the field of roller compaction, powder particles are subjected to high levels of friction, deformation, and fragmentation that could significantly increase ribbon temperature and subsequently affect its adhesion tendency. Osborn et al. [8] used a thermal imaging technique to on-line record the surface temperature profile of the ribbons. It was found that the ribbon surface temperature is a material-dependent phenomenon; the temperature being generated by friction and stress applied to the material during processing. Altering some processing parameters such as hydraulic pressure, gap distance, roller speed and the lubricant concentration can significantly affect the temperature of the ribbon (Figure 2-13). On the other hand, changing other processing parameters such as the use of a cooling system did not have an effect on the ribbon temperature. However, it is worth mentioning that the use of a cooling system appeared to limit the sticking of maltodextrin at high compaction pressures [8].

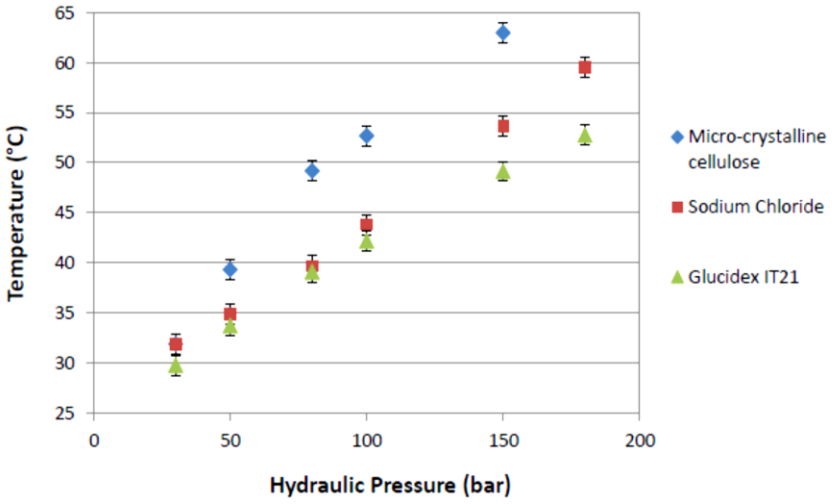

Figure 2-13: Temperature increase of ribbons of different materials during roller compaction at varying hydraulic pressures [8].

In a more detailed study, Omar et al. [56] employed an online thermal imaging technique to determine ribbon surface temperatures at a wide range of processing parameters. α-lactose monohydrate was used as a model material for this study. Ribbon surface temperature was shown to increase slightly with increasing roller speed; this was attributed to both 1) the increase in powder internal friction at higher powder velocities when powder particles pass between the rollers and 2) the increase in the feeder screw speed at constant gap distance. Similarly and due to the same reasons, increasing either gap distance or screw speed lead to higher of ribbon surface temperatures.

More recently Wiedey and Kleinebudde [57] evaluated the use of thermography technology to monitor the cohesion property of the ribbon in terms of its solid fraction. The applicability of this technique was tested on a wide range of fillers that possess different mechanical and thermal properties and at various levels of magnesium stearate. A calibration curve was developed to correlate ribbon surface temperature with the solid fraction. The curve was then applied to determine ribbon solid fraction at a wide range of processing parameters. The authors reported that calibration curves varied substantially in terms of slope and offset so that a new calibration curve has to be devised for every formulation. For all tested materials, the ribbon surface temperature increased at higher solid fractions, however this relationship varied significantly in the case of roller sticking occurrence; plastic materials with no roller sticking showed high R^2, whereas moderately sticking DCPA showed a lower value and the extremely sticking mannitol showed a much lower correlation value (Table 2-2). The authors referred that to the reduction in the gap

distance when material permanently adhere to the roller surface. Moreover, the study showed that adding magnesium stearate to the powder lead to higher heat development especially when a pair of smooth rollers were employed; this was claimed to be a result of the accumulation of powder around the tamping auger, which by friction increased the temperature of the powder prior to compaction.

Table 2-2: Correlation between sticking to roller surface and the adjusted coefficient of determination [57].

Material	Roller sticking	R^2
Isomalt	None	0.9999
MCC	None	0.9884
DCPA	Moderate	0.9505
mannitol	Massive	0.7893

2.2 Compact defect due to improper interaction between powder particles (cohesion-induced defects)

In addition to the compact defects induced by the powder-metal interaction (adhesion induced compact defect), a compact defect can also originate from the response of the compacted material to the applied stress (cohesion-induced defects), this is similar to the capping and lamination encountered during tabletting processes. Several hypotheses were made to understand the incidence of such kind of failure. Dwivedi [58] hypothesised that compact failure during decompression occurs when the bonds formed during compression cannot withstand the elastic recovery during decompression. Furthermore, Wu et al. [59] used the finite element method (FEM) to investigate the compaction behaviour of powder during compaction. Lactose powder was modelled as an elastoplastic continuum using the Drucker-Prager Cap (DPC) model. The FEM showed a heterogeneous density distribution across tablet dimensions; very dense zone at the top edge of the tablet and a relatively low density at the lower edge (Figure 2-14-A).

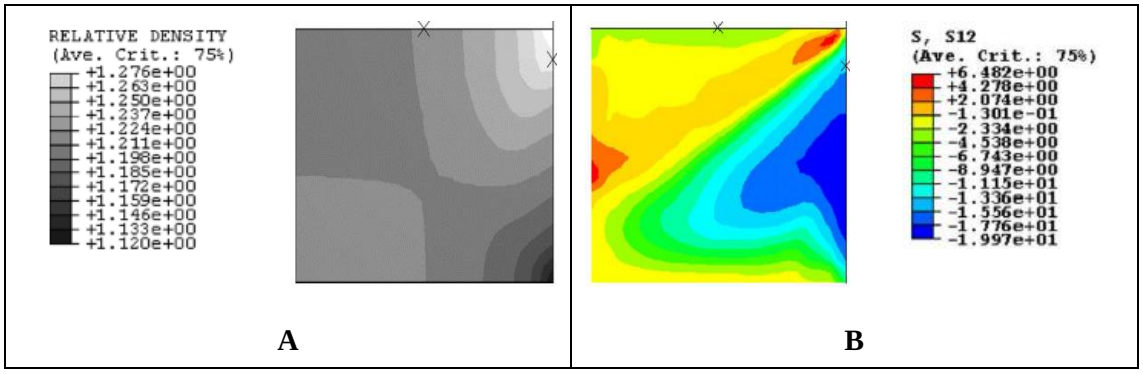

Figure 2-14: the distribution of (A) density at maximum compaction pressure and (B) Shear stresses as reported in Wu et al. [59].

This heterogeneity was attributed to the friction along the die wall that inhibits powder movement as the punch moves downwards. The heterogeneity of the density distribution indicates more relaxation at the tablet top compared with that at the bottom. Tablet recovery was associated with intensive shear bands that propagate from the surface towards the centre edge (Figure 2-14-B); this shear band was considered to be the main cause of capping during de-compaction. The results of the density distribution and development of failure were all demonstrated experimentally using X-ray microtomographic images. This mechanism of compact failure has also been reported in a similar study [17].

It has been suggested that other contributory factors could also participate in the development of the compact defects such as air entrapment, which prevents strong bond formation during compaction [60], friction conditions between the powder and the die wall [17], and the deformation characteristics of the compacted materials [15,61].

On the other hand, so far there is no clear understanding of the cohesion-induced compact failures that take place in the roller compaction processes. However, a few researches reported the occurrence of such defects during roller compaction; no clear understanding of the underlying mechanism was provided. Wu et al. [62] investigated the effects of the moisture content of microcrystalline cellulose (MCC) as a feed powder and noted that the ribbons produced at high values (>11.44 %) tended to split across the width. It was ascribed to the resulting reduction in the tensile strength of the ribbons. Ende et al. [63] reported that, for a range of powder feeds, the occurrence of ribbon splitting (the exact location of the splitting was not mentioned) was minimised when the gap was < 2.6 mm. Cunningham et al. [64] suggested, based on finite element modelling that the reversal of the direction of the shear stress at the neutral angle could be a contributory factor given

that particle compacts are weak in shear. However, it would be difficult to evaluate experimentally.

Similar to the capping phenomenon in tabletting, ribbon failure during roller compaction could be a result of serious flaws that may have its impact on the final product attributes. Accordingly, building a mechanistic understanding of this phenomenon might assist formulators and designers to avoid the underlying cause of splitting.

2.2.1 Factors affecting defects due to improper particle-particle interaction

2.2.1.1 Material related causes

2.2.1.1.1 Effect of materials mechanical properties

Material mechanical properties are one of the main contributory factors to the occurrence of the cohesion-induced defects such as capping and lamination in tabletting or ribbon splitting encountered in the roller compaction process. In the case of the tabletting process, Mullarney and Hancock [65] investigated the capping tendency of six different pharmaceutical excipients that have various degrees of deformability. Cubic compacts were made using a uniaxial compaction machine; the compacts were then subjected to indentation and transverse tensile testing in different orientations. The degree of compact anisotropy was then determined based on dimensionless ratios namely, the axial to radial tensile strength and the side to top indentation hardness. The study showed that compacts with higher anisotropy levels showed higher brittle fracture values. The degree of anisotropy was compared with tablet tensile strength to assess capping tendency. For example, α-lactose monohydrate showed moderate to high anisotropy values coupled with a relatively low compact tensile strength, which suggested that this material has a higher tendency for capping. On the other hand, MCC was unexpectedly found to have a comparatively high level of anisotropy, however, the authors claimed that the very high tensile strength of the compact acts to compensate for its anisotropy and thus prevented any capping.

In another study, Paul and Sun [66] examined the in-die compaction data in an attempt to understand the mechanism of tablet failure (capping/lamination). The authors investigated the capping propensity of an acetaminophen-containing formulation, which is a well-known poorly compressible drug. The deformability of the formulation was varied by increasing the API concentration by 25% increments in a binary mixture with

MCC. An instrumented compaction simulator was then used to make tablets over a pressure range of 25-300 MPa; the maximum die wall pressure (MDP), residual die wall pressure (RDP), and the ejection force were recorded for each tablet. The deformability of the different formulations was determined using Heckel's analysis. Using the in-die compaction date, the following results were found and used to build an empirical equation for capping prediction: 1) high powder yield strength resulted in mechanically weak tablets and higher capping probability; 2) the maximum die wall pressure was independent of composition and compaction speed and had no effect on capping; 3) the in-die tablet elastic recovery (IER) increased at both higher compaction pressures and higher drug loadings and lead to higher levels of capping; 4) the residual die wall pressure was insensitive to the increase in drug loading up to 50%, however, increasing the drug loading to 75% and 100% significantly reduced the residual die wall pressure, which was attributed to the occurrence of capping inside the tablet; 5) increasing both compaction pressure and API concentration resulted in a higher Poisson's ratio (p_r) and greater capping propensity. Figure 2-15 shows the capping and non-capping zones in relation to the most statistically significant affecting processing parameters.

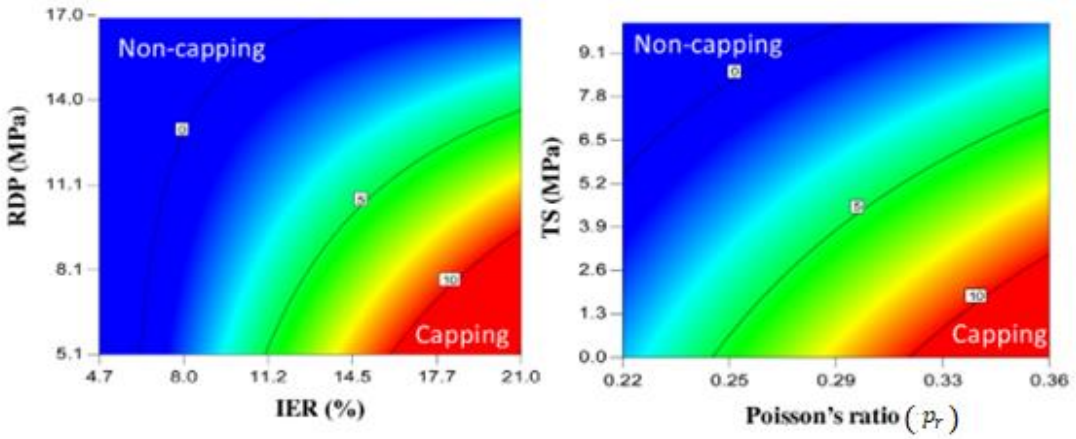

(A) (B)

Figure 2-15: Contour plots of capping and non-capping zones at (A) constant tensile strength and Poisson's ratio and (B) constant in-die recovery and residual die pressure [66].

Eventually, the most statistically significant capping factors were implemented in a two factor-interaction model to predict capping propensity (CP) as follows:

$$CP = -2.29 + 0.65.IER - 8.5.RDP - 5.73.TS + 6.24.p_r - 5.44.RDP.TS - 0.44.TS.p_r \quad \text{Equation 2-4}$$

Similarly, Kuppuswamy et al. [67] investigated the role of powder mechanical properties on the capping tendency; three sets of binary mixtures were chosen to represent three different types of deformation combinations namely, plastic-plastic, brittle-plastic and brittle-brittle. MCC and magnesium stearate (MgSt) were selected as plastic model materials, while dicalcium phosphate dihydrate (DCP) and acetaminophen (APAP) were chosen as brittle materials. The capping propensity was evaluated by conducting indentation hardness measurements on the surfaces of the different tablets; the study classified capping tendency according to the indentation depth at which a crack takes place, while the surface crack is evaluated based on images taken by light and scanning electron microscopes. If the indentation test leads to cracks at an indentation depth of 0.5 mm or lower, the tested material is then classified as susceptible to fail upon compaction. Also, if no cracks occurred up to 0.7 mm, this indicates low failure risk. Nevertheless, cracks initiated between 0.5 and 0.7 mm and then the material has to be treated with caution. The results are mainly attributed to the ability of the plastic material to prevent crack propagation.

Similar findings were reported in another study [15]; however, so far, no attempts have been conducted to understand the developments of such compact defects in the field of roller compaction.

2.2.1.1.2 Effect of lubrication

Lubricants are well known to reduce both powder/tooling and powder/powder friction, which could be beneficial in minimising compact defects [68]. Factors like lubricant concentration [69], type [70], method of application [71], and drug-lubricant interaction [72] are the main factors that should be optimised before lubrication. Takeuchi et al. [71] assessed the effects of lubrication on the capping tendency of two different pharmaceutical excipients, namely lactose and mannitol, during tabletting. MgSt was either added by internal or external methods; in the case of the external method, the lubricant was applied directly on the die wall using a cotton bud. Whereas in the case of internal lubrication, each excipient was mixed with different concentrations of MgSt in the range of 0.1 to 1%. The capping tendency was evaluated based on the several compaction parameters including MDP (mean die wall pressure), RDP (residual die wall pressure), and the ratio of RDP/MDP. The study presented RDP/MDP as a novel index to predict capping propensity even in the case of external lubrication. A lower index value

suggests a higher degree of bond formation and lower capping tendency; this is because of the higher stress transition at the maximum applied normal stress as indicated by the MDP, in addition to the lower friction with the die wall as presented by the RDP. The effect of lubricant addition on the suggested capping index is shown in (Figure 2-16); the use of external lubrication for lactose and mannitol corresponds to 1% and 0.5% for those internally lubricated tablets. As seen in the figure, adding lubricant either internally or externally was successful in minimising tablet capping, which extensively happened without lubrication. Capping occurrence a is represented by (*).

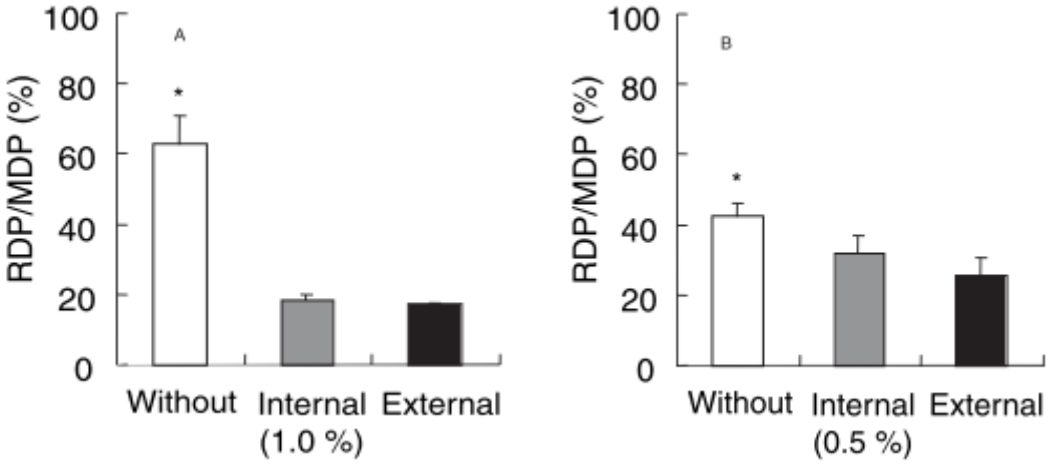

(A) (B)

Figure 2-16: effect of external and internal lubrication on the RDP/MDP for A: lactose and B: mannitol. * Capping was observed during tabletting [71].

Similar findings were reported by Zuurman et al. [73] who investigated the effect of MgSt on the level of particle bonding of two materials with different deformation behaviour namely, MCC (predominantly plastically deformable) and sorbitol (more brittle in nature). In comparison with sorbitol, MCC tablets showed a higher lubricant sensitivity as indicated by the higher reduction in tensile strength when lubricant was added (Figure 2-17 A-B). This was attributed to the fragmentation of sorbitol aggregates, which destroys lubricant films and create new clean particle surfaces that are free for interparticular bonding. However, the brittle nature of sorbitol made it more susceptible to the occurrence of capping, which was denoted by the higher discrepancy of the sorbitol tablet tensile strength data when plotted against its compaction pressure. The data plotted by an astrix represent unlubricated sorbitol tablets that do not fit the corresponding curve. Adding MgSt resulted in weaker tablets with more consistent data to the fitting line, which was associated with no capping incidence (Figure 2-17).

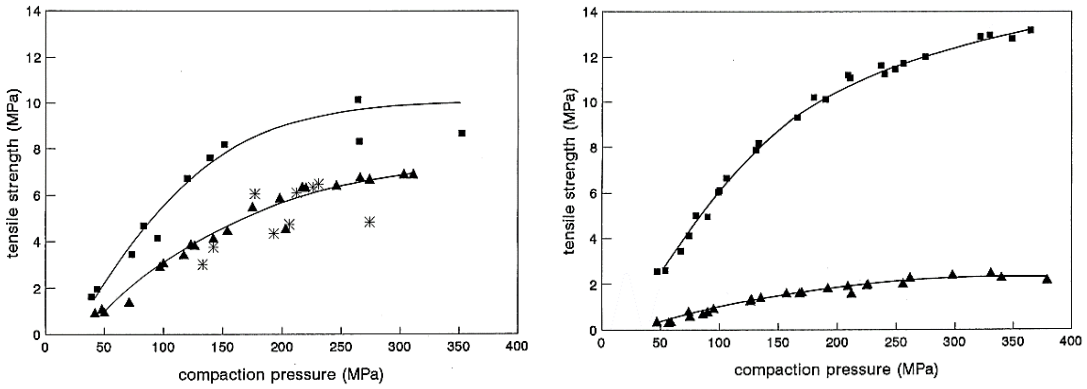

(A) (B)

Figure 2-17: Tensile strength of unlubricated (■) and lubricated (▲) tablets of sorbitol (A) and MCC (B) at a range of compaction pressures. (*) represents unlubricated sorbitol tablets which show start of capping [73].

A different conclusion was made by Dudhat et al. [74] who evaluated the capping propensity of the tablets that are made from a blend of pharmaceutical powders (APAP/MCC) based on their rheological properties and more specifically the powder air permeability. Powders with higher air permeability are more able to relieve the entrapped air and reduce the occurrence of compact defects. The permeability of the powder blend was measured by compacting the blend at a series of normal stresses by a vented piston. Subsequently the powder bed base was subjected to a constant velocity air stream. The permeability was then determined according to the pressure drop across the powder bed. The study showed that increasing APAP (API) contents lead to a significant increase in the pressure drop at about 80 % API content (Figure 2-18). The authors claimed that this significant change in the pressure drop was responsible for the high capping propensity at this API %. Adding 0.5% MgSt to the APAP formulations showed a higher level of pressure drop compared with the non-lubricated formulation (Figure 2-18), i.e. lubrication did not ease the ability of the powder bed to relieve the entrapped air. This could eventually explain the inefficacy of using MgSt to prevent the occurrence of capping with these formulations.

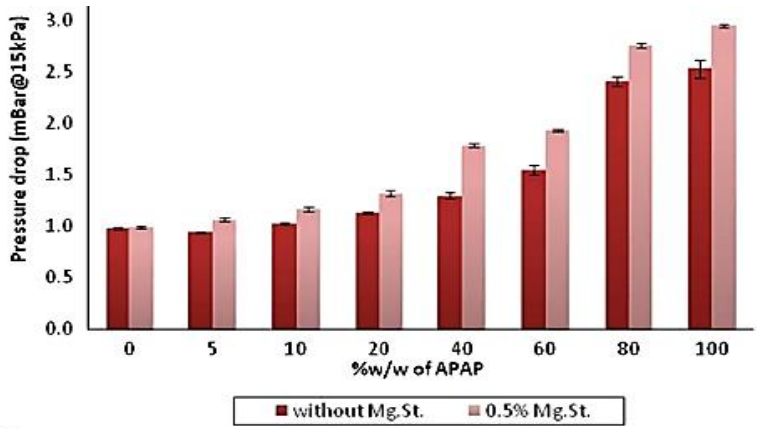

Figure 2-18: Permeability of powder bed expressed as the pressure drop across the powder bed at 15 kPa as a function of API contents. The measurements were conducted with and without 0.5% MgSt

In conclusion, there is considerable research that has investigated lubrication as a strategy to alleviate the occurrence of compact defects during tabletting. However, so far, no research trials were conducted to investigate such a strategy in the field of roller compaction.

2.2.1.2 Process related factors

2.2.1.2.1 Effect of compaction pressure and speed

During powder compaction, particles are subjected to an increasing pressure by which particles undergo various deformation mechanisms, including elastic deformation followed by plastic deformation and/or fragmentation. This is followed by the unloading stage during which some of the stored elastic strain is restored. Excessive elastic deformation could lead to compact defects if it is high enough to overcome the interparticular bonding formed in the compaction phase. The level and rate of pressure application are critical factors for both the interparticular bonding and elastic recovery in the unloading phase. Akseli et al. [75] investigated the effect of compaction pressure and speed on the capping propensity during the tabletting process. The authors developed a non-destructive method to predict capping propensity based on the acoustic property of the compact; tablet axial and radial sound wave propagation velocity was determined and correlated with the elastic property of the compact at different orientations. The degree of capping was then evaluated using a dimensionless ratio as EG = $E_{\text{axial}} / E_{\text{radial}}$ which is the ratio of the axial to radial Young's modulus of the tablet. Based on the experimental results higher EG values indicate more homogenous compact and less probability of capping. A diverse set of pharmaceutical formulations (28 blends) were compacted at a

rage of compaction forces (5-25 kN) and compaction speeds (25, 40 and 80 rpm) and the resulted tablets were analysed for their acoustic properties using a pair of 5 MHz transducers operating in pitch-catch mode. The study showed that increasing compaction force led to lower EG values and subsequently higher capping tendency. In terms of compact porosity, capping was more pronounced at porosities less than 25%. This was ascribed to the higher stored elastic strains at higher compaction forces, this strain is restored at the decompression phase and act as a stress concentrator to decrease the compact integrity. Additionally, the authors mentioned that overcompaction of the powder bed could result in intensive shear bands during decompression which may break the already formed interparticular bonds and cause compact defects. On the other hand, increasing compaction speed generally coincided with a higher degree of compact defects. However, no scientific evidence was provided to support this finding.

The previous results were further confirmed by Paul and Sun [66] who investigated the effect of both compaction pressure and speed on the occurrence of tablet defects. Different amounts of acetaminophen powder were mixed with MCC and MgSt, the blends were then compacted over a pressure range of 25-300 MPa and at a dwell time of 10, 15, 25, and 100 ms. The study showed that increasing both compaction pressure and speed tends to increase the propensity of capping. This was ascribed to the increased in the level of elastic recovery as indicated by the measured in-die elastic recovery (IER %), this could weaken the interparticular bonding and enhance the probability of compact defects (Figure 2-19-A). Moreover, reducing tabletting speed at constant pressure tends to improve bond formation and reduce capping (Figure 2-19-B). Excessive increases of the applied pressure (>200 MPa) was associated with a sudden fall in the measured tensile strength which was claimed to be a result of the development of macro cracks in the tablet structure. Consequently, the measured tensile strength, in this case, represents the energy of crack propagation rather than the interparticular strength (Figure 2-19-B).

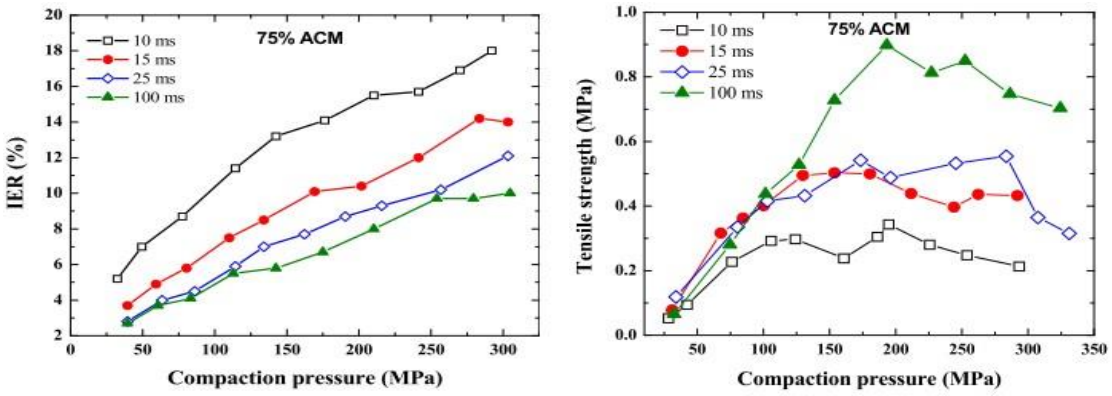

(A) (B)

Figure 2-19: the effect of compaction pressure on A: in-die elastic recover (IER %) and (B) tablet tensile strength for a formulation containing 75% Acetaminophen [66]. The time shown on the figures is the dwell time.

In the field of roller compaction, limited or no research trials have been carried out to understand the effect of roller pressure and speed on the development of ribbon defects; the literature has mainly focused on the impact of these parameters on some of the ribbon properties such as the ribbon strength and density. It is generally believed that the roller compaction pressure is the most influencing parameter on ribbon and granules properties; increasing compaction pressure increases ribbon density and strength and has the same impact on granules properties [76–78].

On the contrary, increasing roller speed at constant feeder screw speed was found to reduce the ribbon tensile strength and density; this is believed to be due to the fact that increasing roller speed at constant feeder screw speed reduces the amount of powder delivered to the compaction zone and subsequently reduces the ribbon width, thickness, and breaking force [77,79].

2.2.1.2.2 Effect of tooling geometry/roughness

Tooling design and specifications such as the punch curvature/die wall roughness in tabletting process or roller surface features in roller compaction process are one of the parameters that could influence the properties of the compact during the compaction process. However, very limited research works have been carried out to understand its impact on compact integrity. In tabletting, changing punch curvature/roughness was found to change the pressure distribution and affect defects behaviour upon decompression; Wu et al. [80] have conducted a numerical and experimental study to investigate the occurrence of capping. The study demonstrated that the main cause of

capping is the intensive shear bands formed during decompression. The authors explored different approaches to alleviate capping propensity; based on FE numerical modelling, the study evaluated capping propensity by analysing the pattern of the shear stress distribution under different process parameters. It was found that decreasing die-wall coefficient of friction did not eliminate the development of the shear bands; the results showed intensive shear bands running from the top edge to the mid-centre at both low and high die-wall friction values (Figure 2-20 A-B). Moreover, the results showed less intensive shear bands for convex tablets comparing with flat-faced tablets (Figure 2-20 B-D). This agreed with the experimental observations, where less capping was observed when increasing the concavity of the punches used.

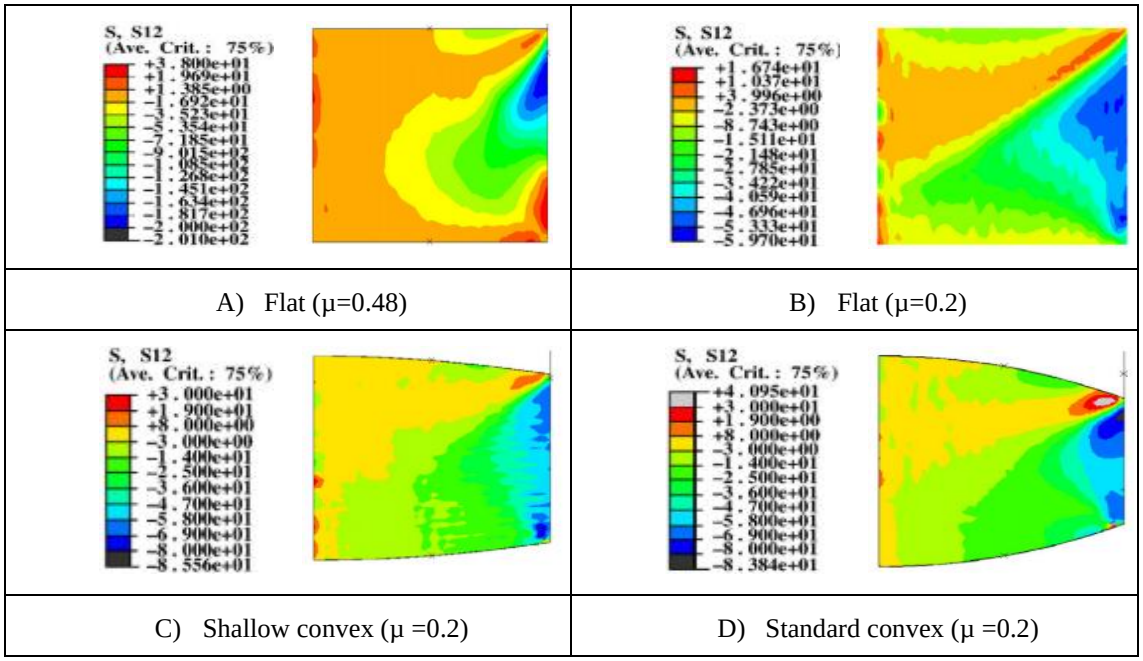

A) Flat (μ=0.48) | B) Flat (μ=0.2)

C) Shallow convex (μ =0.2) | D) Standard convex (μ =0.2)

Figure 2-20: The shear stress distribution during decompression for compaction with different die-wall friction and surface curvatures [80].

Similarly, Akseli et al. [75] reported in their study that a better tabletting performance and lower capping propensity was observed when a more rounded punch surface was used. Moreover, in another study, Paul and Sun [66] reported that increasing the API% in the formulation increased the coefficient of friction between powder and die wall, however at a higher API percentage (i.e. >75%), there was a remarkable decrease in the coefficient value which was attributed to the occurrence of capping.

In the field of roller compaction, there have been no studies so far concerning the role of roller surface specification in the occurrence of ribbon defects i.e. ribbon splitting.

However, some efforts have been made to understand the role of roller surface features such as roller knurling and roughness on ribbon density, which could improve our understanding to the development of ribbon defects i.e. ribbon splitting. Daugherity and Chu [81] investigated the effect of roller serration volume on ribbon thickness; a set of four different rollers with various roller serration volumes were employed to roller compact a formulation of lactose, MCC and MgSt into ribbons. The results showed that at the same processing condition i.e. constant roller pressure/auger speed/roller speed, ribbons produced with more serrated roller surface have higher ribbon thickness. This was attributed to the fact that more serrated rollers can draw more powders into the compaction area and increase both gap distance and ribbon thickness. More recently, as a part of their study, Csordas et al. [82] investigated the effect of roller surface on ribbon relative density; two pairs of smooth and knurled rollers were used to compact MCC and mannitol, mixtures of MCC/mannitol into ribbons. Comparing all relative density results it was found that denser ribbons were obtained for all studied materials when roller compaction was performed with smooth rollers (Figure 2-21 A-B). The ribbon relative density was determined from the ratio of the envelope to true density; envelop density was measured using a Geopyc powder pycnometer, so that only an average value was taken to represent ribbon density, i.e. the study did not take the effect of the well-reported density heterogeneity into consideration when making this argument. The authors attributed this to the greater contact area achieved when knurled rollers are used; this resulted in less stress than the one exerted by the smooth rollers. Moreover, the study mentioned that all ribbons made with mannitol showed significantly higher ribbon relative density than MCC or MCC/mannitol mixture.

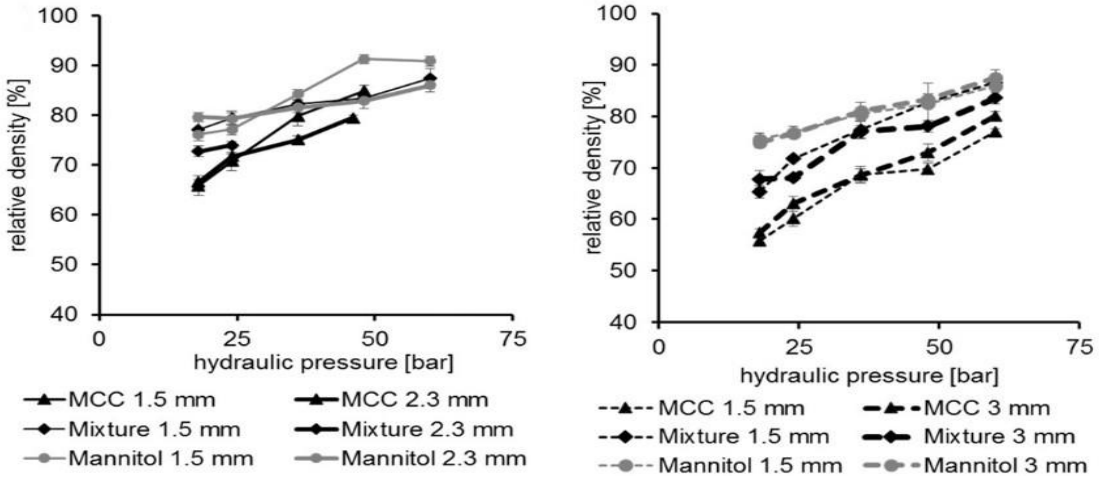

(A) smooth **(B) knurled**

Figure 2-21: Relative density of MCC, mannitol, and MCC/mannitol ribbons produced using a pair of smooth (A) and knurled (B) rollers [82].

2.3 Predictive models in roller compaction

Various theoretical models have been developed to enhance our understanding of the roller compaction mechanics which is essential when trying to optimise, design, control, and overcome challenges. These models have been developed to predict different critical attributes such as the maximum normal stress and ribbon density. The maximum stress applied during compaction is considered to be the most influential parameter over ribbon physical properties such as ribbon density and strength. Thus, building a predictive model for the stress profile of roller compaction could be of great importance to improve our understanding of the process as well as reducing time and efforts spent during trial and errors experiments.

2.3.1 Johanson's Model

Johanson [47] has developed a comprehensive model based on the Jenike yield criteria for particle steady flow in hoppers and silos. This model assumes the powder to be isotropic, compressible, frictional and cohesive. The model uses both equipment geometry specifications and three main physical properties, namely, the effective angle of internal friction (δ_E), the angle of wall friction ($\emptyset_w$), and the compressibility factor (K) to determine the nip angle and the maximum stress applied to the material. Both effective angle of internal friction (δ_E) and angel wall friction ($\emptyset_w$) can be measured experimentally using a shear cell. The compressibility factor (K), can be determined from

the slope of the logarithmic plot of the density ρ as a function of the pressure p during uniaxial compression.

$$\log\frac{p_1}{p_2} = \mathrm{K}\log\frac{\rho_1}{\rho_2} \qquad \text{Equation 2-5}$$

The model divided the compaction zone into two zones according to their angular positions. Assuming that slip (roller speed is higher than powder speed) is happening along a certain angular range of the roller surface, Johanson described the pressure distribution in this area by the following equation [47]:

$$\left(\frac{d\sigma}{dx}\right)_{slip} = \frac{4\sigma_\theta\left(\frac{\pi}{2}-\theta-\nu\right)tan\delta_E}{\frac{d_r}{2}\left(1+\frac{s}{d_r}-cos\theta\right)cot(A-\mu)-cot(A+\mu)} \qquad \text{Equation 2-6}$$

where σ_θ is the mean normal stress at position θ, θ is the angular position in roll bite, δ_E is the effective angle of the internal friction (related to material flow property), d_r is the roll diameter, and s is the gap between the rollers.

A is a parameter given by:

$$\mathrm{A} = \frac{\theta+\nu+\frac{\pi}{2}}{2} \qquad \text{Equation 2-7}$$

ν is described by the following equation:

$$\nu = \frac{1}{2}\left(\pi - sin^{-1}\frac{sin\emptyset_w}{sin\sigma_\theta} - \emptyset_w\right) \qquad \text{Equation 2-8}$$

where $\emptyset_w$ is the angle of wall friction (related to material flow property), and μ can be calculated by the following equation [47]:

$$\mu = \frac{\pi}{4} - \frac{\sigma_\theta}{2} \qquad \text{Equation 2-9}$$

As the materials arrive to the nip area where no slipping is occurring, all materials are trapped and compressed to the thickness of the roll gap and the stress distribution in this area is covered by the following equation [47]:

$$\left(\frac{d\sigma}{dx}\right)_{Nip} = \frac{K\sigma_\theta\,(2\,cos\theta - 1 - (s/d_r))\,tan\theta}{(d_r/2)\,[d/d_r + (1 + (s/d_r) - cos\theta)\,cos\theta]} \qquad \text{Equation 2-10}$$

where d can be defined as the average thickness of the ribbon rolled when the roll gap S is zero.

The angle at which the pressure gradient of both the slip and nip areas are equal is called the nip angle (α) and is determined by equating the pressure distribution in Equation 2-6 and Equation 2-10 as shown in Equation 2-11 :

$$\left(\frac{d\sigma}{dx}\right)_{Nip} = \left(\frac{\mathrm{d}\sigma}{\mathrm{dx}}\right)_{\mathrm{slip}} \qquad \text{Equation 2-11}$$

Subsequently, the maximum stress applied to the material can be calculated by the following equation [47]:

$$p_{\max} = \frac{2\mathrm{R_f}}{\mathrm{W}\,d_r\,\mathrm{f}} \qquad \text{Equation 2-12}$$

Where R_f is the roller separating force, W is the roller width, and f_{fac} is the force factor and is given by the following equation [47]:

$$f_{fac} = \int_{\theta=0}^{\theta=\alpha} \left[\frac{{}^{s}/_{d_r}}{\left(1 + {}^{s}/_{d_r} - \cos\theta\right)\cos\theta}\right]^{\mathrm{K}} \cos\theta \mathrm{d}\theta \qquad \text{Equation 2-13}$$

Johanson's model has been validated by many researchers to predict the pressure profile along the roller surface; Bindhumadhavan et al. [83] used an instrumented roller press equipped with a piezoelectric transducer to validate the maximum normal stress predicted by Johanson's model. In this study microcrystalline cellulose was compacted at a range of processing parameters using a gravity feeding system, the study showed a close agreement between the experimentally measured maximum stress and that calculated by Jonahson's theory for a range of gap sizes (Figure 2-22).

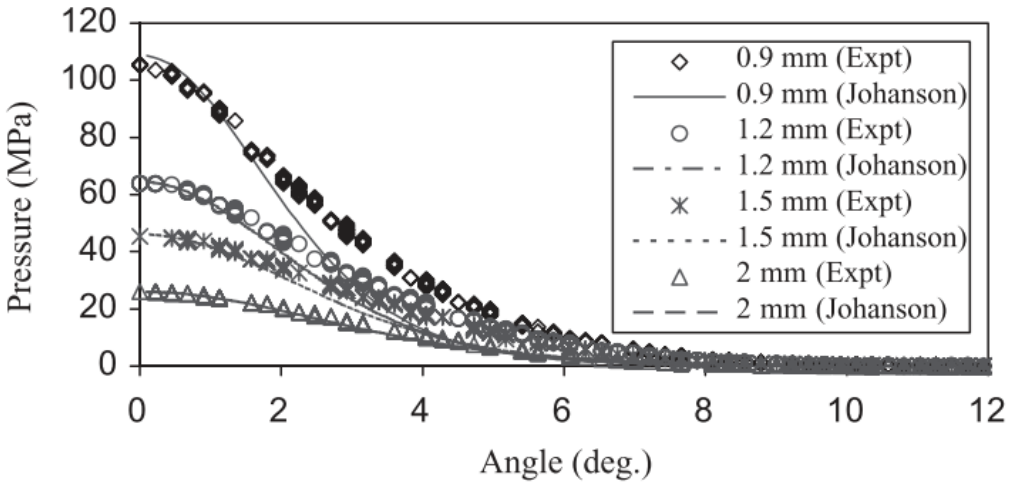

Figure 2-22: Comparison between experimentally and predicted stress profile calculated using Johanson's model at a range of gap distances [83].

In another study, Yousef et al. validated Johanson's theory by comparing the predicted Johanson's values of roller separating force and roller torque with those measured experimentally. The study mentioned that the predicted values of the model were in reasonable agreement with the experimental results.

The theory is widely applied in the field of roller compaction [7,41,84]. However, in addition to its weakness with respect to predicting variations associated with changing roller speed, another limitation of Johanson's theory was introduced by Patel et al. [85]; the authors mentioned that the compressibility determined by the power-law relationship between the stress and the ribbon density does not capture the behaviour at small pressures. Alternatively, a uniaxial compaction data was fitted to the relationship developed by Adams et al. [86] that was adopted in [85]. The relationship is given by the following equation:

$$ln\,\sigma = ln[1 - exp\,(-\kappa\varepsilon)] + ln\left(\frac{\tau_0}{\kappa}\right) + \kappa\varepsilon \qquad \text{Equation 2-14}$$

where κ is the modified compressibility factor, τ_0 is related to the mechanical strength of the particles and ε is the compressive natural strain given by:

$$\varepsilon = ln\frac{h_i}{h_c} \qquad \text{Equation 2-15}$$

where h_i is the initial height of the powder and h_c is the current powder bed height.

If the roll separation distance s_α at the nip angle α is calculated using the following equation [85]:

$$s_\theta = s + d_r(1 - cos\,\theta) \qquad \text{Equation 2-16}$$

where s_θ is roll separation distance at an angular position (θ).

The roll separation distance s_β at the true nip angle β can then be calculated using the following equation [85]:

$$\left(\frac{s_\beta}{s_\alpha}\right)^k \left\{1 - exp\left[-k\,ln\frac{s_\beta}{s}\right]\right\} = 1 \qquad \text{Equation 2-17}$$

and the true nip angle (β) is then calculated accordingly (Equation 2-16).

2.3.2 Finite element Modelling (FEM)

FEM is a numerical method for solving engineering problems. The modelling is based on subdividing the system using a mesh consisting of smaller elements that are interconnected by nodes. Each element is assigned certain geometrical and material properties and analysed under specific boundary conditions that could include force, temperature and displacement. The solutions of all individual elements are assembled to describe the response of the whole system [87]. The FEM approach was used by several researchers to investigate powder behaviour during roller compaction; Dec et al, [84] built a two dimensional FEM model to investigate MCC powder behaviour during roller compaction. The model was developed using a commercially available ABAQUS code based on a modified Drucker-Prager cap model (DBC) as the constitutive model. This material model is a pressure-dependent yielding plasticity model with linear elasticity which was calibrated by conducting a series of simple and diametrical compression tests in an instrumented die. The model assumed no cohesion between powder particles. Also, while the angle of internal friction was estimated to be 65º, the angle of wall friction was assumed to follow the Coulomb law of friction with coefficient of friction values ranging from 0.35 to 0.5. Modelling was conducted until constant values of roll force and roll torque were obtained.

The study showed that feeding stress has a significant effect on the roller pressure; increasing feeding stress led to higher roller stresses at constant friction coefficient.

Additionally, the study demonstrated that both roll force and roll torque have increased when increasing the friction coefficient and feeding stress. The authors mentioned that the main challenge of the FEM approach is to have a constitutional material model that could better describe material behaviour during compaction.

In another study, Cunningham et al. [64] developed 2D and 3D FEM models to evaluate the variation in the roller compaction process. The modelling trials were followed by roller compaction experiments using an instrumented roller that was equipped with load cells distributed across the roller width. The cells are capable of measuring both normal and shear stresses across the roller width. The DBC constitutive model was used to describe the mechanical properties of MCC powder, which is the model powder for this study. Experimentally, the authors found that the normal pressure started to increase at about 10º, reached its maximum value at the roll width centre close to 0º, and reduced back to zero at about 5 to 8º (Figure 2-23). On the other hand, the shear stresses built up to about 24 MPa close to the entry angle and then decrease to zero at the neutral angle. In the exit region, the shear stress reversed its direction and increased rapidly to about 28-100 MPa at about 2º (Figure 2-23). The predicted shear stress after the neutral angle is about 3 times higher than those before the neutral angle, this is suggested to contribute to properties of the ribbons in terms of fracture or lamination. Additionally, the modelling explains the pressure variation across a ribbon width based on the heterogeneity in the feeding across the width and the frictional properties of the side sealing.

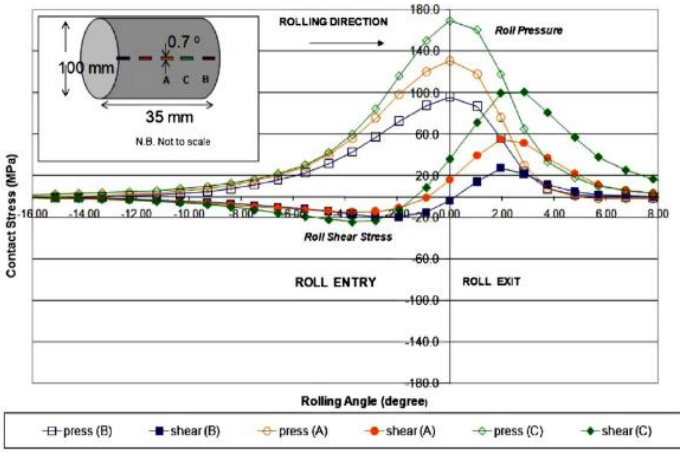

Figure 2-23: Normal and shear pressure distribution as a function of angular position and position across roll width [64].

Michrafy et al. [88] used a 2D FEM model to the roller compaction of MCC powder. The study theoretically divided the area of compaction into three distinct regions; firstly, the slip region controlled by sliding of the particles between the rollers. Secondly, the stick region of the powder moves at the velocity of the rollers. Finally, there is the ejection phase in which the shear stress reverses its sign and the ribbon is released at a speed higher than the roller speed. In agreement with Cunningham et al. [64], both the maximum pressure and maximum ribbon density reached the highest level before the minimum gap distance when there was no shear stress.

In a more recent study [89], FEM was successfully implemented to investigate MCC behaviour during compaction; the study included a comparison between Johanson and FEM modelling. It showed an agreement in the trend between the two approaches except for some discrepancies when changing the effective friction angle, i.e. unlike Johanson's approach; the FEM model predicted nip angle values that decreased when increasing effective friction angle.

2.3.3 Discrete Element Modelling (DEM)

DEM is a numerical modelling method at the particle scale. It computes the dynamics of particles (typically spherical) based on their inter-particular interaction, which is governed by contact models due to external forces such as gravity and interactions with the surrounding geometrical objects such as walls or mixing blades [90]. Odagi et al. [91] developed a 2D DEM model to simulate the powder behaviour in roller compaction. The authors assumed that the particles were spherical and mono-sized. The inter-particular interactions were expressed as adhesion forces obtained experimentally by measuring the tensile strength of the ribbons. The study showed that the model failed to simulate densification and compaction into a ribbon when the adhesion forces were not considered. However, introducing adhesion forces to the model improved the predictability of the model; the mass throughput was directly proportional to the roller speed, which followed the trend of the experimental results. The authors pointed out that a significant variation between experimental and predicted stress distribution was observed, this was referred to the modelling assumption that did not take the role of air in account, additionally assuming spherical particles could also contribute to the variation in the results.

In a more recent study, Mazor et al. [90] exploited the advantages of both DEM and FEM to model the two mechanisms involved in the roller compaction process; DEM which is

more suitable to simulate particle flow was used to model the feeding of particles to the compaction area. While FEM was implemented to simulate particle deformation under certain frictional and mechanical properties. The velocity of particles at the end of the screw feeder was determined by DEM modelling and used as input data for the subsequent FEM simulation of the compaction zone (Figure 2-24).

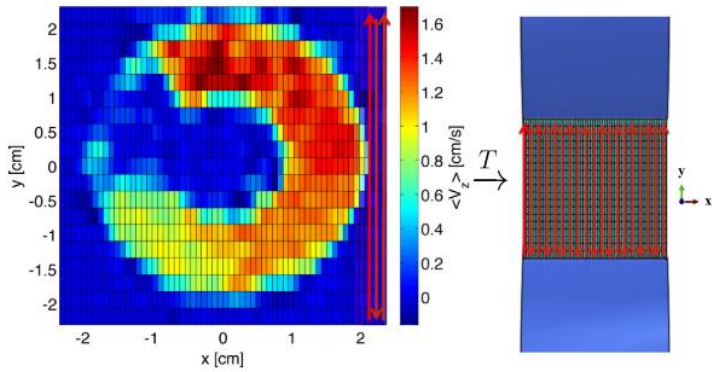

Figure 2-24: Schematic representation to the approach used by Mazor et al. [90]; the predicted particle axial velocity used as an inlet velocity for the FEM model.

The study showed how the inhomogeneity of the feeding velocity due to screw feeder rotation could affect the density distribution in the resultant ribbons; a sinusoidal pattern of roll pressure and relative density was observed in which the period of variation was equal the screw feeder rotation time. However, no experimental validation was conducted to validate the developed model.

2.3.4 Artificial neural network (ANN) modelling

ANN is a data-driven modelling system that is based on a set of algorithms inspired by the human brain mechanism of information analysis [92]. Turkoglu et al. [93] used ANN and genetic algorithm to analyse the data of 42 different experiments in which acetaminophen had been roller compacted using different binders types, binder concentrations, and number of roller compactor passes. Data analysis was conducted in an attempt to optimise the final tablet properties in terms of disintegration time, strength, ejection force, and friability. The study showed that the ANN was able to predict tablet crushing strength with $R^2 = 0.9064$, which was comparable with the genetic algorithm results. However, the authors pointed out that genetic algorithms had higher predictability for the rest of tablet characteristics in comparison with ANN. In another study, Inghelbrecht et al. [76] successfully used ANN technology to predict granule quality in

terms of friability while the input of this model were four different process parameters, namely, roller speed, velocities of both horizontal and vertical screw feeders, and air pressure. The results showed that unlike polynomial fitting, the developed ANN model was able to predict the friability of the roller compacted granules more accurately. Based on the ANN inter-correlation, the most two influential parameters on granule's friability are both horizontal screw speed and air pressure; these two parameters should be kept low to maintain high granule quality. The study also mentioned that the quality of granules could be improved if the ratio between roller speed and horizontal screw speed is maintained to be around 0.5 (Figure 2-25).

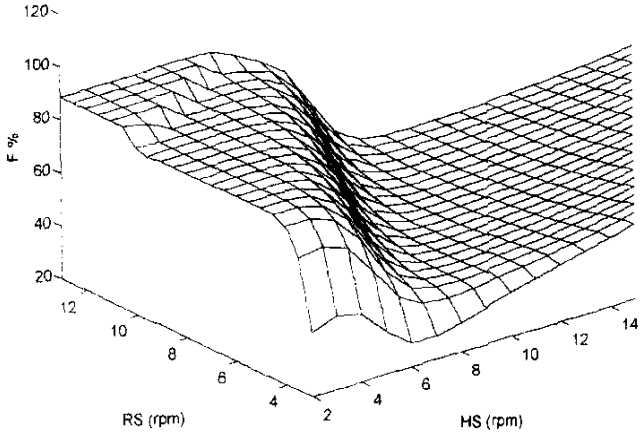

Figure 2-25: ANN predicted granule friability as a function of horizontal screw speed (HS) and roller speed (RC) [76].

More recently, Sajjia, et al. [94] developed an ANN model to predict MCC ribbon average density based on two process parameters as inputs including roller force and screw speed. Ribbon average density was measured using Geopic technology and the data from 16 roller compaction experiments were divided into 3 data sets; 10 for training, 3 for validation and 3 for testing. ANN topology was optimised and the best results were obtained when 3 hidden layers were used. The predicted results of the developed ANN was compared with Johanson's model results; the average deviation of prediction of ANN was 0.9% against 4.6% for Johanson's model. However, roller compaction is a complicated process which involves more process and material parameters than those considered in this study. Additionally, the mean envelop density predicted in this study does not reflect the real quality of the final product as it ignores the variation of ribbon density caused by the heterogeneous nature of this process.

2.3.5 Theoretical Modelling-Summary

Different approaches have been exploited to simulate powder behaviour during compaction and each method has advantages and disadvantages. In terms of computer modelling, FEM requires a constitutive model that could accurately prescribe material mechanical properties. DEM could be beneficial to investigate particle flow mechanisms involved during the feeding stage of roller compaction process, however, by its nature, the DEM approach is not suitable to deal with particle deformation and/or breakage that could develop during roller compaction, this could limit its applicability for compaction studies.

In spite of the limitations, Johanson's theory was confirmed by a number of researches to provide a reasonable agreement with the experimental measurements and is still viewed by engineers as a satisfactory model to predict product properties as a function of process variables [41,89,95]. The main advantages of this model being computationally economical and very simple as only a limited number of powder parameters, which can easily be measured experimentally, are required to implement this theory. Concurrently, efforts have been elaborated in order to enhance its predictability [7,85]. The modified Johanson's model proposed by Patel et al. [85] was used to calculate the maximum stress of compaction in this work.

In terms of data-driven modelling and more certainly ANN modelling, there is only limited research in terms of inputs used, which will diminish the applicability of the developed model in the field of real process control. Moreover, in terms of model outputs, most of the existing work focuses on average ribbon porosity and does not take the well-known variation of porosity across a ribbon width into account. A better model for process control purposes would predict the variation of ribbon porosity considering more material and process parameters so that it could respond to both process and formulation related variations. This will to be discussed in more detail in Chapter-7.

2.4 Aim of the research

The work is aiming to investigate the following points:

- The aim of the current work is to elucidate the mechanisms of ribbon splitting by an experimental study involving single-component powders with a range of yield strengths, including those that are commonly used as excipients.

- Assess the effects of knurled and smooth roller surfaces on ribbon density distribution and ribbon splitting occurrence.

- Assess the role of powder and metal surface energy in powder sticking during roller compaction.

- To further improve our understanding of the roller compaction in terms of the inhomogeneity of ribbon properties. A new neural network model is proposed, which accounts for different process and material properties.

CHAPTER 3 MATERIALS AND METHODS

3.1 Materials

Seven different powders with a range of mechanical properties were selected: calcium carbonate ($CaCO_3$) (Longcliffe Quarries Ltd., UK), maltodextrin (Glucidex 6, Roquette, France), α-lactose monohydrate 200M (GranuLac® 200, MEGGLE Germany), microcrystalline cellulose (MCC) (VIVAPUR®101, JRS PHARMA, Germany), anhydrous lactose (NF-DT, Kerry bioscience, USA), mannitol C160 (Pearltol®C160, Roquette, France), pregelatinized maize starch (Starch 1500®, Colorcon, UK) and magnesium stearate (MgSt) (Peter-Greven). The particle size in terms of distributions and (d10, d50 and d90) was measured using a Camsizer XT (Retsch Technology GmbH, Germany) as shown in Figure 3-1 and Table 3-1 respectively. Scanning electron micrographs of the particles are shown in Figure 3-2. Moreover, the true density of the studied feed powders are tabulated in Table 3-1.

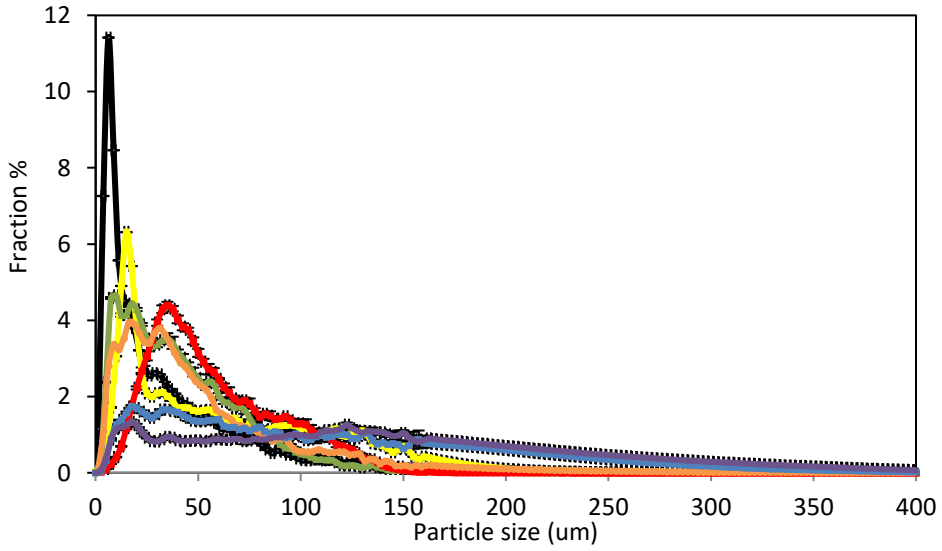

Figure 3-1: Primary powder particle size distribution for $CaCO_3$ (—), mannitol (—), lactose 200M (—), anhydrous lactose (—), starch (—), maltodextrin (—) and MCC (—).

Table 3-1: Primary powder particle size data.

Material	d_{10} (µm)	d_{50} (µm)	d_{90} (µm)	True density (kg/m^3) [96]
$CaCO_3$	5	23	87	2930
mannitol	12	40	138	1514
lactose 200M	9	35	82	1545
Anhydrous lactose	26.5	132	281	1589
maltodextrin	21.5	100	241	1449
MCC	23	49	104.5	1440
starch	14.8	54	138	1594

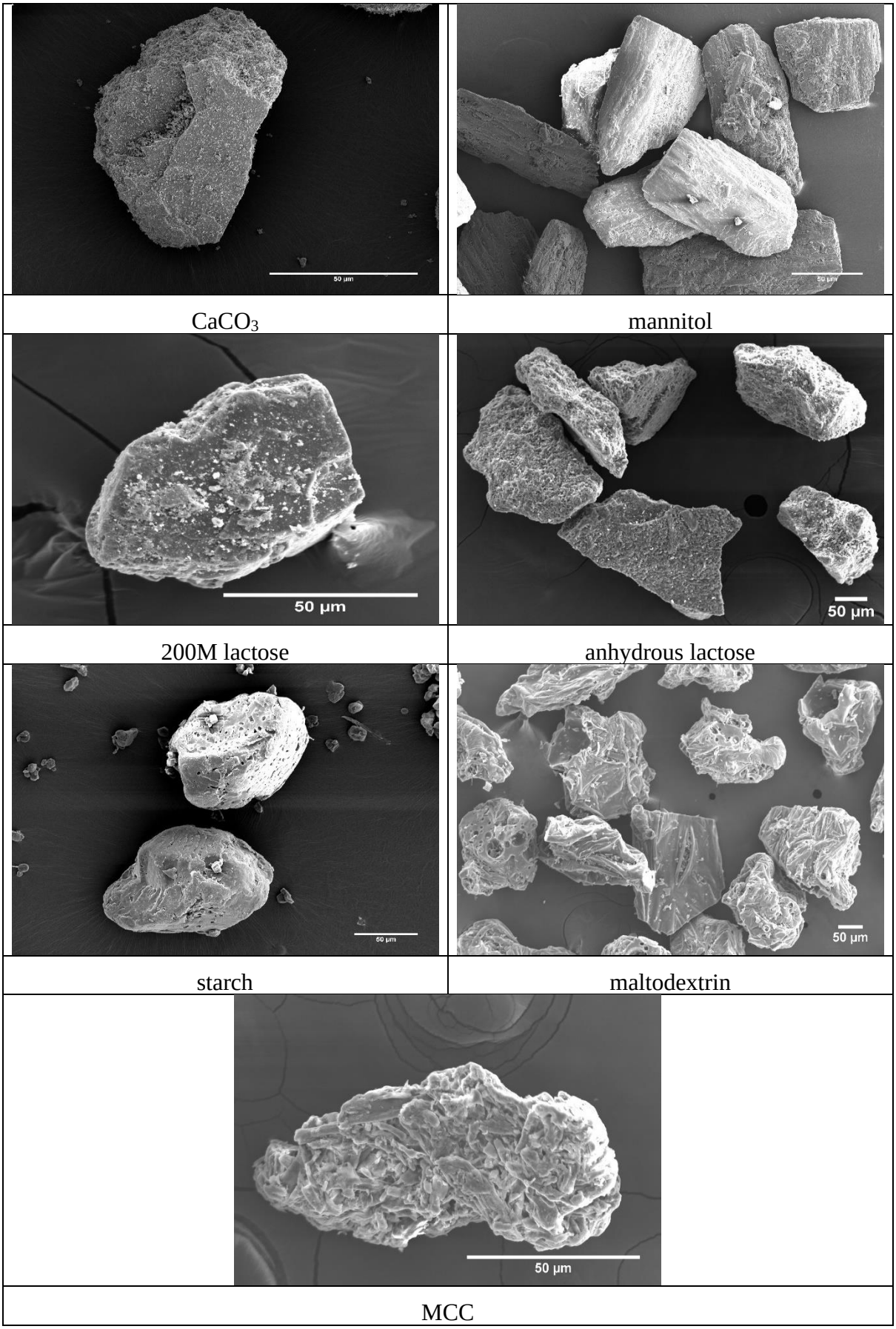

$CaCO_3$	mannitol
200M lactose	anhydrous lactose
starch	maltodextrin
MCC	

Figure 3-2: SEM images for the primary particles used in this study.

3.1.1 Calcium carbonate ($CaCO_3$)

Calcium carbonate is an odourless and tasteless powder. It can be extracted from nature by mining or chemically prepared using calcium oxide. This powder is used in pharmaceutical solid dosage forms as a diluent, or as a dissolution aid in dispersible tablets. Also, in the food industry calcium carbonate can be used as a food additive [96].

3.1.2 Mannitol C160

Mannitol is a white, odourless, water-soluble powder that has a sweet taste. It is widely used in pharmaceutical and food industry for a variety of purposes. As pharmaceutical excipient mannitol can be added to the tablet formulation as a filler or sweetening agent in chewable tablets. Additionally, mannitol can be used as a carrier in dry powder inhalers or as a bulking agent in the food industry. According to the processing conditions, mannitol can exist in three different crystalline forms. It is worth mentioning that the mannitol powder used in this study composed of 99% β-mannitol which known to be the most stable polymorph of mannitol [97].

3.1.3 Lactose

Lactose is reducing disaccharide which consists of two hexose sugar glucose and galactose. In the solid-state, lactose powder occurs as odourless and white to off-white crystalline particles with slightly sweet-tasting. Depending on the processing conditions, lactose can exist in different amorphous and crystalline forms with different properties in terms of solubility, mechanical properties and morphology. Changing crystallisation and drying conditions can result in different crystalline isomeric forms of lactose ranging from α-lactose monohydrate, anhydrous β-lactose and anhydrous α-lactose [98].

Two different types of lactose were used in this study; firstly, α-lactose monohydrate which is produced by slow crystallisation from a supersaturated lactose solution below 93.5 °C, the slow crystallization will enable the water molecules to get incorporated in the crystalline lattice forming what is so-called the water of crystallisation, where each lactose molecule is strongly bonded to one molecule of water. Secondly, anhydrous β-lactose (anhydrous lactose NF-DT, Kerry bioscience, USA), which is industrially produced by roller drying of a supersaturated lactose solution on high temperature above 93.5 °C, is more brittle than the α-lactose monohydrate and has no crystal water in its crystal lattice. Figure 3-2 shows the difference in particle structure and the surface

roughness between the sharp-edged and smooth surface α-lactose monohydrate and the rough surface and kite shape anhydrous β-lactose.

According to a previous research work [99], the two types of lactose have a different amount of amorphous content. While anhydrous β-lactose is reported to contain no amorphous material, α-lactose monohydrate is expected to have ~1-4% amorphous material. The work also mentioned that the difference in amorphous content has led to subsequent changes in the final product attributes.

3.1.4 Starch 1500

Starch 1500 is a white free-flowing pregelatinised maize starch that is composed of two polymers, amylose and amylopectin. This material is commonly used in the pharmaceutical industry as a filler, disintegrant, binder, or even as flow-aid due to its lubrication properties [97].

3.1.5 Maltodextrin

Maltodextrin (Glucidex 6, IMCD, UK), is a spray-dried amorphous polysaccharide, produced by partial enzymatic hydrolysis of the starch. In addition to its application in food industries as a bulking agent, due to its colourless and flavourless characteristics, it is preferably used in pharmaceutical tablet industries as a diluent and coating material [100].

3.1.6 Microcrystalline cellulose (MCC)

Microcrystalline cellulose (VIVAPUR®101) is a free-flowing, plastically deforming material. It is produced by severe acid hydrolysis of α-celluloses which results in a polymer with both crystalline and amorphous regions. Using X-ray diffraction, previous research works have proven that the amorphous content of MCC is about ~30% which is almost the same in different commercial grades of MCC [101]. This material has lots of applications in the pharmaceutical industry where it is primarily used as a binder/diluent in oral tablet and capsule formulations.

3.2 Methods

3.2.1 Powder preparation

Prior to any experiment, the powders were equilibrated for three days at a relative humidity of 40% and temperature of 25°C in a humidity chamber (Binder KMF 240 climatic chamber, Binder, UK).

3.2.2 Powder characterisation

3.2.2.1 Powder yield strength

The yield strength (σ_Y) of the particles were estimated using Heckle equation, which is based on the compact density as a function of the applied stress (Equation 3-1) [102].

$$\ln\frac{1}{1-Y} = Xp + C_h \qquad \text{Equation 3-1}$$

where Y is the relative density at any given compaction pressure (p), which is the ratio of the compact envelope to the true density. C_h is a constant related to the volume reduction of the powder as a result of particle rearrangement and die filling. X is a material related constant, and it is related to the response of the material to reduce void fraction as a response to the applied pressure.

So $\ln(1/1-Y)$ is plotted against the compaction pressure p, the gradient of the linear part of the plot can be fitted to a straight line where the slope of this line (X) has been used as an indicator of the material plasticity [103]. Heckel has shown experimentally that the reciprocal of the slope of this line can be used to determine the yield strength of the materials (σ_Y).

Although it involves a number of limitations [104] it is still used as a valuable tool for comparing the mechanical properties of the powders. There are two types of Heckle analysis in common use namely, in-die and out-die analyses [103]. The difference between these methods depends on the way of density data collection, i.e. in case of the in-die analysis; the data is collected during compaction whereas in the other method tablet density is determined after ejection of the compact. For comparison purposes, both methods are used in this work.

For the out die method, powders of the same mass were added in a 12 mm diameter polished stainless steel die and compressed at a speed of 1 mm/min using a universal testing machine (Instron 3367, USA) at different compaction forces (1, 3, 5, 7, 10, 12, and 15 kN). Consequently, the compact density was determined from its mass and volume; tablet thickness was measured using two decimal points electronic calliper and used to determine tablet volume. The resulted tablet density was then divided by powder true density to calculate compact relative density. Eventually, both the stresses applied on the powder and compacts relative densities were fitted to Equation 3-1; the reciprocal of the slope of the resulted line is used to determine powder yield strength.

On the hand, for the in-die heckle analysis, force and displacement of tablets prepared at 15 kN have been recorded during compaction and used to determine stress and relative densities similar to the procedure followed for the in-die analysis.

3.2.2.2 Single-particle compression test

To further investigate the mechanical properties of the studied feed powders; powders have been sieved to the sieve size range (212-250 µm). Subsequently, the single powder particle has been compressed at a compaction speed 0.05 mm/min using Zwick/Roell Z 0.5 (Zwick/Roell, Germany) test machine which was equipped with 5 N capacity load cell and a rigid metal base fitted with a glass plate (8 mm thickness) in order to place the particle on it. Moreover, a Dino-Light camera (Premier, AM-4013, Taiwan) has been fixed under the glass plate in order to record the change in the projection area during the compression test. The test has been repeated for at least 25 times for each powder material.

3.2.2.3 Compressibility factor of the powders

Raw powders have been compacted using a uniaxial compaction machine (Instron 3367, USA) in a 12 mm inner diameter polished stainless steel die at a force of 15 kN and a compaction speed of 1 mm/min. The compaction data were fit to Equation 2-14 and the compressibility constant calculated accordingly. A minimum of five replicates were conducted for each raw powder.

3.2.2.4 Powder flow properties: Shear cell tester

A ring-shear cell tester RST-XS.s (Dr Dietmar Schulze, Germany) was used to measure both the effective angle of internal friction (δ_E)° and angle of wall friction

($\emptyset_w$)°.To measure δ_E, the powder was pre-consolidated by applying a certain normal load and pre-sheared until a steady state was reached. Subsequently, shearing took place under reduced normal load steps. Stress of 5000 Pa was used as a pre-shear normal stress and three different normal stresses of 1500, 2750, and 4000 Pa were applied sequentially.

The measurement of wall friction is based on determining the sliding resistance between the powder and a metal surface at different applied normal forces with 5000 Pa as a pre-shear. The shear stress was measured against a smooth stainless steel coupon and a knurled stainless steel coupon which have similar surface finishing as the rollers. The knurled coupon was machined using wire-electrical discharge machine (EDM) to have the same diagonal cross hatch cuts of the knurled rollers.

3.2.2.5 Work of elastic recovery

Powder sample of the same mass has been poured in a 4 mm die. Consequently, stresses equivalent to the stresses applied during roller compaction have calculated using Johanson's theory (Equation 2-12) and applied on the powder at a speed of 1 mm/min. Displacement recording started at a force threshold of 2 N when the punch started to touch the powder bed. The loading and unloading energies were calculated from the recorded force-displacement data. The elastic recovery was then calculated using the following expression [105]:

$$\varepsilon_R = \varepsilon_U / \varepsilon_L \qquad \text{Equation 3-2}$$

Where ε_L and ε_U are the loading and unloading energies (J) such that $\varepsilon_R = 0$ corresponds to perfectly plastic deformation and $\varepsilon_R = 1$ to perfectly elastic deformation. As shown in Figure 3-3, the loading energy is calculated from the area under the OB curve which represents the total work input. While the area under the CB curve represents the elastic recovered work and used for the unloading energy calculation.

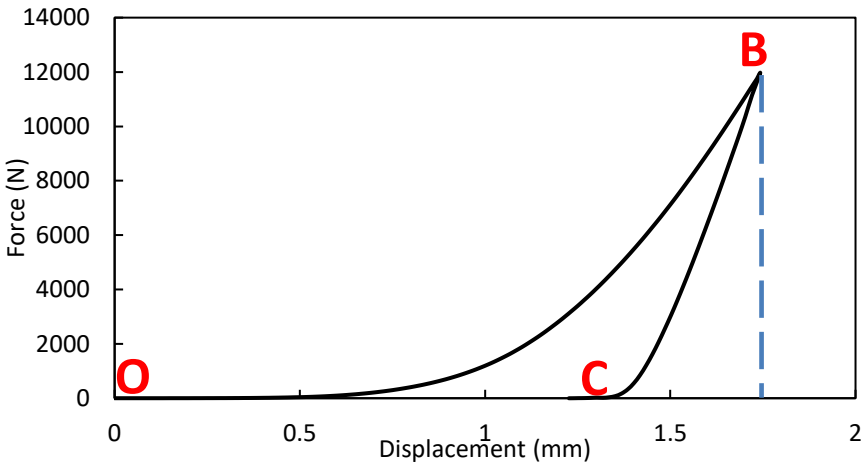

Figure 3-3: An example of loading /unloading curve that used is to calculate compact elastic recovery.

3.2.3 Roller compaction

Alexanderwerk WP120 (Alexanderwerk, Germany) roller compactor was used, which incorporates a feeding, compaction, and milling system (Figure 3-4). Additionally, the roller compactor is equipped with a de-aeration system that can enhance the powder flowability and play a role in reducing the amount of fines. The counter-rotating rollers have widths of 4 cm and diameters of 12 cm. The feeding system is a horizontal auger and the rotational speed and, hence the applied pressure can be varied. The gap between the two rollers is sealed with two side cheek plates that are designed to prevent powder leakage during compaction. Metallic scrapers are fixed at about 0.1 mm distance from the roller surfaces. There is a gap feedback system that controls the screw feeder speed in order to deliver the powder flow rate that will maintain the required gap between the rollers. The relationship between roller separating force and hydraulic pressure is given by the manufacturer (Alexanderwerk) [45] and tabulated in Table 3-2.

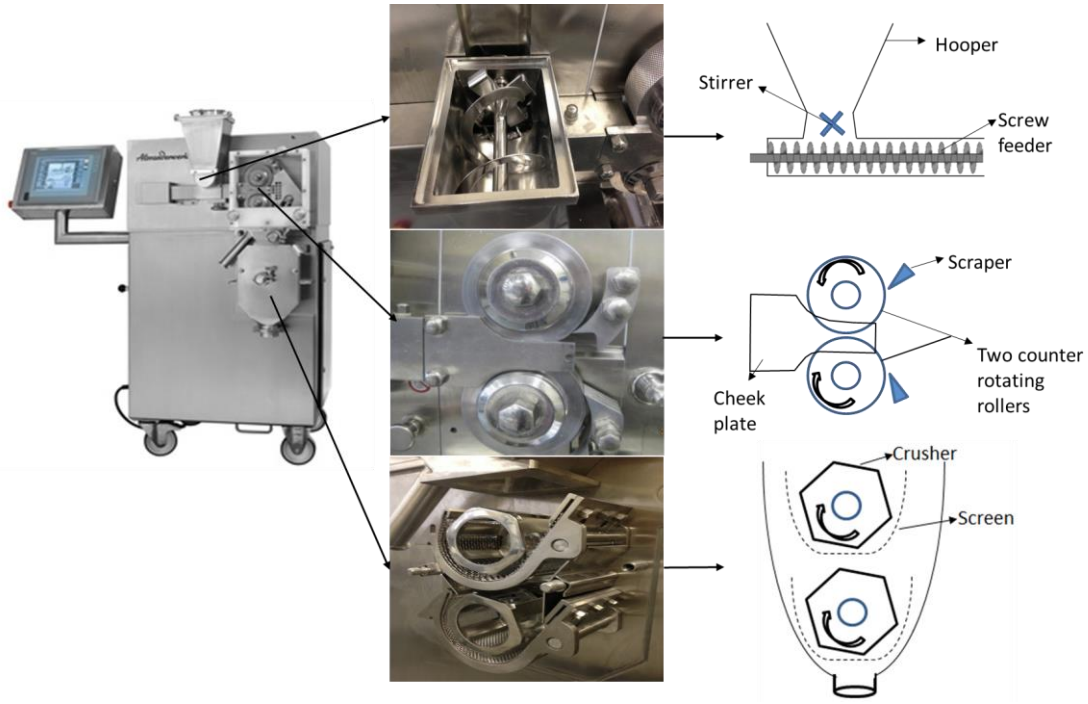

Figure 3-4: Alexanderwerk WP120 Roller Compaction with schematic drawings of the main three systems involved in roller compaction i.e. feeding, compaction, and milling system.

Table 3-2: The relationship between roller separating force and hydraulic pressure as given by the manufacturer (Alexanderwerk) [45].

Hydraulic pressure (bar)	**Roller separating force (kN)**
18	7.46
30	12.43
50	20.72
80	33.15
120	49.76
150	62.16
230	95.38

To examine the effects of the surface topography of the rollers, two pairs of rollers with different surfaces (knurled and smooth) were used in this study (Figure 3-5). The indentation depth of the knurled roller is about 0.5 mm and it was measured with a digital microscope (Keyence VHX-5000).

The conditioned powder was compacted at different hydraulic pressures in the range 18 - 230 bar. A fixed roller gap of 2 mm and a fixed roller speed of 3 rpm were employed. In order to investigate the effects of adhesion between the ribbons and rollers, 0.25 g of

MgSt as a lubricant was applied on each roller surface using a brush, the same amount of the lubricant was applied for each roller cycle. The ribbons were only collected after a steady-state hydraulic pressure and roller gap was achieved. Additionally, another approach of lubrication was investigated; MgSt was mixed with each feed powder at 0.5 and 1%. Mixing was conducted at 50 RPM for 4 min using Roto Junior high shear mixer (Zanchetta & C, Italy).

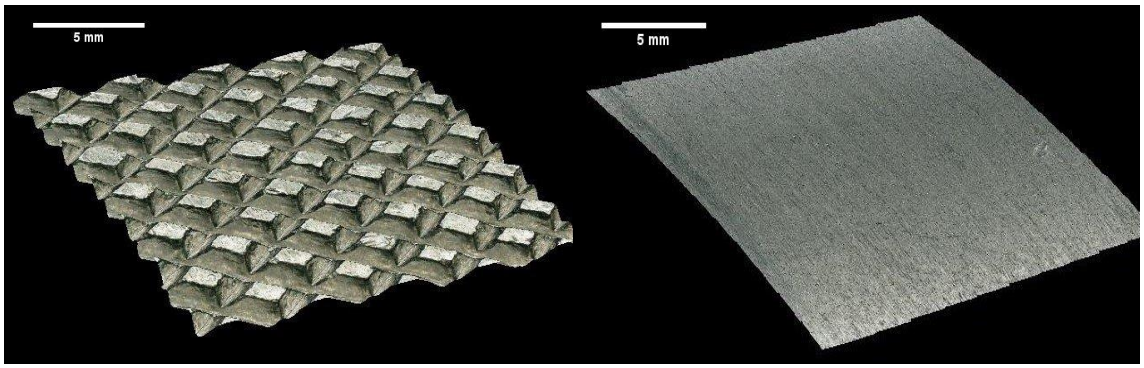

(a) (b)

Figure 3-5: Optical image of a section of the knurled roller surface (a) and the smooth roller surface (b).

3.2.4 Roller surface coverage monitoring

Adhesion of powder during roller compaction experiments was recorded using a high-speed camera (Photron Fastcam 1024 PCI, Itronx Imaging Technologies, CA) that was set to capture 60 frames per second. Knowing that the used roller speed is 3rpm, six-minute long videos were taken for all roller compactor experiments. In another word, about 21600 images were taken for the roller surface during roller compaction and from which only the first roller cycle for every minute (1200 Images) was processed using ImageJ (National Institutes of Health (NIH), USA) software. The recording area was fixed on 30 x 40 mm.

This software uses a greyscale system that ranges from 0 to 255; where zero is complete black and 255 is complete white. The images were converted to binary images using the same binary threshold in all images, and subsequently, the software was used to quantify the percentage of white pixels which represent the powder particles out of the total number of pixels. Figure 3-6 shows a schematic diagram of the setup used in these experiments.

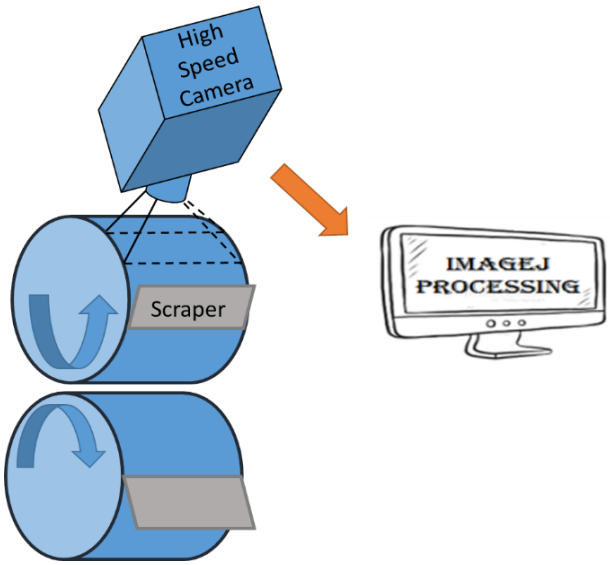

Figure 3-6: Schematic drawing of the set used for roller surface coverage monitoring.

3.2.5 Online thermal imaging

A thermal camera (FLIR A655sc, Sweden) was fixed to face both rollers and record the ribbon surface temperature after it emerged from the minimum gap. Ribbon surface temperature was recorded for 60 seconds after the gap and screw speed reach steady state. The recording was conducted at 50 fps, and the recorded images were analysed using FLIR R&D software to get the temperature profile across ribbon width. In order to record the ribbon surface temperature, it is important to measure the emissivity of the materials. The emissivity can be defined as the energy emitted per unit area per unit time and more certainly, it is essentially the ratio between the amounts of energy emitted by an object to the amount of energy emitted by a black body that absorbs all of the incident energy regardless of the angle of incidence or frequency of incidence [106]. The emissivity of the ribbon was measured by heating the ribbon up to 60°C using a hotplate; the actual temperature of the ribbon was monitored using a thermometer. The thermal camera was used to measure the ribbon temperature simultaneously. The actual temperature measured by the thermometer was then used to correct the thermal camera reading in order to get the ribbon emissivity. The emissivity of mannitol, lactose, MCC are 0.96, 0.97 and 0.94 respectively.

3.2.6 Determination of un-compacted fine percentage

The amount of fines, un-compacted powder, is defined as particles that are smaller than the d_{90} of the original powder. The entire product (ribbons and fines) were collected

for a set period of time. The ribbons were separated from the fines by sieving (Retsch GmbH, Germany) and the mesh size was selected according to the d_{90} of the used powder. The mass of the entire product was weighed together with that of the mass of separated fines to calculate the weight percentage of the fines.

3.2.7 Ribbon strength measurement-three point bend testing

The strength of the ribbons was measured using a three-point bend configuration. This involved two sharp metal plates to support the ribbon and a sharp metal plate that is attached to a Zwick/Roell Z 0.5 (Zwick/Roell, Germany) test machine (Figure 3-7). The test machine applies the load at the centre of the ribbon at a rate of 1 mm/min.

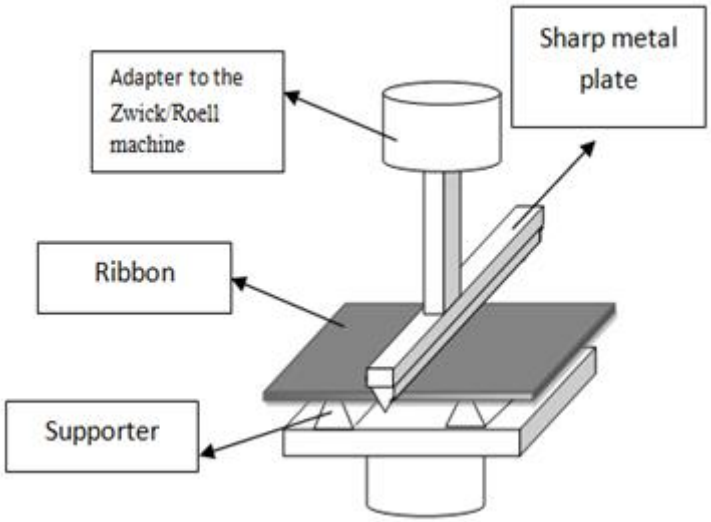

Figure 3-7: Schematic drawing of the setting used for the three points bend test.

The tensile strength was then calculated using the following equation [12, 18, 19]:

$$\sigma_t = \frac{3F_{max}L_s}{2bm^2} \qquad \text{Equation 3-3}$$

where σ_t is the tensile strength, F_{max} is the maximum force required to break the ribbon (N), b and m are the width and thickness of the ribbon respectively, L_s is the distance between the two supports. L_s is set according to the British standards (L_s= m (16 ± 1)) [12, 18, 19]; b is the width of the ribbon (mm), and d is the thickness of ribbon (mm). The measurement procedure was repeated at least ten times for the ribbons produced under each condition.

3.2.8 Ribbon porosity measurement using X-ray tomography

Ribbon porosity was measured using microCT 35 (Scanco Medical AG, Switzerland). X-ray was operated at a voltage of 45 kV, a power of 8 W, and a current of 177 µA. The produced images were then analysed using Image J software which was set to a fixed threshold to distinguish between powder (white pixel) and air (black pixel). The ratio of black to white pixels indicates the porosity of the selected sample area.

3.2.9 Ribbon porosity distribution measurement using Near Infrared Chemical Imaging (NIR-CI)

1- NIR-CI instrumentation

Roller compacted ribbons are scanned using an offline NIR diode array spectrometer (EVK Helios G2-320 class, EVK DI KerschhaggI). The spectrometer has InGaAs detector with 312 x 256 pixels that determine spatial and spectral resolution respectively. So using the highest magnification lens provided by the manufacturer with (1 cm-width FOV), the smallest detectable pixel size is ~32 µm. The spectrometer works in diffuse reflectance mode and collects spectra in the range between 900 to 2300 nm at a frame rate of 120 Hz. Moreover, a broadband quartz tungsten halogen (QTH) light source was positioned so that it could uniformly illuminate the sample surface. The device is equipped with a moving conveyor on which the sample is placed and moved under the detector at a constant velocity; the velocity of the belt synchronised with the camera frame rate to avoid any image shrinking or elongation. The camera records one line of 312 adjacent pixels per frame and the more lines are recorded while the belt is moving. Figure 3-8 shows a schematic representation of the configuration of the hyperspectral imaging system used in this study.

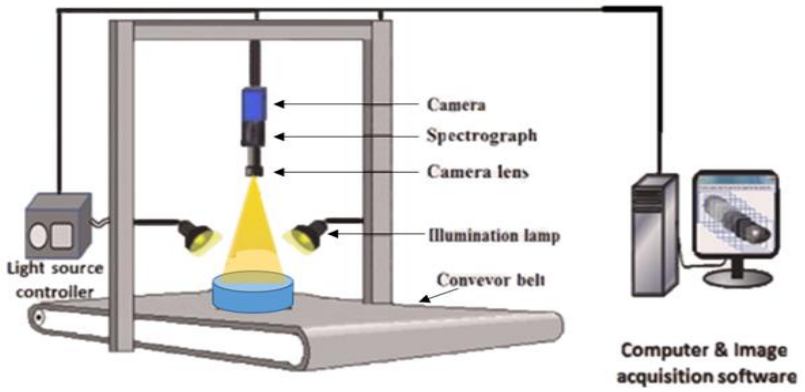

Figure 3-8: A schematic of the hyperspectral imaging system, Adapted-[107].

2- Data processing

(EVK SQALAR software package, Austria) was used for data processing. The software is based on two main multivariate data analyses (MVDA) to qualitatively and quantitatively analyse the spectral data:

a- EC3 mode (qualitative analysis): this mode works based on conducting principal component analysis (PCA) on the spectral data. In summary, PCA is a mathematical procedure that is used to reduce large sets of data into a smaller set while keeping most of the information in the large set. For example: based on its spatial resolution InGaAs-detector collects 312 spectra at the same time, which becomes huge amount of data when line measurement is repeated to cover the whole sample. PCA is applied to reduce this data based on the largest variance within the spectra [108,109]. The wavelength of the highest variation in the spectral data is called the first principle component and the subsequent component accounts for the second-highest variation and so on.

b- Quantitative chemical imaging (QCI) mode (quantitative analysis): this mode uses partial least square analyses (PLS) to build a quantitative predicting model. PLS gives a quantitative dimension to the PCA by assigning each principal component to a reference value.

3- Calibration: a set of 7 tablets were made by compacting ~ 0.1 g of powder material in 4 mm polished stainless steel die; compression was conducted under a range of stresses (equal to the calculated stressed used for smooth rollers mediated roller compaction) and three tablets were compacted at each compaction stress. The same set of tablets was made for the different types of materials used in this study except for $CaCO_3$ which was found to be inert to the operable range of wavelength of the spectrometer. A calibration curve was then created by plotting tablet porosity (1-relative density) against NIR-CI mean absorbance. The calibration was then validated and used for ribbon porosity measurement across ribbon width.

CHAPTER 4 NOVEL UNDERSTANDING OF RIBBON SPLITTING/STICKING PHENOMENA

4.1 Introduction

Ribbon sticking and splitting are among the major factors that can hinder the use of this process for some formulations. Ribbon splitting can occur either transversally (through the ribbon thickness) or longitudinally (through the ribbon width). The current chapter focusses on elucidating the mechanisms of splitting by an experimental study involving single-component powders with a range of yield strengths, including those that are commonly used as excipients. Smooth rollers were employed with and without lubrication by applying magnesium stearate to the rollers. The minimum gap was fixed and the maximum roll stress was varied. It was observed that transverse splitting is commonly associated with sticking of the split ribbons to the rollers and results in an inferior performance of the process. Longitudinal splitting is associated with an across-width distribution of the ribbon density so that there may an adverse effect on the mechanical strength and dissolution properties of the tablets formed from the milled granules.

The observed trends were rationalised in terms of a splitting index, which is a measure of the residual stresses driving crack growth relative to the tensile strength of the ribbons. There was a lower limit at which splitting was observed but the occurrence of transverse splitting decreased and that for longitudinal splitting increased with increasing values of the index, which was accompanied by an increase in mixed transverse-longitudinal splitting. Transverse splitting was always associated with sticking to the rollers and was prevented by external lubrication. A detailed discussion of the mechanisms involved is presented.

4.2 Hypothesis

In the exit region of the rollers, corresponding to upstream angles greater than that the minimum gap, a ribbon will undergo elastic recovery. If the residual stresses are greater than the critical fracture stress, ribbon splitting may be initiated. Moreover, if there is

adhesion to the rollers, the resulting bonding stresses will augment the residual stresses; this may be the case even when there is not visible particle debris on the surfaces of the rollers since adhesive rather than cohesive failure may still impose small opening stresses. As a result of these combined stresses, ribbons can split transversally and/or longitudinally as schematically demonstrated in Figure 4-1.

Longitudinal splitting Transversal splitting

Figure 4-1: A schematic diagram of the two kinds of ribbon splitting investigated.

4.3 Methods

As described in section 3.2.1, feed powders have been conditioned and roller compacted using smooth rollers, fixed roll gap and a variety of maximum roller stresses. The roller surface was monitored online during compaction, to measure the particle debris coverage for a specific roller surface area. The collected ribbons were analysed for their strength using the three-point bending test. A uniaxial compaction test was performed beforehand on the feed powder to determine their yield strength, elastic recovery, and compressibility factors. Furthermore, a shear cell test was used to characterise the feed powder for their flow properties. Full details about the procedures used for characterisation is in chapter-3.

4.4 Results and Discussion

4.4.1 Yield strength

All of the studied powders have been selected to cover a wide range of mechanical properties; this is ranging from $CaCO_3$ as a hard material to the predominantly plastically deformable MCC. Heckel analysis [102] was used to evaluate powder deformability in terms of measuring powder yield strength (σ_Y). Feed powders have compacted at a series

of pressures. The measurement of tablet thickness data have conducted both after ejection for a series of compaction pressures (out-die Heckel analysis) and during compaction at the highest compaction force, i.e. 15 kN (in-die Heckel analysis). The results of data fitting to Equation 3-1 is shown in Figure 4-2. The reciprocal of the slope of the linear part of the line was then calculated as the powder yield strength (Table 4-1). The thickness of the tablets produced using different pressures have been used for the out-die analysis, the fitting results are shown in Figure 4-2-A. Similarly, for the in-die analysis, the linear part of the force-displacement profile of the tablets compacted at the highest pressure (Figure 4-2-B) have been fitted to Equation 3-1 and used to calculate the in-die yield strength (Table 4-1).

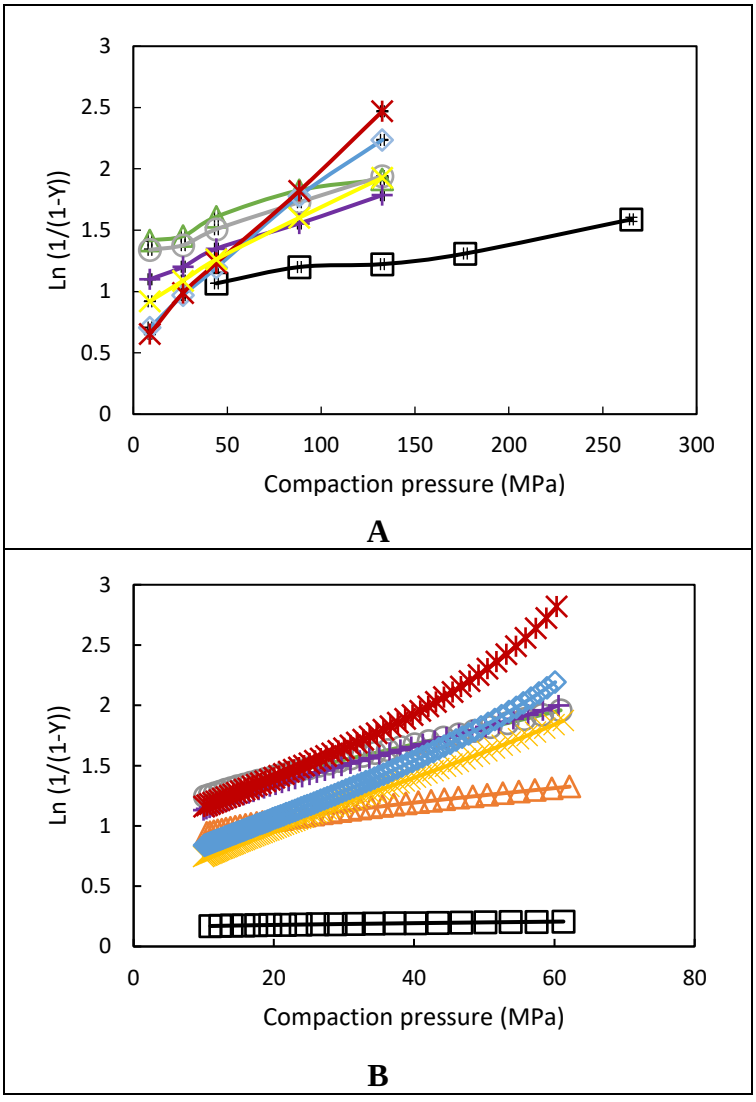

Figure 4-2: Typical Heckel analysis profiles obtained by two approaches; A: out-die and B: in-die. : $CaCO_3$ (□), mannitol (△), lactose 200M (○), anhydrous lactose (+), starch (x), maltodextrin (◇) and MCC (✳).

Table 4-1: Single-particle yield strengths and true densities for the powder feeds.

Materials	In-die yield strength (MPa)	Out-die yield strength (MPa)
$CaCO_3$	435 ± 9	424.6 ± 116
mannitol	233 ± 14	137 ± 17
lactose 200M	200 ± 2	76.6 ± 9.2
anhydrous lactose	182 ± 3.5	54.7 ± 2
starch	123 ± 2.7	43.3 ± 3.5
maltodextrin	81 ± 2	39.2 ± 2.7
MCC	69 ± 1	33.5 ± 0.47

As seen in Table 4-1, both approaches show a similar trend of deformability; the estimated yield strength values are ranging from a more plastically deformable MCC with low yield strength value to the very hard $CaCO_3$. Although the in-die approach tends to be more familiar as it is easier in terms of data collection, the out die approach is known to be more accurate [103]. In a critical evaluation of the two approaches of Heckel analysis, Sun and Grant [103] reported that the in-die analysis resulted in yield strength values that are significantly lower than the true values. This was ascribed to the elastic deformation of particles during pressure application which was found to decrease compact density and cause deviations in the measured yield strength values. The authors concluded that the out-die method describes powder consolidation and compaction more accurately than the in-die method. Consequently, the results obtained by the out die approach is considered to differentiate feed powders deformability in this study.

4.4.2 Single-particle yield strength

To further investigate the deformation behaviour of the studied feed powders, single particle-diametrical compression test has been conducted. Particles from the different types of materials were sieved to the same sieve fraction (212-250 μm) and compressed at the same platen speed (50 μm/min). Figure 4-3 shows examples of the force-displacement compression profiles of the different feeding powders of the study. Two distinctive deformation behaviour have been observed; a brittle behaviour where a clear fracture was detected at a certain force in case of brittle materials, this was the case for $CaCO_3$, mannitol c160, α-lactose monohydrate and anhydrous β-lactose, the recording of force-displacement profiles was continued until fracture occurred. Whereas, in case of

predominantly plastically deforming where no fracture has been recognized during particle compression, the force-displacement recording was conducted until a predetermined maximum displacement (50 μm) has been achieved. This deformation behaviour was observed for MCC, maltodextrin, and starch.

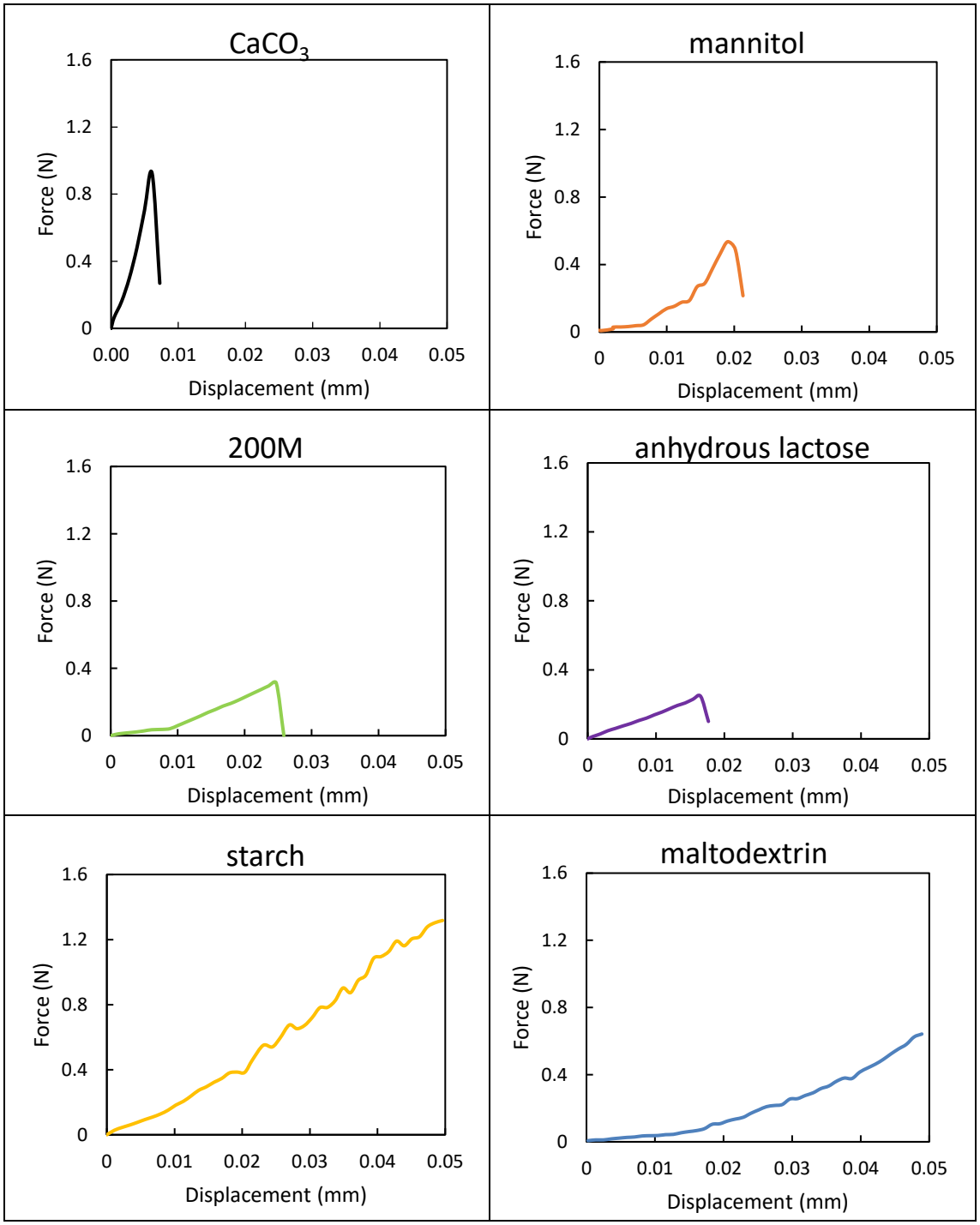

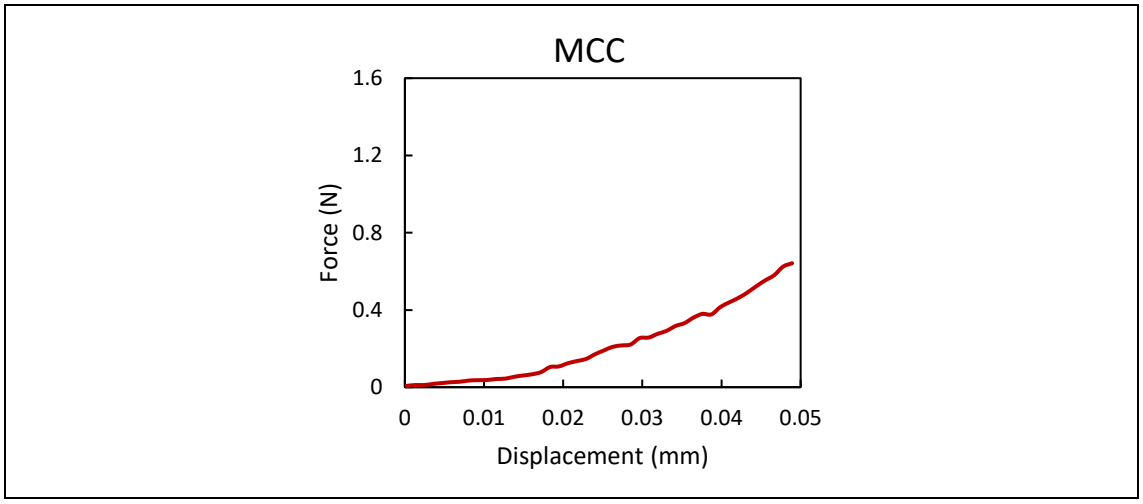

Figure 4-3: Force-displacement curves of the studied powder particles, which are obtained using the single particle-diametrical compression test.

Subsequently, an attempt was made to estimate single-particle yield strength using the previous force-displacement profiles; the elastic region of the curves has to be defined first. This was made by fitting the compaction profiles to Hertz equation which describes the loading of an elastic sphere under diametrical compression test between two plates [110]:

$$F = \sqrt{\frac{2}{3}}\, r^{\frac{1}{2}}\, E^{*}\, {h_m}^{\frac{3}{2}} \qquad \text{Equation 4-1}$$

where r is the radius of the powder particle (mm), E^{*} is the reduced effective young's modulus in GPa and h_m is the displacement of the moving platen in (mm). It should be noticed that the young's modulus of the metallic plates are assumed to be much greater than that of the powder particles so that the effective young's modulus can be simplified by the following equation:

$$E^{*} = \frac{E_p}{1 - {p_r}^2} \qquad \text{Equation 4-2}$$

where; E_p and p_r are Young's modulus and Poisson's ratio of the powder particle respectively. The elastic domain was estimated by plotting F^2 versus h_m^3 of the force-displacement curves as shown in Figure 4-4-A; where the point of deviation from linear-gradient ($R^2 = 0.99$) is considered to be the end of the elastic domain.

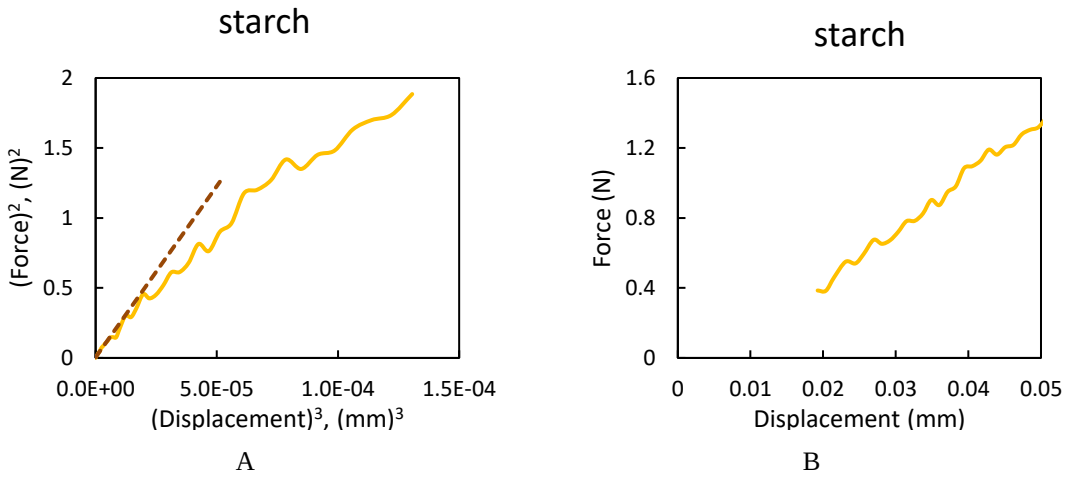

Figure 4-4: A: Fitting the compaction profile of starch particle to Hertz equation (Equation 4-1) to find the elastic deformation limit; the brown dotted line represents the best fitting line to the elastic region. B: the force-displacement range used to determine starch particle yield strength using (Equation 4-3).

When the stress exceeds the elastic limit, the particle starts to deform plastically. Meanwhile, the force-displacement relationship after the elastic limit should be linear and described by the following equation [45,110] (Figure 4-4-B). The remainder of the fitting data for the rest of the studied materials are tabulated in Figure A 1.

$$\frac{dF}{dh_m} = \pi\, r\, p_y \qquad \text{Equation 4-3}$$

where; dF/dh_m *is* the slope of the linear plastic region, and P_y is the particle yield strength in MPa (Table 4-2).

Table 4-2: The yield strength of studied powder materials determined using single-particle diametrical compression test.

Material	Single-particle yield strength (MPa)
$CaCO_3$	510 ± 131
mannitol	255 ± 81
lactose 200M	162 ± 23
anhydrous lactose	143 ± 24
starch	126 ± 22
maltodextrin	76 ± 22
MCC	65 ± 11

As clearly seen in Table 4-2 and Table 4-1, both the single-particle compression test and Heckel analysis showed the same trend of deformability. However, the single-particle method suffered from some weaknesses that could limit its usefulness; an accurate determination of the particle yield strength requires a careful evaluation of the contact surface area, in this case, the particle projected surface area was treated as the contact surface area for this measurement which can lead to a misleading measurement. On the other hand, it has to be mentioned that an R^2 value of 0.99 was taken as criteria for the determination of the elastic region of the force-displacement curves (Figure 4-4-A). This consideration can add to the weakness in the measurement since higher or lower taken R^2 can lead to different evaluation of the elastic region. Unlike single-particle measurements the yield strength values estimated by out-die Heckel analysis are based on compacting the whole size range of the powder bed which is the case during roller compaction; consequently, the yield strength values predicted using out-die Heckel analysis was considered for powder deformability evaluation in the following studies.

4.4.3 Maximum stress in roller compaction

The amount of stress received by any material depends on both the pressure applied by the rollers and the properties of the compacted material; therefore, it is necessary to compare the product properties based on the stress applied on them. To determine the stress applied on the powder during roller compaction, Johanson's mathematical model was used, taking into consideration the process parameters and material properties [83].

The maximum applied roll stress and nip angle were calculated using the analysis developed by Johanson [47] (Equation 2-6 to Equation 2-16), which has been employed by many researchers [83,95]. Recent work has shown that one limitation of the approach is the application of a power-law relationship between the stress and the ribbon density since it does not capture the behaviour at small pressures [85]. Consequently, the uniaxial compaction data was fitted to an alternative relationship (Equation 2-14), developed by Adams et al. [86] that was adopted in [85].

An example of fitting anhydrous lactose compaction data to equation (Equation 2-14), is shown in Figure 4-5. The fitting of the remainder of the studied feed powders is shown in Figure A 2. The resultant fitting parameter (compressibility factor (κ)) of the die

compaction data to Equation 2-14 together with the values of angle of wall and internal friction that have been measured with a ring shear cell test are given in Table 4-3.

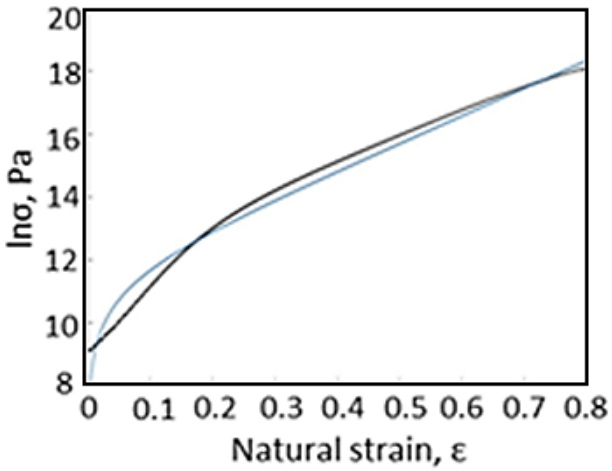

Figure 4-5: Typical stress-strain data for anhydrous lactose during uniaxial compaction test. The blue line represents the best fit to equation (Equation 2-14) and the black line shows anhydrous lactose compaction profile.

Table 4-3: Compressibility factor and flow properties of the materials.

Material	κ	δ_E	$\emptyset_w$
$CaCO_3$	13.2 ± 0.7	44.8 ± 0.3	17.1 ± 0.5
mannitol	10.3 ± 0.2	39.3 ± 0.1	10.3 ± 0.7
lactose 200M	12.7 ± 0.6	46.3 ± 0.3	16.8 ± 1.1
anhydrous lactose	8.8 ± 0.1	40.6 ± 0.2	13.6 ± 1.1
starch	8.4 ± 0.3	34.2 ± 0.1	9.5 ± 1.9
maltodextrin	6.0 ± 0.3	40 ± 0.1	10.2 ± 1.1
MCC	5.3 ± 0.9	44.5 ± 0.2	6.9 ± 0.3

Subsequently, the maximum roll stress as a function of the hydraulic pressure for the unlubricated smooth rollers has been calculated using Equation 2-6 to Equation 2-16 (Figure 4-6).

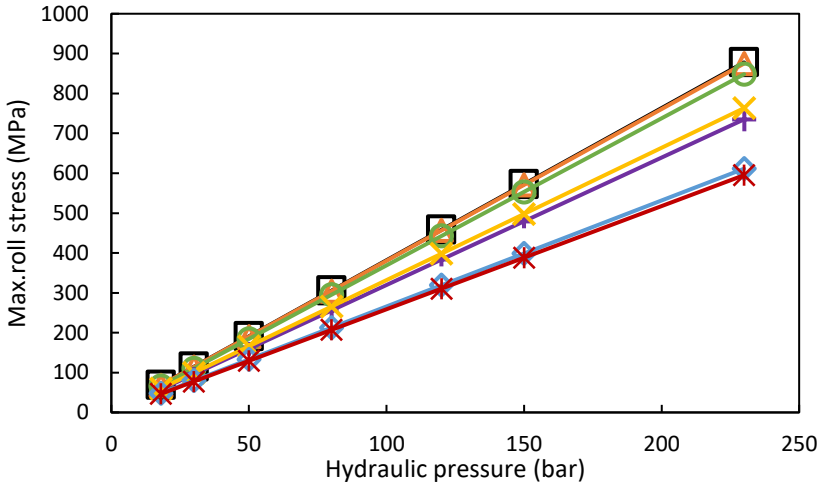

Figure 4-6: Maximum roll stress as a function of the hydraulic pressure for the smooth rollers and the following feed powders: $CaCO_3$ (□), mannitol (△), lactose 200M (○), anhydrous lactose (+), starch (x), maltodextrin (◇) and MCC (✳).

4.4.4 Elastic recovery

The elastic recovery (ε_R) of the powders was calculated based on the loading (ε_L) and unloading (ε_U) energies, which were calculated from the force-displacement data of a powder bed during a confined uniaxial compaction test (Section-3.2.2.5). The area under the curve was calculated and employed in equation (Equation 3-2). Figure 4-7 shows the loading/unloading curves of lactose 200M at stresses equivalent to the stresses applied during roller compaction (stresses calculated based on Johanson's theory (Figure 4-6)). They have been used to calculate elastic recovery. The loading/unloading curves for the remainder of the studied materials are shown in Figure A 3.

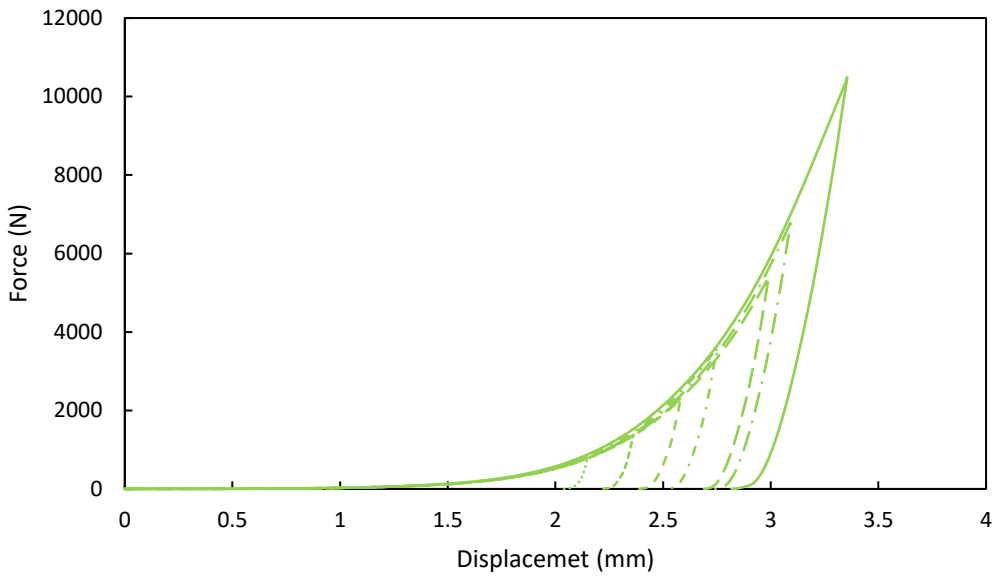

Figure 4-7: The loading/unloading compaction curves of lactose 200M obtained during confined uniaxial compaction test at a series of maximum compaction stresses (…. 66, ---- 110, – – – 184, - · - 295, — — 443, —·— 553, — 848 MPa) respectively equivalent to the hydraulic pressures used during roller compaction which are 18, 30, 50, 80, 120, 150, and 230 bar.

The elastic recoveries as a function of the Heckel yield strength (Table 4-1) for the different maximum stresses are shown in Figure 4-8. For all feed powders, the elastic recovery increases with increasing maximum stress. There is also a small increase with increasing yield strength. The anomalous behaviour of starch in this figure can probably be ascribed to the viscoelasticity of this material. Starch is reported to be more sensitive to the dwell time than the other powders used in this study [111,112]. Al Asady et al. [111] investigated the effects of compaction speed on a similar set of materials to those used in the current study (including $CaCO_3$, lactose 200M, MCC, starch and maltodextrin). The study mentioned that starch has a relatively high dependency on the compaction speed, i.e., unlike the other powder, as reflected in the strength of the compacts.

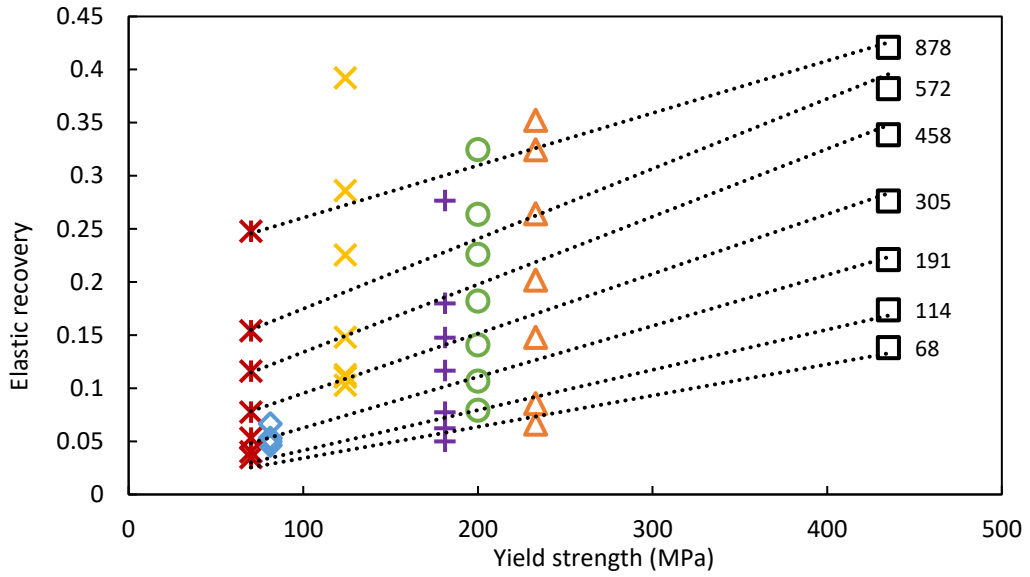

Figure 4-8: The elastic recovery of tablets measured during uniaxial compaction as a function of Heckel yield strength for the range of compressive stresses (MPa) investigated as given to the right of each data set; the lines are to guide the eye. The symbols for the powder feeds correspond to: $CaCO_3$ (□), mannitol (△), lactose 200M (○), anhydrous lactose (+), starch (x), maltodextrin (◇) and MCC (✳).

4.4.5 Ribbon tensile strength

The maximum force required to break the ribbons which were made with smooth rollers was measured and used in combination with the ribbon width and thickness to calculate the ribbon tensile strength (Figure 4-9). As the variations in ribbon width and thickness are considered in Equation 3-3, measurements were conducted on all types of the ribbons including; those that did not split at all, and those that exhibited transversal and longitudinally splitting. Assuming that the ribbon is symmetrical across its centre, the ribbons that split longitudinally were only considered when the splitting occurred through-the-width centre. Moreover, in the case of maltodextrin, due to its thermal sensitivity, ribbons could only be produced at low-stress levels and tensile strength measurements were only conducted on such ribbons. Figure 4-9 shows that upon stress application during roller compaction, MCC and maltodextrin were found to have the highest ribbon strength in comparison to the other materials. This was followed by starch, anhydrous lactose, lactose 200M, mannitol C160, and finally $CaCO_3$.

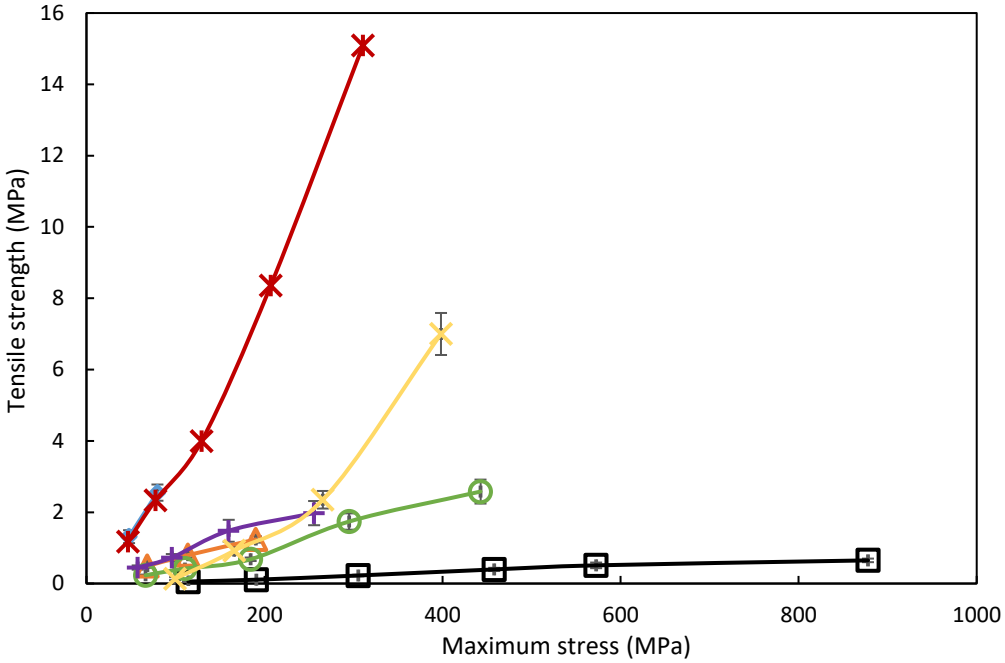

Figure 4-9: The effect of maximum compaction stress on the tensile strength of ribbons.

To first order, the tensile strength of the ribbons increased linearly with increasing maximum roll stress and the mean ratio increases with increasing values of the reciprocal of the yield strength (Figure 4-10). The line in Figure 4-10 is the best linear fit to the data (R^2 = 0.94) and corresponds to the following expression, where the intercept represents the minimum yield strength required to form a coherent ribbon:

$$\frac{\sigma_{\mathrm{T}}}{\sigma_{\mathrm{max}}} = 2.90K^{-1} - 0.01 \qquad \text{(Equation 4-4)}$$

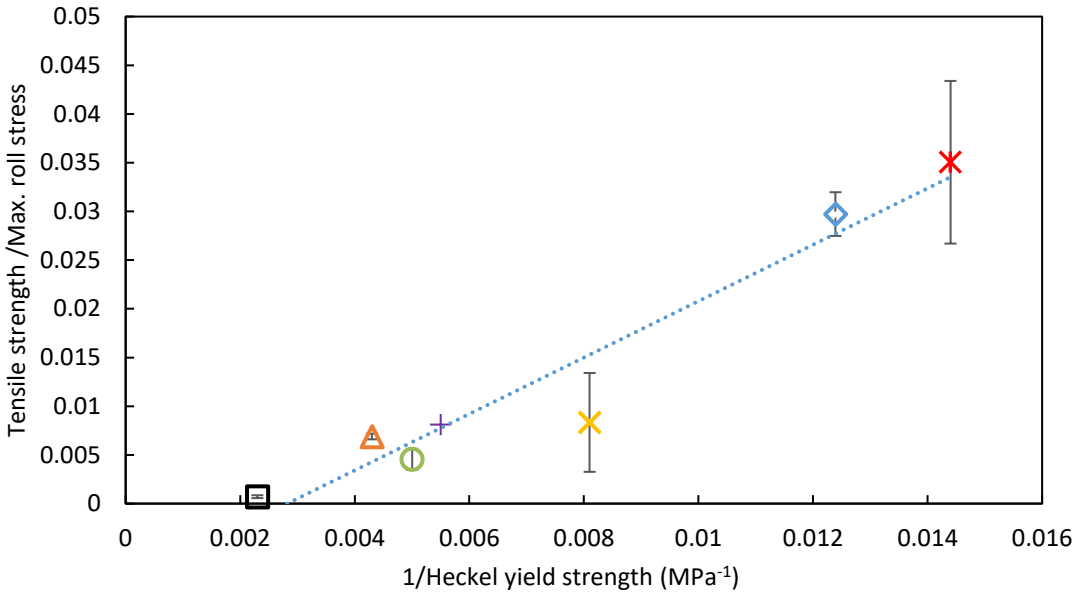

Figure 4-10: The mean ratio of the tensile strength and the maximum roll stress as a function of the reciprocal of the yield strength for $CaCO_3$ (□), mannitol (△), lactose 200M (○), anhydrous lactose (+), starch (x), maltodextrin (◇) and MCC (✳); the line is the best linear fit (Equation 4-4).

4.4.6 Ribbon splitting and sticking observations

As previously explained in section 3.2.3, all ribbons were produced using a fixed minimum gap distance and a variety of hydraulic pressures. Subsequently, ribbons were collected and all observations of ribbon sticking and splitting were recorded. Table 4-4 summarises the effects of the hydraulic pressure on the sticking and splitting behaviour of the different powder feeds in descending order of their Heckel yield strength for the unlubricated smooth rollers. Sticking refers to the physical adhesion of the ribbon to the two rollers and it is more likely associated with transverse splitting. The transversal (through-thickness) and longitudinal (through-width) splitting are classified as 'T' and 'L' respectively. Shaded areas in red indicate the occurrence of the splitting or sticking. Shaded areas in green correspond to conditions under which splitting or sticking does not occur.

Table 4-4: Effect of the maximum roll stress on the splitting and sticking behaviour of the ribbons formed from unlubricated smooth rollers. Grey dotted areas indicate a non-achievable condition. Red regions indicate the occurrence of splitting/sticking. Green regions indicate the non-occurrence of splitting/sticking. Spitting is designated by T (transversal splitting), Ln (longitudinal splitting into n pieces) and L J (longitudinally joined splitting).

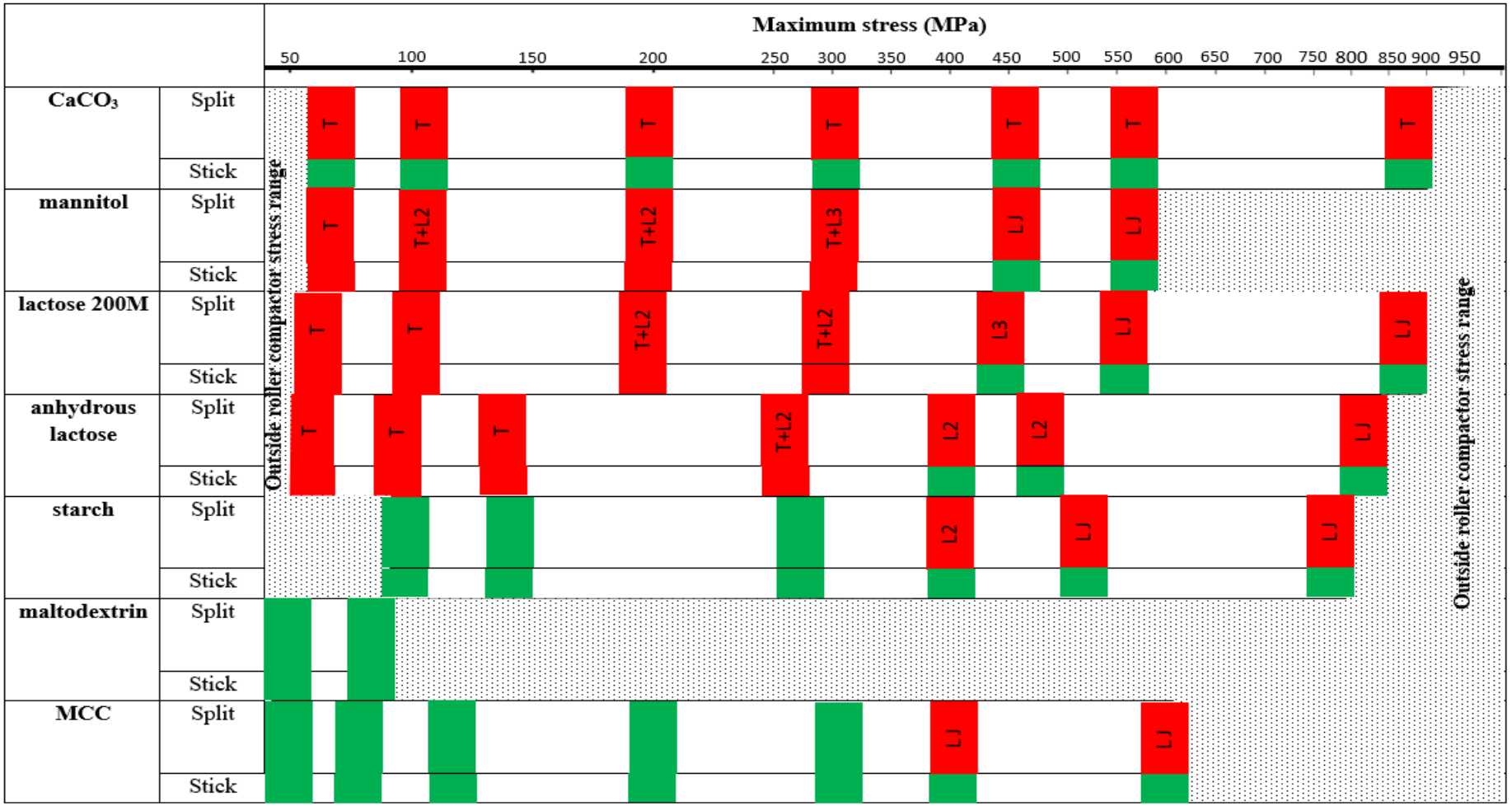

As can be seen in Table 4-4, for all of the produced ribbons with the exception of the $CaCO_3$ ribbons, transverse splitting only occurs when there is sticking to the rollers and thus only longitudinal splitting is possible when the rollers are lubricated. Ribbons made from $CaCO_3$ are the exception in exhibiting transverse splitting even though sticking to the rollers does not occur. The images from Figure 4-11 show the top and the bottom surface of splitting ribbons that were produced at different stress levels. It can be seen that the bottom surface is evidently rougher compared with the top surface (Figure 4-11-B). Because of the limited deformability of this material, the increase in the applied stress was not sufficient to create strong enough bonds to save the integrity of the compacted ribbon (non-splitting ribbon).

A Stress (MPa)	70	877
Top surface	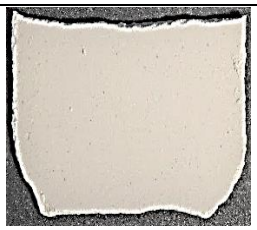	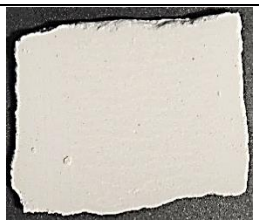
Bottom surface	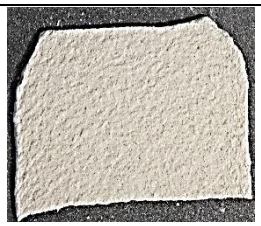	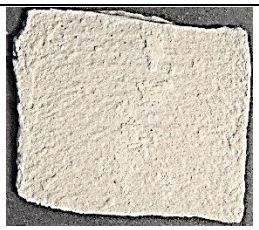
B	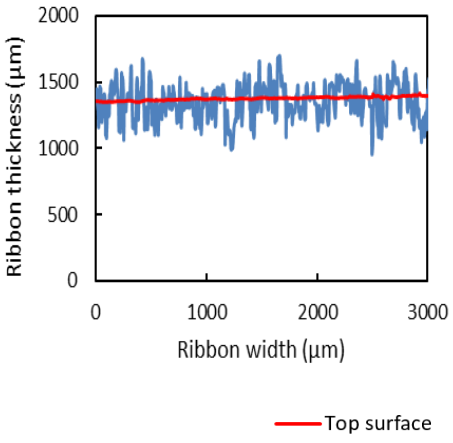	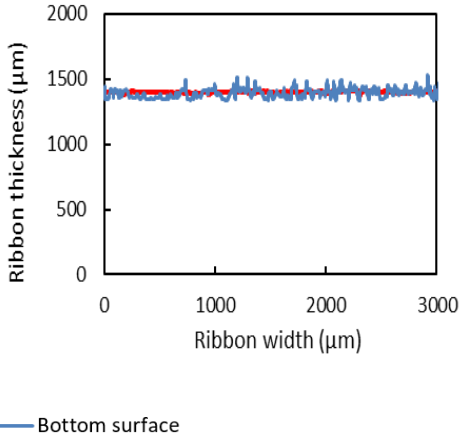
		

Figure 4-11: A: Images of top and bottom surface of calcium carbonate splitting ribbons produced at different stresses, and B: Ribbon thickness profile for the top and the back surface of calcium carbonate splitting ribbons produced at 70 and 877 MPa, the measurements were conducted for 3mm line across the ribbon through the width centre (measured by digital microscope (Keyence VHX-5000).

As exemplified in Figure 4-12, for mannitol ribbons, there are transitions in the longitudinal splitting behaviour with increasing applied stress from the ribbon being coherent at low stress to splitting into two ('L2') and three ('L3') sections and also splitting from the edge so that the cracks are joined ('LJ').

69 MPa	114 MPa	304 MPa	571 MPa
No longitudinal splitting	L2	L3	LJ
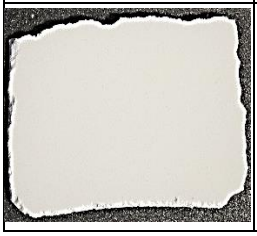	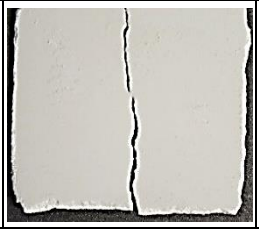		

Figure 4-12: Images of mannitol ribbons that are produced at different maximum roll stresses.

In case of maltodextrin (Figure 4-13), increasing the applied stress (≥122 MPa), resulted in an increase in the ribbon temperature beyond the glass transition temperature of this material (81°C) [113], which caused the ribbons to split transversally and stick to the roller surface. Figure 4-13 shows the top and the bottom surfaces of maltodextrin ribbons which were produced at different stress levels. At low stress (44 and 73 MPa), no splitting occurred, and both ribbon surfaces have similar roughness. At about 122 MPa; ribbon started to split transversally and stick to the roller surface.

Stress (MPa)	44	73	122
Top surface		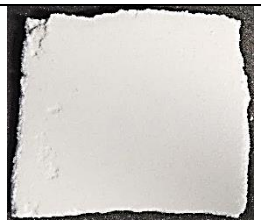	
Bottom surface	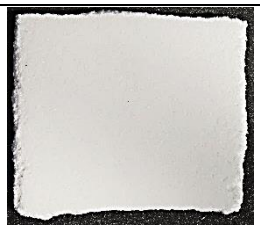	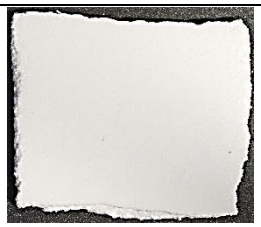	

Figure 4-13: Images of top and bottom surface of maltodextrin ribbons produced at different stresses.

Moreover, it was also observed that the application of MgSt to the rollers completely inhibited sticking and transverse splitting but similar longitudinal splitting was observed.

It was also observed that avoiding transversal splitting/roller sticking by increasing the applied stress was associated with a significant reduction in the amount of fines. The

percentage of fines decreased with increasing roll stress and approximately with decreasing values of the Heckel yield stress as shown for the unlubricated smooth rollers in Figure 4-14. The trends correspond to a reduction in the occurrence of transversal splitting.

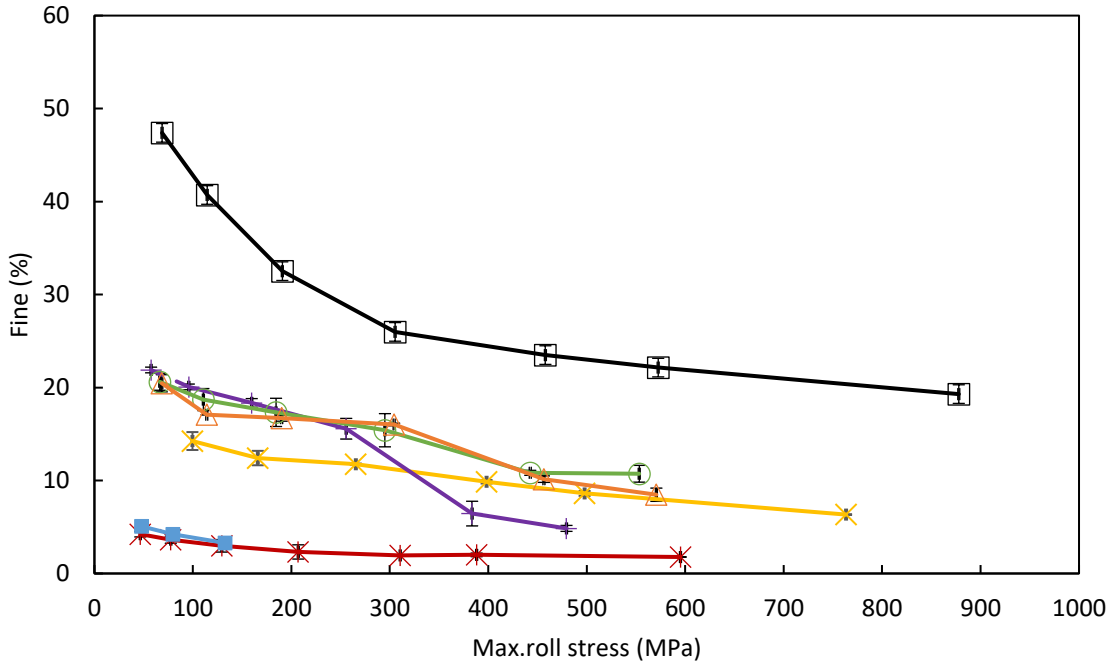

Figure 4-14: The amount of fines (w/w%) produced for the powder feeds with the unlubricated smooth rollers as a function of the maximum roll stress. The symbols for the powder feeds correspond to: $CaCO_3$ (□), mannitol (△), lactose 200M (○), anhydrous lactose (+), starch (x), maltodextrin (◇) and MCC (✳).

4.4.7 Ribbon splitting/sticking: effect of maximum roll stress and yield strength

It is evident from Table 4-4 that the combined influence of the maximum roll stress and the yield strength are critical factors in ribbon splitting. This is more directly clear in the case of pure longitudinal splitting i.e. also excluding mixed longitudinal-transverse splitting. Figure 4-15 maps the transition from no splitting to longitudinal splitting in coordinates of the maximum roll stress and the yield strength for the unlubricated and externally lubricated smooth rollers, for which the results were identical i.e. this includes mixed splitting outcomes that revert to pure longitudinal splitting. It shows that there is a lower limit of the maximum roll stress above which, depending on the yield strength, longitudinal splitting occurs. For a yield strength greater than ~ 130 MPa, the critical roll stress at which such splitting occurs reduces considerably. The sensitivity of longitudinal

splitting to increasing the roll stress and the yield strength is clearly related to the increase in the elastic recovery (Figure 4-8).

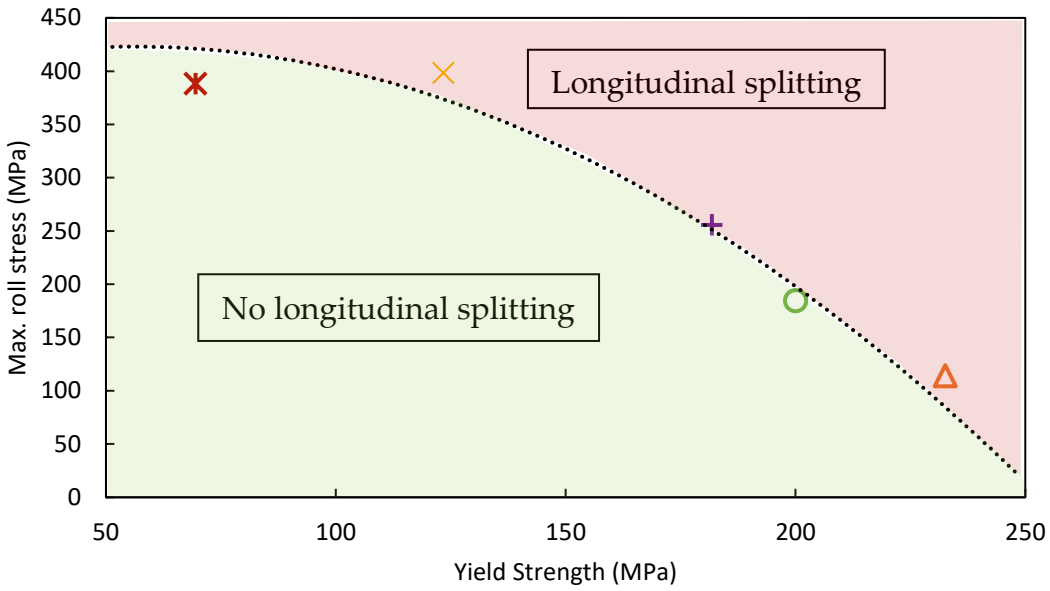

Figure 4-15: A map of the transition from no splitting to longitudinal splitting in coordinates of the maximum roll stress and the Heckel particle yield strength for the unlubricated and externally lubricated smooth rollers. The symbols for the powder feeds correspond to: mannitol (△), lactose 200M (○), anhydrous lactose (+), starch (x), MCC (✳). Longitudinal splitting was not observed for $CaCO_3$.

The compaction of powder assemblies is accommodated by a combination of a number of mechanisms that may include the rearrangement, elastic or elastoplastic deformation and fracture of the particles. It is well established that the stress is not transmitted uniformly but through force chains that increase in number density with increasing stress. Thus, as particles become progressively subjected to increasing stress, it will eventually cause them to deform plastically rather elastically when their yield strength is exceeded, and thus reducing the contribution to the elastic recovery. This would also be the case for particle rearrangement and fracture. Moreover, greater yield strengths are associated with less cohesion of the compacted particles so that the tensile strength of the ribbons decreases with increasing values of the yield strength (Figure 4-10).

A critical factor in longitudinal splitting is the relative difference in the porosity across the ribbons since it is related to the variation in the elastic recovery. Figure 4-16 shows X-ray images of MCC ribbon produced at 204 MPa. The images show a clear difference

in ribbon porosity between the ribbon through-the-width centre and its sides; more air (black pixels) at both edges compared to more powder (white pixels) at the centre.

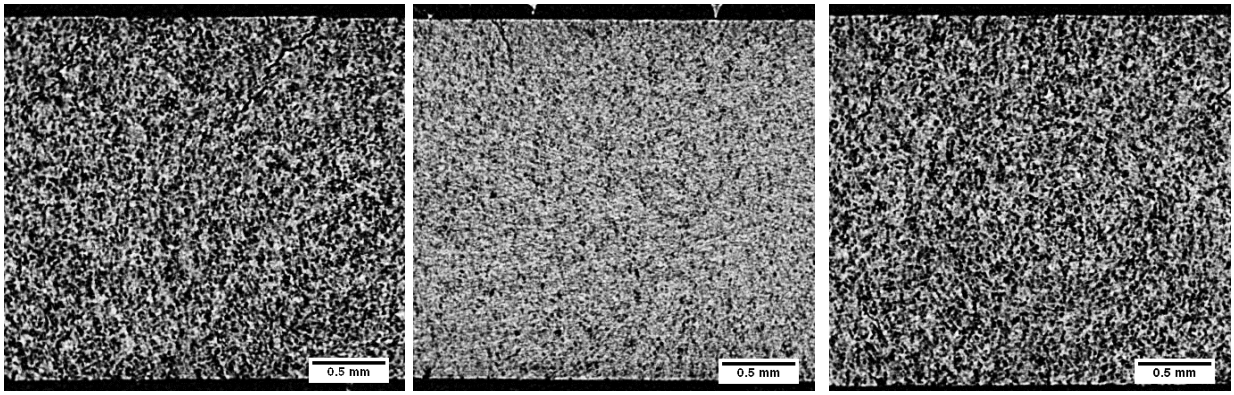

Left side Centre Right side

Figure 4-16: X-ray tomography images of MCC ribbon produced at 204 MPa across its width.

To understand the origin of the relative difference in the porosity, which has been observed previously [114], it is useful to consider roller compaction as a combination of shear and squeeze flow. The squeeze flow component exerts back pressure upstream resulting in the maximum pressure occurring at an angle that is greater than that corresponding to the minimum gap, which is normally taken as zero. This angle is approximately equal to the neutral angle at which the shear stress is zero due to its change of direction [64]. More importantly, the squeeze component results in a lateral pressure distribution that has a maximum value in the centre of the width of the ribbon. Such non-uniform pressure distributions are observed in the compression of all fluids, solids, and granular systems e.g. metals [115] and pastes [116]. They arise from the resistance to deformation/flow caused by no-slip or friction at the contacting walls. As a result, the powder feed in a roller compactor is more compressed in the centre of the ribbon compared to the edges as demonstrated in Figure 4-16. This has important implications for ribbon splitting as discussed below.

Since the porosity is lowest in the centre of a ribbon, the maximum roll stress must be greater in this region compared to the edges. Thus, in the exit region, the stored elastic strain, and hence the expansion of the ribbon, will be greatest in the centre of a ribbon. As a result, longitudinal splitting always occurs in the centre of the width of the ribbons where the crack opening stresses will be greatest. Consequently, bending stresses are developed that increase from zero in the centre of the width to a maximum value on the

edges. The importance of the role of the porosity distribution and bending stresses in the occurrence of longitudinal splitting is discussed in more details in the following chapter.

Given the importance of the maximum roll stress and the yield strength in ribbon splitting occurrence, the ratio is a useful dimensionless quantity for quantifying the ranges under which no splitting and splitting occurs. This is shown in Figure 4-17 for the unlubricated and lubricated smooth rollers as a histogram based on the outcomes per powder type normalised by the total number of outcomes.

For the case of no lubrication, both types of splitting are developed; as this ratio increases in value, there is a general reduction in the number of transversal splitting and an increase in the number of longitudinal splitting outcomes. As the value increases, there is a higher probability for bonding to occur which could overcome the adhesion to roller surface and reduce transversal splitting occurrence. However, higher values indicate more elastic recovery (Figure 4-8) which can cause longitudinal splitting at certain levels. The trend of longitudinal splitting becomes clearer in case of lubricated rollers since no transversal splitting is taking place and all of the mixed transversal-longitudinal splittings has turned into pure longitudinal splittings.

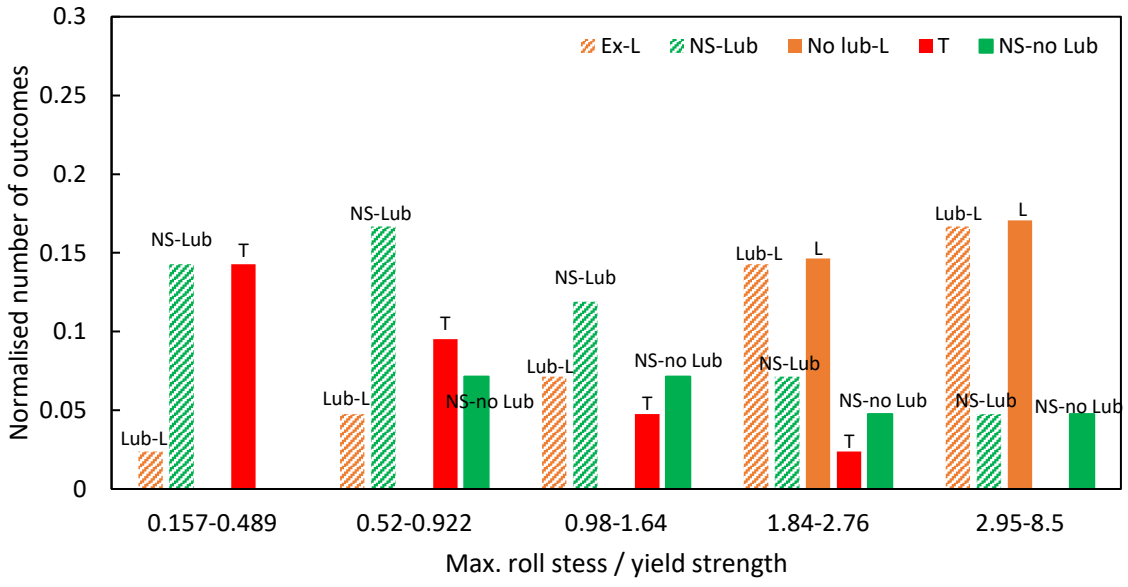

Figure 4-17: A histogram of the number of non-splitting, longitudinal splitting, and transversal splitting outcomes per powder feed normalised by the total number of outcomes that were observed with the unlubricated (solid filling bar) and lubricated smooth rollers (pattern-filled bar) based on the ratio of the maximum roll stress and Heckel particle yield strength. NS refers to no splitting, T to transversal splitting, L to longitudinal splitting and Lub to external roller lubrication.

4.4.8 Splitting index

An alternative dimensionless quantity is a splitting index, I_S:

$$I_S = \varepsilon_R \sigma_{max} / \sigma_t \qquad \text{Equation 4-5}$$

It is more fundamental in terms of its mechanistic interpretation than the ratio σ_{max}/σ_Y but requires that roller compaction has to be carried out in order to measure σ_t before it can be employed for assessing formulations and operating conditions.

This index is based on estimating residual stress and ribbon tensile strength to predict splitting occurrence. However, despite having the largest yield strength (Table 4-1), and hence the highest elastic recovery (Figure 4-8) and weakest ribbons (Figure 4-9), $CaCO_3$ ribbons never split longitudinally (Table 4-4). The probable cause is that the ribbons exhibit stable fracture unlike those formed by the other powder feeds (Figure 4-18).

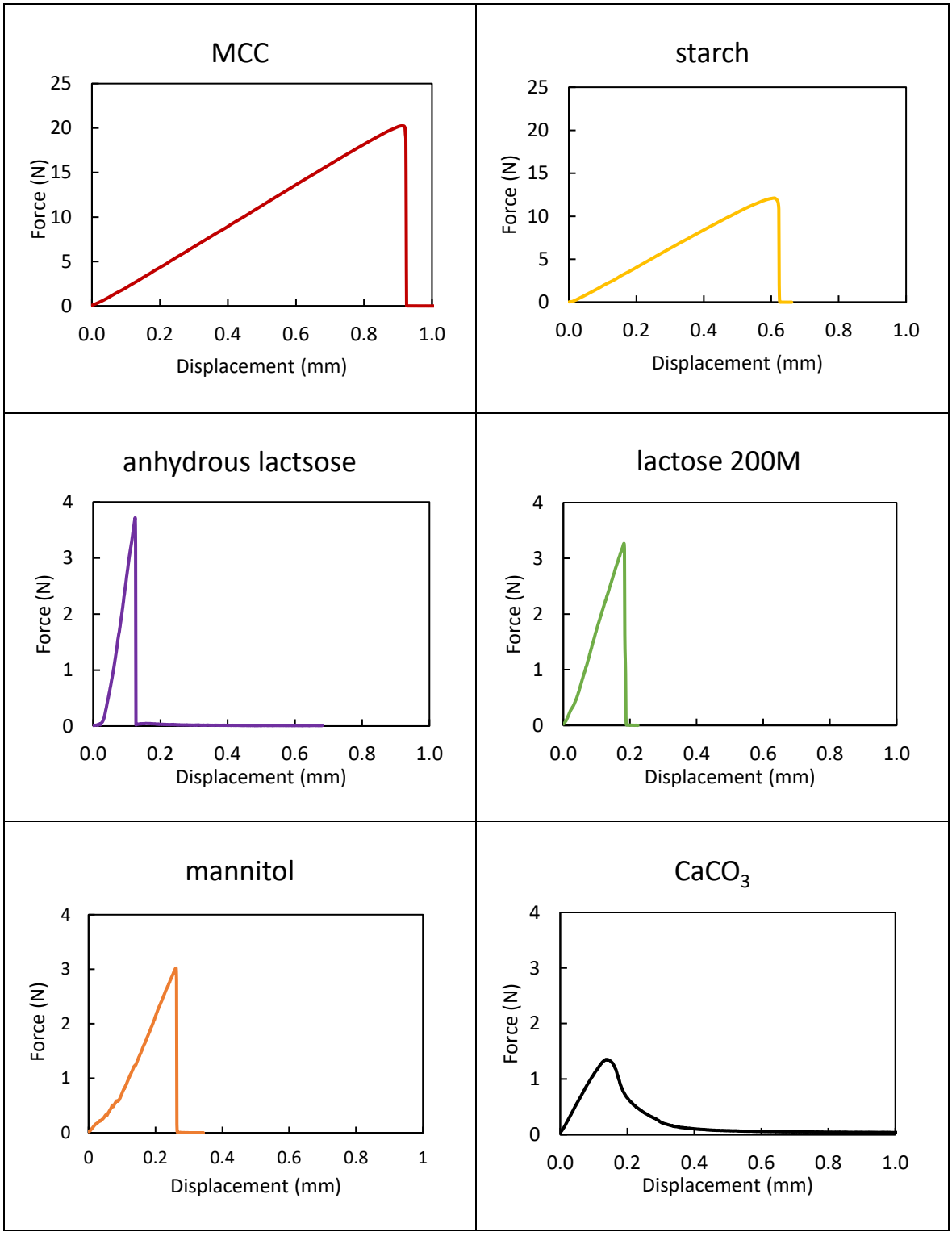

Figure 4-18: The applied force as a function of the displacement for three-point fracture measurements. The ribbons formed from all the powder feeds except those from $CaCO_3$ exhibited unstable fracture at all maximum roll stresses.

A characteristic of stable fractures is that crack propagation is arrested when the driving force or displacement ceases; a common example is tearing a paper. Thus, it may be assumed that the stored elastic strains in $CaCO_3$ ribbons are less than the critical value

required to significantly propagate a longitudinal crack. In the case of the ribbons made from the other powders, the instability of the crack growth will result in catastrophic crack propagating once it is initiated. It is more difficult to understand the factors that result in the $CaCO_3$ ribbons splitting transversely in the absence of observable adhesion to the rollers. It has been argued, on the basis of finite element modelling, that the reversal of the shear stress and strain at the neutral angle may result in fracture/lamination since pharmaceutical powder compacts are generally weak under shear [64]. That is, weak adhesion forces to the rollers may be sufficient to cause such a weak plane to fracture transversely. The $CaCO_3$ ribbons would be particularly susceptible to such a mechanism since they are so mechanically weak in any case. Consequently, $CaCO_3$ splitting data has been excluded for its anomalous splitting behaviour.

When applied, the splitting index leads to a trend of decreasing no splitting and increasing longitudinal splitting as the values of this parameter increases (Figure 4-19). However, there is an upper limit at which splitting always occurs. That the values increase to ~45 rather than the ideal case of the critical condition for splitting being approximately unity arises because the numerator in Equation 4-5 is some measure of the residual stress acting vertically rather than the actual crack opening stress acting at the two surfaces of a ribbon.

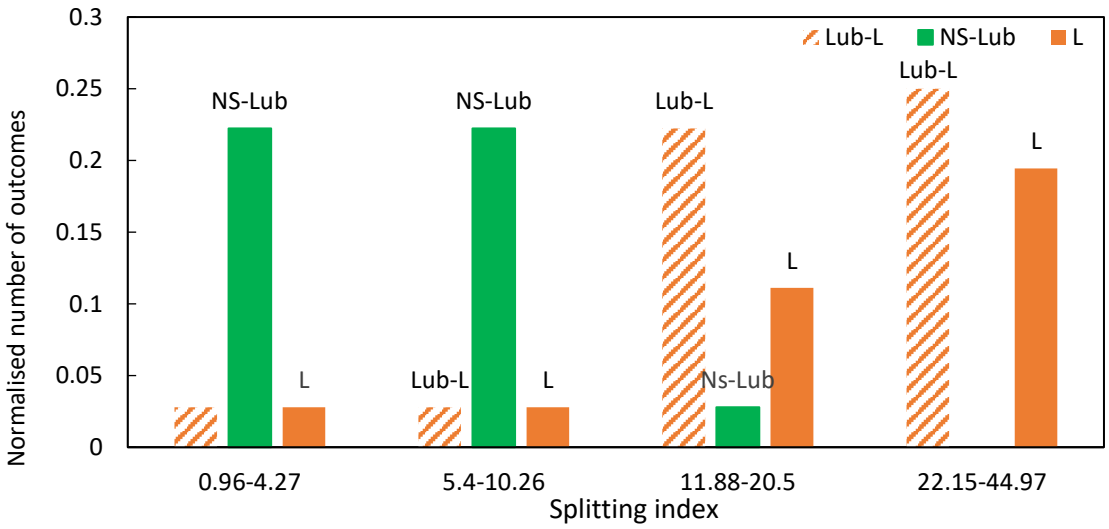

Figure 4-19: A histogram of the number of non-splitting (■) and longitudinal splitting outcomes per powder feed normalised by the total number of outcomes that were observed with the unlubricated (■) and lubricated smooth rollers (▨) based on the splitting index. NS refers to no splitting, L to longitudinal. The data for $CaCO_3$ ribbons are not included since its splitting behaviour is anomalous.

As mentioned previously, with the exception of $CaCO_3$, transverse splitting and also mixed transverse-longitudinal splitting is always associated with sticking of the spilt

ribbons to the rollers (Table 4-4). This has two effects: (a) the adhesive forces acting on a ribbon prevent bending strains being developed as would be the case for a ribbon that was not adhered to the rollers (this will affect longitudinal splitting) and (b) the adhesive forces coupled with the residual stresses result in an increased crack opening stress across the width of a ribbon approximately in the centre of the thickness (this will affect transversal splitting).

The strength of adhesion of the powder feed to the rollers was estimated by recording a specific roller area after one of the scrapers. The particle debris coverage as a function of the maximum roll stress for the powders that exhibited adhesion is shown in Figure 4-20. The extent of the coverage reduces with increasing roll stress and asymptotically approaches zero. The coverage for starch, MCC and $CaCO_3$ were approximately zero, which was also the case for maltodextrin until it melted.

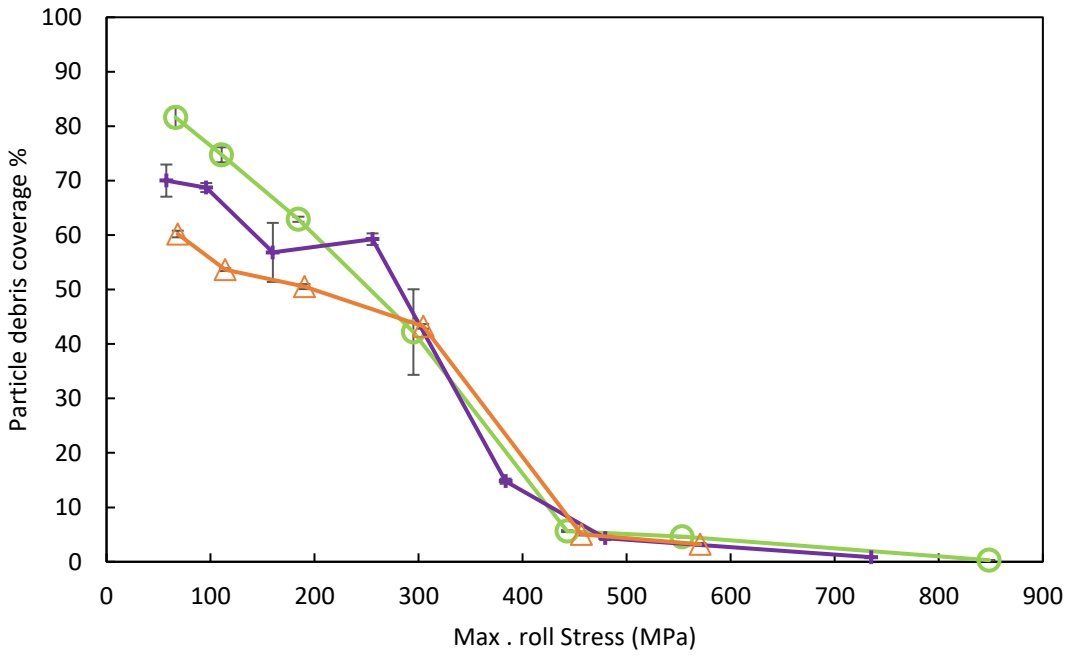

Figure 4-20: The particle debris coverage on the smooth unlubricated rollers measured after the scrapers as a function of the maximum roll stress for the mannitol (△), lactose 200M (○), and anhydrous lactose (+). Adhesion was absent for starch, MCC and $CaCO_3$.

A histogram involving the splitting index for the unlubricated smooth rollers that includes transverse and mixed splitting is presented in Figure 4-21. There is a lower limit at which no splitting occurs after which pure transverse splitting is prevalent but decreases until there is a transition to mixed and longitudinal splitting. While the index is a useful means

of categorising the data for transverse and mixed splitting, it is of less fundamental value since it ignores the adhesive stresses acting on the ribbons.

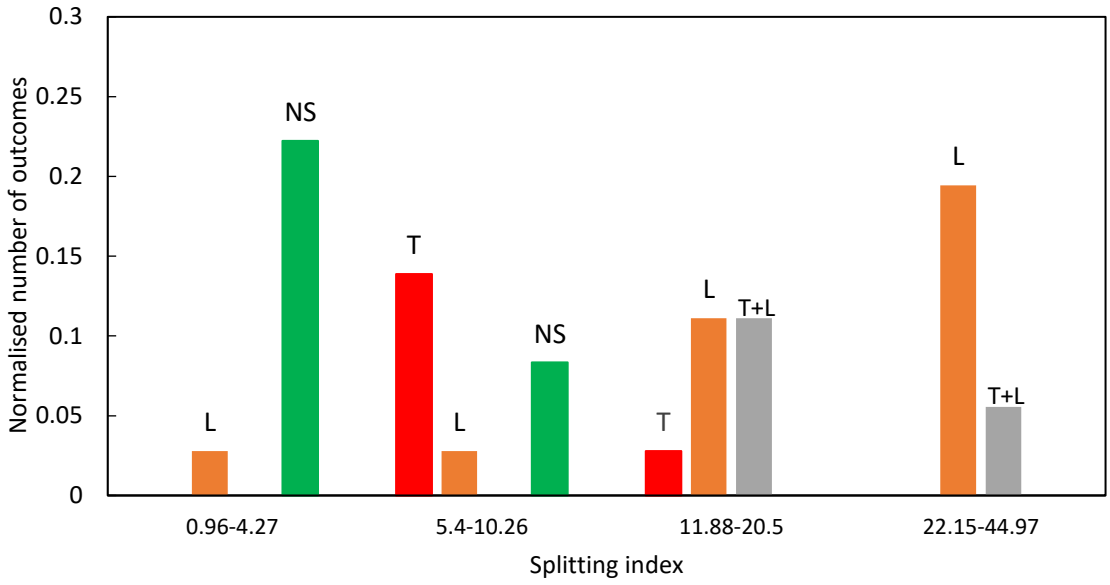

Figure 4-21: A histogram based on the splitting index of the number of non-splitting and splitting outcomes per powder feed normalised by the total number of outcomes that were observed with the unlubricated smooth rollers. The data for $CaCO_3$ ribbons are not included since its splitting behaviour is anomalous. The coding refers to transversal (■, T), longitudinal (■, L), mixed transversal-longitudinal (■, T+L) and no splitting (■, NS).

The use of single powder feeds has allowed the mechanisms of splitting and the critical factors that govern the occurrence of splitting to be established. However, in practice, the feed powders are generally multi-component and include MgSt as an internal lubricant. Some limited studies were carried out to examine the effects of including 1 w/w% MgSt with the same set of powders used before except for maltodextrin which was excluded because of its thermal sensitivity. Powders were roller compacted using the processing condition for the unlubricated powders. The results were relatively similar to the feeds without MgSt except that sticking to the rollers did not occur. In addition, for anhydrous lactose, there was no splitting up to hydraulic pressures of 80 bar whereas without MgSt splitting occurred at all pressures investigated. Adding lubricant to the powder was advantageous in terms of preventing adhesion on the roller surface. However, this came at the cost of reducing the beneficial griping of roller the surface, which is critical to initiate compaction in the roller compaction process. As a result, adding lubricant reduced the range of workability of the process, as the compaction was not achievable when lubricant was mixed with all used powders except for mannitol and anhydrous lactose.

Table 4-5 summarises the effect of hydraulic pressure on the splitting behaviour of the different powder feeds for the lubricated formulations. Shaded areas in red indicate the occurrence of the splitting. Shaded areas in green correspond to conditions under which splitting does not occur.

The compression of practical formulations involving mixtures of powders is complex because it is likely to involve particles of different mechanical properties, shapes and size distributions. Systematic studies over a wide range of mixtures have not been reported for either roller compaction or tabletting although there is some evidence that simple mixture models could be applied [117]. In extending the current work to mixtures, measurements of the effective compressibility factor and yield strength by confined uniaxial compaction would be the most appropriate approach to adopt initially.

Table 4-5: Effect of the hydraulic pressure on the splitting behaviour of the ribbons formed from lubricated formulations. Grey dotted areas indicate a non-achievable condition. Red regions indicate the occurrence of splitting. Green regions indicate the non-occurrence of splitting. Spitting is designated by T (transversal splitting), Ln (longitudinal splitting into n pieces) and LJ (longitudinally joined splitting).

	MgSt %	Hydraulic pressure (Bar)						
		18	30	50	80	120	150	230
CaCO3	1%							
	0%	T	T	T	T	T	T	T
mannitol	1%	T	T	T+L2	L2	LJ	LJ	
	0%	T	T+L2	T+L2	T+L3	LJ	LJ	
lactose 200M	1%							
	0%	T	T	T+L2	T+L2	L3	LJ	LJ
anhydrous Lactose	1%					L2	L2	LJ
	0%	T	T	T	T+L2	L2	L2	LJ
starch	1%							
	0%					L2	L2	LJ
MCC	1%							
	0%						LJ	LJ

4.5 Conclusions

The phenomenon of ribbon splitting/sticking during roller compaction was investigated in a comprehensive perspective. Both longitudinal and transversal splitting are problematic; while transverse splitting is generally associated with adhesion to the rollers that has a serious detrimental effect on the performance of the process, longitudinal splitting does not prevent the ribbons from being milled, it is a result of a distribution of the ribbon density across the width. Consequently, it is not possible to make granules that all have optimal properties in terms of the mechanical strength and dissolution characteristics of the tablets. Transverse splitting/sticking happens at low stresses when there is no enough bonding/deformation across the ribbon thickness that could overcome the adhesion to roller surfaces. This effect was very clear when the rollers are lubricated since transversal splitting/sticking was completely eradicated in case of external lubrication. Increasing the applied stress and/or reducing the yield strength of feed powder increases the inter-particle cohesive strength and thus reduces the probability of adhesion to the rollers and hence transverse splitting. However, this increase in the applied stress increased the probability for longitudinal splitting which is believed to be due to heterogeneous extents of elastic recovery across the ribbon width. The observed trends of splitting were rationalised in terms of a splitting index, which is a measure of the stored elastic energy driving fracture relative to the fracture stress of the ribbons. The elastic recovery increases as the yield strength increases, which is associated with a reduction in the tensile strength of the ribbons and higher probability of longitudinal splitting.

CHAPTER 5 RIBBON SPLITTING: ROLE OF POROSITY DISTRIBUTION

5.1 Introduction

While the main focus of the previous chapter was on elucidating the mechanisms of ribbon splitting, the focus in the current chapter is to further investigate the role of porosity distribution homogeneity in relation to ribbon splitting. The effect of changing roller surface on ribbon splitting behaviour is examined; knurled rollers were employed with and without lubrication by manually applying MgSt to the rollers. The compaction was conducted at the same processing conditions used during smooth rollers experiments and the behaviour of ribbon splitting and sticking was recorded accordingly.

In comparison to the smooth rollers, the application of knurled rollers reduced the occurrence of longitudinal splitting and extended the range of transversal splitting which in some cases occurred without sticking.

The porosity distribution of ribbons was measured by two different approaches namely, X-ray tomography and Near Infrared Chemical Imaging (NIR-CI). An improved splitting index has been developed to cope with the effect of ribbon porosity distribution.

5.1.1 Hypothesis

As discussed in the previous chapter, the varying degree of densification across a ribbon width was due to a non-homogenous stress distribution. This heterogeneity is expected to reflect in a distribution of strain recovery across a ribbon width and subsequently create bending stress that affects the trend of ribbon splitting. Figure 5-1 shows a schematic drawing for the development of bending stress as a result of heterogeneous strain recovery.

In an attempt to investigate the role of porosity heterogeneity in the occurrence of ribbon splitting, a pair of knurled rollers, which in comparison with the smooth rollers have a higher powder-metal contact surface area, were used. Due to the surface engravings, knurled rollers are expected to grip powder more homogenously in the compaction zone; this is expected to reflect in a more uniform porosity distribution across the ribbon width.

Eventually, upon stress release, the ribbon will experience a more uniform strain recovery and less bending stress across its width, which will influence the longitudinal splitting behaviour.

At the same time, increasing the roller surface area by using knurled rollers is expected to change the extent of powder-metal interaction that can affect the occurrence of transversal splitting.

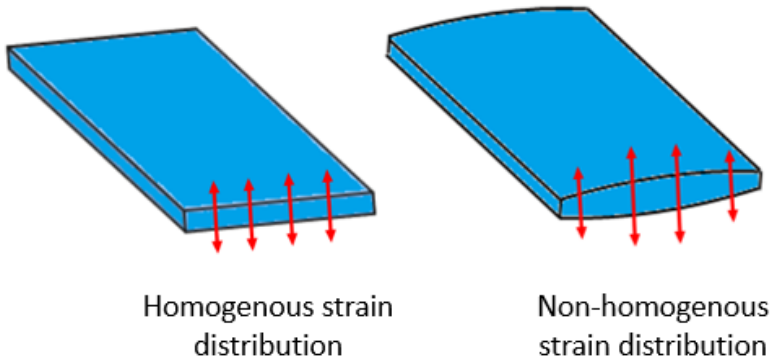

Figure 5-1: A schematic drawing of the development of the proposed bending stress across ribbon width.

5.2 Methods

All primary powders were analysed for their angle of wall friction with the knurled rollers. A specially made shear cell disk to measure the angle of wall friction was used during the test. The values were used with the compressibility factor (K) and the effective angle of internal friction (δ_E) that were measured previously, to calculate the maximum stress applied between the knurled rollers.

Prior to compaction, all powder feeds were conditioned in terms of the humidity as described in section 3.2.1. Powders are then roller compacted at the same processing conditions of that used for smooth rollers experiments: fixed roller gap (2 mm) and roller speed (3 rpm) while activating the feedback-gap controlling system during experiments.

All produced ribbons are analysed for their porosity distribution using X-ray tomography (samples were taken every ~3.5 mm across ribbon width). NIR-chemical imaging was also used in an attempt to overcome some of the X-ray tomography limitations. The NIR needs to be calibrated beforehand; therefore a set of tablets were compressed at a known series of stresses, the tablets were then scanned using NIR-CI and then an intensity vs

porosity relationship was established and used to quantify ribbon porosity distribution across ribbon width.

5.3 Results and discussion

5.3.1 Max stress with knurled rollers

To examine the effect of roller surface on the ribbon splitting behaviour, a pair of knurled rollers with a surface roughness (Ra ~ 119.4 ± 5.9 µm) were used to produce ribbons using the same materials and processing conditions used with the smooth rollers experiments. The roller surface area was measured for a certain section and the whole roller surface area was calculated accordingly (Figure 5-2).

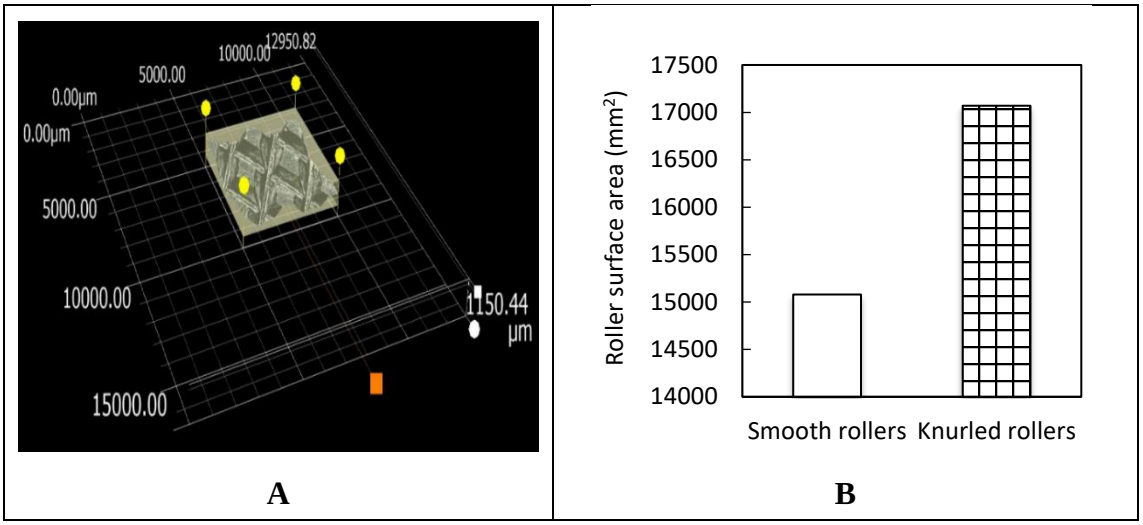

Figure 5-2: A: The surface area of 25 mm^2 roller area measured by a digital microscope (Keyence VHX-5000). B: Calculated roller surface area of smooth and knurled rollers used in this study.

The maximum stress applied between the two knurled rollers was determined using Johanson's theory. To apply this theory, the angle of wall friction ($\emptyset_w$) was measured using a specially made shear cell coupon which has a similar surface to the knurled rollers (Table 5-1). These values were implemented in combination with the effective angle of internal friction (δ_E) and compressibility factor (κ) to calculate the maximum stress (Equation 2-6 to Equation 2-14).

Table 5-1: Angles of wall friction for all powders used.

Material	($\emptyset_w$) knurled coupon
$CaCO_3$	34.35 ± 0.23
mannitol	31.57 ± 0.12
lactose 200M	34.51 ± 0.43
anhydrous lactose	32.19 ± 0.1
starch	27.79 ± 0.11
maltodextrin	31.1 ± 0.29
MCC	35.1 ± 0.21

To calculate the nip angle for the knurled rollers, (d), the thickness of the ribbon when the roll gap (s) is zero, was changed from 0 mm for smooth roller to 1 mm for the knurled roller (Equation 2-10), where each roller has an indentation depth of 0.5 mm. Figure 5-3 shows the maximum stress applied to the material as a function of hydraulic pressure for smooth rollers (A) and knurled rollers (B).

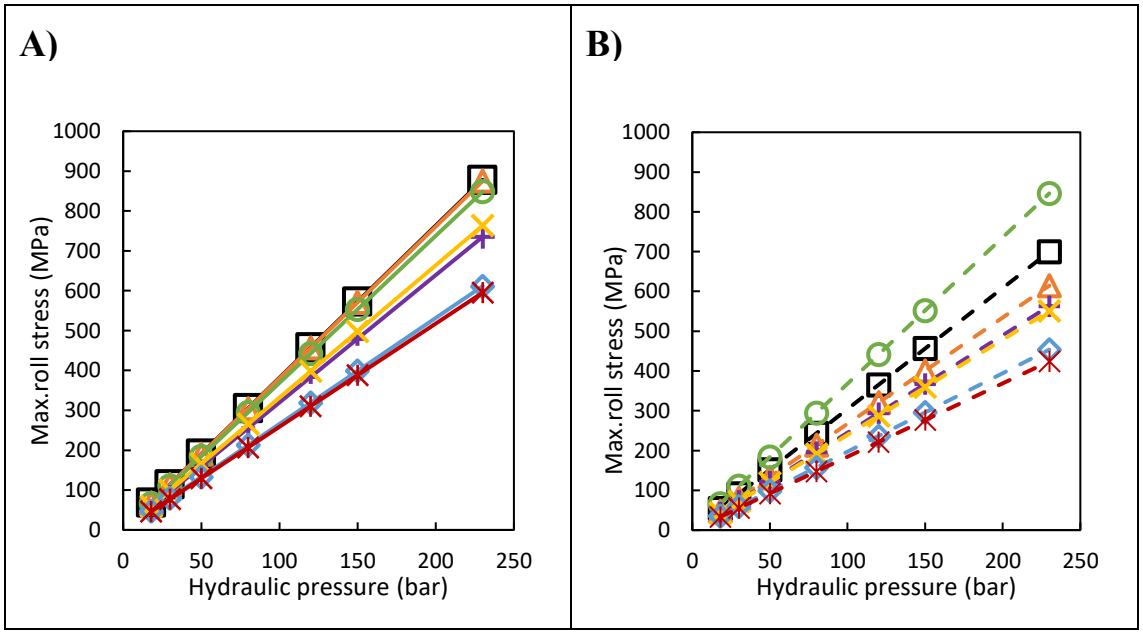

Figure 5-3: Maximum roll stress as a function of the hydraulic pressure for the (A) smooth and (B) knurled rollers and the following feed powders: $CaCO_3$ (□), mannitol (△), lactose 200M (○), anhydrous lactose (+), starch (x), maltodextrin (◇) and MCC (✳).

All feed powders exhibit a linear relationship with the gradients for a given feed powder being greater for the smooth rollers since the nip angles are less (Figure 5-4), i.e. the contact area with the rollers is smaller at a given roll force as defined by the set hydraulic

pressure. Figure 5-4 shows that using knurled rollers could be more advantageous in terms of increasing the nip area, which could enhance the mass throughput of the process [28].

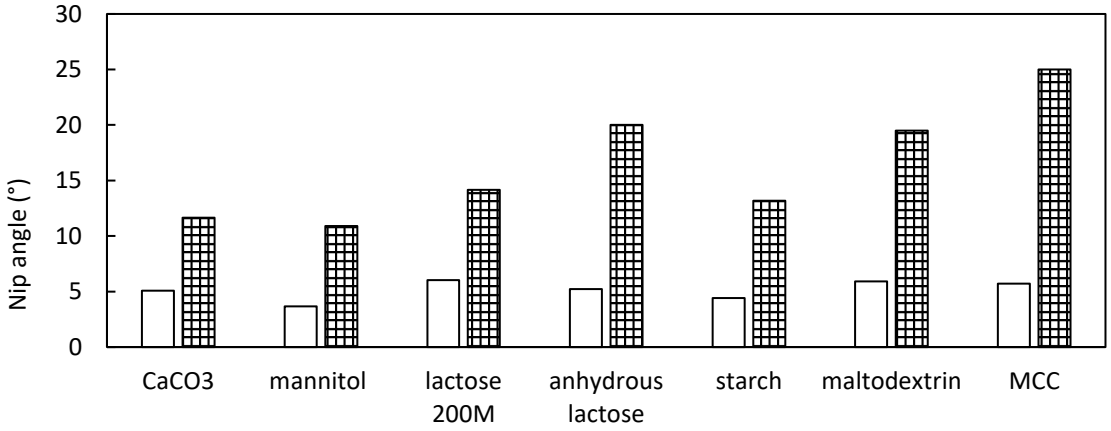

Figure 5-4: The calculated nip angles for the different types of powder feed materials, which were compacted using knurled (⊞) and smooth (□) rollers.

5.3.2 Assessing the roller compaction process using knurled rollers (comparison with smooth rollers mediated RC)

5.3.2.1 Strength of the ribbon

Applying the same hydraulic pressure on both types of rollers i.e. knurled or smooth rollers resulted in stronger ribbons when smooth rollers are used as can be seen in Figure 5-5, this is due to lower nip angle and higher amount of stress applied (Figure 5-3 and Figure 5-4).

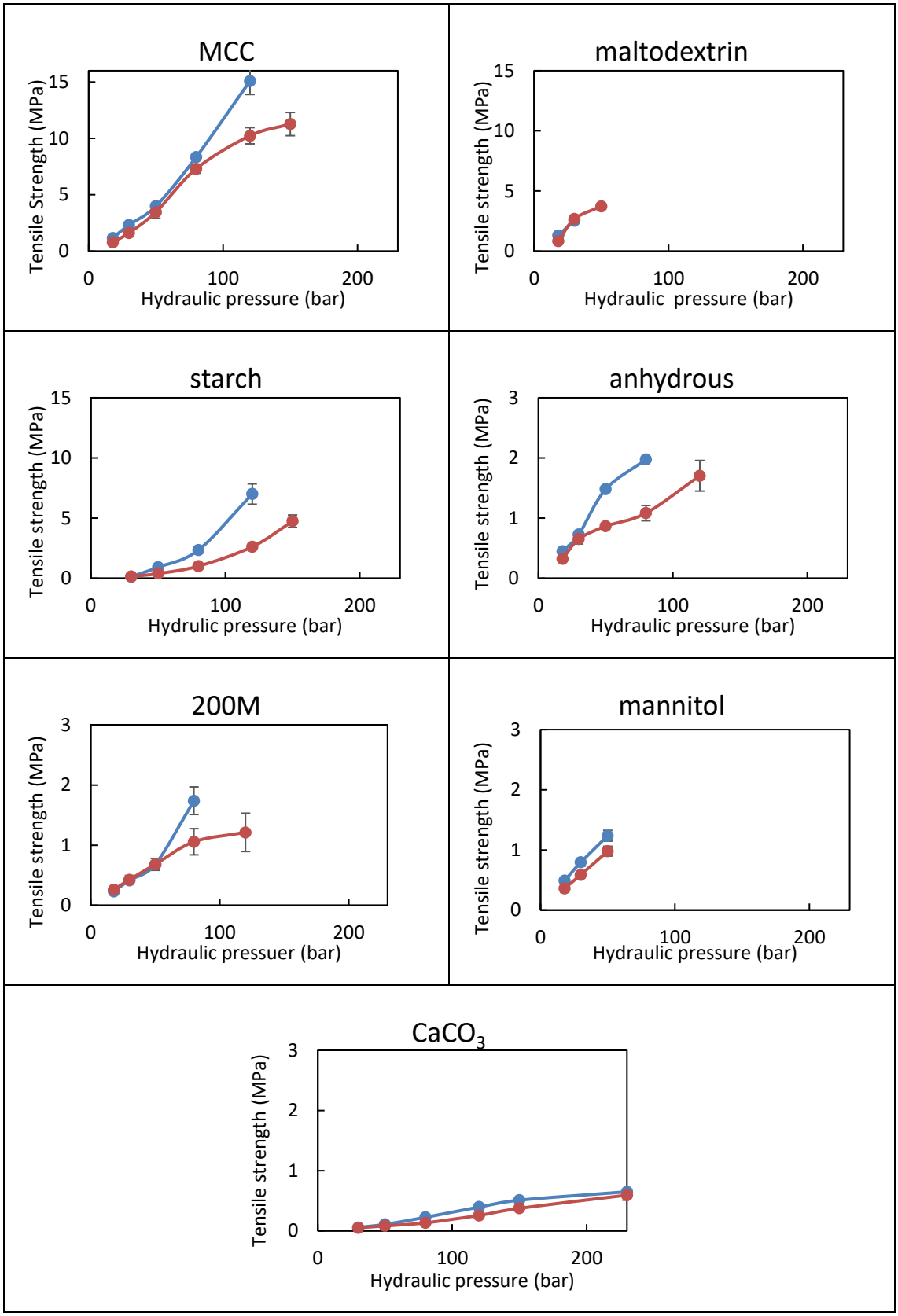

Figure 5-5: comparison of ribbon tensile strength using small knurled rollers at the same set of hydraulic pressures. Red and blue lines represent the ribbon produced by knurled and smooth rollers ribbons respectively.

This is supported by the greater porosity of knurled rollers ribbons at a similar hydraulic pressure as exemplified by the X-ray images in Figure 5-6; there is a greater number of black pixels (air) for the ribbon with the knurled rollers. The results are in agreement with a study conducted by Sheskey and Hendren [118] who roller-compacted different formulations and concluded that whatever the formulation compacted is, the density of the milled granules is higher when made using smooth rollers compared with those made with an axial-grooved roller surface. The same finding was reported by other authors [81,82,119].

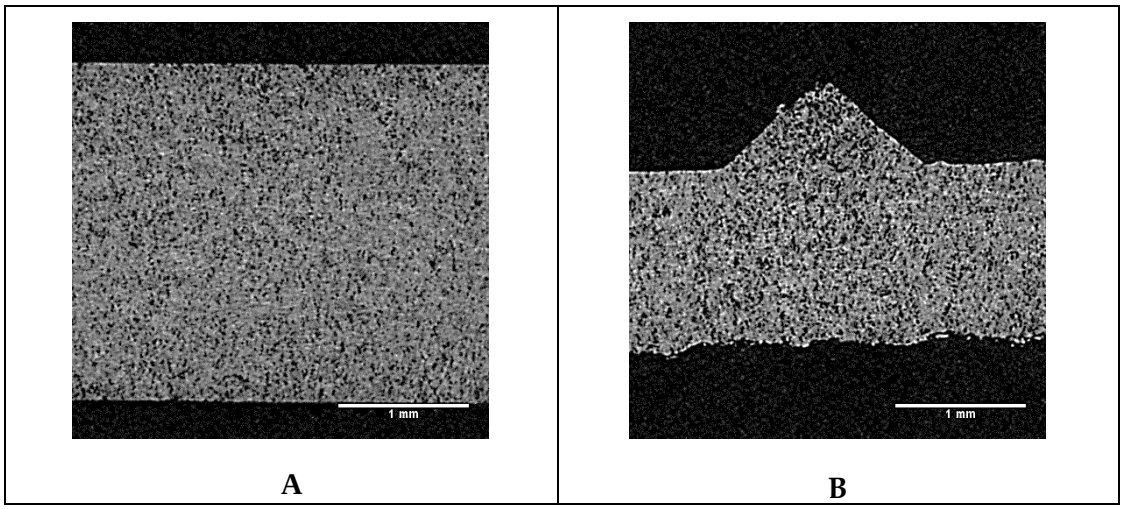

Figure 5-6: X-ray tomography images of MCC ribbons made with the (A) smooth and (B) knurled rollers at maximum roll stresses of 129 and 92 MPa respectively, corresponding to a hydraulic pressure of 50 bar.

5.3.2.2 Ribbon width and un-compacted fines

The flow of powder to the compaction zone is the determinant factor in controlling the distribution of powder in the compaction area [90]. The powder is fed to the compaction area by means of the screw feeder or gravity. Upon contact with the roller surface, powders are drawn in by friction; the velocity of powder increases gradually up to the roller speed. As suggested by Michrafy et al. [88], this slip of powder against roller surface participates in the reorganisation of particles during flow to the nip area which could eventually change the final porosity distribution and the amount of particles dragged near the edges of the rollers. Figure 5-7 shows the width of ribbons produced with different types of powders at different applied stresses.

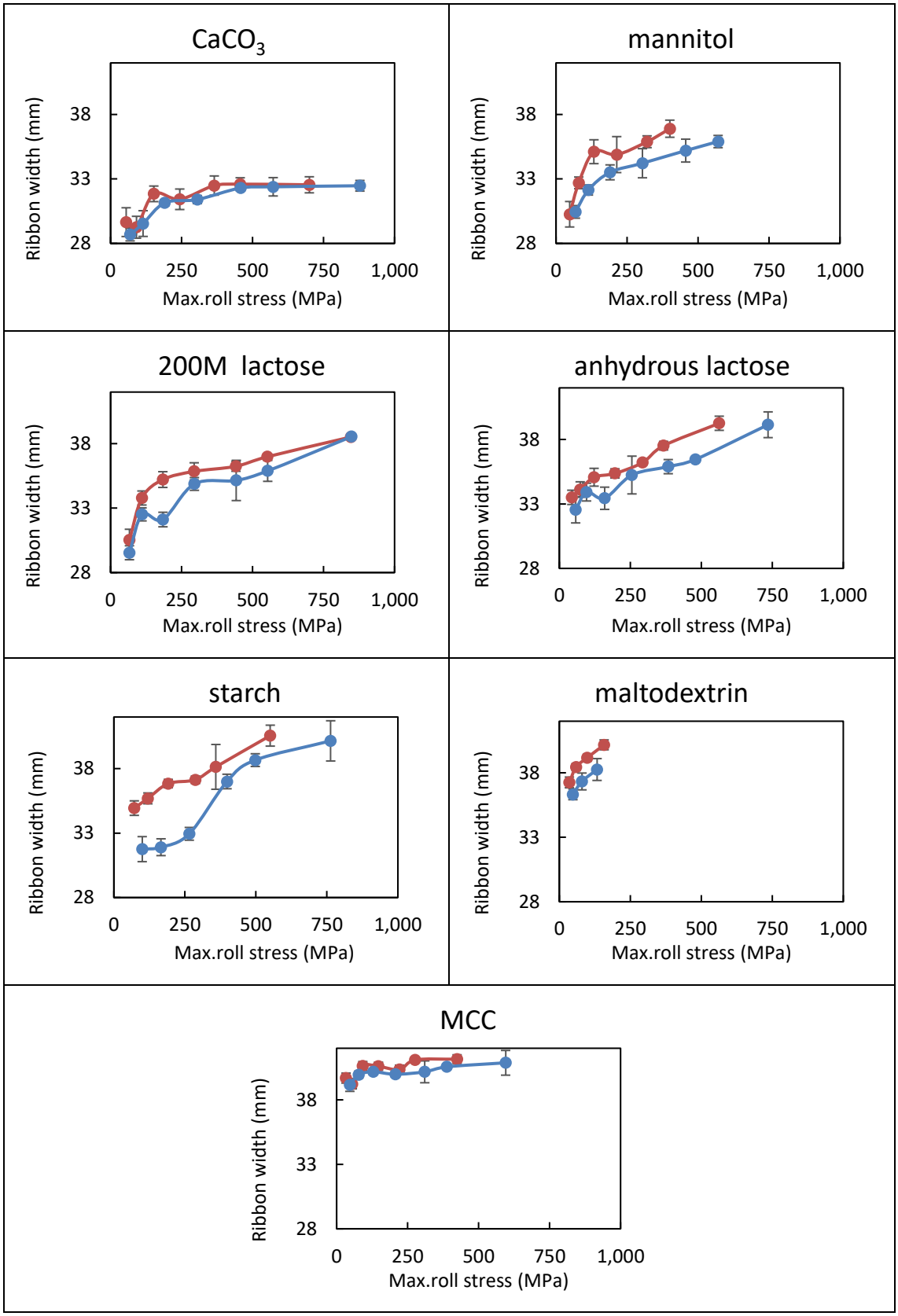

Figure 5-7: Effect of roller maximum stress on the ribbon width. Red and blue lines represent the ribbon produced by knurled and smooth rollers ribbons respectively.

It can be seen that increasing the applied stress or using more deformable material increased the width of the ribbon; this could be due to the higher particle-particle bonding that could save the integrity of the ribbon near the roller edge.

Despite the lower stress applied by the knurled rollers, which resulted in weaker ribbons (Figure 5-3 and Figure 5-5), using this pair of rollers has slightly increased the ribbon width. This could be ascribed to the better gripping ability of the knurled rollers, which could draw more powder near the roller edge and increase the ribbon width. The increase in ribbon width is reflected in a lower amount of un-compacted fines produced when knurled rollers are used (Figure 5-8). The fines usually come from ribbon edges at which knurled rollers grip higher amounts of powder than smooth rollers, and subsequently produce wider ribbons and therefore result in lower amounts of fines.

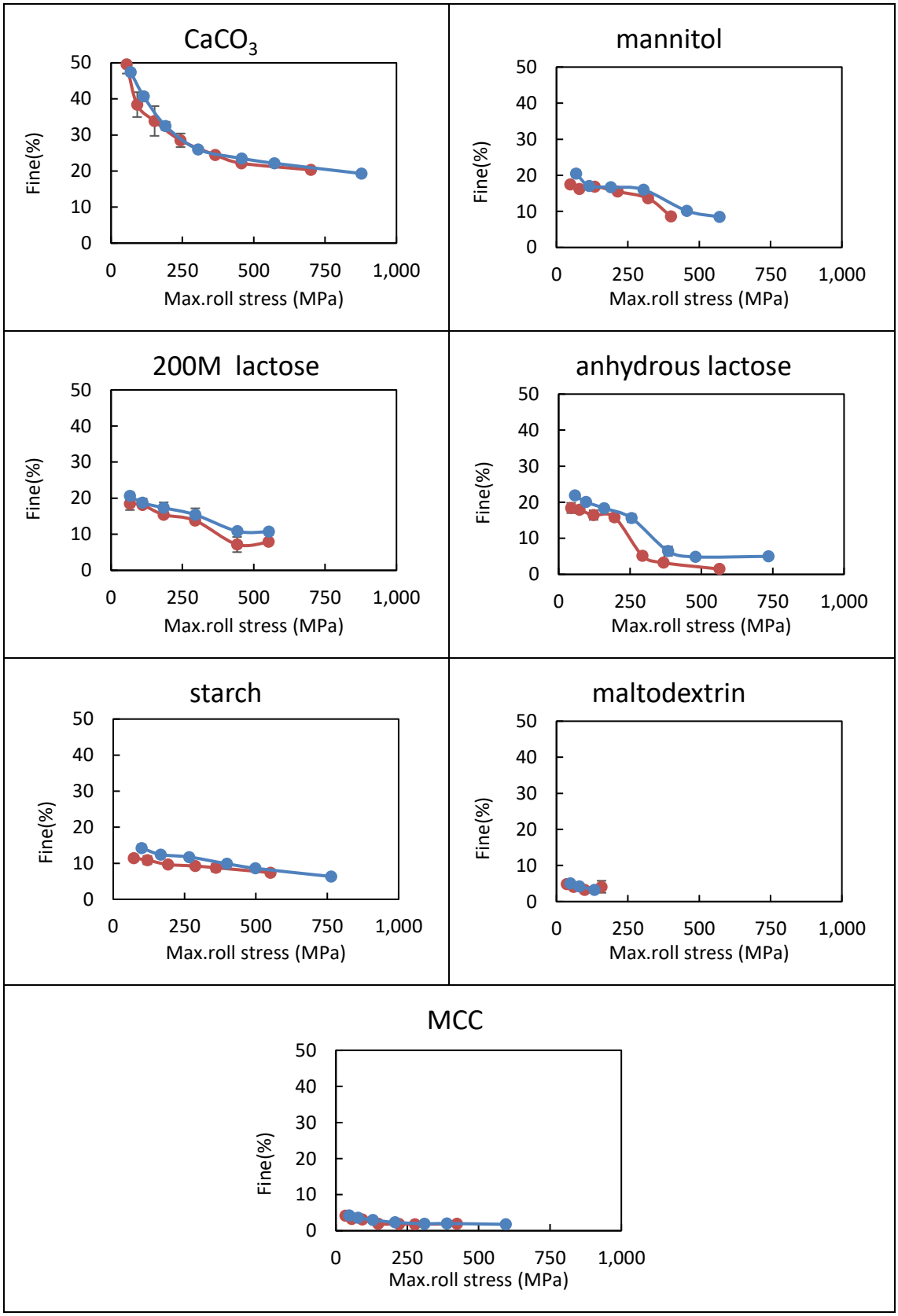

Figure 5-8: Effect of roller maximum stress on the amount of un-compacted fines. Red and blue lines represent the ribbon produced by knurled and smooth rollers ribbons respectively.

It is also interesting to report that in comparison with knurled rollers, using smooth rollers has associated with relatively higher values of feeder screw speed (Figure 5-9); smooth rollers have lower levels of wall friction (Table 5-1 and Table 4-3), subsequently higher screw speeds were required to grab the powder to the nip area and maintain the same roller gap to that used when knurled rollers were implemented. The difference in screw speed values between the two rollers types was less noticeable in case of $CaCO_3$ this could be due to the relatively higher wall friction of this powder for both smooth and knurled rollers (Table 5-1 and Table 4-3). The results are in agreement with a recent study conducted by Csordas et.al [82] using spray-dried mannitol and MCC; the authors mentioned that using of smooth rollers have always been accompanied with higher feeder screw speeds to that of the knurled rollers when both are implemented at the same processing conditions.

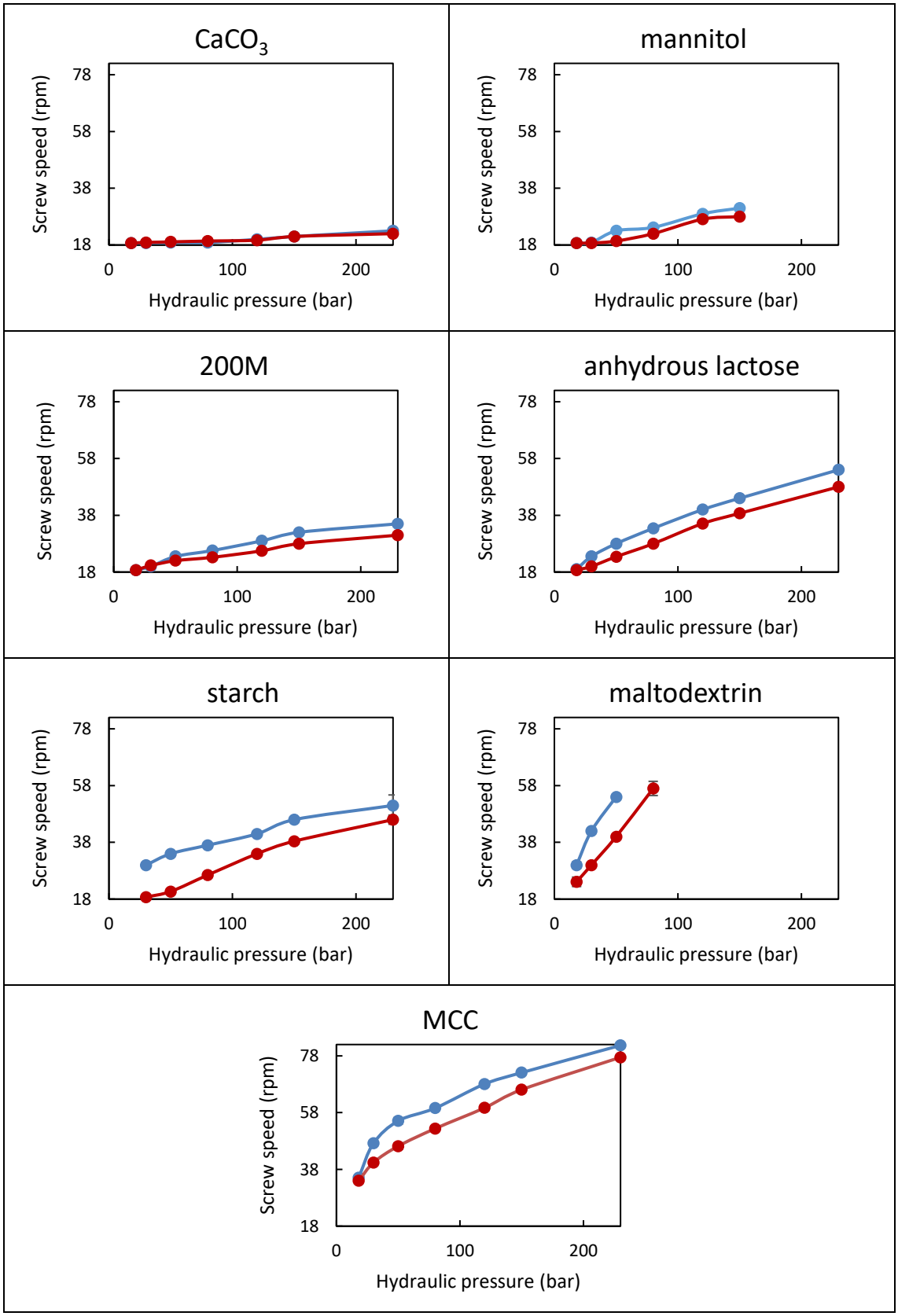

Figure 5-9: Effect of hydraulic pressure on the feeder screw speed at constant gap distance (2 mm) for the different studied powder materials. Red and blue lines represent the ribbon produced by knurled and smooth rollers ribbons respectively.

5.3.3 Ribbon splitting/sticking observations

Table 5-2 shows that the use of knurled rollers produced a similar transversal splitting trend to that of the smooth rollers except that the more plastically deformable powder exhibited such splitting up to greater maximum roll stresses (see Table 4-4 for smooth rollers splitting behaviour). Unlike smooth rollers, where ribbon transversal splitting is always associated with roller sticking, in some cases of knurled rollers, transverse splitting occurred without sticking to the rollers, i.e., ribbons made with starch and MCC. Nevertheless, roller sticking/transversal splitting in both rollers was always prevented by external lubrication.

Similar to the smooth rollers, avoiding transversal splitting/roller sticking by increasing the applied stress significantly reduced the amount of un-compacted fines (Figure 5-8).

In terms of longitudinal splitting, in agreement to the trend noticed with smooth rollers, ribbons made with knurled rollers started to split longitudinally at stress proportional to its feed powder yield stress (Table 5-2). For example, mannitol with relatively high yield stress started to split longitudinally at lower maximum roller stress compared to lactose 200M, which started to split at relatively higher stress, yet the use of knurled rollers improved the compaction performance in terms of reducing the occurrence of longitudinal splitting.

Table 5-2: Effect of the maximum roll stress on the splitting and sticking behaviour of the ribbons formed from unlubricated knurled rollers. Grey dotted areas indicate a non-achievable condition. Red regions indicate the occurrence of splitting/sticking. Green regions indicate the non-occurrence of splitting/sticking. Spitting is designated by T (transversal splitting), Ln (longitudinal splitting into n pieces) and LJ (longitudinally joined splitting).

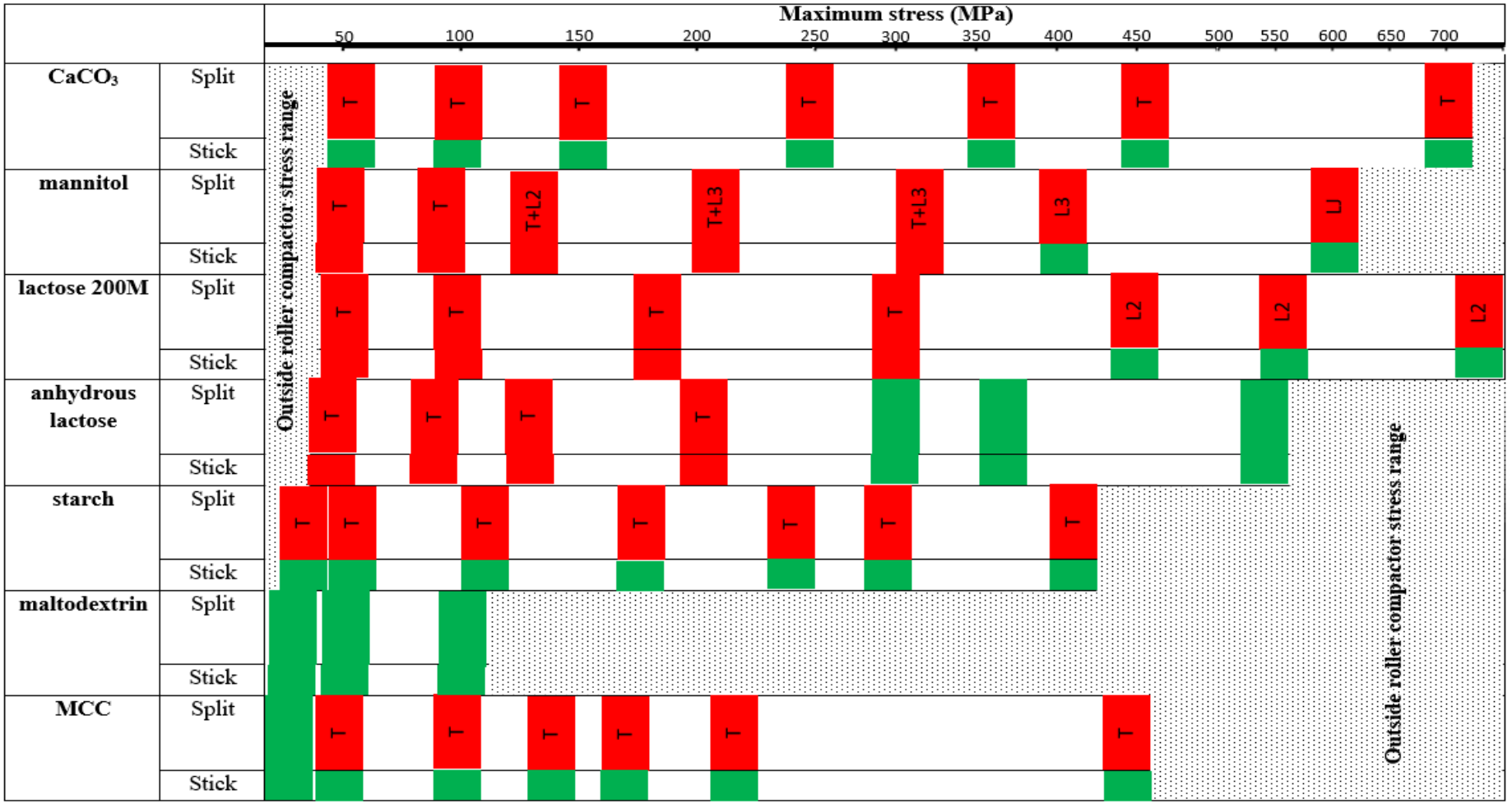

For a better understanding of the underlying mechanisms of splitting, the observed trends for the knurled rollers were rationalised using the splitting index proposed in section 4.4.8. $CaCO_3$ was excluded due to its anomalous splitting behaviour (see section 4.4.8). Ribbon tensile strength and elastic recovery have been determined for all knurled rollers ribbons; (Equation 4-4) and used to calculate the tensile strength of the ribbons from the knurled rollers ribbon tensile strength. The elastic recovery of each material in Figure 4-8 was fitted to a linear relationship with the maximum compaction stress; the relationship was then used to determine the elastic recovery at the stresses used to make the knurled rollers ribbons

A histogram involving the splitting index for the unlubricated and lubricated smooth and knurled rollers that includes longitudinal, transversal, and mixed splitting is presented in Figure 5-10. While applying lubricant on the roller surface has eradicated any sticking/transversal splitting.

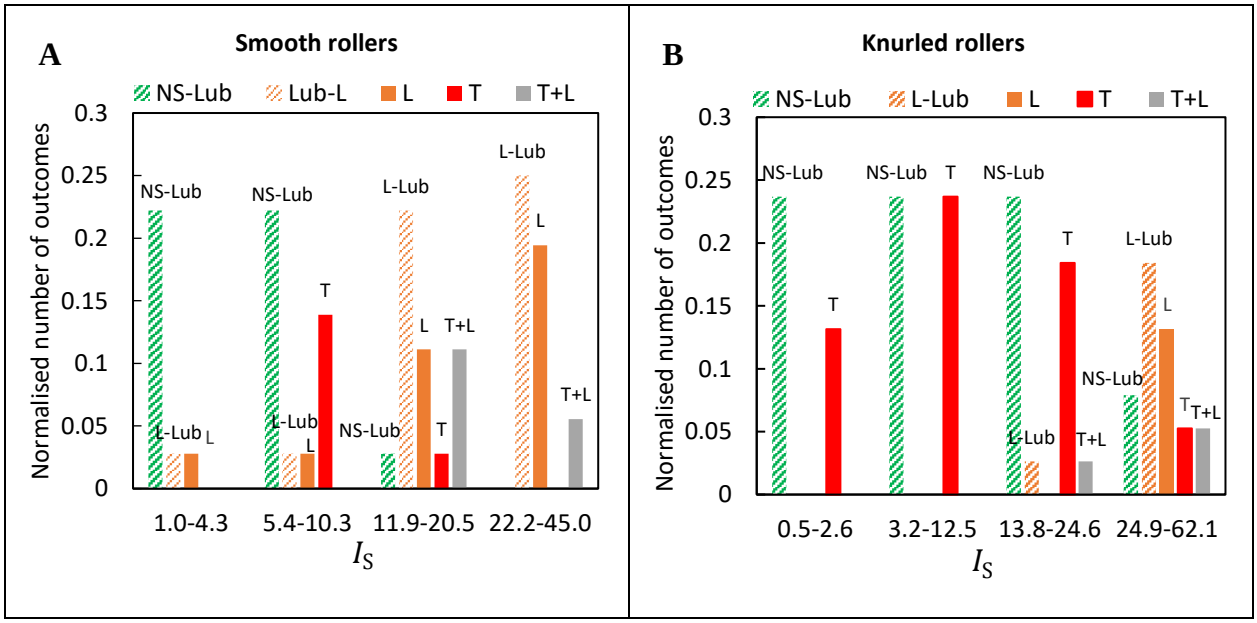

Figure 5-10: A histogram based on the splitting index of the number of non-splitting and splitting outcomes per powder feed normalised by the total number of outcomes that were observed with the smooth (A) and knurled rollers (B). The data for $CaCO_3$ ribbons are not included since its splitting behaviour is anomalous. The coding refers to transversal (T), longitudinal (L), mixed transversal-longitudinal (T+L) and no splitting (NS). Solid and patterned filled bars refer to unlubricated and lubricated cases respectively.

Similar to the smooth rollers, knurled rollers produced a trend of decreasing no splitting and increasing longitudinal splitting as the values of this parameter increases (Figure 5-10 (A-B)). There was a limit at which the occurrence of transverse splitting decreased and that for longitudinal splitting increased with increasing values of the index, which was accompanied by mixed transverse-longitudinal splitting. Transverse splitting was always associated with sticking to the rollers and was prevented by external lubrication. The main difference with the knurled rollers was that in some cases transverse splitting occurred without sticking to the rollers. Figure 5-10 shows that changing to the knurled roller surface increased the transversal splitting and reduced the amount of longitudinal splitting.

The proposed index was poor in terms of predicting the starting value of longitudinal splitting occurrence. In the case of smooth rollers, longitudinal splitting started at a splitting index value between 0.9-4.27 while for knurled rollers, splitting took place between 13.8-24.5. This is believed to be due to the index not accounting for the bending stress. In an attempt to improve this index, it was modified multiplying the splitting index by the relative solid fraction difference. The relative solid fraction difference between ribbon centre and edges is related to the recovery strain difference across the ribbon width which, could develop into bending stress across ribbon thickness. Measurement of ribbons relative solid fraction difference and the application of the modified splitting index (I_S') is discussed in the following sections.

5.3.4 Ribbon heterogeneity across ribbon width

Ribbons made with smooth and knurled rollers were analysed for their porosity distribution using different techniques. The measured porosity is used as an explanation of ribbon splitting phenomenon. The heterogeneity could be investigated using different approaches each have its advantages and disadvantages.

5.3.4.1 X-ray tomography

All ribbons except for $CaCO_3$ which was excluded due to its anomalous splitting behaviour was scanned using X-rays every ~3.5 mm across the width (Figure 5-11). In all cases, the porosity of the ribbons decreased when higher stress was applied and the lowest porosity was concentrated at the ribbon through-the-width ribbon centre. This variation in porosity distribution indicates that the applied stress was always higher in the

across-the-width ribbon centre. In comparison to the ribbon made with smooth rollers, knurled rollers ribbons were more porous at the same applied pressure, as exemplified in Figure 5-12.

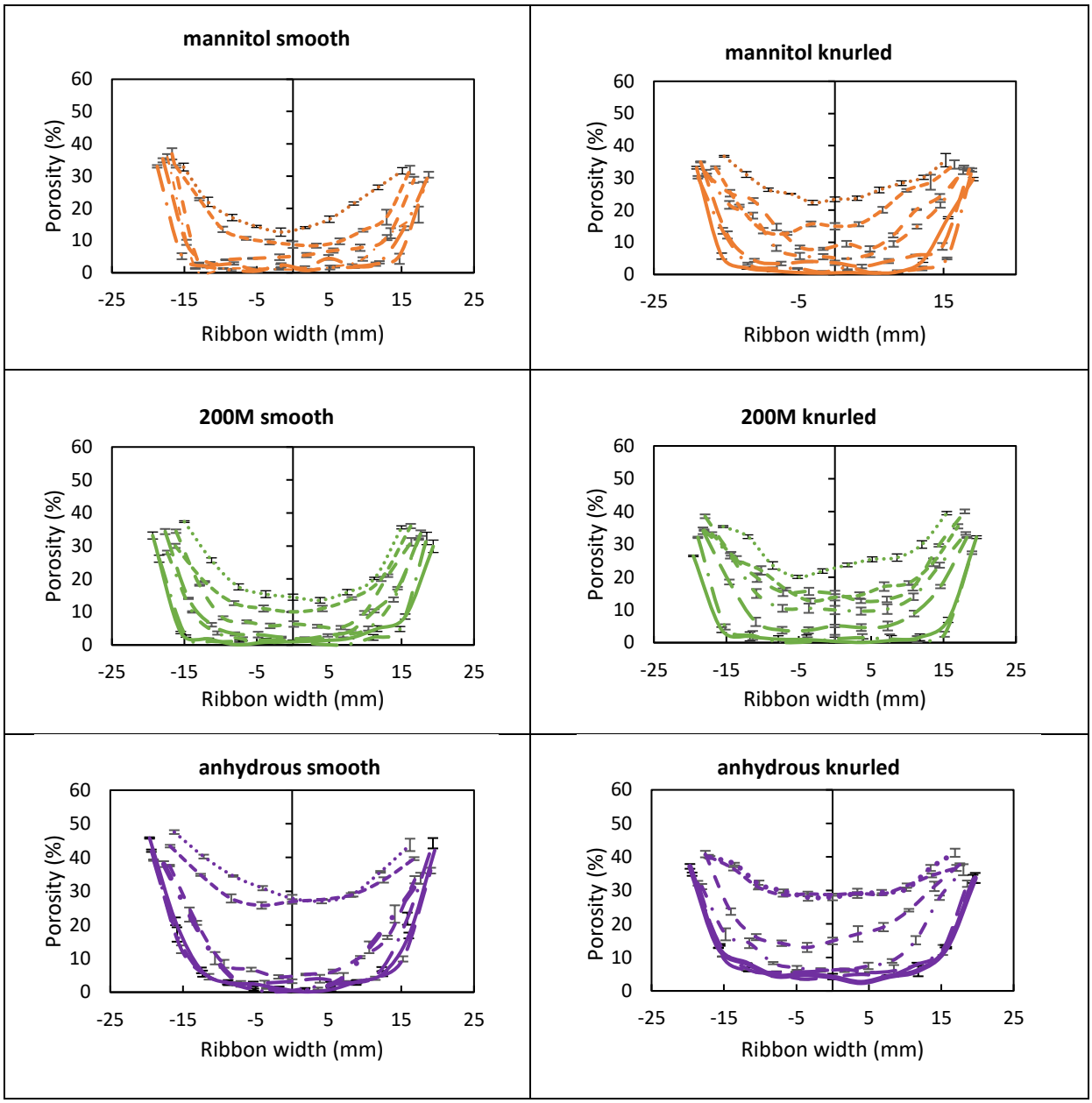

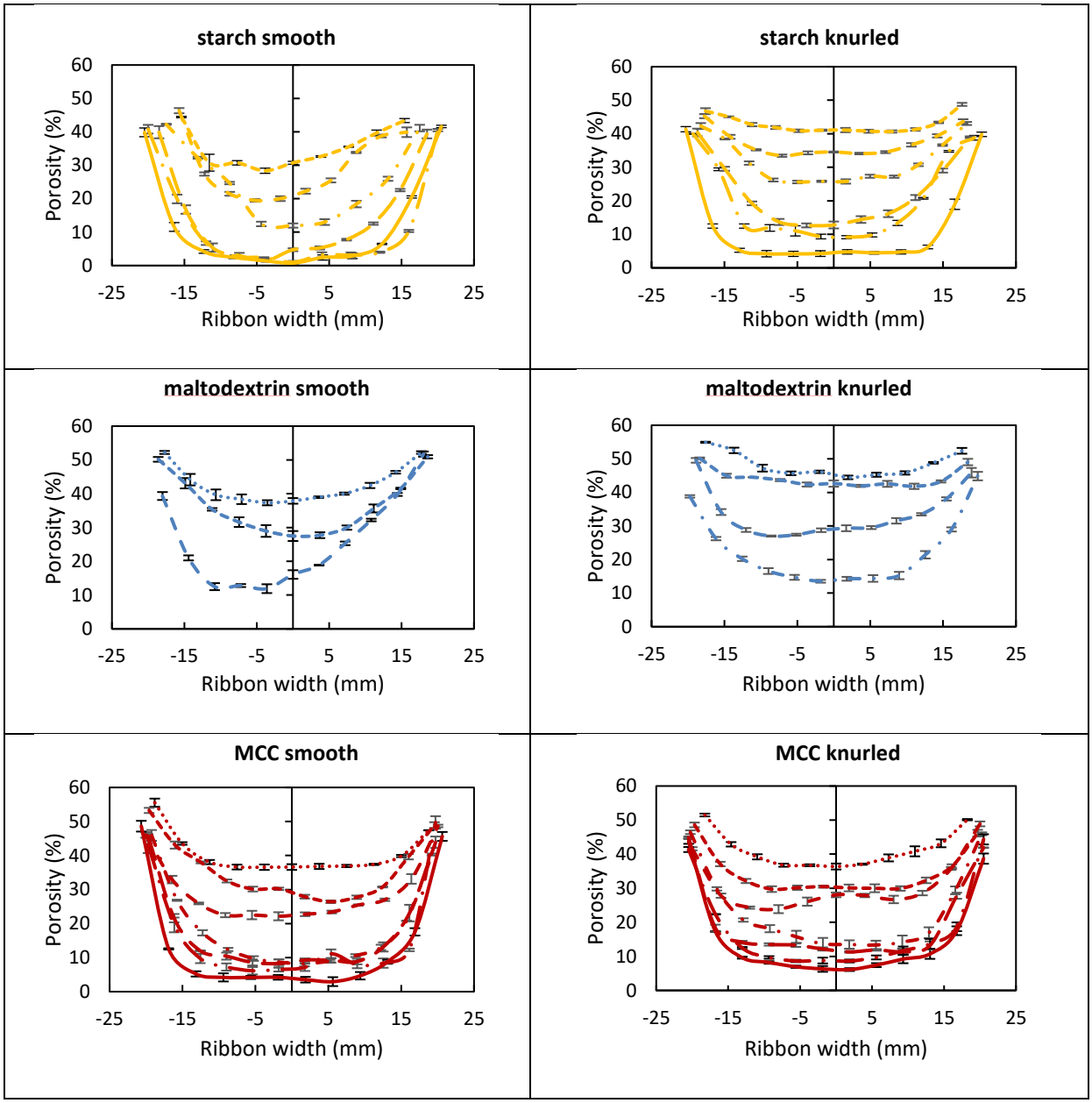

Figure 5-11: The porosity profile across ribbon width for the ribbons produced from all powder feed. The profiles are for the ribbons produced using smooth rollers (left column) and knurled rollers (right column). (Hydraulic pressures used: .... 18, ----- 30, — — —50, - · - 80, —— ——120, ——·—— 150 , and —— 230 bar).

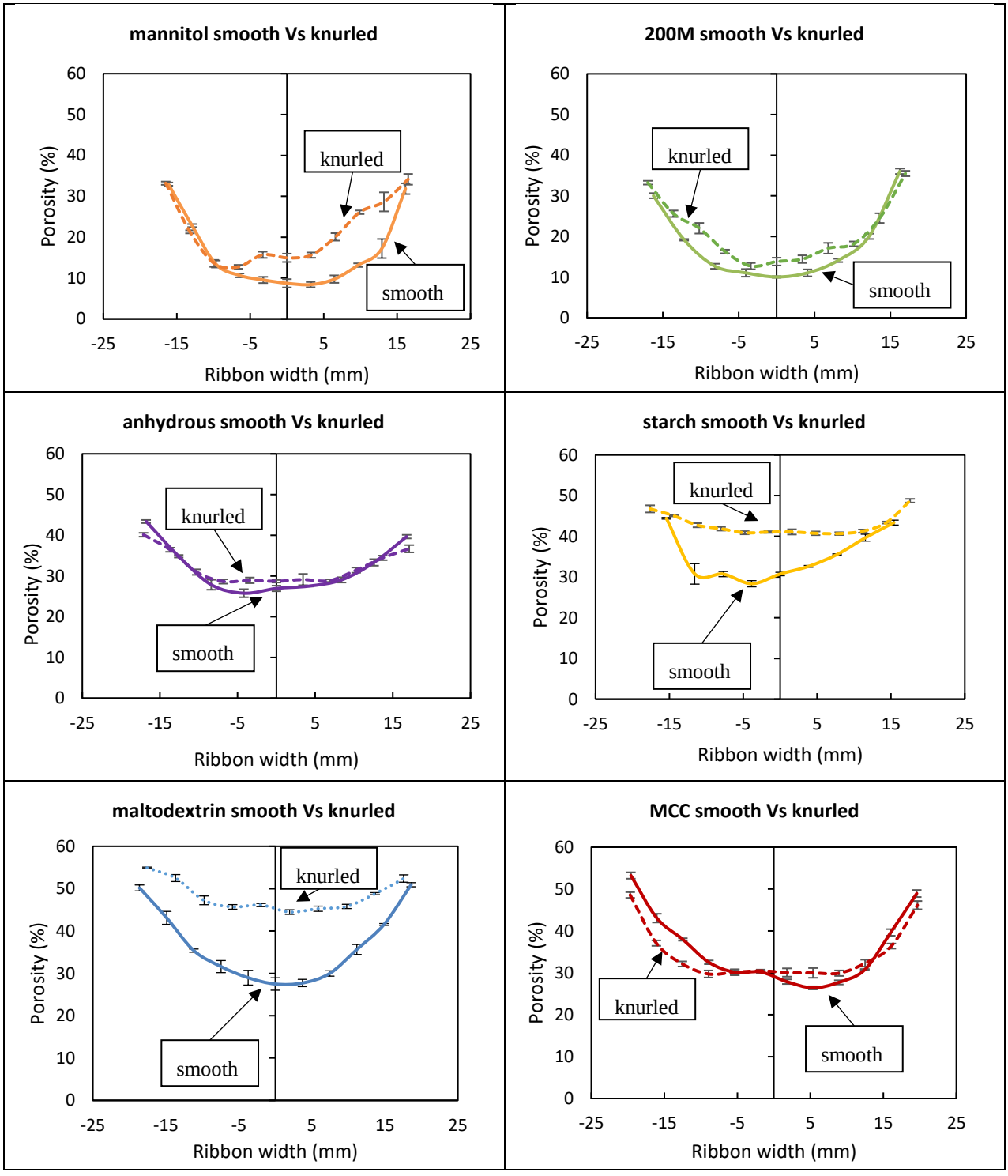

Figure 5-12: Ribbon porosity profiles for ribbons produced at 30 bar using smooth and knurled rollers.

The porosity variation across a ribbon width was quantified using the relative solid fraction difference,$\Delta\beta$, which is defined by the following relationship:

$$\Delta\beta = (\beta_C - \beta_E)/\beta_C \qquad \text{Equation 5-1}$$

where β_C and β_E are the solid fractions at the centre and edges of the ribbons.

The relative difference in the solid fraction across the width of the ribbons as a function of the maximum roll stress is shown in Figure 5-13 for the smooth and knurled rollers. Figure 5-13 shows that the relative differences across the widths of the knurled rollers ribbons were less than for the corresponding ribbons formed with the smooth rollers.

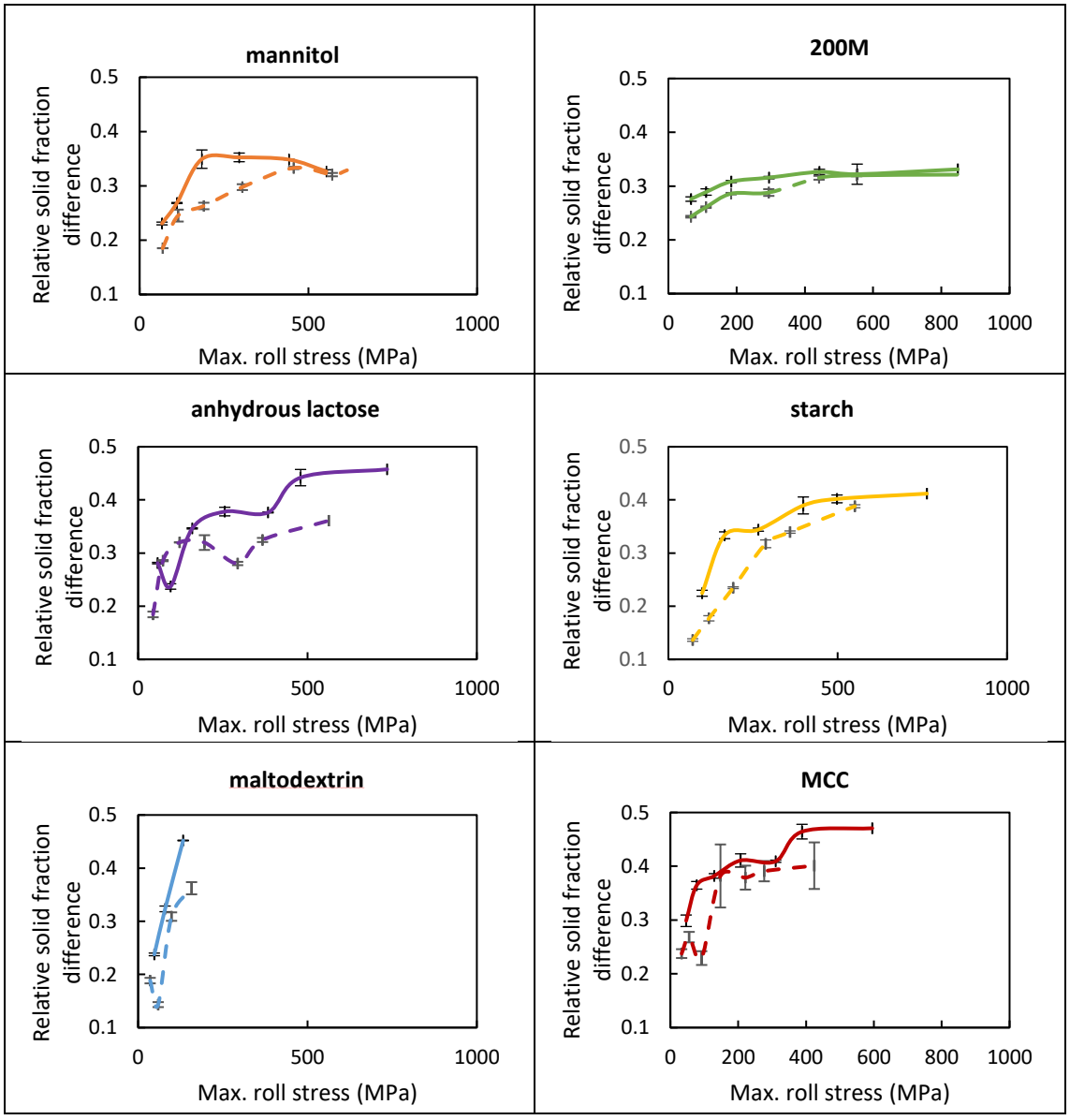

Figure 5-13: The relative solid fraction difference across the ribbons (Equation 5-1) as a function of the maximum roll stress for the ribbons formed with the unlubricated (solid line) smooth and (dashed line) knurled rollers.

Measuring ribbon porosity with X-ray tomography was advantageous in terms of providing high-resolution porosity determination of the internal matrix (up to 16 µm). This is in addition to various advantages of the XµCT technique compared with other porosity measuring techniques [120]. However, there is a trade-off between the sample size, resolution, and scanning time. In this case, the sample size was about 1.3 mm which

at a resolution of 6 µm requires approximately 75 minutes for scanning and 15 minutes for image reconstruction which makes XµCT extremely time-consuming. Thus, a scanning time of about 18 hours is needed to scan a 40 mm width ribbon by taking a scan every ~3.5 mm. Moreover, sample preparation was another artefact; the sample should fit into the sample holder tube and the sample should be strong enough to survive during the cutting stage. In an attempt to overcome these challenges, a faster technique with pixel grade information was used as described in the following section.

5.3.4.2 Near-Infrared Chemical Imaging (NIR-CI)

5.3.4.2.1 Theoretical background

In principle, NIR-CI technology combines conventional digital imaging with NIR spectroscopy to provide both spatial and spectral information. Unlike conventional NIR probes, which average the spectral information for a certain sample area in one spectrum, NIR-CI technology collects and presents the spectral information while preserving their spatial dimension so that each pixel of the captured image contains the NIR spectrum of this specific location. This can be used as a fingerprint to qualitatively and quantitatively characterise every pixel in that image [109,121,122].

The captured images are usually termed in literature as *hypercubes.* These images are constructed in two main ways, namely *pushbroom* (the method used in the current work) and *staring* approaches. The former involves the spectral information of a group of adjacent points in a line; as the sample is moved using a conveyor belt system and the line measurement is repeated so it can cover the whole sample. For the staring approach, the field of view is fixed and a stack of images are taken at one wavelength after another.

The non-destructive and fast nature features of this technology mean that it is very attractive to be used for a wide range of applications such as content uniformity [123,124], porosity in tablets and roller compaction ribbons [125,126], and counterfeit analysis [127,128].

5.3.4.2.2 Technical challenges

As previously discussed, this technology has been used for a wide range of applications, however, NIR-CI still suffers from certain challenges that must be taken into consideration prior to any measurement.

1- Sample preparation: this involved correct positioning of the sample in the field of view of the lens. Additionally, due to the limited penetrating nature of the NIR radiation, sample cross-sectioning is necessary when core information is needed.

2- Sample illumination: illumination should be intense enough so that it can reflect an adequate detectible signal to the detector. However, the intensity should not be too high as it could damage the sample. Moreover, the illumination should be relatively uniform across the sampling area, otherwise, the intensity of the reflected light could vary significantly [109]. This variation could be problematic as most of the data processing systems do not take illumination uniformity into account and inherently assume equivalence between the quality of the collected spectra.

3- Sample surface topography: an irregular surface geometry of the sample could produce similar effect to that of the non-uniform illumination; surface roughness and/or curvature could change the relative path length between the sample surface and the detector, which consequently affects the quality of the reflected signal [122,129]. Wang and Paliwal [129] reported such that light does not reflect back uniformly when scanning a curved surface with NIR-CI; subsequently, no meaningful conclusion can be made. For this reason, a processing algorithm was developed to correct the effect of surface curvature on the quality of the reflected spectra. It successfully reduced spectral variation caused by the inhomogeneous surface geometry. Surface irregularity becomes problematic if the fluctuations of a scanned surface geometry exceed the depth of field of the lens (DOF). DOF is defined as the volume within which the reflected light is sharply focused on the detector [130]. Figure 5-14 shows a schematic example of reflection from two points localised within and out of DOF range. When the reflection takes place from a point within the DOF, the reflected light is sharply focused on the detector; otherwise, the reflected light diverges after the lens and localised at a certain detector distance.

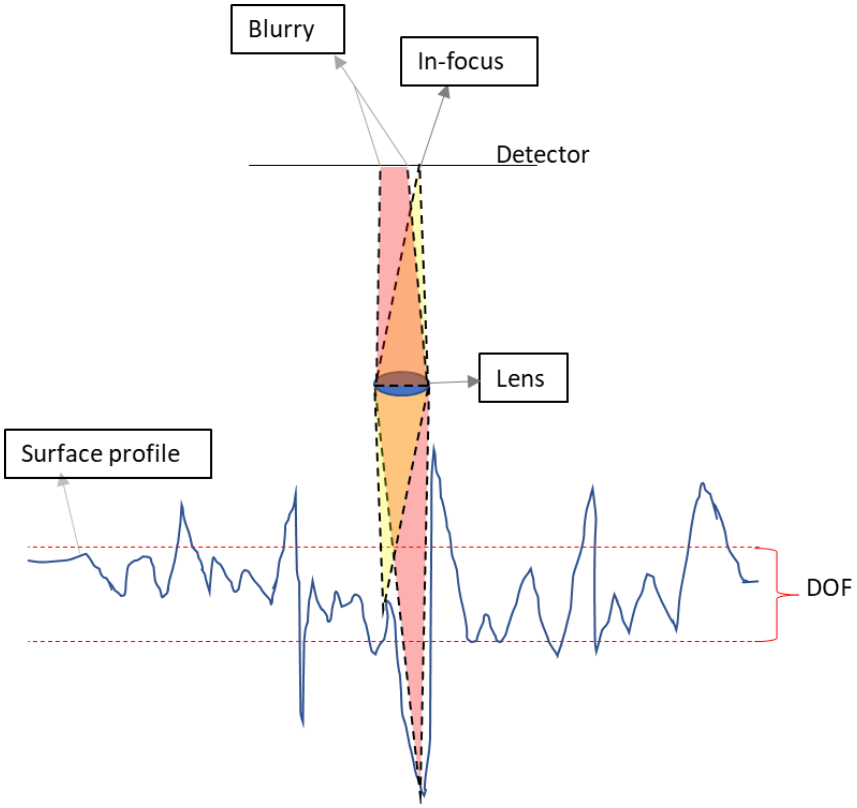

Figure 5-14: A schematic representation of how could surface roughness cause blurry images and affect the distribution of reflected light on the detector.

Generally, when using NIR-CI, it is crucial to make sure that the reflected signal is not affected by any source of variation. In general, publications do not take the aforementioned limitations into account during image acquisition. In the field of porosity investigation which is the main focus of the current work, NIR-CI was exploited by limited number of researchers to spatially characterise compact heterogeneity in terms of its porosity, although, the use of conventional NIR probe to measure the average bulk porosity was reported extensively [131,132]. Khorasani et al. [133] used NIR-CI to map the porosity and active pharmaceutical ingredient distribution in ribbons made with smooth roller mediated roller compaction. The calibration model was based on the correlation between the averaged NIR spectrum of the entire ribbon and the averaged ribbon porosity measured by the oil absorption method. It could be biased as it neglects the porosity variation across the ribbon dimensions. A more consistent approach could be the use of a more uniform compact such as tablets to build the calibration model. The researcher has reported the same calibration procedure in another two published studies [126,131]. These studies used smooth rollers which could reduce the effect of surface topology on the NIR reflectance

however, no information was mentioned about the surface roughness or lens depth of field. Another trial using NIR-CI for ribbon porosity mapping was conducted by Lim et al. [119] for assessing the variation of porosity of roller-compacted MCC ribbons. It successfully predicted ribbon porosity with a correlation of 0.9258 where regions of higher porosity showed higher intensity of reflected NIR light. Although knurled rollers where used (indentation depth was not mentioned), the study did not report any information about the DOF of the lens as this could affect the intensity of the reflected light. Moreover, In a similar study conducted by Khorasani et al. [133], the average pycnometer ribbon porosity was plotted against its mean NIR absorbance. Souihi et al. [134] used NIR-CI for the same purpose and mentioned that despite the use of knurled rollers, the study successfully predicted porosity at the bottom and top of the knurling areas. This could be related to the high DOF of the lens (not mentioned). Based on the discussed limitations and the existing literature, there is a need to assess the role of surface irregularity on the predictability of NIR-CI for the porosity of the ribbon. For this reason, the surface roughness of the scanned surfaces should be measured and compared with the lens DOF in order to evaluate the quality of reflected light and subsequently the appropriateness for predicting the density.

5.3.4.2.3 Determining lens depth of field (DOF)

The lens depth of field was determined by focusing on a plastic micro-scaled ruler, the ruler was then moved gradually (50 µm in each step) toward the detector by placing a number of plates (~50 µm thickness) under the ruler in a stepwise manner. Figure 5-15 shows how the image becomes blurry when the distance to the detector (focus distance) was changed by ~ 350 to 400 µm which was taken as the lens depth of field.

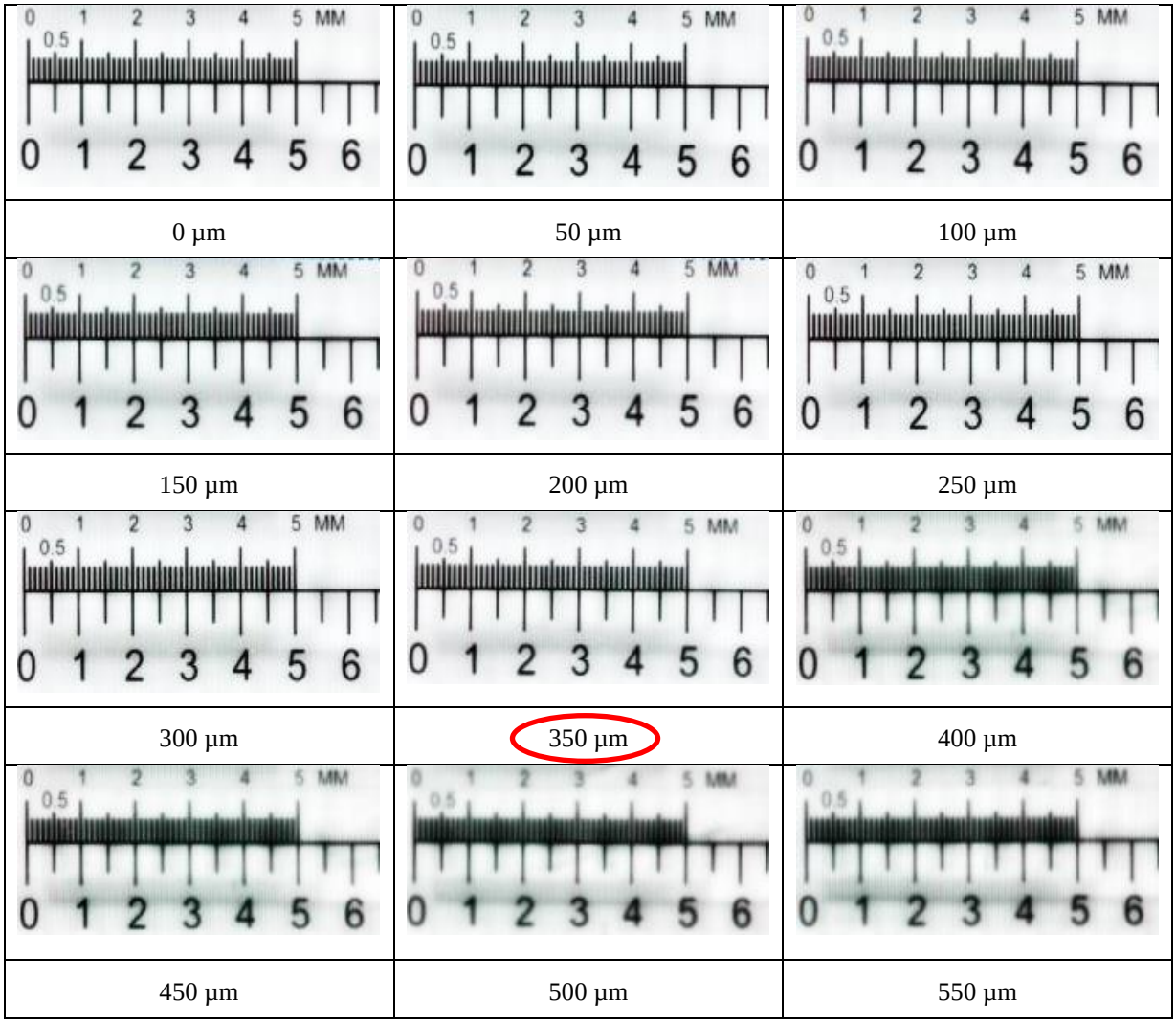

Figure 5-15: Raw images of plastic micro ruler taken with the NIR-CI spectrometer at different distances to the spectrometer detector.

5.3.4.2.4 Compact surface roughness

To assess the role of surface roughness, it was determined for the calibration tablets and roller compacted ribbons at the lowest and highest compaction stresses. This was based on the surface profile which is measured with a digital light microscope (Keyence VHX-5000). Surface roughness can be expressed by different parameters which are selected according to the desired application. To compare surface roughness with lens DOF, the R_z value was selected, which is the average peak to trough deviation and it is more sensitive to high peaks or deep valleys:

$$R_z = \frac{1}{n}\sum_{i}^{n}\left(x_{peak,i} - x_{trough,i}\right)$$ Equation 5-2

where R_z is the surface roughness parameter for the mean distance between the peaks and troughs, i is the ith segment, n is the number of segments, x_{peak} and x_{trough} are the deviation for the peak and the trough in the segment considered, respectively.

Example of mannitol tablets surface profiles at the highest and lowest compaction stresses are shown in Figure 5-16. They were evenly divided into five segments according to the length; subsequently the largest and lowest values of each of the 5 segments were determined and applied in Equation 5-2 to compute Rz value.

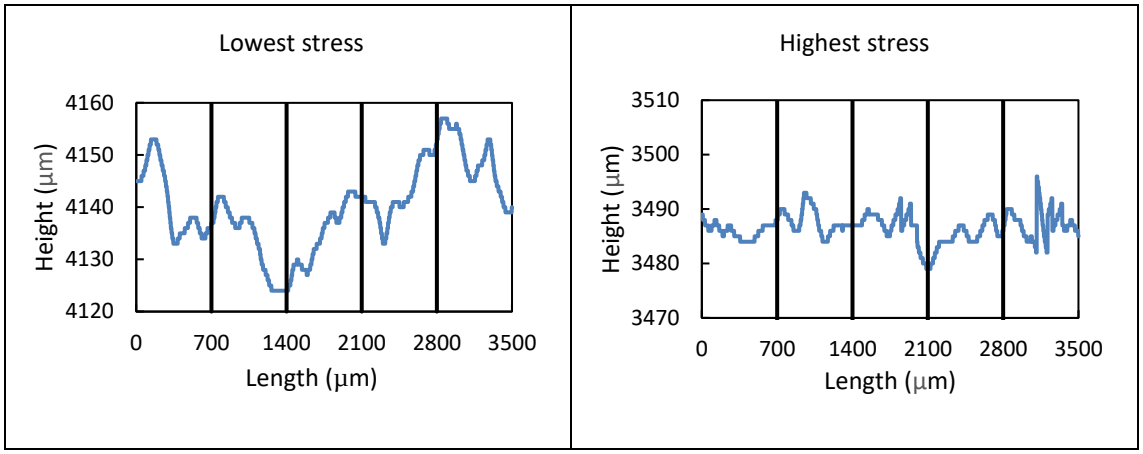

Figure 5-16: Surface profile of mannitol tablet compacted at a stress equivalent to 18 bar (lowest) and 230 bar (Highest) hydraulic pressure in the roller compactor. The profile is divided into five segments to calculate Rz value.

The roughness (Rz) values of all tablets produced at the highest and lowest compaction stresses are shown in Figure 5-17-A. These tablets were later used to calibrate the NIR-CI.

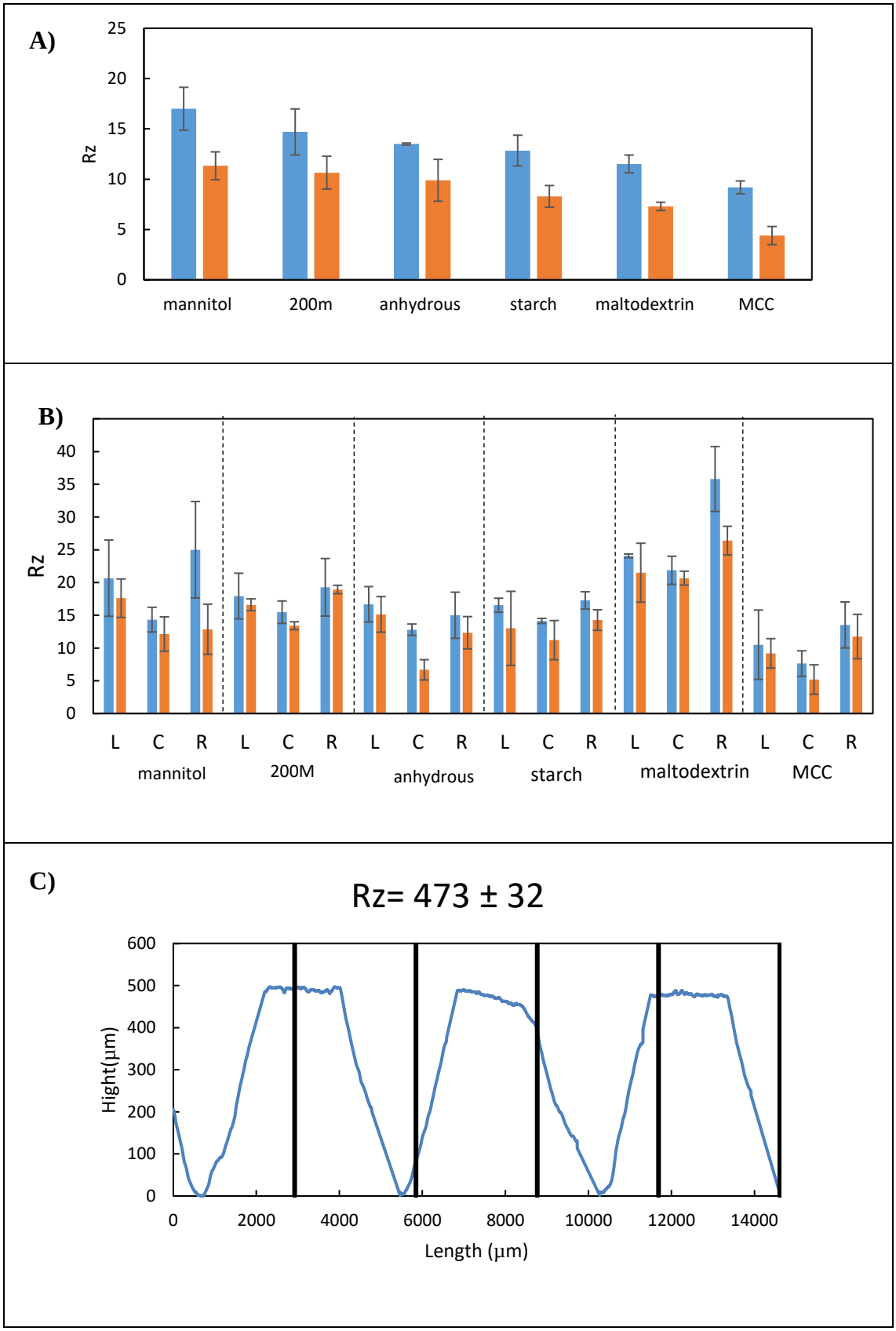

Figure 5-17: Rz values of the calibration tablets (A), and smooth roller ribbons (B). Tablets are made at stresses corresponds to the highest and lowest stresses of roller compaction. Blue and orange bars represent the highest and lowest stresses respectively. L,C, and R are left, centre and right sides of the ribbon respectively. (C) is an example surface profile of knurled ribbon with its Rz value.

It can be seen from Figure 5-15 and Figure 5-17 (A-B) that the Rz values of the calibration tablets and the smooth rollers ribbons are much lower than the DOF of the lens. Consequently, the calibration tablets and smooth rollers ribbons are always in focus through the entire range of compaction stresses. However, because of the indents on the ribbon surface, knurled rollers ribbons have Rz value higher than the DOF of the lens (Figure 5-17-C), which could affect the intensity distribution of the reflected light and consequently affect the NIR-CI predictability. As the porosity distribution measurement depends entirely on the spatial distribution of the reflected intensity of the reflected light, knurled rollers ribbons are not suitable to be measured by this technique.

5.3.4.2.5 Calibration model and ribbon porosity distribution

In order to quantitatively analyse the porosity distribution of smooth roller ribbons, a calibration model was constructed from the average NIR spectra extracted from the known porosity of tablets. The calibration is based on the relationship between the intensity of reflected light and tablet porosity (calibration procedure are explained in more details in section 3.2.9). An example of the average NIR spectra of each of the calibration lactose tablets are shown in Figure 5-18 (NIR spectra of the calibration tablets for the rest of the studied materials are tabulated in Figure A 4). NIR is sensitive to porosity variation and thus, more compacted powder show less intensity of reflected light. The same phenomenon has been used extensively to investigate compact porosity [109,132,135].

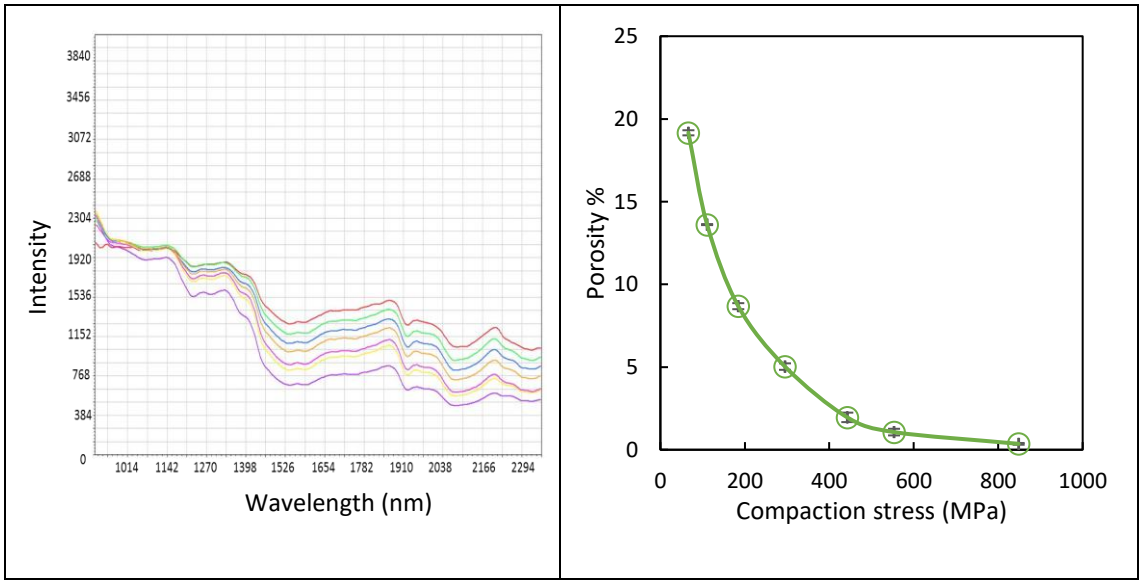

Figure 5-18: A: Raw NIR spectrum of lactose 200M calibration tablets made at stress levels equivalent to the stress applied on lactose 200M during smooth rollers mediated roller compaction. The stresses are ordered ascendingly in the following colour order: (—, —, —, —, —, —, and —). B: porosity of the calibration tablets as a function of applied compaction stress.

The model was evaluated with a set of validation tablets of known porosity, these were not included in the calibration stage. The validation results for lactose 200M tablets are shown in Figure 5-19.

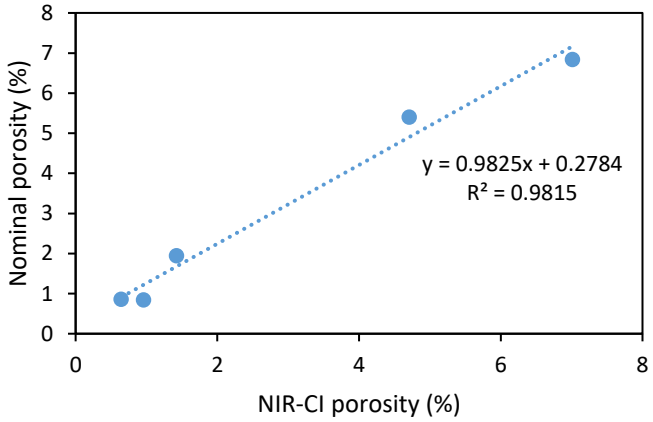

Figure 5-19: Predicted vs. nominal tablet porosity.

The resultant NIR-CI porosity maps for lactose 200M calibration tablets and roller compaction ribbons are shown in Figure 5-20. (NIR-CI porosity maps of the rest of the studied materials are shown in Figure A 5).

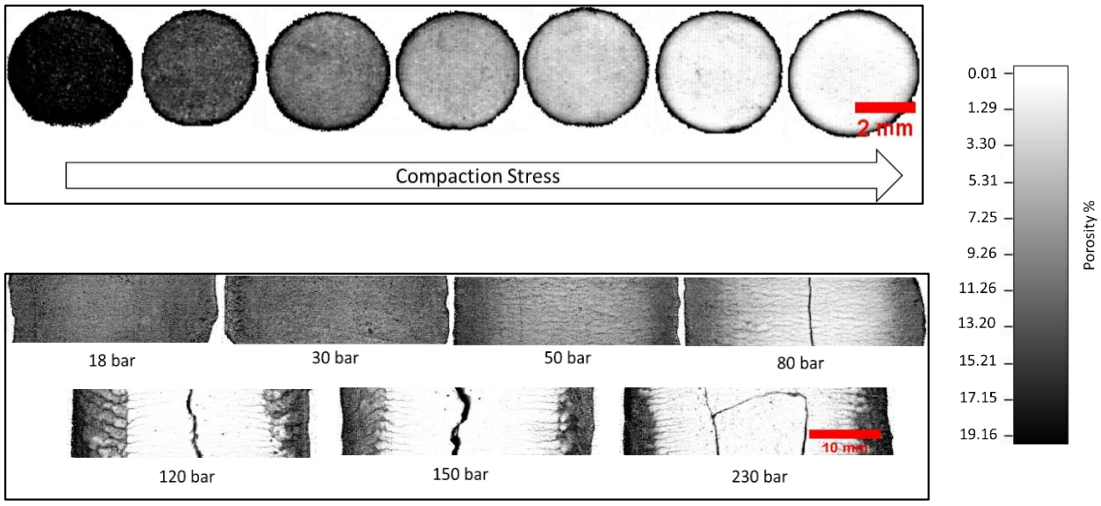

Figure 5-20: NIR-CI porosity maps of lactose 200M calibration tablets (top) and roller compacted ribbons (bottom).

ImageJ software (National Institutes of Health (NIH), USA) was then used to analyse smooth ribbons for porosity distribution across the width. It is based on the greyscale value of the calibration tablets. The mean value of 2 mm diameter circle at the tablet

centre was determined and plotted against tablet porosity. The resultant relationship was used to convert the greyscale value distribution across a ribbon width into a porosity profile. An example of the relationship between the tablet mean greyscale value and the porosity is shown in Figure 5-21.

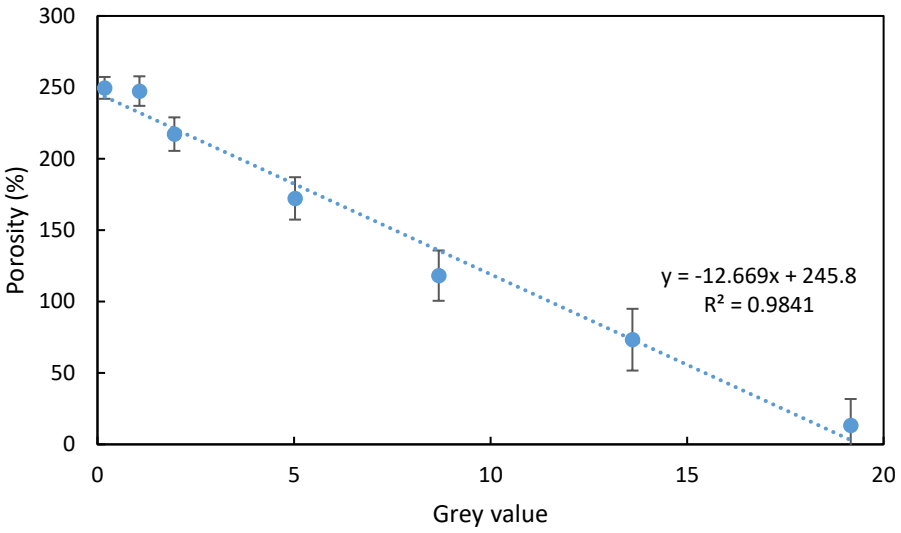

Figure 5-21: Calibration tablets average greyscale value vs. measured porosity (%).

The same procedure was used to analyse the ribbon porosity distribution for the remainder of the ribbons (Figure 5-22).

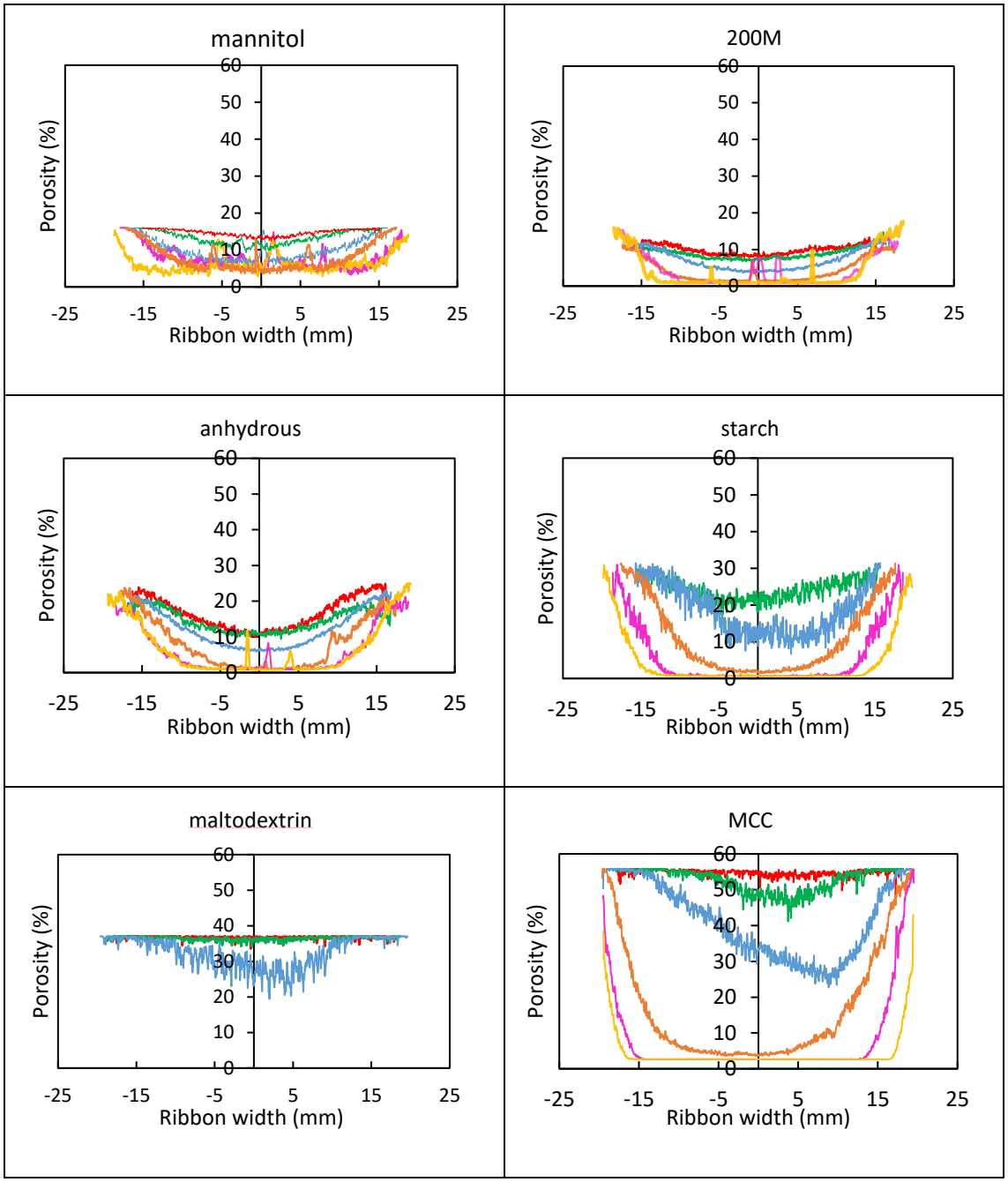

Figure 5-22: Porosity profile as measured by NIR-CI technique. The colour coding are in the following order; —: 18 bar, —: 30, —: 50 bar, —: 80 bar, —:120, —: 150 bar).

5.3.4.3 Thermal imaging

The homogeneity across the ribbon width was further investigated by thermal imaging to measure the temperature profile. The stress acting on the material during compaction brings powder particles closer to each other and generates heat by increasing the frictional interaction at three interfaces: (i) between moving particles, (ii) between powder particles and tool walls and (iii) within the powder particle itself due to plastic deformation and/or breakage [54]. The amount of heat generated is a function of the stress applied, therefore

the profile of across-the-width ribbon temperature could be a powerful characterization technique of the heterogeneity of the applied stress during roller compaction.

Figure 5-23 shows the surface temperature profile across the width of ribbons for four different types of materials compacted using two different pairs of rollers (knurled and smooth) and at the same level of hydraulic pressure. All materials showed higher ribbon surface temperature when smooth rollers were used, this is correlated to the higher amount of stress applied when smooth rollers were used (Figure 5-3).

It can be seen from Figure 5-23 that the uniformity of temperature profile was different when different rollers were used; compared with smooth rollers, knurled rollers showed greater of temperature homogeneity i.e. less temperature difference between the centre and edges. This suggests a more homogenous stress distribution across the ribbon width and this consequently leads to more uniform density distribution as was seen in Figure 5-13.

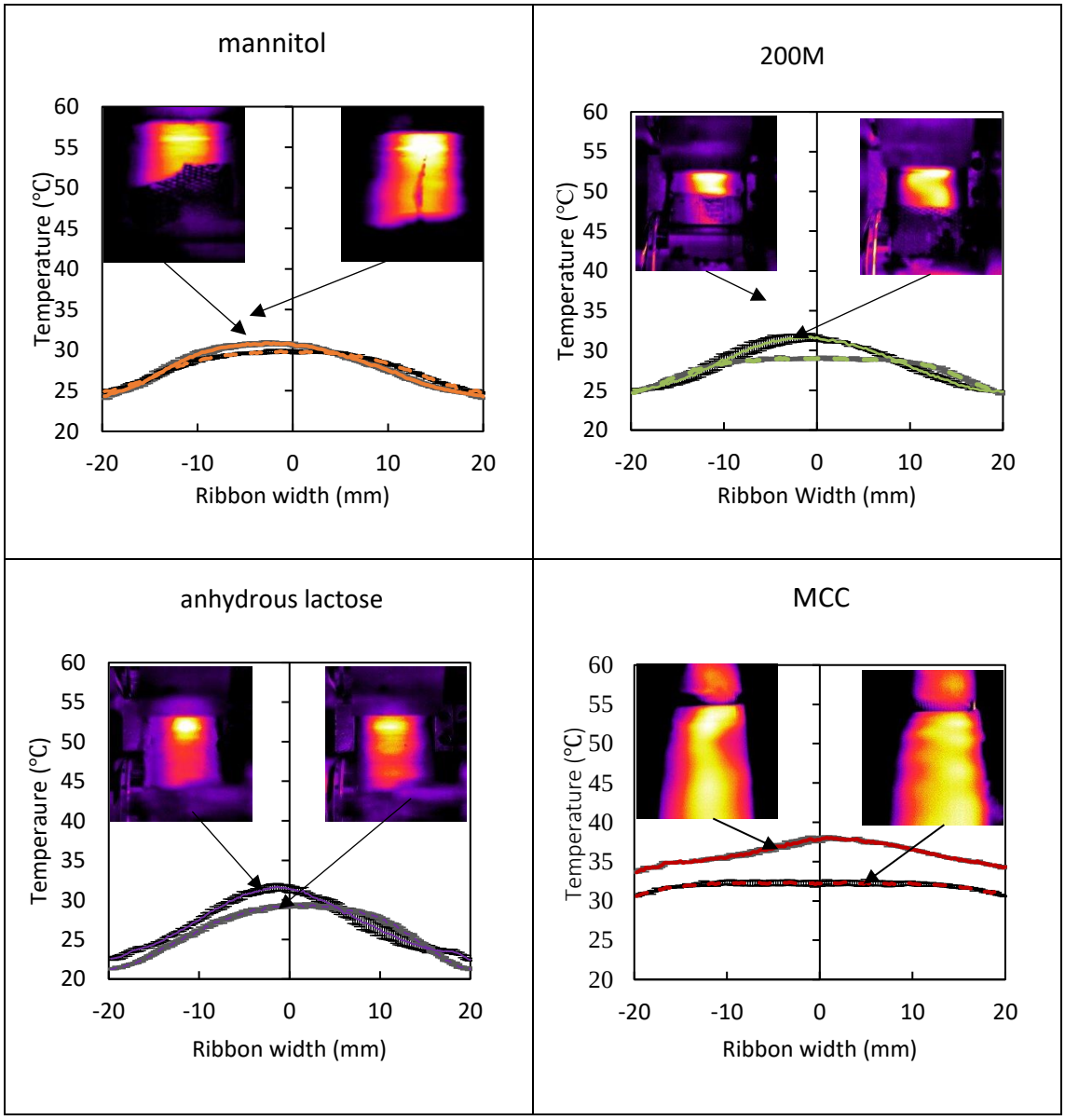

Figure 5-23: The surface temperature profile for four materials across ribbon width; compaction conducted using two different pairs of rollers (smooth and knurled) at 30 bar hydraulic pressure. The dashed line represents knurled rollers whereas continuous line represents smooth rollers.

5.3.5 Modified ribbon splitting index

It was shown that the predictability of the splitting index to the initiation of longitudinal splitting was not adequate when knurled rollers were used; for smooth rollers, longitudinal splitting was initiated at a value of the splitting index in the range between 0.9-4.27 while for knurled rollers, it was 13.8-24.5 (Figure 5-24 (A-C)). This may be due to the index not taking account of the bending stresses. In an attempt to improve the generalisation of the splitting index, the index was modified by incorporating the relative solid fraction difference since the bending stresses should scale with parameter.

The relative solid fraction, $\Delta\beta$, measured by X-ray was preferred over NIR-CI results due to the limitations encountered when NIR-CI has been used i.e. the limited depth of field of the lens compared with the surface the geometry of the knurled rollers ribbons. The modified splitting index, I_S' , is defined as follows:

$$I_S' = \Delta\beta\varepsilon_R\sigma_{max}/\sigma_T \qquad \text{Equation 5-3}$$

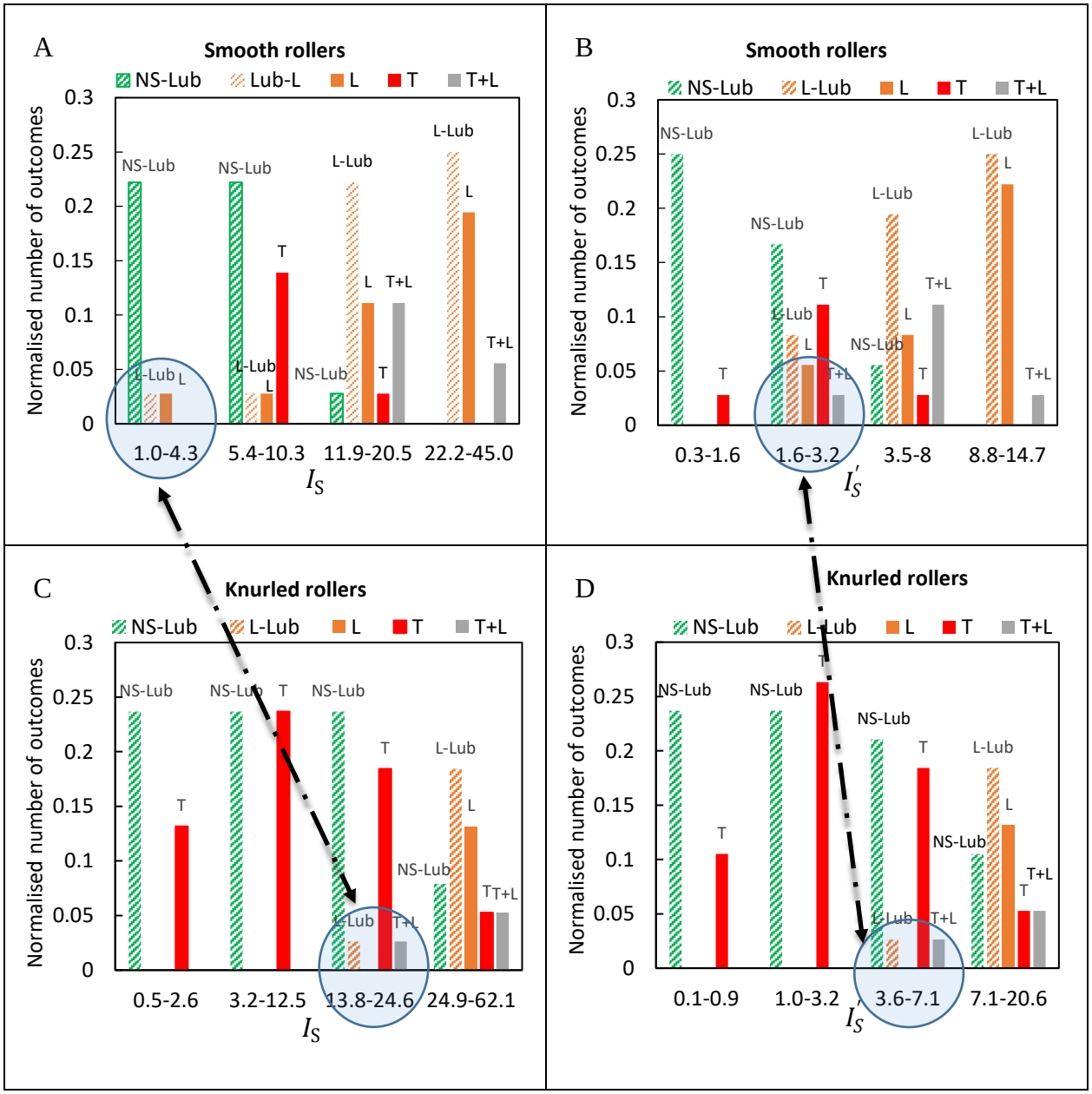

Figure 5-24: A histogram of the number of non-splitting and splitting outcomes per powder feed normalised by the total number of outcomes that were observed with the smooth and knurled rollers . The data for $CaCO_3$ ribbons are not included since its splitting behaviour is anomalous. This based on the splitting index I_S : (A-C) and modified splitting index I_S' (B-D). NS refers to no splitting, L to longitudinal. Coding refers to transversal (T), longitudinal (L), mixed transversal-longitudinal (T+L) and no splitting (NS). Solid and patterned filled bars refer to unlubricated and lubricated cases respectively.

The advantage of this index is that the values correspond to the initiation of longitudinal splitting are more similar for the smooth (1.6 – 3.2) and knurled (1.6 – 7.11) compared with those for the unmodified index, which had values of (1.0 – 4.2) and (13.8 – 24.6). That is, the modified index is more generalised and covers most of the splitting causing factors including maximum applied compaction stress, elastic recovery, bending stress due to non-uniform elastic recovery across ribbon width, and ribbon tensile strength. (Figure 5-24 (B-D)).

5.4 Conclusion

The chapter focuses on extending the predictability of the splitting index developed in Chapter 4 by introducing a factor relating to the bending stresses induced at the exit by incorporating the ribbon solid fraction difference. Knurled rollers have a higher powder/metal contact area that leads to more homogenous stress distribution in comparison with the smooth rollers investigated in Chapter 4. However, the increase in the contact area extends the range of transversal splitting/roller sticking when compared with the smooth rollers and reduces the extent of longitudinal splitting. The ribbons were characterised for their heterogeneity in terms of the porosity distribution using different techniques. X-ray tomography was challenging in terms of being time-consuming, but the use of NIR-CI was promising for providing pixel scale information. Nevertheless, its use for testing knurled rollers ribbons was not possible due to the optical functioning limitation in terms of the low DOF of the lens compared with Rz value of the scanned compact surface. The incorporation of the heterogeneity factor in the splitting index successfully enhanced the predictability for longitudinal splitting initiation.

A reduction in the occurrence of the longitudinal splitting will probably correspond to more homogenous ribbons, which is essential for producing uniform granules properties.

CHAPTER 6 ROLLER STICKING-ROLE OF SURFACE ENERGY

6.1 Introduction

Physical adhesion of powder to equipment surfaces is reported as one of the main problems encountered during powder compaction processes and could lead to serious problems such as poor quality condition of the compact and might cause serious damage to the press machine [19]. The previous chapters demonstrated that the occurrence of sticking/transversal splitting is affected by the stress applied and the mechanical properties of the compacted materials. Therefore, it would be a significant benefit if the sticking problem could be identified from the intermolecular interaction between the contacted bodies i.e. the metal tooling surface and powder particles. Understanding the energies of interaction between contacted bodies has been reported as one of the assisting strategies for predicting sticking problems during tabletting processes [136–138]. It is hypothesised in this chapter that favourable energies of the interaction either between powder particles (cohesion) or between powder particles and a roller surface should follow the trend of sticking/transversal splitting during roller compaction. Inverse gas chromatography (IGC) coupled with a thin-film cell model was used to evaluate energies of interaction between powder particles (W_{co}) and between powder particles and the metal surface (W_{ad}). The trend of the energies of interaction was compared with the sticking behaviour observed in chapter-4.

6.2 Theoretical background

Whenever two solids come into intimate contact, the surface energy of the system will influence their interaction in terms of the stability, adhesion, and cohesion. Surface free energy, γ (mJ/m^2) by definition is a measure of the excess energy of the surface of a material or its the energy required to create a unit area of a surface [139]. It is important in a wide range of applications including; granulation [140,141], crystallisation [142], and tabletting [136,143].

The total surface energy (γ) consists of polar surface energy for acid-base interaction (γ^{ab}) and non-polar surface energy for the dispersive interaction (γ^{d}), and it is calculated by the following equation:

$$\gamma = \gamma^{d} + \gamma^{ab} \quad \text{Equation 6-1}$$

The dispersive surface energy is mainly due to Van der Waals forces and more specifically due to London dispersion forces, on the other hand, the polar surface energy is described by both acidic ($\gamma_a{}^{+}$) and basic properties of the surface ($\gamma_b{}^{-}$).

While surface free energy is referring to the energy of interaction of atoms and molecules at the surface, interfacial surface energy is the energy required to separate two surfaces in a certain medium from intimate molecular contact to infinite separation. This includes the work of cohesion (W_{co}) for the interaction between two surfaces of the same phase and the work of adhesion ($w_{ad_{1-2}}$) for the interaction between two different phases 1 and 2. Both interactions can be calculated using the following equations [144]:

$$w_{co} = 2[\gamma^{d} + (\gamma_a{}^{+} * \gamma_b{}^{-})^{\frac{1}{2}} + (\gamma_b{}^{-} * \gamma_a{}^{+})^{\frac{1}{2}}] \quad \text{Equation 6-2}$$

and

$$w_{ad_{1-2}} = 2[(\gamma^{d}{}_1 * \gamma^{d}{}_2)^{\frac{1}{2}} + (\gamma_a{}^{+}{}_1 * \gamma_b{}^{-}{}_2)^{\frac{1}{2}} + (\gamma_b{}^{-}{}_1 * \gamma_a{}^{+}{}_2)^{\frac{1}{2}}] \quad \text{Equation 6-3}$$

6.2.1 Methods of measuring surface energies and its relation to sticking studies

6.2.1.1 Contact angle

This method is based on placing a liquid droplet on a smooth, flat, isotropic and non-deformable surface. As described by Young [145], once settled on the surface, the droplet will thermodynamically equilibrate with its vapour and possess a unique profile. The angle formed by the tangent of the liquid-vapour interface with the solid-gas interface is the contact angle. The contact angle (Q) is defined by the mechanical equilibrium of the drop that is subjected to the interfacial energies between three interfaces; liquid-vapor(γ_{lv}), solid-vapor(γ_{sv}), and solid-liquid (γ_{sl}) (Equation 6-4).

$$\gamma_{lv} \cos Q = \gamma_{sv} - \gamma_{sl}$$ Equation 6-4

Once determined, the contact angles of known property liquids on the solid surface can then be applied in different approaches to calculate solid surface energy. The approaches existing in the literature vary according to the number of liquids used and subsequently the measured surface energy components, i.e. dispersive, acidic, and basic surface free energy. The most common widely used approaches are Fowkes, Owens-Wendt, and Van Oss-Chaudhury-Good methods [146,147].

In terms of its application in understanding compact stickiness during compaction, Bunker et al. [148] studied the adhesion forces between lactose monohydrate and coated tabletting punches at various RH values. The punches were coated with different materials having various degrees of hydrophilicity/hydrophobicity, which was assessed by measuring static water contact angles on the surface of the punches. The study mentioned that lactose showed a higher adhesion to diamond-like carbon-coated punches in comparison to the other coating materials investigated. This was ascribed to as the formation of capillary bridges due to moisture condensation with the more hydrophilic punch face. Additionally, Matjie et al. [138] investigated the adhesion of aluminium silicate on stainless coupons, which were coated with different materials. The theory of van Oss was used to determine the surface energy of the coated surfaces; this was achieved by measuring the contact angles of known-property polar and non-polar liquids on the coated and non-coated stainless steel coupons. The study showed that coating decreased the surface energy of the coupons surfaces from 43.3 mJ/m^2 for uncoated coupons to values between 23.3-40.7 mJ/m^2 depending on the coating material. The reduction in the surface energy was associated with a 97% decrease in aluminium silicate sticking. The same conclusion was made by Al-Karawi [149], where the contact angles of molten ibuprofen showed a close correlation with the sticking tendencies of various punch tip coatings.

6.2.1.2 Atomic Force Microscopy (AFM)

For this technique, a probe is either coated or loaded with the substrate of interest and it is brought into contact with the studied surface. The movement of the cantilever is monitored by a laser beam reflected off the cantilever on which the probe is mounted. Because of its high sensitivity, the AFM can be used to investigate various types of

interactions such as van der Waal, capillary and electrical forces [147]. Wang et.al [136] used AFM to study the adhesion forces between three different profen compounds and an AFM tip that was coated with iron to resemble the tabletting punches. The profen surface was prepared by the melting /recrystallisation of the material on a glass cover. The measured work of adhesion was reported to be in agreement with the rank order of adhesion measured in a subsequent study [25]; in which a compaction simulator was used to compact the same set of materials and the tablet removal force was considered as the criteria for punch face adhesion. Moreover, Weber et.al [150] investigated the lubrication mechanism of MgSt by studying different combinations of particle interactions; the results showed stronger interaction forces between MgSt and a steel surface when compared to the interaction with MCC or MgSt particles itself. The author suggested that the resultant adhesion interactions are responsible for the lubrication mechanism of MgSt as it reduces the ejection force and sticking to the tabletting punches.

Generally, AFM is useful for investigating the molecular interaction at different levels, while subsequent compaction stresses determine the extent of sticking. However, AFM still suffers from some limitations that should be taken into account prior to any force measurement; this includes the geometry of the particle attached to the probe tip, the limited scanning area, and the difficulty in controlling the electrostatic charges.

6.2.1.3 Inverse Gas Chromatography (IGC)

For this technique, the sample under investigation is packed into a column and acts as a stationary phase while an inert gas (usually helium) passes through the column as a mobile phase. Known property probes are injected through the mobile phase to interact with the investigated stationary phase. A series of non-polar probes such as n-alkanes is be used to investigate the dispersive property of the solid sample. In addition, polar probes are then injected in the column to study the acid-base interactions. The retention time (t_r) is that taken by the gaseous probe to pass through the chromatography column and is obtained as the fundamental parameter measured. The retention time can be converted into a retention volume (V_N) (Equation 6-5), which is directly related to several physiochemical properties of the solid (adsorbent) such as the surface energy [151,152].

$$V_N = F_C.J(t_r - t_0) \qquad \text{Equation 6-5}$$

where,

F_C is the carrier gas flow rate (ml/min) and t_0 is the dead time which is that needed for a non-interacting probe (e.g., methane) to pass through the column. *J* is the James-Martin correction factor which describes the effect of the carrier gas compressibility and is added to the above equation to correct the effect of pressure drop and the packing density of the stationary phase on the retention time, this factor is calculated by the following equation [153]:

$$J = \frac{3}{2} * \frac{(P_i/P_o)^2 - 1}{(P_i/P_o)^3 - 1}$$ Equation 6-6

where, P_0 and P_i are the outlet and inlet pressures respectively.

Once the retention volume is determined, it can be applied in one of the two commonly used methods in the literature, namely the Doris-Gray and Schultz methods [151], to calculate the dispersive surface energy of the solid packed material. The former one is applied in this study which involves plotting $R_gTln(V_N)$ a function of the carbon number (of the injected alkane probe), which should produce a linear correlation (Figure 6-1). Where R_g is the gas constant (8.314 $J.mol^{-1}$) and T is the column temperature (kelvin).

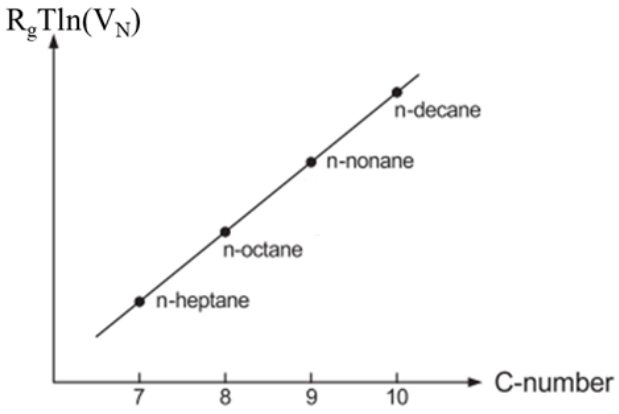

Figure 6-1: Determination of surface free energy based on Dorris-Gray approach [151].

The slope of the alkane line in Figure 6-1 can be used to determine the dispersive component of the surface energy (γ_s^d) using the following equation [153]:

$$\gamma_s^d = slope^2/4{N_A}^2 * \gamma_{CH2} * (\alpha_{CH2})^2$$ Equation 6-7

where, γ_{CH2} is the surface free energy of a solid contains methylene groups only such as polyethylene, N_A is Avogadro's number ($6.022 \times 10^{23}\ mol^{-1}$), and α_{CH2} is the cross-sectional area of a methylene molecule (6 $Å^2$).

This method can only be used to calculate the dispersive component of surface energy so that methods such as polarisation can be used to determine the specific part of the surface energy. The same parameter ($R_gTln(V_N)$) used with Dorris-Gray method is plotted against the molar deformation polarisation of the gaseous probe (P_D, $cm^3\ mol^{-1}$), which is an intrinsic parameter given by the following equation [153] :

$$P_D = \frac{{w_{ri}}^2 - 1}{{w_{ri}}^2 + 2}\frac{M}{\rho} \qquad \text{Equation 6-8}$$

where M, w and ρ are the molar mass ($g\ mol^{-1}$), refractive index, and density ($g\ cm^{-3}$) of the probe molecule respectively. The resultant plot should be a straight line for the injected alkanes, while the points representing the polar probes are located above the alkane straight line; the vertical distance to the straight line is equal to the specific component of the free energy of adsorption (ΔG_a^{sp}) (Figure 6-2).

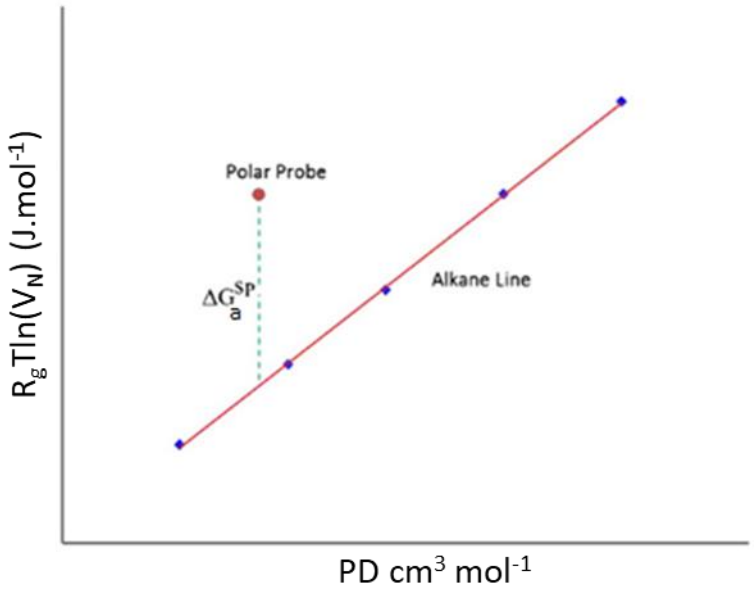

Figure 6-2: The typical plot of the polarisation method which is used to determine the specific surface energy of adsorption ΔG_a^{sp}[153].

Subsequently, based on the van Oss approach, the specific surface energies (γ_s^{ab}) of the samples can be calculated, in which the specific contribution is subdivided into an acidic (γ_a^+) and a basic (γ_b^-) parameter of the surface energy:

$$\Delta G_a^{sp} = 2N_A[(\gamma_g^+)^{1/2} * (\gamma_s^-)^{1/2} + (\gamma_g^-)^{1/2} * (\gamma_s^+)^{1/2}] \quad \text{Equation 6-9}$$

Two main probes should be used to solve Equation 6-9; a monopolar electron acceptor probe which has no (γ_g^-) such as dichloromethane and monopolar electron donor probe which has no (γ_g^+).

If the specific surface area of the sample is provided, the IGC can be automatically programmed to inject the precise amount of probe vapour in order to achieve different user-defined surface coverages. The measurement of surface properties at different surface coverages will result in a surface heterogeneity profile of the sample. The understanding of energy distributions is particularly useful at interface boundaries of formulations, as well as to distinguish subtle differences in the surface chemistry of samples. Sample specific surface area is commonly determined using BET theory, in which a monolayer of a weakly adsorbing gas is adsorbed on the sample solid surface while adsorption isotherm is assumed to follow type II or IV adsorption mechanism. Any gas can be used if the gas is physically adsorbed by weak bonds and can be desorbed by decreasing the pressure at the same temperature. The theory relates condensation and evaporation rates of the gas molecules in the adsorbed layer, the linear form of this relationship is called the BET equation [154,155]:

$$\frac{P_{eq}}{n(P_{sat} - P_{eq})} = \frac{1}{n_m C} + \frac{C-1}{n_m C}\left(\frac{P_{eq}}{P_{sat}}\right) \quad \text{Equation 6-10}$$

where, P_{eq} and P_{sat} are the equilibrium and saturation pressure of adsorbates at a constant temperature. n is the amount of gas adsorbed at equilibrium pressure and n_m is the amount of gas adsorbed in a monolayer. *C* is the BET or sorption constant related to the heat of adsorption and condensation.

BET theory is only valid at arrange of relative pressure $\left(\frac{P_{eq}}{P_{sat}}\right)$ between 0.05-0.35, at which the relationship between $\frac{P_{eq}}{n(P_{sat}-P_{eq})}$ and $\left(\frac{P_{eq}}{P_{sat}}\right)$ is suggested to be linear. The slope and

intercept of this linear relationship can be used to calculate (n_m) as shown in the following equation:

$$n_m = \frac{1 - intercept}{slope} \qquad \text{Equation 6-11}$$

Subsequently the BET specific surface area (s_{BET}) is calculated from:

$$s_{BET} = \frac{n_m N_A \alpha_{ads}}{V m_{ads}} \qquad \text{Equation 6-12}$$

where α_{ads} is the cross-sectional area of the adsorbing gas molecule, N_A is the Avogadro number ($6.022 \times 10^{23}\ mol^{-1}$), V is the molar volume of the adsorbed gas and m_{ads} is the mass of the adsorbent in (g). The monolayer capacity, n_m is the amount of the adsorbent used to occupy all adsorption sites on the solid sample, It can then be used as a criterion for the IGC to achieve different user-defined surface coverages [154].

In terms of its use to understand particle-particle interaction involved in compact formation, IGC was used by Fichtner et.al [143] to study the impact of surface energy on the compactibility of lactose monohydrate. Three powders of lactose with different levels of surface energy were prepared by spray drying with different proportions of surfactant polysorbate 80. All powder properties were similar in terms of particle size, shape and surface area. The produced powders of lactose were compacted with the same compaction pressure; the study showed a lower tablet tensile strength at higher surfactant concentrations. This was attributed to the decrease in the powder surface energy, which led to a lower formation of intermolecular forces at the same compaction pressure. Moreover, Jacob and Berg [156] discussed the limitations associated with determining the work of adhesion of porous and granular material using the contact angle technique. They compared the results of the work of adhesion measured by contact angle and IGC approaches. Both techniques have been used to measure the work of adhesion between different polymers ((polyvinyl chloride) PVC and polymethyl methacrylate (PMMA)) and chemi-thermo-mechanical wood pulp fibres (CTMP). The study showed a close agreement between the works of adhesion values determined by both techniques.

6.2.2 Summary

In summary, the aforementioned techniques suffer from some limitations that should be considered prior to any surface energy determination; using the contact angle approach on powder particles or granules is complicated by the presence of porous architecture that still exists even when powder particles are compacted into a tablet. Rougher surfaces have been reported to produce higher contact angle values when compared with smooth surfaces with the same composition [157]. Additionally, when compressed, the topmost particles could undergo plastic deformation which could give different results when compared with an uncompacted powder [158]. On the other hand, AFM force resolution is limited by the properties of the cantilever used including stiffness and sensitivity to thermal noise [159].

As mentioned previously, both AFM and contact angle techniques were used as assisting approaches to understand adhesion between surfaces in terms of intermolecular interactions and more specifically by measuring the thermodynamic work of adhesion. In an attempt to overcome some of the challenges associated with these techniques, the inverse gas chromatography has been utilised as an alternative technique. It has been shown in the literature that determining intermolecular interaction between powder and metal surfaces could be beneficial in terms of predicting sticking during the compaction processes; metal-powder interaction determines the potential of the interaction and any subsequent mechanical process affect the extent of adhesion. In an attempt to extend our understanding to ribbon transversal splitting/sticking, powder-powder and powder-metal intermolecular interaction in terms of thermodynamic work of cohesion/adhesion were determined using IGC. Energies of interaction have been examined for any correlation with the trend of roller sticking described in Chapter-4.

6.3 Methods

A commercial inverse gas chromatography (IGC SEA, Surface Measurement Systems Ltd., London, UK) was used to analyse the surface energy of both powders and metal surface.

To determine the powder surface energy, about 600 mg of powder was packed into a standard IGC salinized glass column of 4 mm inner diameter and 300 mm in length. All

powders were conditioned as previously described in section (3.1). Although it is been reported that the packing method does not significantly influence the surface energy results [160], for better consistency, prior to inclusion in the IGC oven, the packed columns were tapped for 5 min so that a homogeneous powder plug with no channels or cracks were formed. The columns were sealed by glass wool to support the powder sample. Temperature and humidity were controlled and set to 40% RH and 25°C respectively throughout the pre-conditioning and experiments. A series of four non-polar alkanes (hexane, heptane, octane, and nonane) was used to measure the dispersive component of the surface energy while two polar probes dichloromethane and ethyl acetate were used for measuring the polar surface energies. Simultaneously, methane was used for dead time corrections and nitrogen as the carrier gas. The characteristics of the probe gases used in the study are summarised in Table 6-1. All gases were set at flow rate of 10 ml/min. The IGC used was coupled with a flame ionization detector to measure the gas retention times.

To measure stainless steel surface energy, a piece of steel of grade 4140 and Ra~ 2.44 ± 0.3 µm (the same steel grade as used to make the rollers) was cut to specified dimensions (60 x 210 x 10 mm) to fit in the IGC film cell (Figure 6-3). Prior to the measurements, the steel piece was cleaned ultrasonically in an ethanol bath for 5 min and subsequently rinsed with deionised water and dried under nitrogen before placing it in the IGC cell [148].

The machine was then run at a series of surface coverages in triplicate, and the resulting data were analysed using the advance SEA analysis software, where peak-max values were used in the Dorris-Gray approach for surface energy determination.

The specific surface area was measured using a series of injections of octane at different injection volumes starting from a high volume and gradually decreasing the volume for each injection. Once entered into the tube, the gas will adsorb on the sample surface and the pressure in the tube will fall until an equilibrium is achieved. The amount of gas adsorbed (n) at equilibrium pressure is calculated from the difference between the amount of the injected gas and the amount of non-adsorbed gas in the gas phase. The use of BET theory requires at least three measurements of the adsorbed gas amounts at different values of relative pressure $\left(\frac{P_{eq}}{P_{sat}}\right)$, the resulting data were then fitted using the BET theory

(Equation 6-10) and the specific surface area calculated accordingly. Once this is measured, the system can accurately inject a specific amount of probe vapour in order to achieve the predefined surface coverages. The experiments were conducted in triplicate and the results were analysed using the SMS analysis software V1.3 (SMS, Middlesex, London, UK).

Table 6-1: Characteristics of probes gases used in the IGC study [161].

Test compound	α_{ads} [m²]	(γ_g^d) [J/m²]	(γ_g^+) [mJ/m²]	(γ_g^-) [mJ/m²]	Character
hexane	5.15×10^{-19}	0.0179	–	–	nonpolar
heptane	5.73×10^{-19}	0.0203	–	–	nonpolar
octane	6.30×10^{-19}	0.0213	–	–	nonpolar
nonane	6.90×10^{-19}	0.0227	–	–	nonpolar
Dichloromethane	2.45×10^{-19}	0.0245	124.58	0.0	acceptor of electron
ethyl acetate	3.30×10^{-19}	0.0196	0.0	457.67	donor of electron

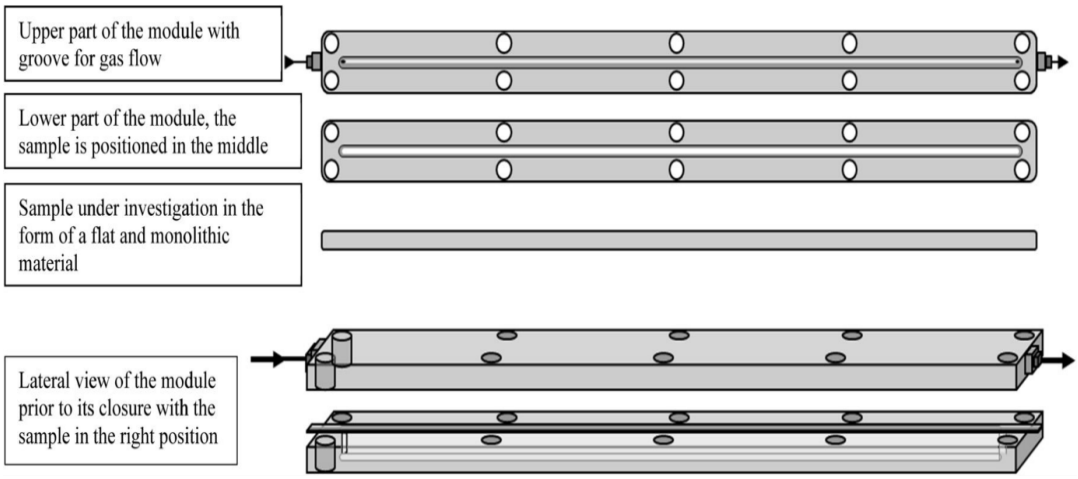

Figure 6-3: Technical drawing of the film cell module for IGC (60 × 210 × 11 mm). The arrows show gas flow [162].

6.4 Results and Discussion:

6.4.1 BET specific surface area

The BET specific surface areas of all samples were determined using octane adsorption isotherm. The use of IGC for surface area determination has been previously reported to give acceptable and reproducible results [163,164]. As an example, Figure 6-4 shows the adsorption isotherm of starch which was used to calculate the specific surface area using Equation 6-10 to Equation 6-12. The BET specific surface area and the fitting parameters for all the studied materials are summarised in Table 6-2.

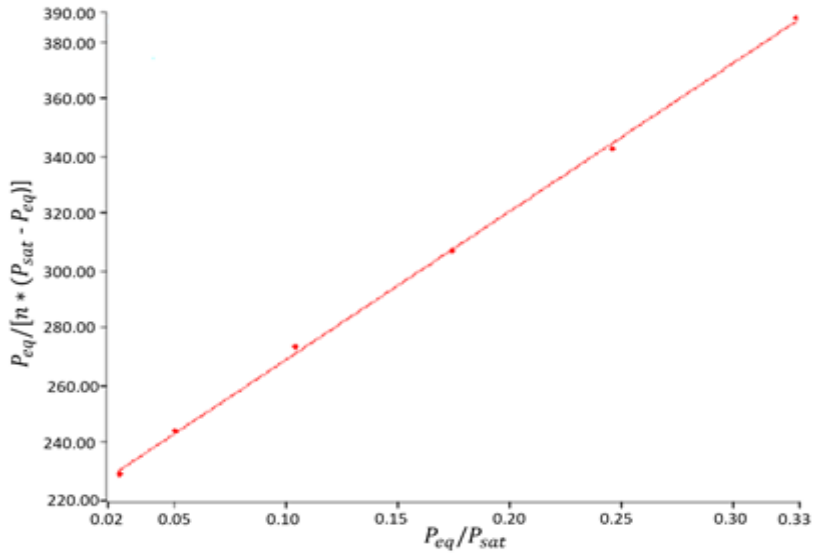

Figure 6-4: Octane isotherms (amount adsorbed n as a function of partial pressure P_{eq}/P_{sat}) for starch sample 298 K)

Table 6-2: Specific surface area parameters determined using octane isotherm.

Material	Sorption constant (C)	Monolayer capacity (n_m) (mMol/g)	BET surface area (m^2/g)
Steel	2.0122	0.0034	1.3407
$CaCO_3$	11.6807	0.0025	0.9554
mannitol	2.0745	0.0029	1.0826
200M	4.3443	0.0018	0.6963
anhydrous lactose	2.4619	0.0022	0.8254
starch	3.373	0.0014	0.517
maltodextrin	2.0584	0.0031	1.1905
MCC	2.1048	0.0039	1.3407
MgSt	4.4208	0.1862	7.24235

6.4.2 Dispersive and specific surface energies of powders and metal surface

IGC was employed to detect and quantify the surface energy components of both powder and steel surfaces. All surface energy measurements were conducted at low surface coverage using low solute concentrations ranging from (0.02-0.1 P/P_0). The approach of infinite dilution represents over 95% of IGC papers published so far and is used to avoid complexity associated with determining retention behaviour of the solute when solute-solute interactions become significant at high solute concentration [151]. Figure 6-5 shows the change in surface energy in terms of its fundamental components i.e. the dispersive and specific surface energy as a function of surface coverage. Similar values were reported in other studies [139,165–169]

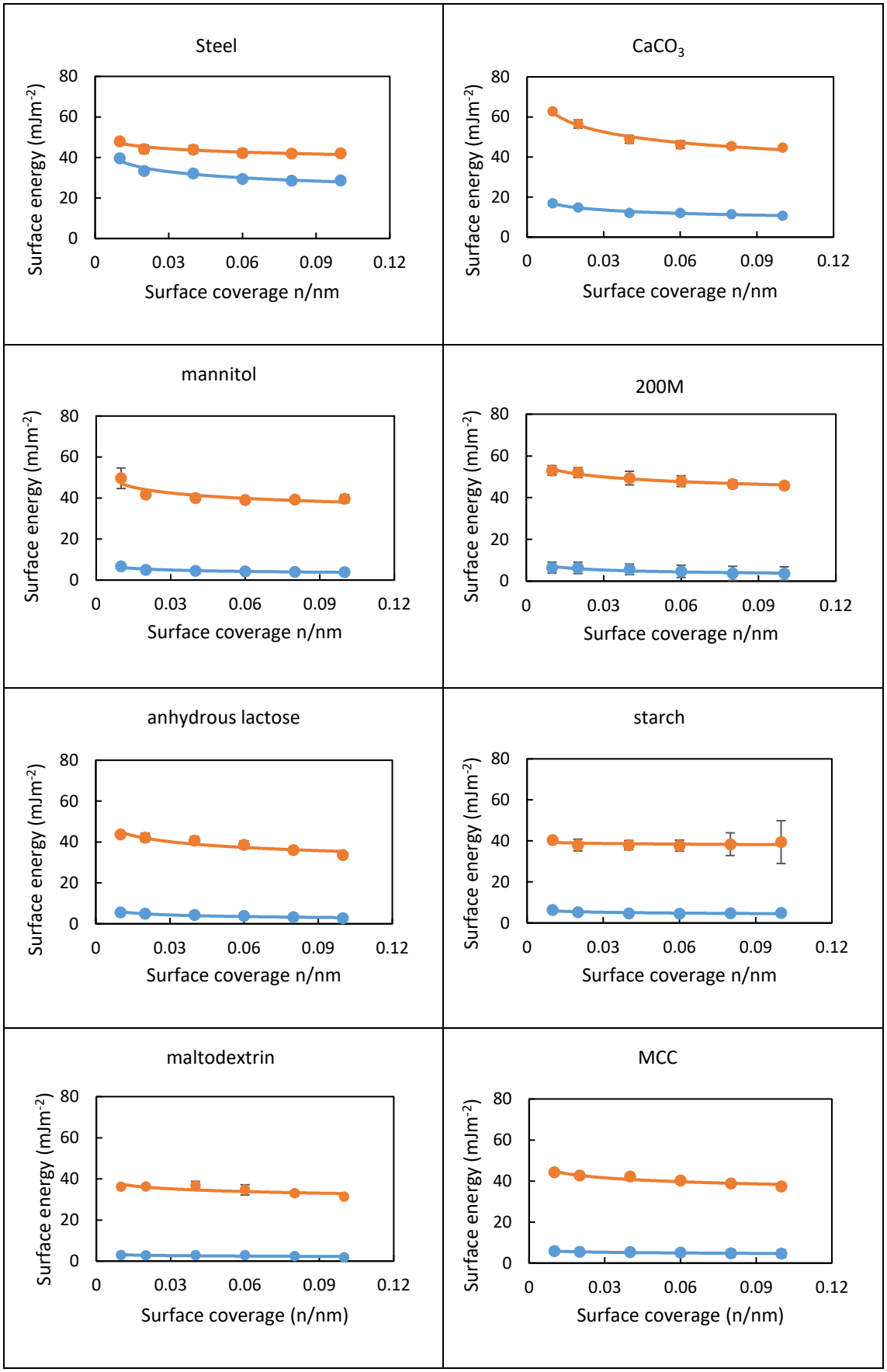
Steel
Surface energy (mJm-2)
Surface coverage n/nm
CaCO3
mannitol
200M
anhydrous lactose
starch
maltodextrin
Surface coverage (n/nm)
MCC
0
20
40
60
80
0.03
0.06
0.09
0.12

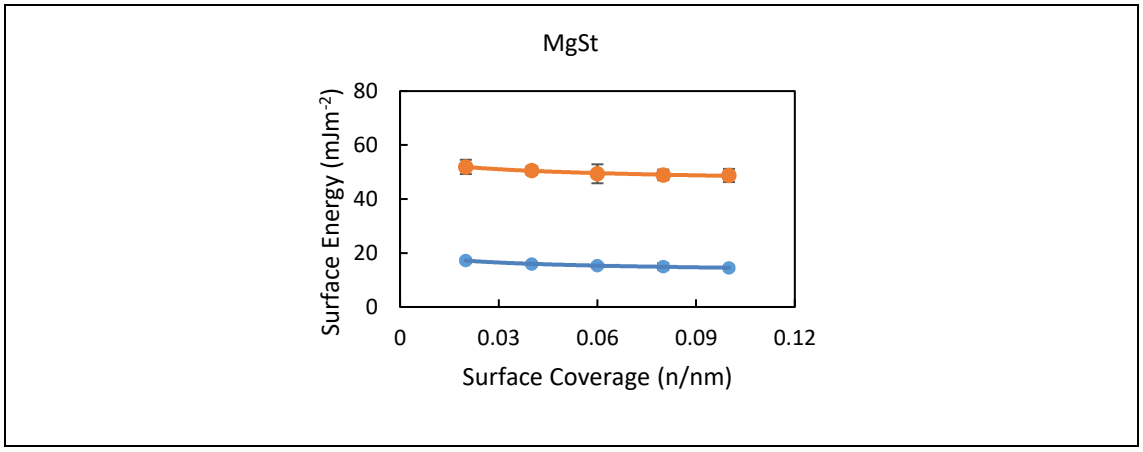

Figure 6-5: Dispersive and polar surface energy distribution profiles as a function of surface coverage; orange and blue colours represent dispersive and specific surface energies respectively.

As can be seen in Figure 6-5, there is a general trend of decreasing surface energy as a function of surface coverage. This can be attributed to the variation in surface energy of the different active sites of the interacted surfaces; at a low surface coverage, the higher energy sites of the powder surface are preferentially occupied first. Subsequently, the lower energy sites are then occupied at higher surface coverage [153]. This heterogeneity of surface energy generally originates from different degrees of local crystallinity, variation in the surface functional groups, or the presence of impurities. It was more noticeable in the case of $CaCO_3$, where a higher difference in surface energy was observed between the high and low surface coverage.

6.4.3 Work of cohesion and adhesion

As stated previously, thermodynamic work of adhesion is the work required to reversibly separate an interface between two bulk phases to a separation distance of infinity, which is valid if irreversible chemical interactions are neglected and only physical interactions are present [170]. If the surface energy components of the interacted surfaces are determined, the total work of adhesion and cohesion between them can be calculated according to the geometric mean method (Equation 6-2 and Equation 6-3).

As denoted from the energy calculations of the work of cohesion and adhesion in Figure 6-6, all of the studied feed powders tend to interact more with the steel surface (W_{ad}) compared to their particle-particle interaction (W_{co}).

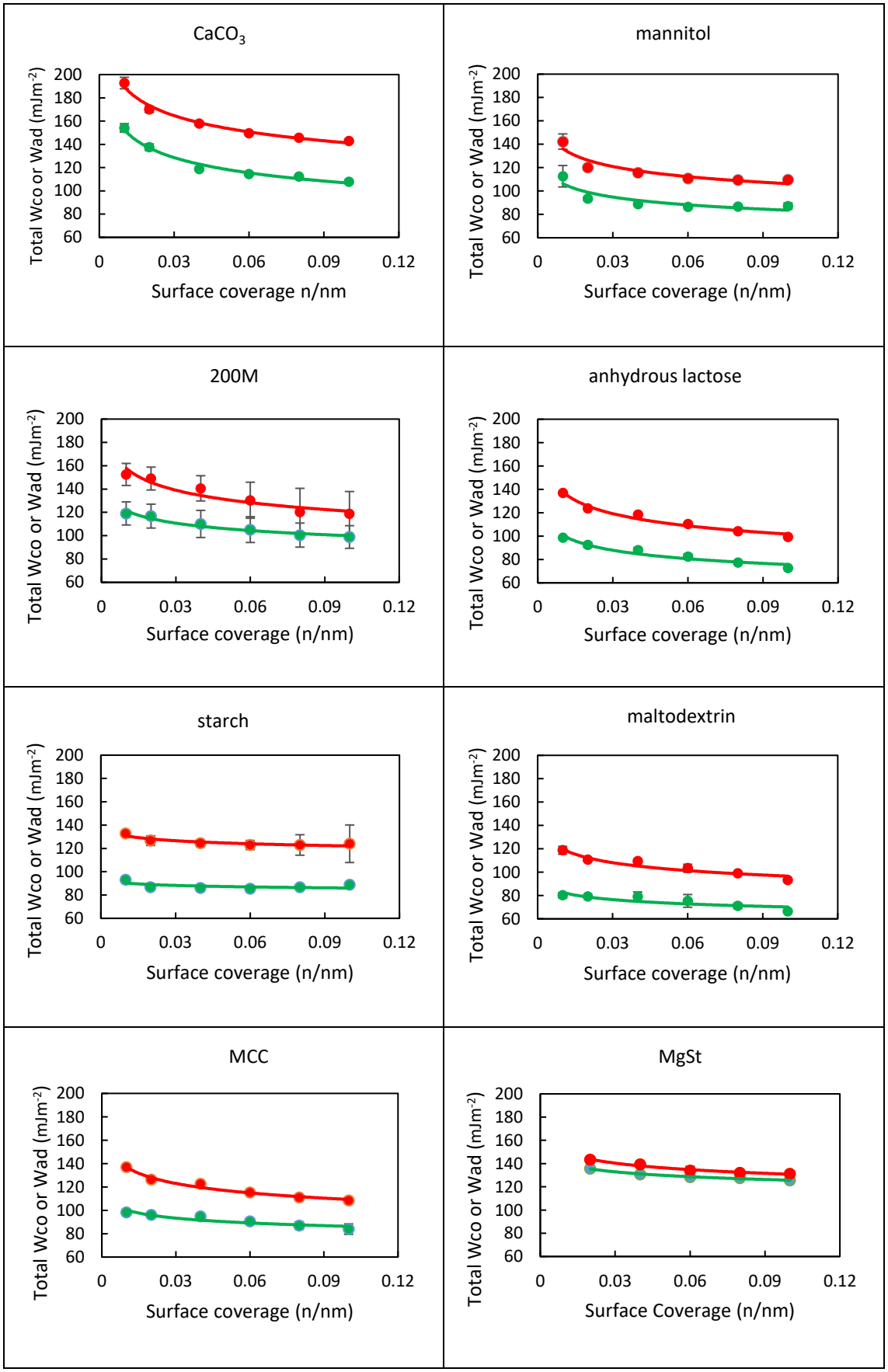

Figure 6-6: The profiles of work of adhesion and cohesion between the powders and metal surface determined by IGC. Red and green colours represent work of adhesion and work of cohesion respectively.

When compared to the trend of material sticking observed in Figure 4-20, where both types of lactose and mannitol showed a considerable sticking to the roller surface, the calculated ratio of W_{ad}/W_{co} at any surface coverage did not show any preferential adhesion interaction that could contribute to understanding the sticking behaviour of lactose and mannitol during roller compaction. The trend shown in Figure 6-7 is an example of the W_{ad}/W_{co} at 0.04 n/nm surface coverage.

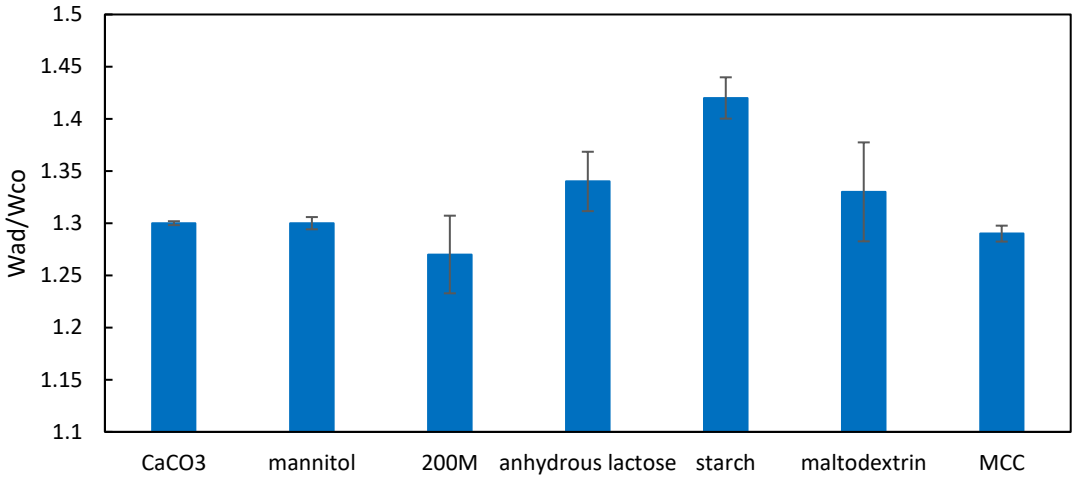

Figure 6-7: The ratio of work of adhesion to work of cohesion (Wad/Wco) at 0.04 n/nm surface coverage.

As explained previously 2.1), sticking could take place if the strength of bonding to the metal is greater than the interparticular bonding between the compacted powder particles, i.e. the removal of a compact will result in an interparticular failure (cohesion failure) where part of the compact sticks to the metal surface. The total strength of bonding either between metal-particle or particle-particle is mainly controlled by both interparticular bonding area and bonding strength [171]. The measured surface energies and work of cohesion/adhesion seen in Figure 6-5 and Figure 6-6 could give an idea about the nature of bonding and bonding strength; dispersive and specific surface energies are an indication of the main forces involved during compact formation, i.e. van der Waals and hydrogen bonding respectively. On the other hand, Wco and Wad is an estimation of the strength of bonding. However, compaction processes involve a series of rearrangement, deformation, and breakage processes that develop under the applied stress to increase the bonding area and enhance the total interparticular contact area over which molecular interactions are in effect. This is mainly controlled by the mechanical properties of the

compacted materials where more plastically deformable materials such MCC respond to the applied stress by generating higher surface area for bonding.

The results suggest that the studies conducted in the literature which correlates interparticular bonding to the sticking tendency [136,148,149], could only be valid when dealing with particles of similar mechanical properties. However, for materials that possess various mechanical properties, it is necessary to incorporate the effects of deformation that seems to be the limiting step for sticking as most of the studied materials have a similar range of surface energies.

In summary, the data in Figure 6-7 would suggest that the release of all compacts of the powders considered would involve cohesive rather than interfacial failure. However, the values of W_{ad} and W_{co} could be reduced by the asperities on the surfaces of the powder particles, which will store elastic energy when compacted. Moreover, any failure including the release of compacts involves crack propagation, and the values could be increased by dissipative processes, e.g. viscoelastic or plastic deformation, at the crack tip, which would increase the values of these parameters. Such effects are not taken into account by measurements of the interfacial free energy.

6.4.4 Understanding the mechanism of lubrication as a function of surface energy

As suggested by Weber et.al [150], the lubrication mechanism of MgSt can be elaborated by considering the different interactions between the contacting surfaces. The study showed that MgSt interaction with the steel is greater than most of the possible interparticular interactions that could take place during compaction including; MgSt-MgSt, MCC-MCC, MCC-steel, and MgSt-steel (Figure 6-8). According to the authors, this could contribute to the explanation of the lubrication mechanism of MgSt during compaction processes.

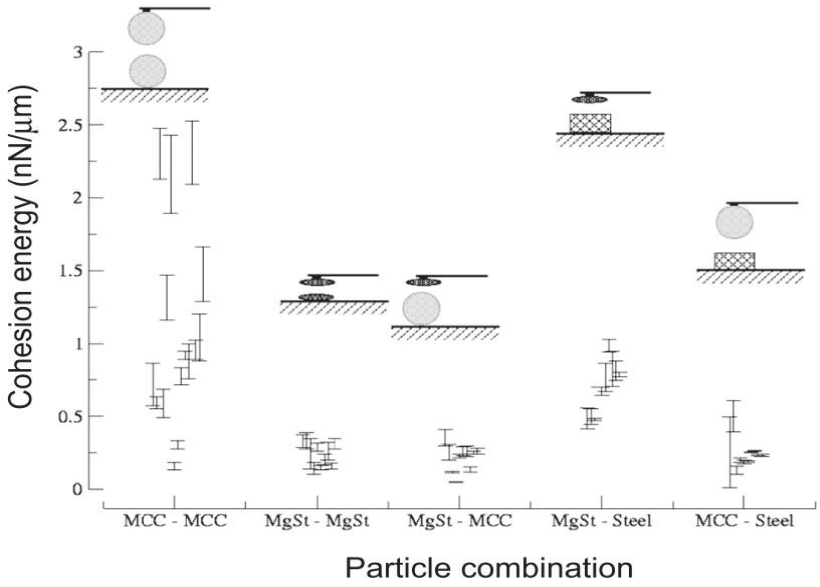

Figure 6-8: Cohesion energy measured between different particle combinations [150].

In this study, the work of cohesion and adhesion of MgSt to the steel and to all of the studied feed powders have been calculated using the IGC surface energy measurements shown in Figure 6-5, according to Equation 6-2 and Equation 6-3. The results are presented in Figure 6-9; the figure also shows the work of cohesion between feed powder particles and work of adhesion between powder particles and steel to compare all of the possible interactions.

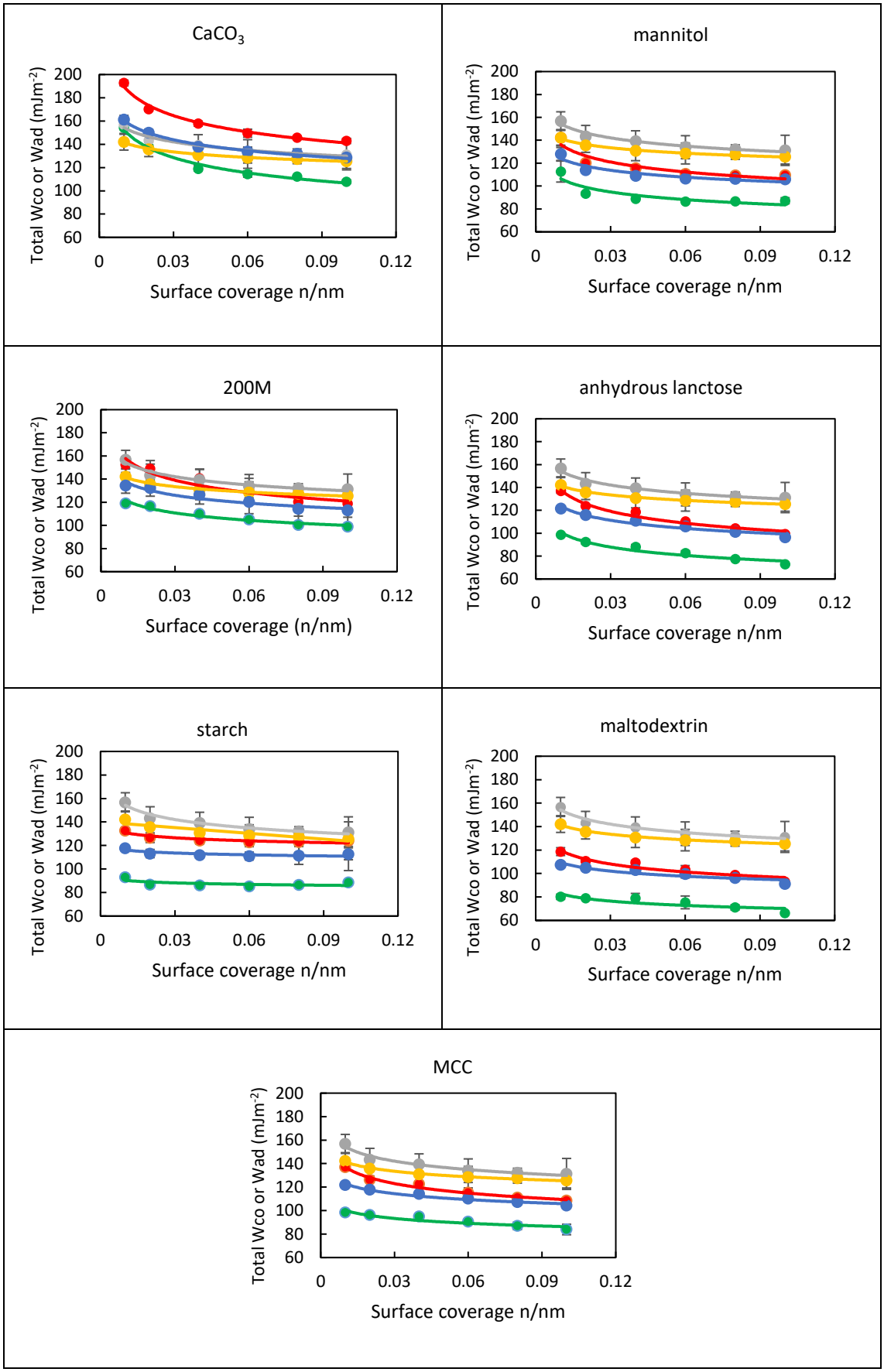

Figure 6-9: Work of cohesion and adhesion between MgSt-MgSt (—), MgSt-steel (—), PP-PP (—), PP-steel (—), and MgSt-PP (—). (PP: stands for powder particle).

The results in Figure 6-9 show that in most of the cases MgSt tends to interact more preferentially to the steel surface in comparison with its interaction to the other surfaces. The results support the main mechanism of lubrication suggested in the literature i.e. boundary lubrication mechanism by which the lubricant forms a layer around the compacted particles or on the metal surface. According to JKR theory [70], there are two main approaches by which this layer can reduce the adhesive interactions; 1) reducing the interfacial interactions between powder particles and the metal surface, which could apply to all of the tested powders except for the case of $CaCO_3$ since there is a greater interaction between all of the tested powders and the metal surface compared to the other interactions (Figure 6-9); 2) reducing the contact area between powder particles and metal surface. The anomalous behaviour of CaCO3 can be attributed to its high degree of impurity; the used CaCO3 in this study was sourced by grinding of marbles. It is known to contain $MgCO_3$ and Fe_2O_3 which could explain its high polar surface energy values [172,173].

6.5 Conclusions

IGC SEA was used to determine the surface energetics and surface chemistry of the samples in an attempt to determine if there were any preferential intermolecular interaction between steel surface and compacted powder that could lead to powder sticking on the roller surface. This study was able to differentiate the differences in surface energetics and surface chemistry of the samples. The surface energetics and surface chemistry of materials are known to have important implications in processes involving interfacial interactions such as in wetting, coating, cohesion/adhesion etc.

The surface energy profiles show that all the samples are energetically heterogeneous since the surface energies change as a function of surface coverage. In addition, it can be clearly observed that the dispersive component contributes a major part of the surface energy.

No clear correlation between the work of adhesion/cohesion and sticking probability was found which suggests that particle deformation is a dominant factor in sticking during compaction. However, the result could contribute to the elaboration of the lubrication mechanism of MgSt during powder compaction, as MgSt tends to interact more preferentially with the steel when compared to the other possible surface interactions.

CHAPTER 7 PRDICTIVE MODEL FOR THE RIBBON POROSITY DISTRIBUTION USING THE ARTIFICIAL NEURAL NETWORK

7.1 Abstract

It was shown in Chapter 5 that the heterogeneous distribution porosity across ribbon width can affect the trend of ribbon splitting. Such heterogeneity may also have a negative effect on the properties of the downstream granules [174,175]. In this chapter, a data-driven model was developed to predict the ribbon porosity distribution using the artificial neural network approach (ANN). Various process-related parameters (e.g. roller force and roller surface indent depth) and material properties (e.g. the angle of wall friction, effective angle of internal friction and the material compressibility) were considered as the inputs of the ANN. While the outputs of such a network were the porosity which was experimentally measured by X-ray tomography at every 3.5 mm across the ribbon width. It is worth mentioning that the best number of hidden neurons was the one that corresponded to the minimum error. Once the model is successfully developed and optimized, one can accurately predict the porosity distribution across the ribbon width. Experimental results showed that the ANN was able to successfully map various material and process parameters to the ribbon porosity distribution across ribbon width, which is considered to be one of the most important quality attributes in the roller compaction process. Furthermore, the obtained results are considered as a promising development in the roller compaction that may positively affect the design, control and the scale-up of the roller compaction process.

7.2 Introduction

Roller compaction is a continuous compaction process. However, incorporating this process in a continuous manufacturing line requires effective control strategy that controls the process through a feedback control systems, this is essential to achieve the designed critical quality attributes in the presence of disturbances generated by the process and/or feed materials. Model predictive control (MPC) is one of the most powerful control technique; this system relies on the models of each unit operation within

the contentious line to take a control action [176]. Therefore, to apply such a control system there is a need to develop robust and rapid models so it can be implemented in the controlling system [177].

Various predictive modelling approaches have been used to simulate the roller compaction process. Finite element method (FEM) has been used extensively by many researchers to model the roller compaction process in order to investigate variation of normal and shear stresses across ribbon width [64], predicting three-dimensional ribbon density distribution [175] and examining the effect of varying material parameters on the maximum stress and nip angle [88]. Additionally, DEM approach was also implemented to simulate the roller compaction process; Odagi et al. [91] developed a 2D-DEM model to evaluate the effect of cohesion force and roll speed on the particle flow rate and pressure distribution on the roller surface. In a more recent study [90], a combined three dimensional DEM/FEM model was utilised to model the relative density of the roller compacted ribbons; DEM was used to simulate the flow of material in the feeding zone and the results of this model was used as a boundary inlet condition for the subsequent FEM modelling. (The use of these modelling approach in the field of roller compaction process is highlighted in more details in section 2.3).

All of the aforementioned models are of great importance for enhancing the mechanistic understanding of the roller compaction process. However, these models still suffer from the long processing time which hinders its applicability in the control system of the manufacturing line. Providing that MPC system requires any process model to run in a few seconds so it can be implemented in the controlling system. From here comes the strength of data-driven models such as ANN to overcome such a problem. ANN can be trained and exploited to simulate complex processes with multiple inputs and outputs.

A limited number of researchers attempted to use ANN to model such a complicated process; Turkoglu et al. [93] used ANN and genetic algorithm approach to optimise the tablet tensile strength; binder type, concentration, and the number of roller passes were used as inputs in a multilayer feedforward network. Inghelbrecht et al. [76] utilized ANN modelling to study the effect of roll speed, horizontal and vertical screw speeds and air pressure on the friability of the produced granules. In a more recent attempt Sajjia, et al. [94] used roller force and screw speed as inputs, and average envelope density of MCC ribbons as outputs. Though, the developed network is greatly limited in terms of its

application as it did not take into consideration material properties and the variation of density across ribbon width.

In summary, ANN can be trained to predict complex trends; this study revisits ANN approach to provide a fast and reliable model that link various material and process proprieties to predict porosity distribution across the ribbon width. Many theoretical models addressed this problem; nevertheless, these models are of great value in terms of providing a detailed mechanistic understanding of the process, due to their long processing time, it still hard to implement them in the control system across the manufacturing line.

7.2.1 Theoretical background

7.2.1.1 Machine learning and ANN

Since physical models may not exist or may be too complex to be developed and implemented, data-based models are, more often than not, used to represent complex processes by utilising the computing capacity of computers. An artificial Neural network (ANN), as a data-driven model, is a set of algorithms that are inspired by the biological neural networks. In case of biological neurons, neurons are connected to each other by the so-called *synapses*, signals can only be transmitted between neurons when the intensity of the received signals exceed the neuron threshold, the neuron then becomes active and the signal will be allowed to pass to the neighbouring neuron. Similarly, the artificial neural network consists of interconnected nodes, synapses that are represented by a single number or weight and each input is multiplied by a certain weight before being sent to the node body. In the node body, the sum of the weighted signals is processed using a certain activation function. Figure 7-1 shows a schematic representation of the neuron of both the biological and the artificial network. An example of the activation function is the step function, where the sum of all weighted signals is compared to a predefined threshold. The node output is “1” when the sum of the weighted signals is higher than the defined threshold otherwise the node output is “0” [92].

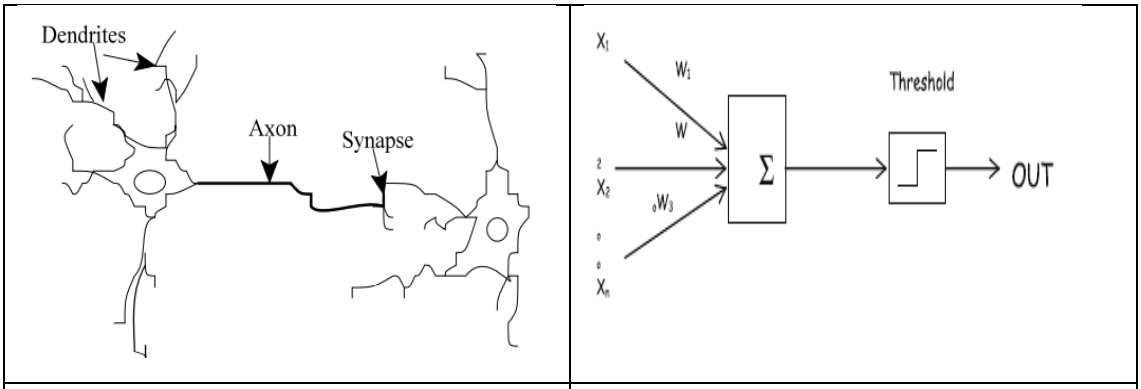

Biological neuron	Computational model of ANN neuoron

Figure 7-1: A comparison between Biological and ANN neuron, figures adapted from [178].

The ANN data processing can be mathematically expressed using the following equation [92]:

$$y_{prd} = f\left(\sum_{i=0}^{n} w_i x_i - T\right) \qquad \text{Equation 7-1}$$

where, y_{prd} is the predicted output of the node, w_i is the weight of x_i input, T is the threshold value, is f the activation function. The activation function is usually selected according to the nature of the problem under investigation. The simplest one is the step function which is more useful for binary classification problems. While the most common function is the sigmoid function (Equation 7-2) which produces results between 0 and 1 and its curve is less sharp than step function so that the predicted results can take a range of numbers. Figure 7-2 shows the difference between the two most common activation functions; using the sigmoid function, the output can be described by the following equation [92]:

$$y_{prd} = \frac{1}{1 + e^{-\left[\sum_{i=0}^{n} w_i x_i - T\right]}} \qquad \text{Equation 7-2}$$

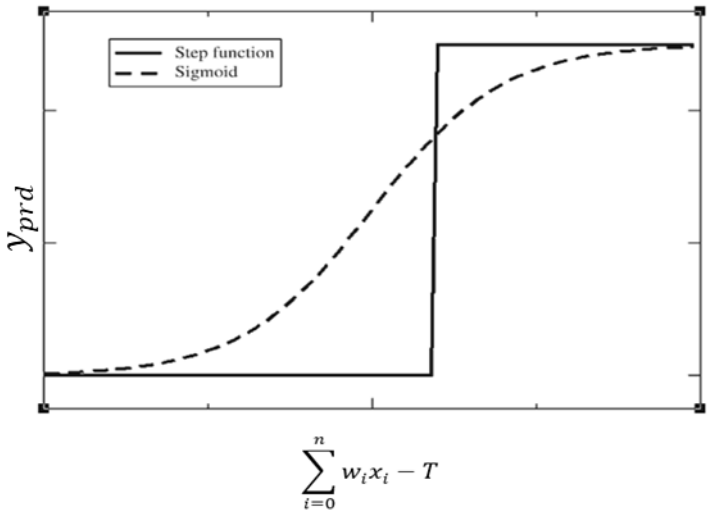

Figure 7-2: Sigmoid and step activations functions [92].

In summary, each network is characterized by three main factors:

1- Node character: this determines the signal processing by the node, which is controlled by many variables such as the number of inputs and outputs connected with the node, the weight of each input, and the activation function.

2- Network topology: In the ANN, nodes are distributed in three main layers: input, hidden and output layer (Figure 7-3). Designing a neural network involves determining the number of nodes, number hidden layers, and the way they are connected. Figure 7-3 shows the two main types of connection between nodes: feedforward connection in which the signal travels in one-way with no-loop back and feedback connection where the output of the node could be an input for another node [92].

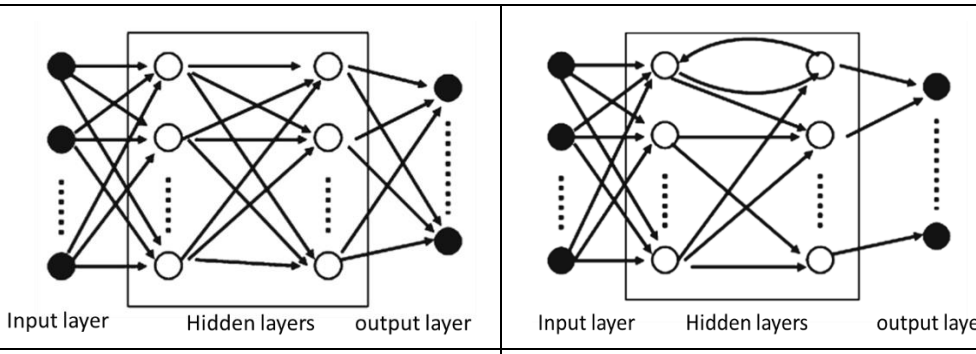

Feedforward ANN	Feedback ANN

Figure 7-3: The two main types of topologies of ANN networks [92].

3- Learning: During this stage, the available data are classified and used in three main separate processes i.e. training, validation and testing. Firstly, the training process of the network has two main categories; supervised learning (the approach used to develop neural network in this work) in which a set of examples of inputs and their associated outputs are introduced to the network; the set of inputs are used to estimate the predicted outputs, then the difference between the predicted and the target outputs are utilized in a weight adjustment process in order to minimize the error between predicted and actual output. Such a process is governed by an algorithm called backpropagation learning algorithm. Once this is performed, the adjusted weights are then utilized to re-estimate the predicted output. In the case of unsupervised learning, there is no target output, alternatively, the network will try to learn some internal features or patterns from the inputs provided. The next set of data is used to validate the trained model in a process called validation, this is to make sure that the trained model is not overtrained to the training set and developed model parameters are tuned accordingly. This step also helps in adjusting the weights associated with the inputs. The last step is the test process and is used to assess the performance of the validated model in terms of its prediction power [23,178].

7.3 Experimental

7.3.1 Method

A range of materials with different mechanical properties was roller compacted using two different roller surfaces (knurled and smooth) using a range of roller forces. The roller speed of 3 rpm and a gap distance of 2 mm were applied and kept constant throughout the whole experiments. Prior to compaction, feed powders were conditioned and analysed for their flow properties in terms of their wall and internal friction using shear cell tester. Additionally, a uniaxial compaction test was performed to determine their compressibility values. The produced ribbons were then analysed for their across the width ribbon porosity profile, and this is performed by conducting an X-ray scan at every about 3.5 mm across ribbon width (12 outputs). More details about the ribbon production and characterisation procedures can be found in Chapter-3.

7.3.2 Modelling and simulation

Matlab R2018a was utilised to develop an ANN model using the following parameters as inputs: roller force (kN), roller surface indentation depth (mm), material yield strength (MPa), effective angle of internal friction (º), angle of wall friction (º), and the compressibility factor (K). On the other hand, ribbon porosities at about every 3.5 mm across the ribbon width were considered as outputs. All input and output data are tabulated in Table A 1.

In order to improve network performance for porosity prediction, multiple inputs single-output (MISO) structure was used [179]; 12 multilayer feedforward networks with backpropagation learning algorithm (scaled conjugate gradient) were optimized for their topology [180]. Figure 7-4 depicts the ANN structure developed to predict porosity at a specific location across the ribbon width.

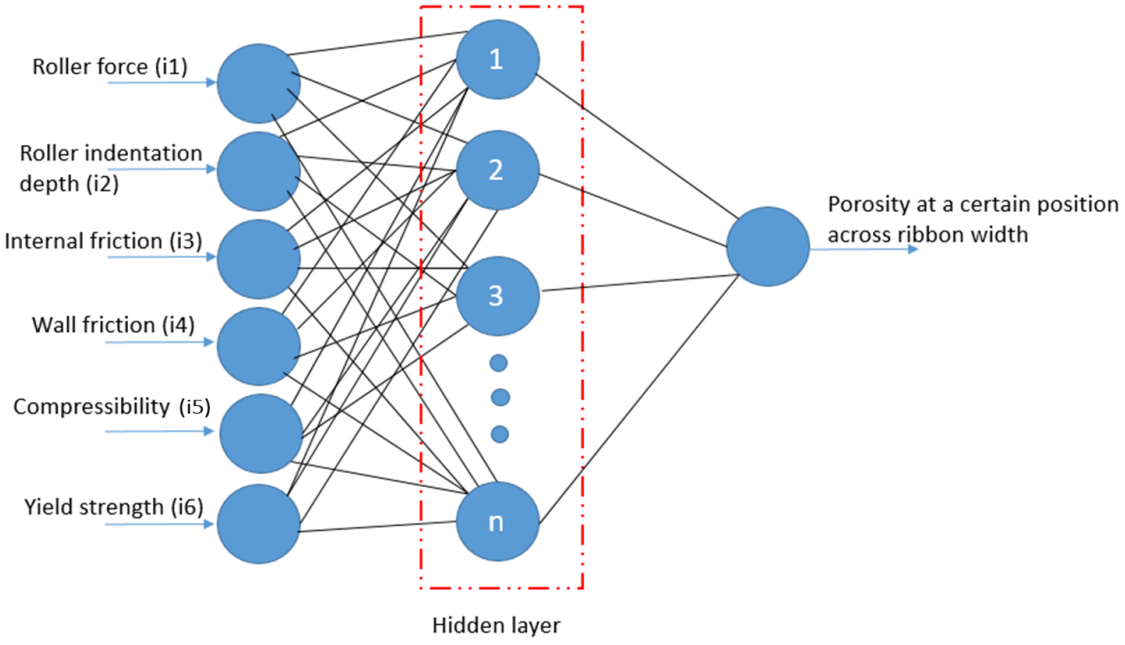

Figure 7-4: Schematic diagram of the ANN simulation process.

Each network link the inputs with one local porosity across the ribbon width. To cope with different magnitudes in the input and output data, normalisation of data were carried out according to the following formula:

$$x_n = \frac{x_i - \min(x)}{\max(x) - \min(x)}$$ Equation 7-3

where x_n is the normalised value of the input, x refers to the actual values of the inputs, and i represents the set of experimental runs.

Optimizing network topology in terms of finding the best number of hidden layers and nodes within each layer is challenging; a trial and error approach is performed to estimate the best network topology. Therefore, the number of hidden layers and nodes within each hidden layer were increased systematically, and the optimum network topology was determined according to the value of the error between actual and predicted outputs throughout all the regression results including; training, validation, and testing. This error was represented in terms of coefficient of correlation (R) which is given by the following equation:

$$R = \frac{\sum_{i=0}^{n}(x_i - \overline{x}_i)\left(y_{prd} - \overline{y_{prd}}\right)}{\sqrt{\sum_{i=0}^{n}\left((x_i - \overline{x}_i)^2\left(y_{prd} - \overline{y_{prd}}\right)^2\right)}}$$ Equation 7-4

Where $\overline{x}_i$ and $\overline{y_{prd}}$ are the means of x_i and y_{prd} respectively.

The training was performed on the developed networks, the number of nodes and layers was increased systematically to improve the prediction performance in terms of R-value. The training has proceeded in the range between 1-25 nodes on single and double hidden layer networks and the best performing network in terms of its (R-value) was selected for ribbon porosity profile prediction.

7.4 Results and Discussion

7.4.1 Statistical analysis

Simpler regression models were used in an attempt to predict porosity distribution across ribbon width. Thus, input and output data were correlated using simpler statistical tests i.e. Pearson correlation and quadratic data fitting. By definition, Pearson correlation can be used to assess the strength of the linear relationship between two numeric variables. The coefficient of this correlation (R) can take on values between -1 to +1 depending on the strength and direction of the linear relationship. The further R-value away from zero,

the stronger the linearity will be. Positive and negative R-value indicates direct and inverse relationship respectively. On the other hand, quadratic regression is the process of finding the equation of the parabola that best fit the relationship in a set of data. In this case, the closer the R-value to 1 the more accurate the fitting is.

All inputs including; roller force, angle of wall friction, angle of internal friction, powder compressibility, powder yield strength, and roller's indentation depth were correlated with one output which is the porosity at a single position across ribbon width (Table A 1). The same procedure has been repeated on all outputs. The results for both Pearson correlation and quadratic regression are shown in Figure 7-5.

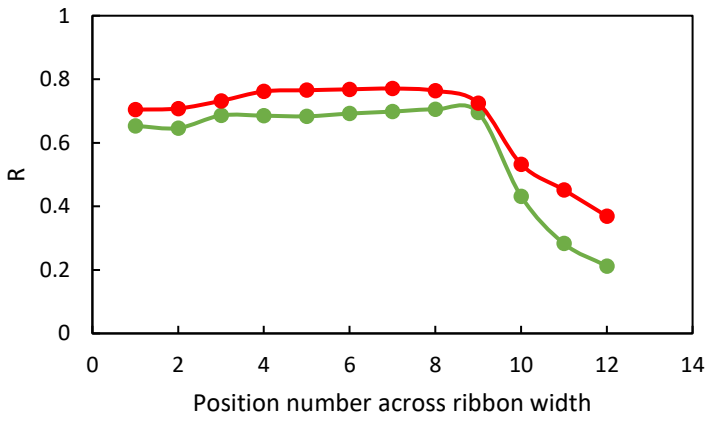

Figure 7-5: Prediction performance of Pearson correlation (green-line) and quadratic fitting (red-line).

It can be seen from the fitting results that in comparison with the Pearson correlation, the quadratic approach provided higher correlation between inputs and outputs. However, both approaches poorly prescribed the correlation in the last three points across the ribbon width, this is believed to be due to the absence of some points when narrower ribbons are analysed. In an attempt to build an improved model with higher predictability, the ANN approach has been employed.

7.4.2 Neural network topology optimization

Network consists of layers and nodes; determining the number of hidden layers is a compromise between network accuracy and generalisation. Increasing the number of hidden layers, enhance network accuracy but diminish its predictability outside the boundaries of data set. On the other hand, a lower number of hidden layer improve the generalisation of the network, but this comes at the cost of lower accuracy [23]. The 65

data sets used in this study (Table A 1) were normalised using Equation 7-3 and distributed between 3 data sets 70% for training, 15% validation, and 15% for testing. Once divided, the data was then used to model a one hidden layer network. The number of nodes in the hidden layer was increased from 1 to 25 while recording the resulted model performance in terms of (R) value. Figure 7-6 shows the performance values of these 25 hidden layer networks.

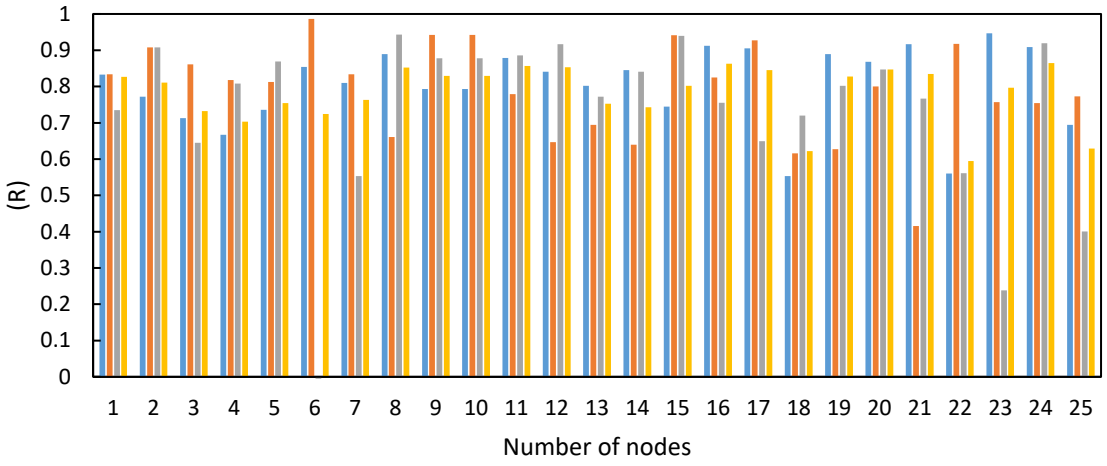

Figure 7-6: Performance of the 25- single hidden layer networks; Number of nodes was increased while recording R-value. ■ corresponds to training, ■ to validation, ■ to testing, and ■ to all.

As seen in Figure 7-6, the obtained performance values were not satisfactory, as none of these networks has high (R) values for training, validation and testing together. Considering this, an attempt was made to enhance the accuracy of the model by adding another hidden layer. Subsequently, an optimisation of the number of nodes within the two hidden layers was conducted; the number of nodes was systematically increased while monitoring its performance in terms of (R) value.

Subsequently, once the best network in terms of R-value was determined, the run was repeated for 10 times and the average predicted results were calculated accordingly. The resulted optimised networks with their regression results are shown in Table 7-1. Compared with the single hidden layer networks performance (Figure 7-6), the developed networks showed a better performance in terms of the coefficient of correlation (R). The results showed that adding another hidden layer is advantageous for making more accurate and robust ANN.

Table 7-1: Optimum neural network topologies for process simulation and their regression results.

Output No	Network topology	Regression results (R)			
		Test	Validation	Training	All
1	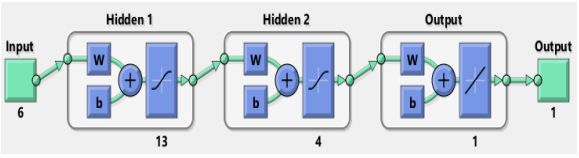	0.91	0.92	0.93	0.91
2	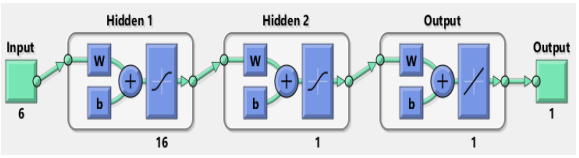	0.95	0.96	0.96	0.95
3	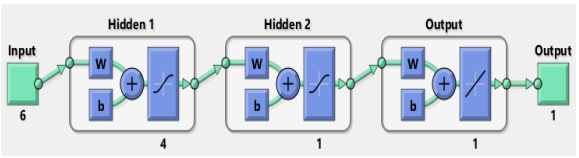	0.96	0.96	0.95	0.96
4	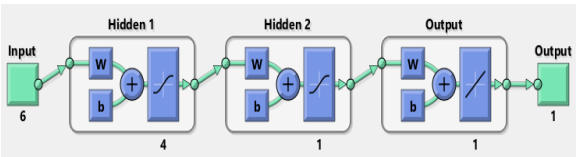	0.94	0.95	0.94	0.94
5	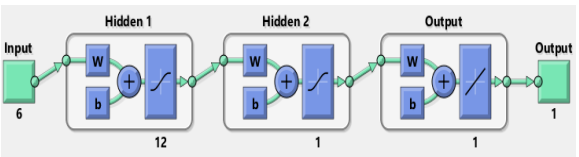	0.99	0.95	0.98	0.98
6	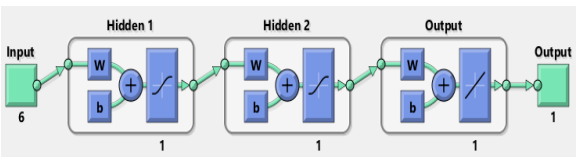	0.93	0.96	0.96	0.94
7	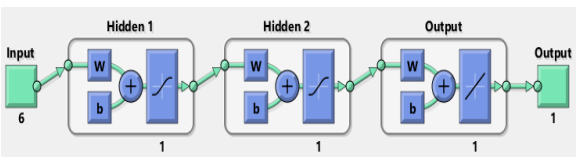	0.96	0.95	0.94	0.95
8	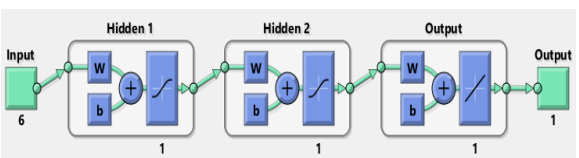	0.97	0.96	0.94	0.96
9	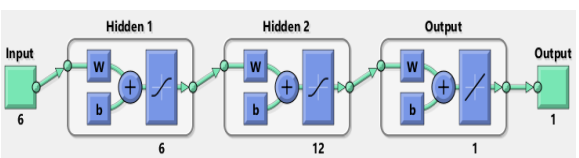	0.96	0.97	0.97	0.95

10	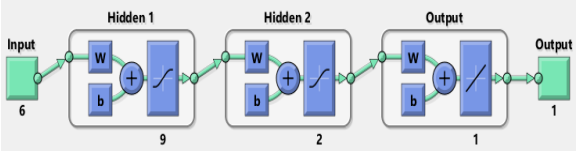	0.93	0.94	0.94	0.93
11	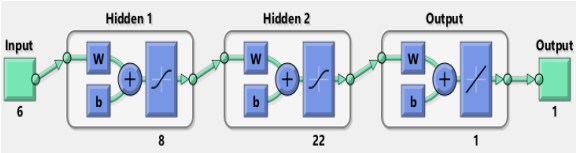	0.9	0.93	0.91	0.9
12	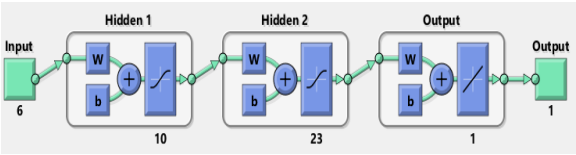	0.91	0.94	0.9	0.91

Figure 7-7 shows an example of fitting 65 data sets for ribbon porosity at about 17.5 mm from ribbon edge; 45 data sets were used for training, 10 data sets for validation and 10 datasets for testing. The figure also shows the performance results (R-value) of the optimum network. The regression results of fitting porosity values at the rest of the positions across the ribbon width are shown in Figure A 6.

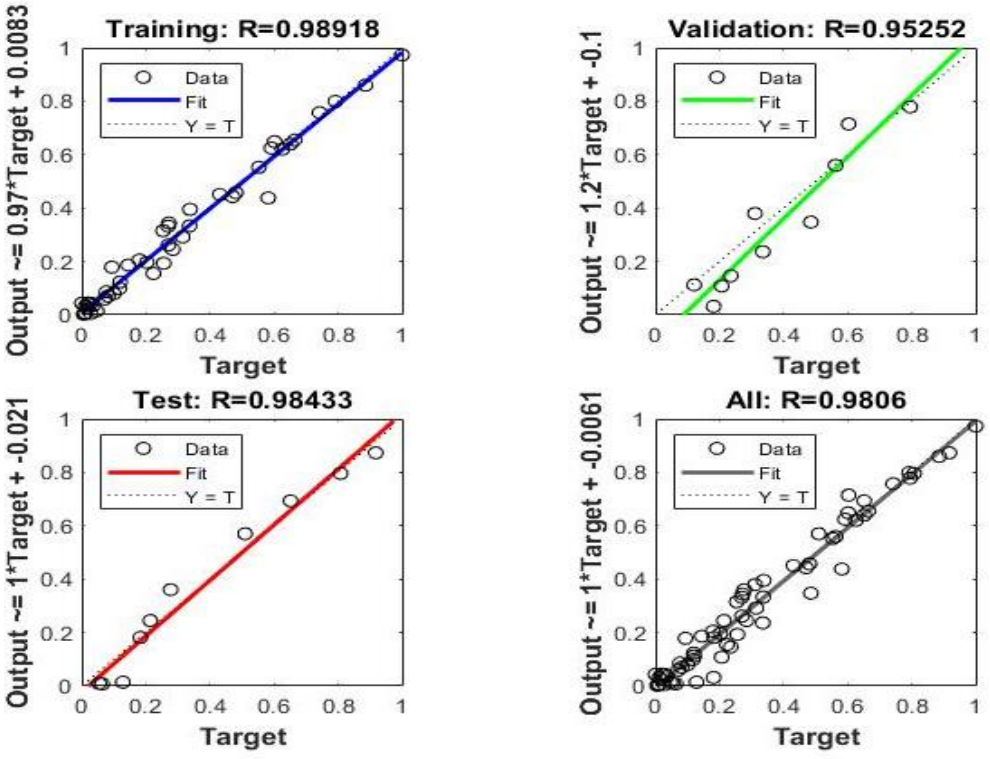

Figure 7-7: Regression results of fitting porosity results at position 5 (output 5) across ribbon width

7.4.3 Prediction results

The predicted results developed by ANN were compared with the actual experimental results to evaluate the accuracy of the networks in predicting porosity across ribbon width. Figure 7-8 and Figure 7-9 show a comparison example between the predicted (de-normalised using Equation 7-3) and experimentally measured ribbon porosity profiles for the six different materials used in this study, this is for ribbons produced using the two different pairs of rollers i.e. knurled and smooth rollers at 20.72 kN roller force. The rest of the prediction results are tabulated in Table A 2.

The developed model successfully predicted porosity distribution across ribbon width; as presented in Figure 7-8 and Figure 7-9, a high degree of matching could be observed between predicted and experimentally measured results for almost all cases. However, a high variation between predicted and experimental results can be observed for maltodextrin ribbons which were produced using smooth rollers (Figure 7-8). This could be referred to the thermal sensitivity of this material as it is expected to melt at a relatively low temperature ($Tg \simeq 81°C$)[113]. This matched with the observations of ribbon sticking at equivalent processing conditions (Table 4-4). In extending the current work for better predictability, a material thermal property such as melting point or glass transition temperature could be combined with the model inputs to cover any temperature effect developed upon stress application. Once developed, the ANN model can be used to predict the effect of various process and material parameters on the heterogeneity of porosity across ribbon width. To the best of our knowledge, the application of ANN to predict porosity distribution homogeneity has not been reported yet.

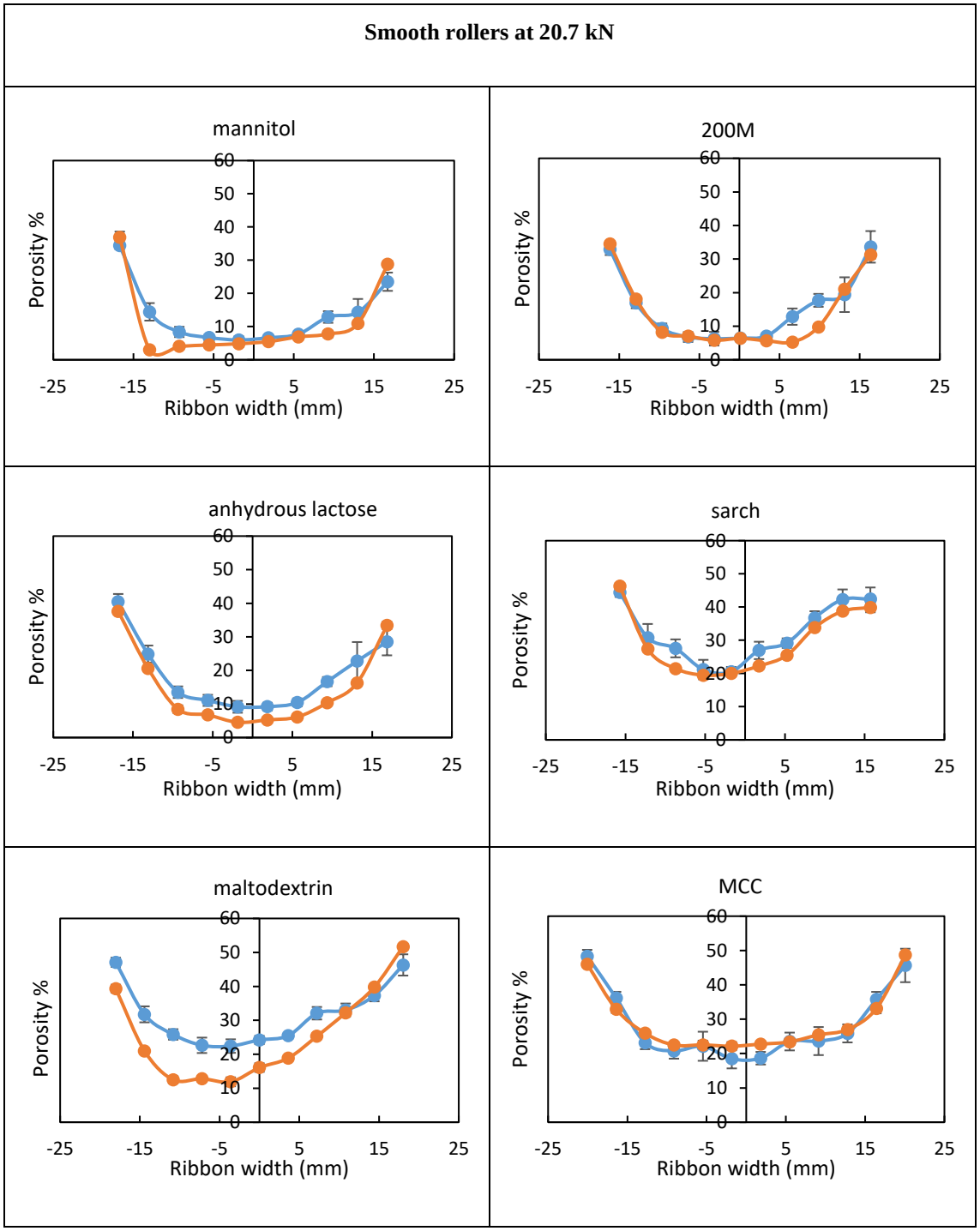

Figure 7-8: Predicted and experimentally measured ribbon porosity distribution across ribbon width for ribbons produced at 20.72 kN roller force using smooth rollers. The blue line represents predicted values and the orange line for the X-ray measured results.

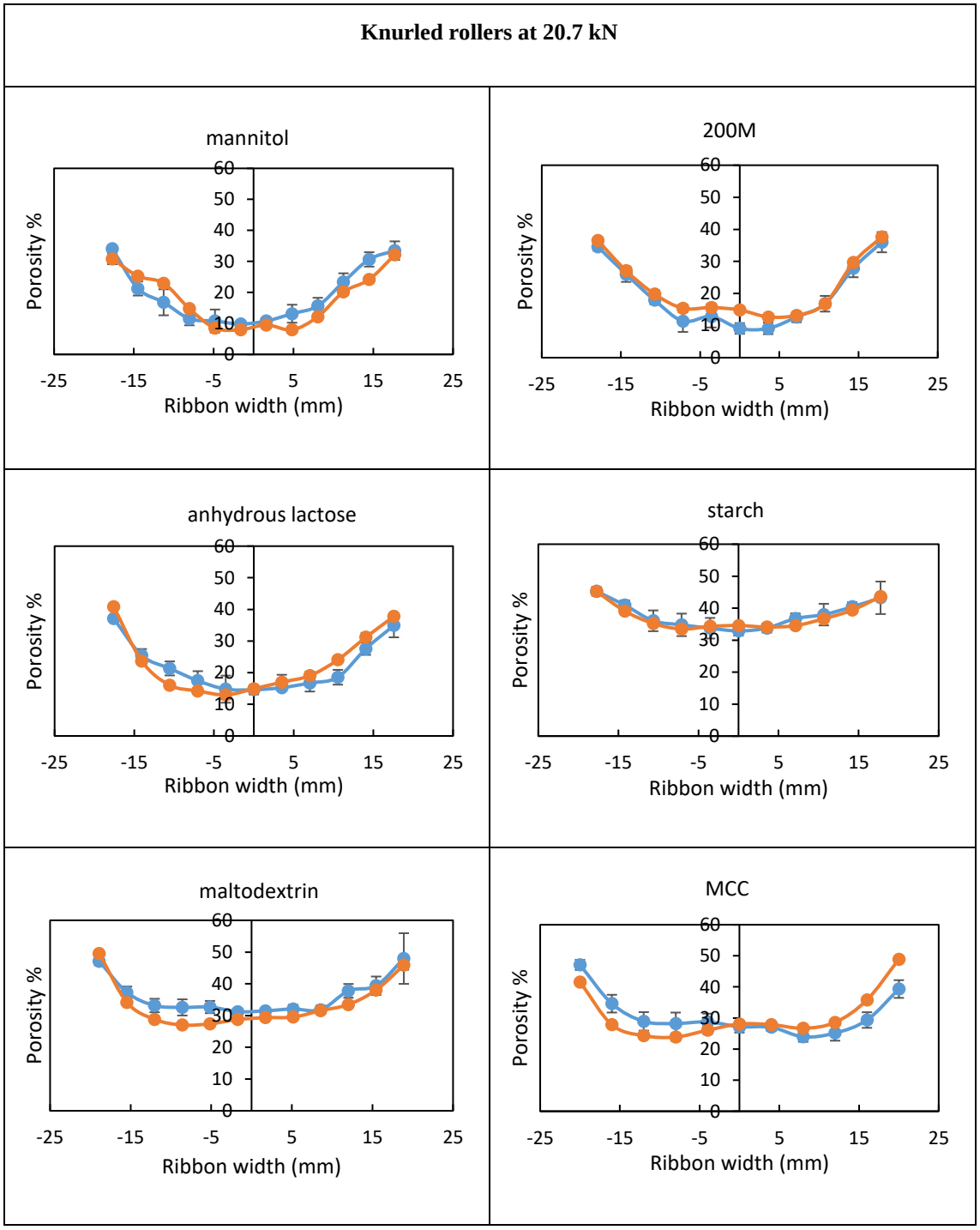

Figure 7-9: Predicted and experimentally measured ribbon porosity distribution across ribbon width for ribbons produced at 20.72 kN roller force using knurled rollers. Blueline represents predicted values and the orange line for the X-ray measured results.

7.5 Conclusions

ANN model was successfully developed to predict porosity distribution across ribbon width. A series of 12 networks were optimised for the best topology and used to link various material and process parameters with experimentally measured ribbon porosity at different positions across ribbon width. The developed model showed high robustness, accuracy, and low processing time so it can be implemented in the manufacturing controlling system to predict and control ribbon porosity heterogeneity during processing.

In agreement with theoretically develop model, ANN developed model could also be used improve our understanding about the effect of different material and processing parameters on the heterogeneity of the produced ribbons which is one of the most important ribbon quality attributes. This revealed that the developed ANN model is an attractive tool for the design, optimisation, and scale-up of the roller compaction process, applicable to the pharmaceutical processing for the achievement of quality-by-design approach in this industry.

CHAPTER 8 GENERAL CONCLUSIONS AND FUTURE WORK

8.1 Conclusions

The phenomenon of ribbon splitting/sticking during roller compaction was investigated in a comprehensive perspective. Both longitudinal and transversal splitting have been mapped for their occurrence as a function of yield strength and maximum applied stress during smooth roller mediated roller compaction. Subsequently, the observed trends of splitting were rationalised in terms of a splitting index, which is a measure of the stored elastic ener gy driving fracture relative to the fracture stress of the ribbons. The splitting index leads to a trend of decreasing no splitting and increasing longitudinal splitting as the values of this parameter increases. However, the index did not mechanistically interpret the occurrence of transversal splitting as increasing the index lead to a lower occurrence of the transversal splitting. This could be due to the index not taking into account the role of adhesion acting on the ribbons. The observed trend of splitting was also rationalised in terms of the ratio of roll stress/powder yield strength. An increase in its value is an indication for a higher level of bonding to occur which could overcome the adhesion to roller surface and reduce the occurrence transversal splitting. However, higher values indicate more elastic recovery which can cause longitudinal splitting at certain levels.

This approach of analysis is a useful means of categorising the data for transversal and longitudinal splitting. However, in practice, the feed powders are generally multi-component and the formulation could contain a variety of excipients, APIs and lubricants, therefore there is a need to investigate its effect on the splitting occurrence and applicability of splitting index prediction.

A similar map has been developed using knurled rollers; the map showed an increase in the probability of transversal splitting/roller sticking when compared to the smooth rollers and reduction in the occurrence of longitudinal splitting. The incorporation of solid fraction heterogeneity factor in the splitting index successfully enhanced the predictability for splitting initiation.

Powder/metal interaction was further investigated using inverse gas chromatography to determine the surface energy of the feed powders and steel (roller surface), this was conducted in an attempt to determine if there is any preferential intermolecular interaction between the steel surface and the compacted powder that could lead to ribbon sticking/transversal splitting on the roller surface. No clear correlation between the work of adhesion/cohesion and sticking probability was found which suggests that particle deformation/contact area is a dominant factor in sticking during compaction. However, the results could contribute to the elaboration of the lubrication mechanism of MgSt during powder compaction as MgSt tends to interact more preferentially with the steel when compared to the other possible surface interactions.

The work also investigated the use of ANN to predict the porosity distribution across ribbon width which is a critical factor for the longitudinal splitting occurrence. To benefit from the contribution of this approach, the constitution of a large database on material properties is useful. ANN model was successfully developed to predict porosity distribution across ribbon width. The developed model showed high robustness and accuracy so that it could be implemented in the manufacturing controlling system to predict and control ribbon porosity heterogeneity during processing.

8.2 Future work

1- It was shown in chapter-4 that transversal splitting/sticking is more noticeable with brittle materials, this was attributed to the insufficient bonding/deformation across ribbon thickness to overcome the adhesion to the roller surface. Using spherical particles such as PMMA (Viscoelastic in nature) could help to investigate the different extents of breakage across ribbon dimensions.

2- It was shown in chapter-5 that the longitudinal splitting is affected by the heterogeneity of density distribution across ribbon width. It is also of interest to investigate the effect of improving the homogeneity of density distribution as a mitigating approach to the occurrence of longitudinal splitting. This can be conducted using curved rollers [181] or feeding guiders [13].

3- The work involved in chapter-6 showed the thermodynamic work of cohesion/adhesion is not significant in predicting the sticking behaviour of the materials after stress application. Therefore, there is a need to compliment the trend of energies of interaction by taking the change in contact surface area after compaction into account. This could be done by computational modelling such as DEM. The increase in contact surface areas as a result of plastic deformation and fragmentation affect the extent of particle bonding whether it was between the powder particles such as (2, 3, and 4 Figure 8-1) or between the powder particles and touching metal surface (1-Figure 8-1). During compaction, the stress distribution will always be maximum on the powder/metal interface and this will cause a higher contact surface area and a higher degree of adhesion with the metal surface unless the summation of the contact surface areas with the neighbouring particles is higher (i.e. 2+3+4 > 1). In this case, the particle will detach from the metal surface.

As it is difficult to model the inter-particle forces using continuum models and at the same time it is difficult to handle fragmentation of particles using DEM, in the future work the particle will be treated as an assembly of small cohesive powder particles in order to deal with particle fragmentation using DEM.

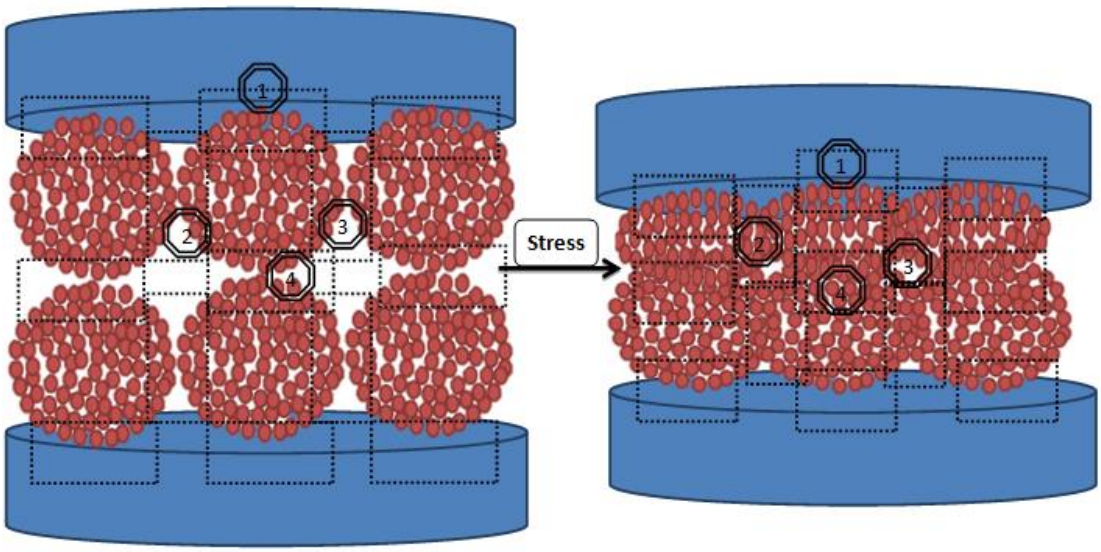

Figure 8-1: Schematic representation of the particle deformation and the increase in contact surface area upon stress application.

4- The work involved in chapter-6 investigated the thermodynamic interaction between powder particles and steel (roller surface) for any possible correlation with sticking tendency during roller compaction. It would be of interest to investigate powder/metal interaction using different metallic alloys with a range of surface energies.

REFERENCES

[1] M. Jivraj, L.G. Martini, C.M. Thomson, An overview of the different excipients useful for the direct compression of tablets, Pharmaceutical Science and Technology Today. 3 (2000) 58–63.

[2] R.W. Miller, Roller Compaction Technology, in: D.M. Parikh (Ed.), Handbook of Pharmaceutical Granulation Technology, 2nd ed., Taylor & Francis Group, North Calorina: Boca Raton, 2005.

[3] P. Guigon, O. Simon, K. Saleh, G. Bindhumadhavan, M.J. Adams, J.P.K. Seville, Roll Pressing, in: A.D. Salman, M.J. Hounslow, J.P.K. SevillE (Eds.), Handbook of Powder Technology-Granulation, Elsevier, Amsterdam, 1996.

[4] G. Peck, J.P. Soh, K. Morris, Dry Granulation, in: S.W.H. Larry L. Augsburger (Ed.), Pharmaceutical Dosage Forms - Tablets, CRC Press, Boca Raton, 2008.

[5] J.C. Cunningham, Experimental studies and modeling of the roller compaction of pharmaceutical powders. PhD Thesis, Drexel University, 2005.

[6] P. Kleinebudde, Roll compaction/dry granulation: Pharmaceutical applications, European Journal of Pharmaceutics and Biopharmaceutics. 58 (2004) 317–326.

[7] G. Reynolds, R. Ingale, R. Roberts, S. Kothari, B. Gururajan, Practical application of roller compaction process modeling, Computers and Chemical Engineering. 34 (2010) 1049–1057.

[8] J. Osborne, Bonding Mechanisms Involved in the Roller Compaction of an Amorphous Food Material. PhD Thesis., The Uniersity of Sheffield, 2013.

[9] S. Malkowska, K. a. Khan, R. Lentle, J. Marchant, G. Elger, Effect of Re-Compression on the Properties of Tablets Prepared by Moist Granulation, Drug Development and Industrial Pharmacy. 9 (1983) 349–361.

[10] C. Sun, M.W. Himmelspach, Reduced tabletability of roller compacted granules as a result of granule size enlargement, Journal of Pharmaceutical Sciences. 95 (2006) 200–206.

[11] P. Guigon, O. Simon, Roll press design - Influence of force feed systems on compaction, Powder Technology. 130 (2003) 41–48.

[12] A. Michrafy, H. Diarra, J.A. Dodds, M. Michrafy, Experimental and numerical analyses of homogeneity over strip width in roll compaction, Powder Technology. 206 (2011) 154–160.

[13] M. Yu, C. Omar, A. Schmidt, J.D. Litster, A.D. Salman, Improving feeding powder distribution to the compaction zone in the roller compaction, European Journal of Pharmaceutics and Biopharmaceutics. 128 (2018) 57–68.

[14] O. Mahmah, M.J. Adams, C.S. Omar, B. Gururajan, A.D. Salman, Roller compaction: Ribbon splitting and sticking, International Journal of Pharmaceutics. 559 (2019) 156–172.

[15] I. Akseli, N. Ladyzhynsky, J. Katz, X. He, Development of predictive tools to assess capping tendency of tablet formulations, Powder Technology. 236 (2013) 139–148.

[16] B.C. Hancock, A.C. Bentham, A. Mills, G.E. Amidon, R. Cameron, S. Best, L.H. Han, J. Elliott, Numerical Simulation on Pharmaceutical Powder Compaction, Materials Science Forum. 575–578 (2009) 560–565.

[17] I.C. Sinka, J.C. Cunningham, A. Zavaliangos, Analysis of tablet compaction. II. Finite element analysis of density distributions in convex tablets, Journal of Pharmaceutical Sciences. 93 (2004) 2040–2053.

[18] J. Dawes, C. Allenspach, J.F. Gamble, R. Greenwood, P. Robbins, M. Tobyn, Application of external lubrication during the roller compaction of adhesive pharmaceutical formulations, Pharmaceutical Development and Technology. 18 (2012) 1–11.

[19] I. Saniocki, New Insights into Tablet Sticking : Characterization and Quantification of Sticking to Punch Surfaces during Tablet Manufacture by Direct Compaction. PhD thesis., University of Hamburg, 2014.

[20] J. V Thomas, Evaluation and study on the adhesion of powder onto punch faces during tablet compaction. PhD Thesis., Drexel University, 2015.

[21] R.B. Al Asady, NRoller compaction: Mechanical Properties of Primery Particles, Pre-compacted Body and Ribbon. PhD Thesiso Title, The University of Sheffield, 2016.

[22] H. Rumpf, The strength of granules and agglomerates, in: Knepper WA (Ed.), Agglomeration, John Wiley and Sons, New York, 1962: p. 379.

[23] G. Buckton, Pharmaceutical Powder Compaction Technology, in: M. Çelik (Ed.), Informa, North Carolina, 2016.

[24] G. Buckton, Aulton's Pharmaceutics: The Design and Manufacture of Medicines, in: M.E. Aulton, K. Taylor (Eds.), 4th ed., Elsevier, Edinbugh: Churchill Livingstone, 2013.

[25] J.J. Wang, M. a. Guillot, S.D. Bateman, K.R. Morris, Modeling of Adhesion in Tablet Compression. II. Compaction Studies Using a Compaction Simulator and an Instrumented Tablet Press, Journal of Pharmaceutical Sciences. 93 (2004) 407–417.

[26] F. Waimer, M. Krumme, P. Danz, U. Tenter, P.C. Schmidt, A novel method for the detection of sticking of tablets., Pharmaceutical Development and Technology. 4 (1999) 359–367.

[27] I.M. Hamdan, G. V. Reklaitis, V. Venkatasubramanian, Exceptional events management applied to roller compaction of pharmaceutical powders, Journal of Pharmaceutical Innovation. 5 (2010) 147–160.

[28] J. Dawes, J.F. Gamble, R. Greenwood, P. Robbins, M. Tobyn, An investigation into the impact of magnesium stearate on powder feeding during roller compaction., Drug Development and Industrial Pharmacy. 38 (2012) 111–22.

[29] Na. Armstrong, Lubricants, Glidants and Antiadherents, in: S.W.H. Larry L. Augsburger (Ed.), Pharmaceutical Dosage Forms - Tablets, Third Edition, CRC Press, Raton, Boca, 2008.

[30] N. Rasenack, B.W. Müller, Crystal habit and tableting behavior, International Journal of Pharmaceutics. 244 (2002) 45–57.

[31] K. Kakimi, T. Niwa, K. Danjo, Influence of compression pressure and die-wall

pressure on tablet sticking, Chemical & Pharmaceutical Bulletin. 131 (2011) 597–601.

[32] K. Danjo, K. Kamiya, A. Otsuka, Effect of Temperature on the Sticking of Low Melting Point Materials, Chemical & Pharmaceutical Bulletin. 41 (1993) 1423–1427.

[33] K. Danjo, S. Kojima, cheng Y. Chen, H. Sunada, Effect of Water Content on Sticking during Compression, Chemical & Pharmaceutical Bulletin. 45 (1997).

[34] Fridrun Podczeck, Fuundimental of adhesion of particles to surfaces, in: F. Podczeck (Ed.), Particle-Particle Adhesion in Pharmaceutical Powder Handling, Iimperial College Press, London, 1998.

[35] S. Berbner, F. Löffler, Influence of high temperatures on particle adhesion, Powder Technology. 78 (1994) 273–280.

[36] K. Toyoshima, M. Yasumura, N. Ohnishi, Y. Ueda, Quantitative evaluation of tablet sticking by surface roughness measurement, International Journal of Pharmaceutics. 46 (1988) 211–215.

[37] S. Paul, K. Wang, L.J. Taylor, B. Murphy, J. Krzyzaniak, N. Dawson, M.P. Mullarney, P. Meenan, C.C. Sun, Dependence of Punch Sticking on Compaction Pressure—Roles of Particle Deformability and Tablet Tensile Strength, Journal of Pharmaceutical Sciences. 106 (2017) 2060–2067.

[38] T. Gengenbach, K.P. Hapgood, J.A. Denman, Q. (Tony) Zhou, D.A. V. Morton, M. Gamlen, P.J. Stewart, L. Qu, Investigation of the potential for direct compaction of a fine ibuprofen powder dry-coated with magnesium stearate, Drug Development and Industrial Pharmacy. 41 (2014) 825–837.

[39] S. Chattoraj, P. Daugherity, T. McDermott, A. Olsofsky, W.J. Roth, M. Tobyn, Sticking and Picking in Pharmaceutical Tablet Compression: An IQ Consortium Review, Journal of Pharmaceutical Sciences. 107 (2018) 2267–2282.

[40] A.P. Association, Tableting Specification Manual, 5th ed., American pharmacist association, Washington, D.C, 2001.

[41] N. Souihi, G. Reynolds, P. Tajarobi, H. Wikström, G. Haeffler, M. Josefson, J.

Trygg, Roll compaction process modeling: Transfer between equipment and impact of process parameters, International Journal of Pharmaceutics. 484 (2015) 192–206.

[42] E. Hadzovic, Roller Compaction of Theophylline. PhD Thesis., The University of Basel, 2008.

[43] F. Waimer, M. Krumme, P. Danz, U. Tenter, P.C. Chmidt, The Influence of Engravings on the Sticking of Tablets. Investigations with an Instrumented Upper Punch, Pharmaceutical Development and Technology. 4 (2002) 369–375.

[44] M. Roberts, J.L. Ford, G.S. MacLeod, J.T. Fell, G.W. Smith, P.H. Rowe, Effects of surface roughness and chrome plating of punch tips on the sticking tendencies of model ibuprofen formulations., The Journal of Pharmacy and Pharmacology. 55 (2003) 1223–1228.

[45] R.B. Al-Asady, J.D. Osborne, M.J. Hounslow, A.D. Salman, Roller compactor: The effect of mechanical properties of primary particles., International Journal of Pharmaceutics. 496 (2015) 124–136.

[46] S. Abdel-hamid, G. Betz, A novel tool for the prediction of tablet sticking during high speed compaction, Pharmaceutical Development and Technology. 17 (2012) 747–754.

[47] J.R. Johanson, A Rolling Theory for Granular Solids, Journal of Applied Mechanics. 32 (1965) 842.

[48] J. Li, Y. Wu, Lubricants in Pharmaceutical Solid Dosage Forms, Lubricants. 2 (2014) 21–43.

[49] M.P. Mullarney, bruce C. MacDonald, A. Hutchins, Assessing Tablet-Sticking Propensity: weighing accumulated powder on a removable punch tip, Pharmaceutical Technology. 36 (2012) 57–62.

[50] T.S. McDermott, J. Farrenkopf, A. Hlinak, J.P. Neilly, D. Sauer, A material sparing method for quantitatively measuring tablet sticking, Powder Technology. 212 (2011) 240–252.

[51] M. Roberts, J.L. Ford, G.S. MacLeod, J.T. Fell, G.W. Smith, P.H. Rowe, A.M.

Dyas, Effect of lubricant type and concentration on the punch tip adherence of model ibuprofen formulations, Journal of Pharmacy and Pharmacology. 56 (2004) 299–305.

[52] S.R. Bechard, G.R.B. Down, Infrared Imaging of Pharmaceutical Materials Undergoing Compaction, Pharmaceutical Research. 9 (1992) 521–528.

[53] S. Esezobo, N. Pilpel, The effect of temperature on the plasto-elasticity of some pharmaceutical powders and on the tensile strengths of their tablets, Journal of Pharmacy and Pharmacology. 38 (1986) 409–413.

[54] A. Zavaliangos, S. Galen, J. Cunningham, D. Winstead, Temperature Evolution during Compaction of Pharmaceutical Powders, Journal of Pharmaceutical Sciences. 97 (2007).

[55] M. Cespi, G. Bonacucina, L. Casettari, S. Ronchi, G.F. Palmieri, Effect of temperature increase during the tableting of pharmaceutical materials, International Journal of Pharmaceutics. 448 (2013) 320–326.

[56] C.S. Omar, M.J. Hounslow, A.D. Salman, Implementation of an online thermal imaging to study the effect of process parameters of roller compactor, Drug Delivery and Translational Research. 8 (2018) 1604–1614.

[57] R. Wiedey, P. Kleinebudde, Potentials and limitations of thermography as an in-line tool for determining ribbon solid fraction, Powder Technology. 341 (2019) 2–10.

[58] S.K. Dwivedi, R.J. Oates, A.G. Mitchell, Estimation of Elastic Recovery, Work of Decompression and Young's Modulus Using a Rotary Tablet Press, Journal of Pharmacy and Pharmacology. 44 (1992) 459–466.

[59] C.-Y. Wu, O.M. Ruddy, A.C. Bentham, B.C. Hancock, S.M. Best, J.A. Elliott, Modelling the mechanical behaviour of pharmaceutical powders during compaction, Powder Technology. 152 (2005) 107–117.

[60] V. Mazel, V. Busignies, H. Diarra, P. Tchoreloff, Lamination of pharmaceutical tablets due to air entrapment: Direct visualization and influence of the compact thickness, International Journal of Pharmaceutics. 478 (2015) 702–704.

[61] I. Akseli, D. Dey, C. Cetinkaya, Mechanical Property Characterization of Bilayered Tablets using Nondestructive Air-Coupled Acoustics, American Association of Pharmaceutical Scientists. 11 (2010) 90–102.

[62] C.Y. Wu, W.L. Hung, A.M. Miguélez-Morán, B. Gururajan, J.P.K. Seville, Roller compaction of moist pharmaceutical powders, International Journal of Pharmaceutics. 391 (2010) 90–97.

[63] M.T.A. Ende, S.K. Moses, A.J. Carella, R.A. Gadkari, T.W. Graul, A.L. Otano, R.J. Timpano, Improving the content uniformity of a low-dose tablet formulation through roller compaction optimization, Pharmaceutical Development and Technology. 12 (2007) 391–404.

[64] J.C. Cunningham, D. Winstead, A. Zavaliangos, Understanding variation in roller compaction through finite element-based process modeling, Computers and Chemical Engineering. 34 (2010) 1058–1071.

[65] M.P. Mullarney, B.C. Hancock, Mechanical property anisotropy of pharmaceutical excipient compacts, International Journal of Pharmaceutics. 314 (2006) 9–14.

[66] S. Paul, C.C. Sun, Gaining insight into tablet capping tendency from compaction simulation, International Journal of Pharmaceutics. 524 (2017) 111–120.

[67] R. Kuppuswamy, S.R. Anderson, L.L. Augsburger, S.W. Hoag, Estimation of capping incidence by indentation fracture tests, American Association of Pharmaceutical Scientists. 3 (2003) 54–65.

[68] F. Ebba, P. Piccerelle, P. Prinderre, D. Opota, J. Joachim, Stress relaxation studies of granules as a function of different lubricants, European Journal of Pharmaceutics and Biopharmaceutics. 52 (2001) 211–220.

[69] J. Mosig, P. Kleinebudde, Evaluation of lubrication methods: How to generate a comparable lubrication for dry granules and powder material for tableting processes, Powder Technology. 266 (2014) 156–166.

[70] J. Wang, H. Wen, D. Desai, Lubrication in tablet formulations, European Journal of Pharmaceutics and Biopharmaceutics. 75 (2010) 1–15.

[71] H. Takeuchi, S. Nagira, M. Aikawa, H. Yamamoto, Y. Kawashima, Effect of

lubrication on the compaction properties of pharmaceutical excipients as measured by die wall pressure, Journal of Drug Delivery Science and Technology. 15 (2015) 177–182.

[72] Z.T. Chowhan, L.H. Chi, Drug-excipient interactions resulting from powder mixing IV: Role of lubricants and their effect on in vitro dissolution, Journal of Pharmaceutical Sciences. 75 (1986) 542–545.

[73] K. Zuurman, K.V. der V. Maarschalk, G.K. Bolhuis, Effect of magnesium stearate on bonding and porosity expansion of tablets produced from materials with different consolidation properties, 179 (1999) 107–115.

[74] S.M. Dudhat, C.N. Kettler, R.H. Dave, To Study Capping or Lamination Tendency of Tablets Through Evaluation of Powder Rheological Properties and Tablet Mechanical Properties of Directly Compressible Blends, American Association of Pharmaceutical Scientists. 18 (2016) 1177–1189.

[75] I. Akseli, A. Stecuła, X. He, N. Ladyzhynsky, Quantitative correlation of the effect of process conditions on the capping tendencies of tablet formulations, Journal of Pharmaceutical Sciences. 103 (2014) 1652–1663.

[76] S. Inghelbrecht, J.P. Remon, P. Fernandes De Aguiar, B. Walczak, D.L. Massart, F. Van De Velde, P. De Baets, H. Vermeersch, P. De Backer, Instrumentation of a roll compactor and the evaluation of the parameter settings by neural networks, International Journal of Pharmaceutics. 148 (1997) 103–115.

[77] A. Gupta, G.E. Peck, R.W. Miller, K.R. Morris, Effect of the variation in the ambient moisture on the compaction behavior of powder undergoing roller-compaction and on the characteristics of tablets produced from the post-milled granules, Journal of Pharmaceutical Sciences. 94 (2005) 2314–2326.

[78] J.D. Osborne, T. Althaus, L. Forny, G. Niederreiter, S. Palzer, M.J. Hounslow, A.D. Salman, Investigating the influence of moisture content and pressure on the bonding mechanisms during roller compaction of an amorphous material, Chemical Engineering Science. 86 (2013) 61–69.

[79] A. Gupta, G.E. Peck, R.W. Miller, K.R. Morris, Nondestructive Measurements of the Compact Strength and the Particle-Size Distribution after Milling of Roller

Compacted Powders by Near-Infrared Spectroscopy, Journal of Pharmaceutical Sciences. 93 (2004) 1047–1053.

[80] C.Y. Wu, B.C. Hancock, A. Mills, A.C. Bentham, S.M. Best, J.A. Elliott, Numerical and experimental investigation of capping mechanisms during pharmaceutical tablet compaction, Powder Technology. 181 (2008) 121–129.

[81] P.D. Daugherity, J.H. Chu, Investigation of serrated roll surface differences on ribbon thickness during roller compaction., Pharmaceutical Development and Technology. 12 (2007) 603–608.

[82] K. Csordas, R. Wiedey, P. Kleinebudde, Impact of roll compaction design, process parameters, and material deformation behaviour on ribbon relative density, Drug Development and Industrial Pharmacy. 44 (2018) 1295–1306.

[83] G. Bindhumadhavan, J.P.K. Seville, M.J. Adams, R.W. Greenwood, S. Fitzpatrick, Roll compaction of a pharmaceutical excipient: Experimental validation of rolling theory for granular solids, Chemical Engineering Science. 60 (2005) 3891–3897.

[84] R.T. Dec, A. Zavaliangos, J.C. Cunningham, Comparison of various modeling methods for analysis of powder compaction in roller press, Powder Technology. 130 (2003) 265–271.

[85] B.A. Patel, M.J. Adams, N. Turnbull, A.C. Bentham, C.Y. Wu, Predicting the pressure distribution during roll compaction from uniaxial compaction measurements, Chemical Engineering Journal. 164 (2010) 410–417.

[86] M.J. Adams, M.A. Mullier, J.P.K. Seville, Agglomerate strength measurement using a uniaxial confined compression test, Powder Technology. 78 (1994) 5–13.

[87] T.M. Nejad, C. Foster, D. Gongal, Finite element modelling of cornea mechanics: A review, Arquivos Brasileiros de Oftalmologia. 77 (2014) 60–65.

[88] A. Michrafy, H. Diarra, J.A. Dodds, M. Michrafy, L. Penazzi, Analysis of strain stress state in roller compaction process, Powder Technology. 208 (2011) 417–422.

[89] A.R. Muliadi, J.D. Litster, C.R. Wassgren, Modeling the powder roll compaction process: Comparison of 2-D finite element method and the rolling theory for

granular solids (Johanson's model), Powder Technology. 221 (2012) 90–100.

[90] A. Mazor, L. Orefice, A. Michrafy, A. de Ryck, J.G. Khinast, A combined DEM & FEM approach for modelling roll compaction process, Powder Technology. 337 (2018) 3–16.

[91] K. Odagi, T. Tanaka, Y. Tsuji, Compressive Flow Property of Powder in Roll-type Presses, Journal of the Society of Powder Technology. 38 (2001) 150–159.

[92] J. Zou, Y. Han, S.-S. So, Overview of Artificial Neural Networks, in: David J. Lvingstone (Ed.), Artificial Neural Networks: Methods and Applications, Humana Press, Sandown, 2009.

[93] M. Turkoglu, I. Aydin, M. Murray, A. Sakr, Modeling of a roller-compaction process using neural networks and genetic algorithms, European Journal of Pharmaceutics and Biopharmaceutics. 48 (1999) 239–45.

[94] M. Sajjia, S. Shirazian, C.B. Kelly, A.B. Albadarin, G. Walker, ANN Analysis of a Roller Compaction Process in the Pharmaceutical Industry, Chemical Engineering and Technology. 40 (2017) 487–492.

[95] Y.A. Yusof, A.C. Smith, B.J. Briscoe, Roll compaction of maize powder, Chemical Engineering Science. 60 (2005) 3919–3931.

[96] N. Armstrong, Handbook Pharmaceutical Excipients, Sixth Edition, in: R.C. Rowe, P.J. Sheskey, M.E. Quinn (Eds.), Pharmaceutical Press, London, 2009.

[97] M.G. Cares-Pacheco, G. Vaca-Medina, R. Calvet, F. Espitalier, J.J. Letourneau, A. Rouilly, E. Rodier, Physicochemical characterization of d-mannitol polymorphs: The challenging surface energy determination by inverse gas chromatography in the infinite dilution region, International Journal of Pharmaceutics. 475 (2014) 69–81.

[98] K.D. Foster, The prediction of sticking in dairy powders. PhD Thesis., Massey University, 2002.

[99] C.S. Omar, R.M. Dhenge, J.D. Osborne, T.O. Althaus, S. Palzer, M.J. Hounslow, A.D. Salman, Roller compaction: Effect of morphology and amorphous content of lactose powder on product quality., International Journal of Pharmaceutics. 496

(2015) 63–74.

[100] A. Parikh, S. Agarwal, K. Raut, a Review on Applications of Maltodextrin in Pharmaceutical Industry, International Journal of Pharmacy and Biological Sciences. 4 (2014) 67–74.

[101] K.M. Picker, S.W. Hoag, Characterization of the thermal properties of microcrystalline cellulose by modulated temperature differential scanning calorimetry, Journal of Pharmaceutical Sciences. 91 (2002) 342–349.

[102] R.W. Heckel, Density-Pressure Relationships in Powder Compaction, Transactions of the Metallurgical Society of AIME. 221 (1961) 671–675.

[103] C. Sun, D.J.W. Grant, Influence of elastic deformation of particles on Heckel analysis, Pharmaceutical Development and Technology. 6 (2001) 193–200.

[104] J.M. Sonnergaard, A critical evaluation of the Heckel equation, International Journal of Pharmaceutics. 193 (1999) 63–71.

[105] A. Aburub, D. Mishra, I. Buckner, Use of compaction energetics for understanding particle deformation mechanism, Pharmaceutical Development and Technology. 12 (2007) 405–414.

[106] J.P. Holman, Heat Transfer, McGraw-Hill, New York, 2010.

[107] G.M. Elmasry, S. Nakauchi, Image analysis operations applied to hyperspectral images for non-invasive sensing of food quality - A comprehensive review, Biosystems Engineering. 142 (2015) 53–82.

[108] J. Moor, Application of NIR Imaging and multivariate data analysis for pharmaceutical products. Diploma Thesis., University of Applied Sciences Munchen, 2010.

[109] A. Gerich, J. Dubois, L.H. Kidder, NIR Imaging Applications in the Pharmaceutical Industry, in: S. Sasic, Y. Ozaki (Eds.), Raman, Infrared, and Near Infrared Chemical Imaging, WILEY, New Jersey, 2010.

[110] C. Mangwandi, Y.S. Cheong, M.J. Adams, M.J. Hounslow, A.D. Salman, The coefficient of restitution of different representative types of granules, Chemical

Engineering Science. 62 (2007) 437–450.

[111] R.B. Al Asady, M.J. Hounslow, A.D. Salman, Roller compaction: the effect of plastic deformation of primary particles with wide range of mechanical properties, Drug Delivery and Translational Research. 8 (2018) 1615–1634.

[112] C.K. Chang, F.A. Alvarez–Nunez, J. V. Rinella Jr., L.-E. Magnusson, K. Sueda, Roller Compaction, Granulation and Capsule Product Dissolution of Drug Formulations Containing a Lactose or Mannitol Filler, Starch, and Talc, American Association of Pharmaceutical Scientists. 9 (2008) 597–604.

[113] N. Castro, V. Durrieu, C. Raynaud, A. Rouilly, Influence of DE-value on the physicochemical properties of maltodextrin for melt extrusion processes, Carbohydrate Polymers. 144 (2016) 464–473.

[114] A.M. Miguélez-Morán, C.Y. Wu, H. Dong, J.P.K. Seville, Characterisation of density distributions in roller-compacted ribbons using micro-indentation and X-ray micro-computed tomography, European Journal of Pharmaceutics and Biopharmaceutics. 72 (2009) 173–182.

[115] W. Johnson, P.B. Mellor, Engineering plasticity, in: Van Nostrand-Reinhold, London, 1973.

[116] M.J. Adams, I. Aydin, B.J. Briscoe, S.K. Sinha, A finite element analysis of the squeeze flow of an elasto-viscoplastic paste material, Journal of Non-Newtonian Fluid Mechanics. 71 (1997) 41–57.

[117] G. Frenning, J. Nordström, G. Alderborn, Effective Kawakita parameters for binary mixtures, Powder Technology. 189 (2009) 270–275.

[118] P.J. Sheskey, J. Hendren, The effects of roll compaction equipment variables, granulation technique, and HPMC polymer level on a controlled-release matrix model drug formulation, Pharmaceutical Technology. 23 (1999) 90–106.

[119] H. Lim, V.S. Dave, L. Kidder, E. Neil Lewis, R. Fahmy, S.W. Hoag, Assessment of the critical factors affecting the porosity of roller compacted ribbons and the feasibility of using NIR chemical imaging to evaluate the porosity distribution, International Journal of Pharmaceutics. 410 (2011) 1–8.

[120] D. Markl, A. Strobel, R. Schlossnikl, J. Bøtker, P. Bawuah, C. Ridgway, J. Rantanen, T. Rades, P. Gane, K.E. Peiponen, J.A. Zeitler, Characterisation of pore structures of pharmaceutical tablets: A review, International Journal of Pharmaceutics. 538 (2018) 188–214.

[121] A.A. Gowen, C.P.O. Donnell, P.J. Cullen, G. Downey, J.M. Frias, Hyperspectral imaging - an emerging process analytical tool for food quality and safety control, Trends in Food Science & Technology. 18 (2007) 590–598.

[122] A.A. Gowen, C.P. O'Donnell, J.C. P, S.E.J. Bell, Recent applications of Chemical Imaging to pharmaceutical process monitoring and quality control, European Journal of Pharmaceutics and Biopharmaceutics. 69 (2008) 10–22.

[123] H. Ma, C. Anderson, Characterization of Pharmaceutical Powder Blends by NIR Chemical Imaging, Journal of Pharmaceutical Sciences. 97 (2008) 3305–3320.

[124] L.R. Hilden, C.J. Pommier, S.I.F. Badawy, E.M. Friedman, NIR chemical imaging to guide / support BMS-561389 tablet formulation development, International Journal of Pharmaceutics. 353 (2008) 283–290.

[125] J. Ropero, Y. Colón, B. Johnson-Restrepo, R.J. Romañch, Near-infrared chemical imaging slope as a new method to study tablet compaction and tablet relaxation, Applied Spectroscopy. 65 (2011) 459–465.

[126] M. Khorasani, J.M. Amigo, J. Sonnergaard, P. Olsen, P. Bertelsen, J. Rantanen, Visualization and prediction of porosity in roller compacted ribbons with near-infrared chemical imaging (NIR-CI), Journal of Pharmaceutical and Biomedical Analysis. 109 (2015) 11–17.

[127] M.B. Lopes, J. Wolff, Investigation into classification / sourcing of suspect counterfeit Heptodin TM tablets by near infrared chemical imaging, Analytica Chimica Acta. 633 (2009) 149–155.

[128] O. Ye, L.P. Houmøller, A.L. Pomerantsev, P. Geladi, J. Burger, V.L. Dorofeyev, A.P. Arzamastsev, NIR spectrometry for counterfeit drug detection A feasibility study, Analytica Chimica Acta. 549 (2005) 151–158.

[129] W. Wang, J. Paliwal, Correction of Curvature-Induced Spectral Variability in

Hyperspectral Images of Wheat Kernels, in: ASAE Annual International Meeting. Paper Number: 053070., Tampa, Florida, 2005.

[130] J.B. Phillips, H. Eliasson, Camera Image Quality Benchmarking, WILEY, West Sussex, 2018.

[131] M. Khorasani, J.M. Amigo, P. Bertelsen, C.C. Sun, J. Rantanen, Process optimization of dry granulation based tableting line: Extracting physical material characteristics from granules, ribbons and tablets using near-IR (NIR) spectroscopic measurement, Powder Technology. 300 (2016) 120–125.

[132] M. Donoso, D.O. Kildsig, E.S. Ghaly, Prediction of Tablet Hardness and Porosity Using Near-Infrared Diffuse Reflectance Spectroscopy as a Nondestructive Method, 8 (2003) 357–366.

[133] M. Khorasani, J.M. Amigo, C.C. Sun, P. Bertelsen, J. Rantanen, Near-infrared chemical imaging (NIR-CI) as a process monitoring solution for a production line of roll compaction and tableting, European Journal of Pharmaceutics and Biopharmaceutics. 93 (2015) 293–302.

[134] N. Souihi, D. Nilsson, M. Josefson, J. Trygg, Near-infrared chemical imaging (NIR-CI) on roll compacted ribbons and tablets – multivariate mapping of physical and chemical properties, International Journal of Pharmaceutics. 483 (2015) 200–211.

[135] G. Reich, Near-infrared spectroscopy and imaging : Basic principles and pharmaceutical applications, Advanced Drug Delivery Reviews. 57 (2005) 1109–1143.

[136] J.J. Wang, T. Li, S.D. Bateman, R. Erck, K.R. Morris, Modeling of adhesion in tablet compression-I. Atomic force microscopy and molecular simulation., Journal of Pharmaceutical Sciences. 92 (2003) 798–814.

[137] M.B. Tejedor, N. Nordgren, M. Schuleit, M.W. Rutland, A. Millqvist-Fureby, Tablet mechanics depend on nano and micro scale adhesion, lubrication and structure, International Journal of Pharmaceutics. 486 (2015) 315–323.

[138] R. Matjie, S. Zhang, Q. Zhao, N. Mabuza, J.R. Bunt, Tailored surface energy of

stainless steel plate coupons to reduce the adhesion of aluminium silicate deposit, Fuel. 181 (2016) 573–578.

[139] I.M. Grimsey, J.C. Feeley, P. York, Analysis of the surface energy of pharmaceutical powders by inverse gas chromatography, Journal of Pharmaceutical Sciences. 91 (2002) 571–583.

[140] R.C. Rowe, Binder-substrate interactions in granulation: a theoretical approach based on surface free energy and polarity, International Journal of Pharmaceutics. 52 (1989) 149–154.

[141] L. Zajic, G. Buckton, The use of surface energy values to predict optimum binder selection for granulations, International Journal of Pharmaceutics. 59 (1990) 155–164.

[142] J.C. Hooton, C.S. German, M.C. Davies, C.J. Roberts, A comparison of morphology and surface energy characteristics of sulfathiazole polymorphs based upon single particle studies, European Journal of Pharmaceutical Sciences. 28 (2006) 315–324.

[143] F. Fichtner, D. Mahlin, K. Welch, S. Gaisford, G. Alderborn, Effect of surface energy on powder compactibility, Pharmaceutical Research. 25 (2008) 2750–2759.

[144] B. Strzemiecka, A. Voelkel, Estimation of the work of adhesion by means of inverse gas chromatography for polymer complex systems, International Journal of Adhesion and Adhesives. 38 (2012).

[145] T. Young, An Essay on the Cohesion of Fluids, Philosophical Transactions of the Royal Society of London. 95 (2016) 65–87.

[146] Ż. Marian, Methods for the calculation of surface free energy of solids, JOurnal of Achievements in Materials and Manufacturing Engineering. 24 (2007).

[147] J.Y.Y. Heng, D.R. Williams, Microscopy, in: R.A. Storey, I. Ymen (Eds.), Solid State Characterization of Pharmaceuticals, WILEY, Chichester, 2011.

[148] M. Bunker, J. Zhang, R. Blanchard, C.J. Roberts, Characterising the surface adhesive behavior of tablet tooling components by atomic force microscopy, Drug Development and Industrial Pharmacy. 37 (2011) 875–885.

[149] C. Al-Karawi, C.S. Leopold, A comparative study on the sticking tendency of ibuprofen and ibuprofen sodium dihydrate to differently coated tablet punches, European Journal of Pharmaceutics and Biopharmaceutics. 128 (2018) 107–118.

[150] D. Weber, Y. Pu, C.L. Cooney, Quantification of lubricant activity of magnesium stearate by atomic force microscopy, Drug Development and Industrial Pharmacy. 34 (2008) 1097–1099.

[151] R. Ho, J.Y.Y. Heng, A review of inverse gas chromatography and its development as a tool to characterize anisotropic surface properties of pharmaceutical solids, KONA Powder and Particle Journal. 30 (2012) 164–180.

[152] G. Steele, T. Austin, Pharmaceutical Preformulation and Formulation edited by, in: M. Gibson (Ed.), Informa, New York, 2009.

[153] S. Mohammadi-Jam, K.E. Waters, Inverse gas chromatography applications: A review, Advances in Colloid and Interface Science. 212 (2014) 21–44.

[154] A. Newman, Physical Characterization of Pharmaceutical Solids, in: H.G. Brittain (Ed.), Marcel Dekker, New Jersey, 1995.

[155] P.A. Webb, Surface area, porosity, and related physical characteristics, in: L.L. Augsburger, S.W. Hoag (Eds.), PHARMACEUTICAL DOSAGE FORMS: TABLETS, Third, Informa, Boca Raton, 2008.

[156] P.N. Jacob, J.C. Berg, A comparison of the work of adhesion obtained from wetting and vapor adsorption measurements, The Journal of Adhesion. 54 (1995) 115–131.

[157] D. Hansford, D.J.W. Grant, N. J, M, The Influence of Processing phobic Powder, Powder Technology. 26 (1980) 119–126.

[158] Y. Yuan, T.R. Lee, Contact Angle and Wetting Properties, in: G. Bracco, B. Holst (Eds.), Surface Science Techniques, Springer, New York, 2013.

[159] J.L. Hutter, J. Bechhoefer, Calibration of atomic-force microscope tips, Review of Scientific Instruments. 64 (1993) 1868–1873.

[160] E. Hadjittofis, G.G.Z. Zhang, J.Y.Y. Heng, Influence of sample preparation on IGC measurements: the cases of silanised glass wool and packing structure, RSC

Advances. 7 (2017) 12194–12200.

[161] S.S.M. Ali, J.Y.Y. Heng, A.A. Nikolaev, K.E. Waters, Introducing inverse gas chromatography as a method of determining the surface heterogeneity of minerals for flotation, Powder Technology. 249 (2013) 373–377.

[162] G.L. Klein, G. Pierre, M.N. Bellon-Fontaine, M. Graber, Inverse gas chromatography with film cell unit: An attractive alternative method to characterize surface properties of thin films, Journal of Chromatographic Science. 53 (2015) 1–6.

[163] S.C. Das, Q. Zhou, D.A. V Morton, I. Larson, P.J. Stewart, Use of surface energy distributions by inverse gas chromatography to understand mechanofusion processing and functionality of lactose coated with magnesium stearate, European Journal of Pharmaceutical Sciences. 43 (2011) 325–333.

[164] F. Thielmann, D.J. Burnett, J.Y.Y. Heng, Determination of the surface energy distributions of different processed lactose, Drug Development and Industrial Pharmacy. 33 (2007) 1240–1253.

[165] D.F. Steele, R.C. Moreton, J.N. Staniforth, P.M. Young, M.J. Tobyn, S. Edge, Surface Energy of Microcrystalline Cellulose Determined by Capillary Intrusion and Inverse Gas Chromatography, American Association of Pharmaceutical Scientists. 10 (2008) 494–503.

[166] O. Planinšek, J. Zadnik, Š. Rozman, M. Kunaver, R. Dreu, S. Srčič, Influence of inverse gas chromatography measurement conditions on surface energy parameters of lactose monohydrate, International Journal of Pharmaceutics. 256 (2003) 17–23.

[167] I.M. Grimsey, M. Sunkersett, J.C. Osborn, P. York, R.C. Rowe, Interpretation of the differences in the surface energetics of two optical forms of mannitol by inverse gas chromatography and molecular modelling, International Journal of Pharmaceutics. 191 (1999) 43–50.

[168] T. Tay, S. Das, P. Stewart, Magnesium stearate increases salbutamol sulphate dispersion: What is the mechanism?, International Journal of Pharmaceutics. 383 (2010) 62–69.

[169] D. Steven Keller, P. Luner, Surface energetics of calcium carbonates using inverse gas chromatography, Colloids and Surfaces A: Physicochemical and Engineering Aspects. 161 (2000) 401–415.

[170] S. Ebnesajjad, C.F. Ebnesajjad, Surface Tension and Its Measurement, in: Surface Treatment of Materials for Adhesive Bonding, 2nd ed., Elsevier, Oxford, 2014.

[171] C.C. Sun, Decoding powder tabletability: Roles of particle adhesion and plasticity, Journal of Adhesion Science and Technology. 25 (2011) 483–499.

[172] I. Gabbott, Designer granules : Beating the trade-off between granule Strength and Dissolution Time. PhD thesis, University of Sheffield, 2007.

[173] F. Aqra, A. Ayyad, Surface energies of metals in both liquid and solid states, Applied Surface Science. 257 (2011) 6372–6379.

[174] P. Kleinebudde, Roll compaction/dry granulation: Pharmaceutical applications, European Journal of Pharmaceutics and Biopharmaceutics. 58 (2004) 317–326.

[175] A.R. Muliadi, J.D. Litster, C.R. Wassgren, Validation of 3-D finite element analysis for predicting the density distribution of roll compacted pharmaceutical powder, Powder Technology. 237 (2013) 386–399.

[176] A. Mesbah, J.A. Paulson, R. Lakerveld, R.D. Braatz, Model Predictive Control of an Integrated Continuous Pharmaceutical Manufacturing Pilot Plant, Organic Process Research and Development. 21 (2017) 844–854.

[177] G.M.W. Saeed Shirazian, Manuel Kuhs, Shaza Darwish, Denise Croker, Artificial neural network modelling of continuous wet granulation using a twin-screw extruder, Science and Technology of Advanced Materials. 16 (2017) 102–109.

[178] S. Shanmuganathan, Artificial Neural Netwok Modelling, in: S. Samarasinghe (Ed.), Studies in Computational Intelligence, Springer, Warsaw, 2016.

[179] Z. Abdullah, Z. Ahmad, N. Aziz, Multiple input-single output (MISO) Feedforward Artificial Neural network (FANN) models for pilot plant binary distillation column, Proceedings - 2011 6th International Conference on Bio-Inspired Computing: Theories and Applications, BIC-TA 2011. (2011) 157–160.

[180] M.F. Møller, A scaled conjugate gradient algorithm for fast supervised learning, Neural Networks. 6 (1993) 525–533.

[181] C.S. Omar, R.B. Al-Asady, A.D. Salman, Roller compaction: Improving the homogeneity of ribbon properties along the roller width, Powder Technology. 342 (2019) 464–474.

APPENDIX A

A	B
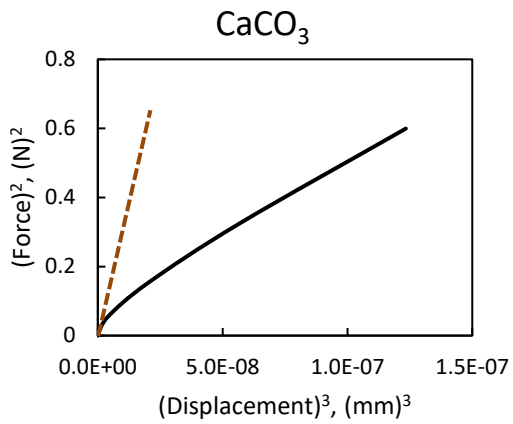	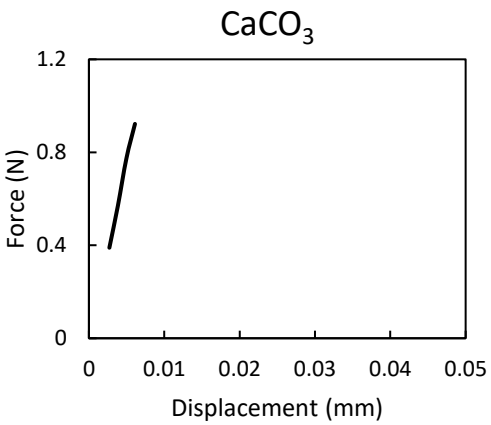
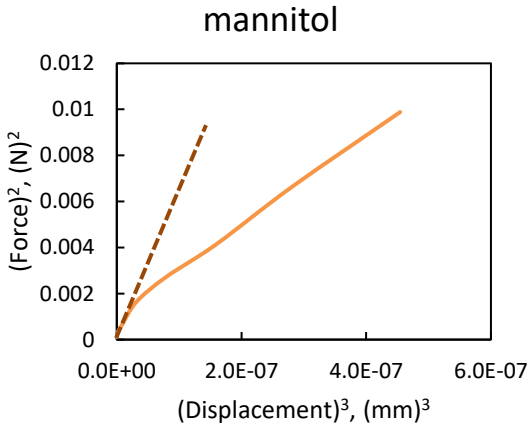	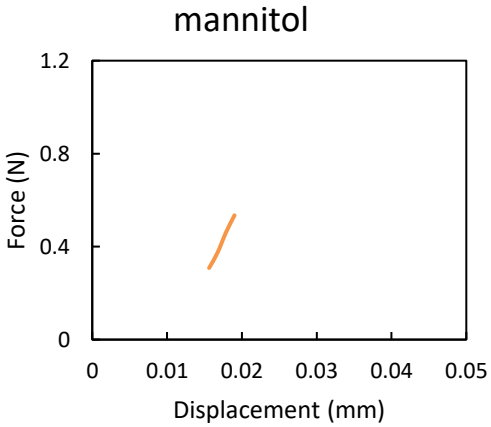
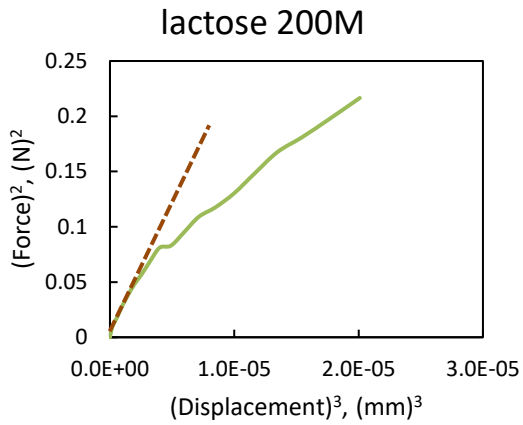	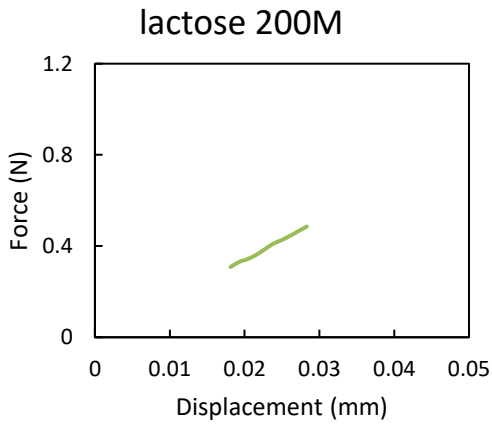

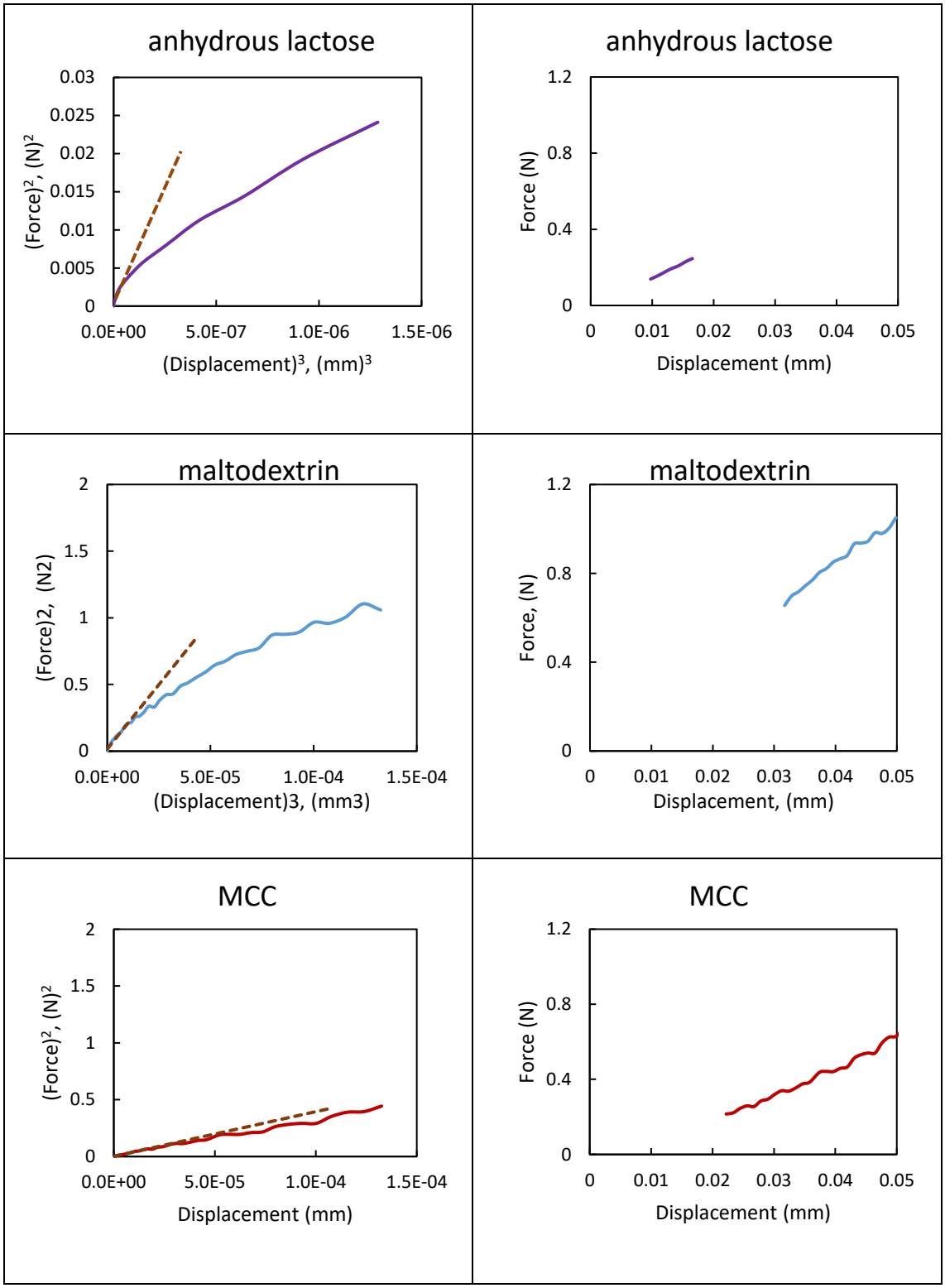

Figure A 1: Column A: Linearized form of Hertz equation to find the elastic limit of deformation during single particle diametrical compaction and column B: the plastic region of the force-displacement curve that is used to calculate particle yield strength.

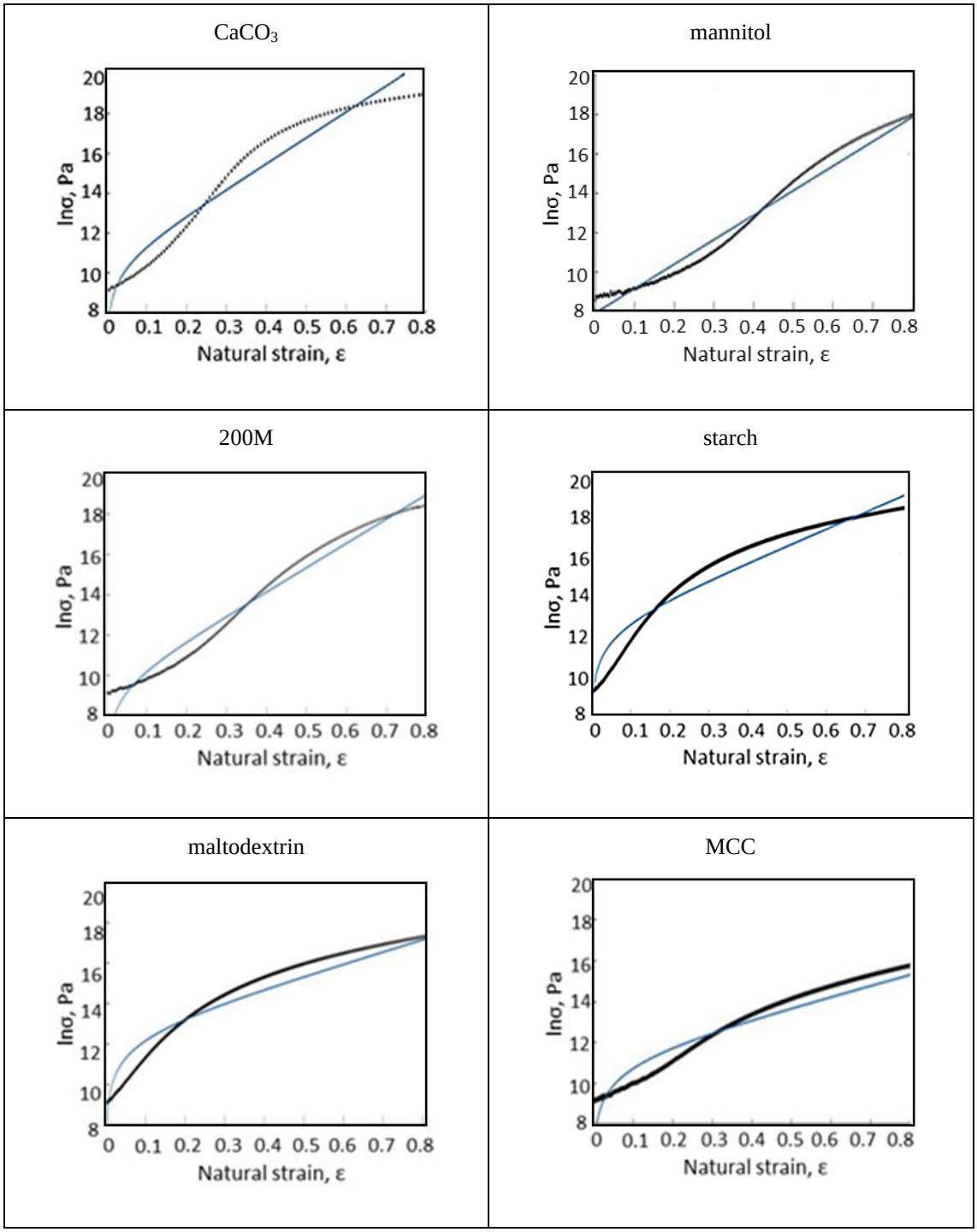

Figure A 2: Typical stress-strain data for the studied feed powder during uniaxial compaction test. The blue line represents the best fit to equation (Equation 2-14), and the black line shows compaction profile.

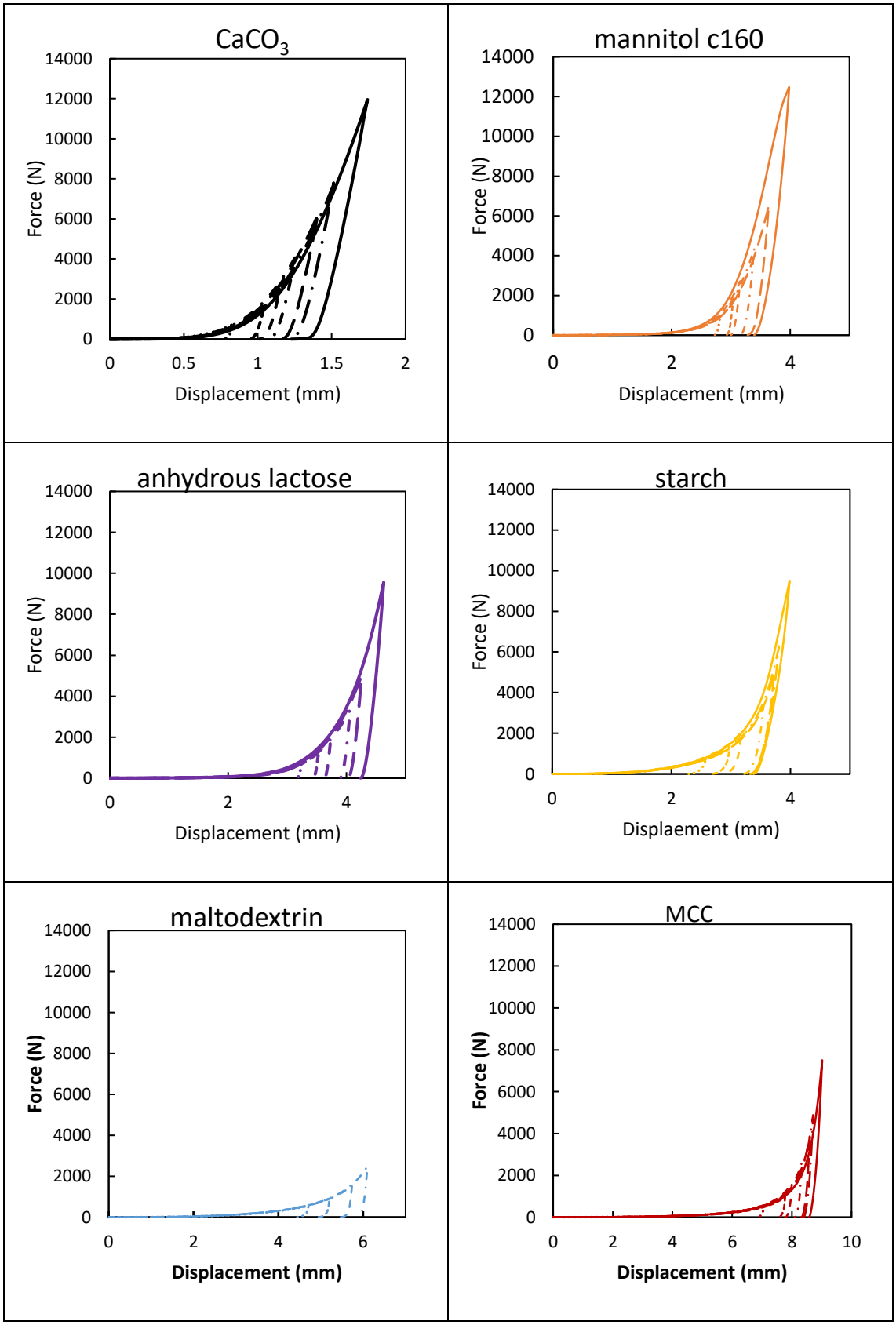

Figure A 3: Loading/unloading curves of the studied materials which are used to calculate compact elastic recovery. The tablets have compressed at stresses equivalent to the hydraulic pressure used in roller compaction (Hydraulic pressures used: …. 18, ---- 30, – – –50, - · - 80, — —120, —·— 150, and — 230 bar)

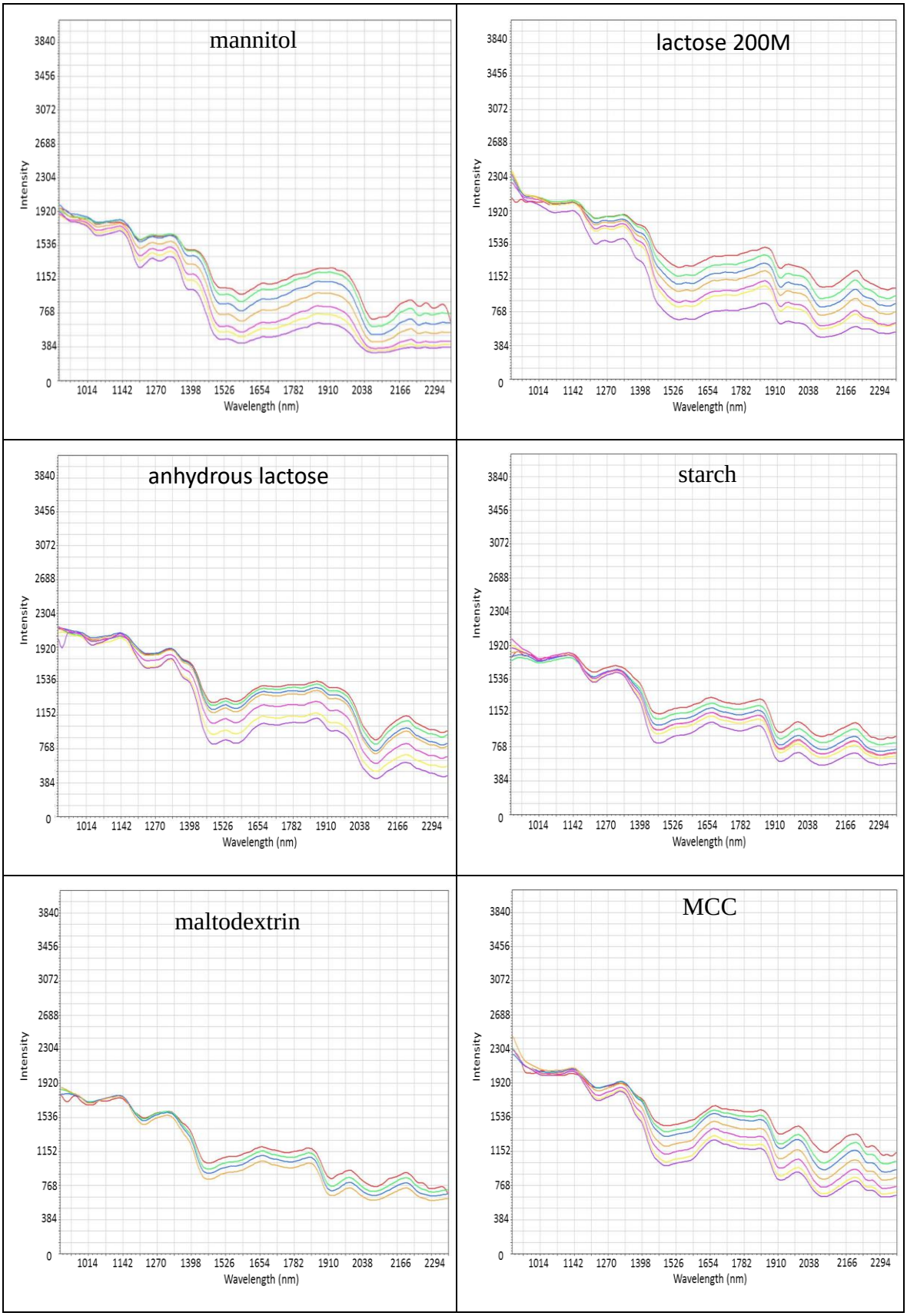

Figure A 4: NIR spectrum for the calibration tablets which was compacted at stresses equivalent to the smooth-roller mediated roller compaction. The stresses are ordered discerningly in the following colour order: (—— ,—— ,—— ,—— ,—— ,—— , and ——).

mannitol

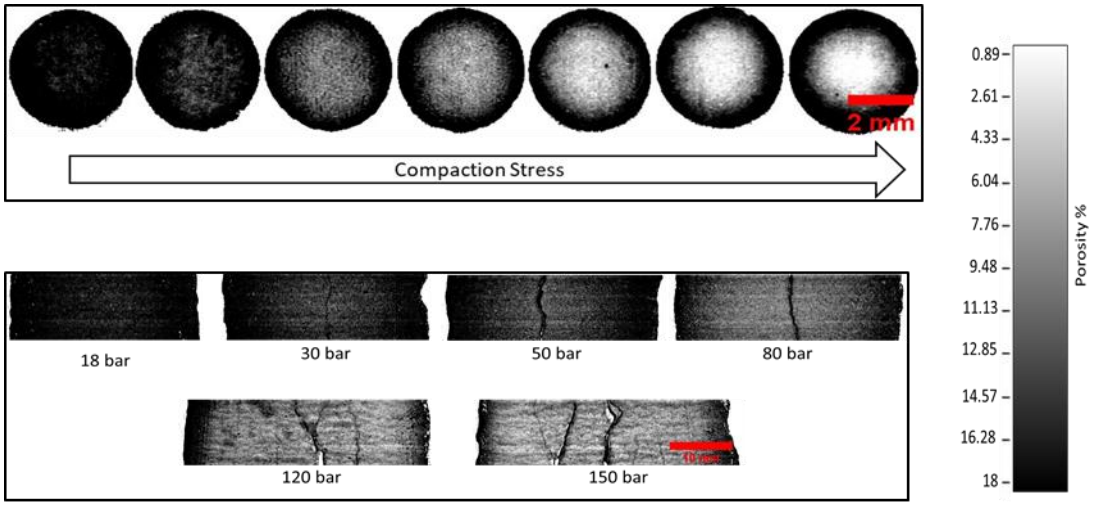

anhydrous lactose

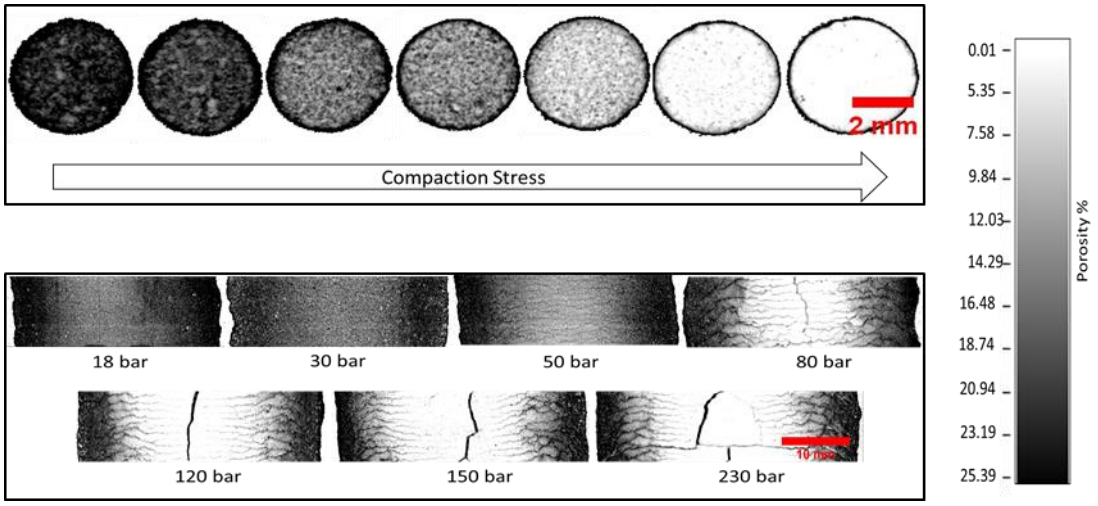

starch

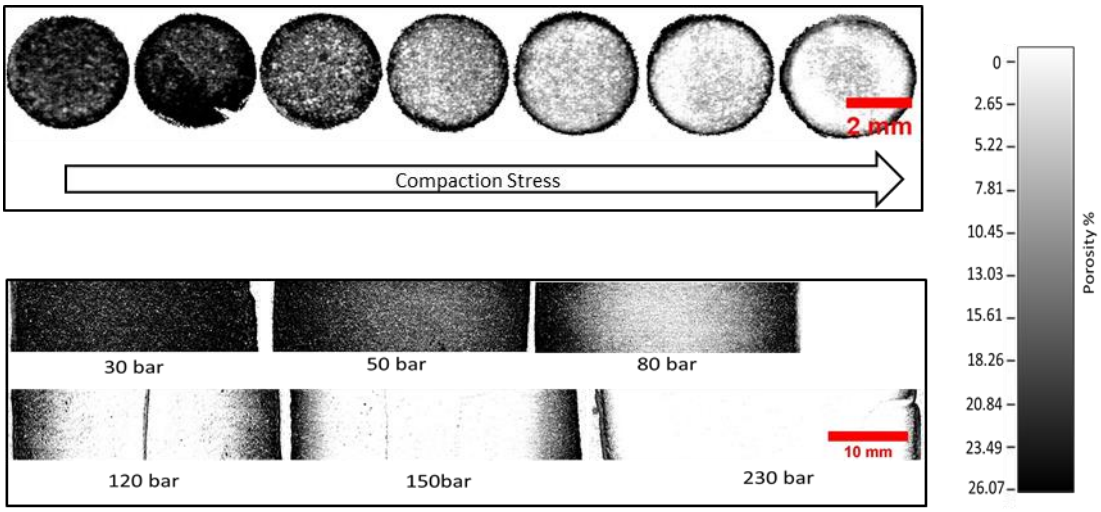

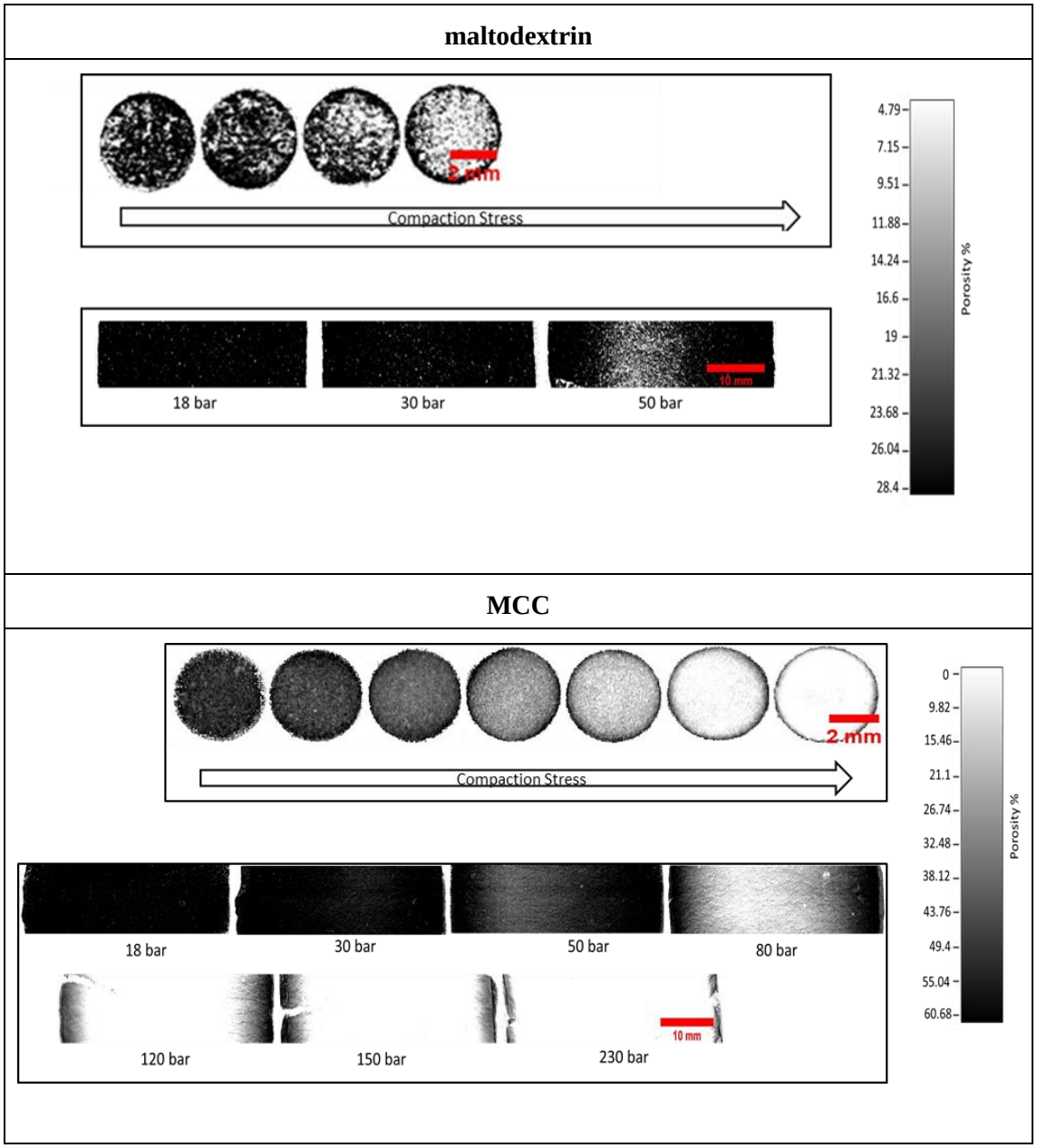

Figure A 5: NIR-CI porosity maps of studied materials; calibration tablets (top) and roller compacted ribbons (bottom).

Output 1	Output 2
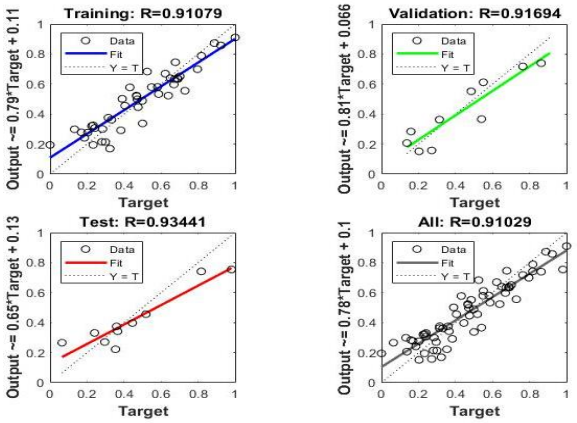	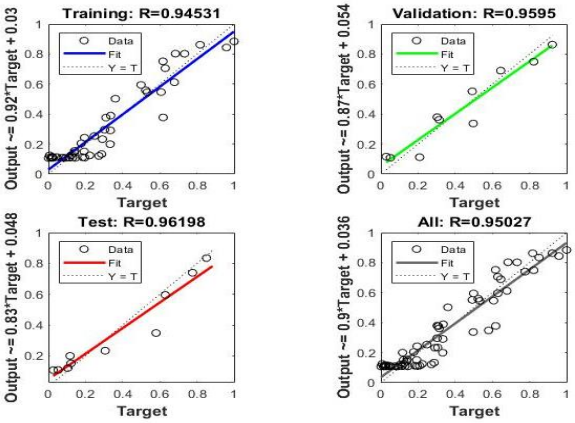
Output 3	**Output 4**
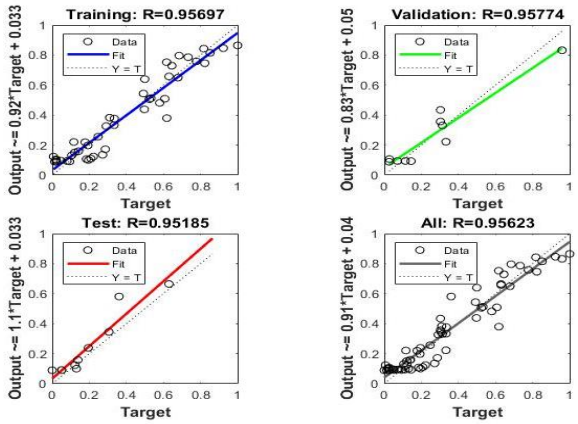	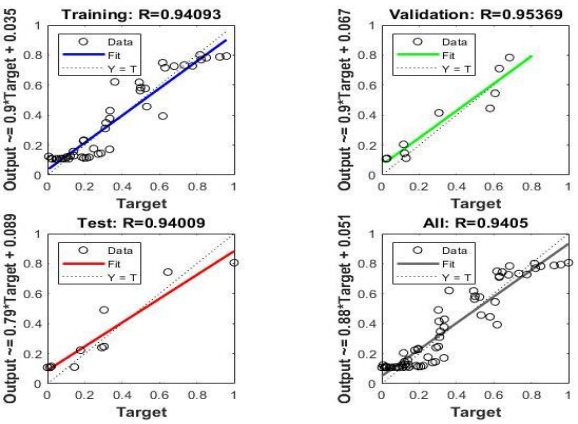
Output 6	**Output 7**
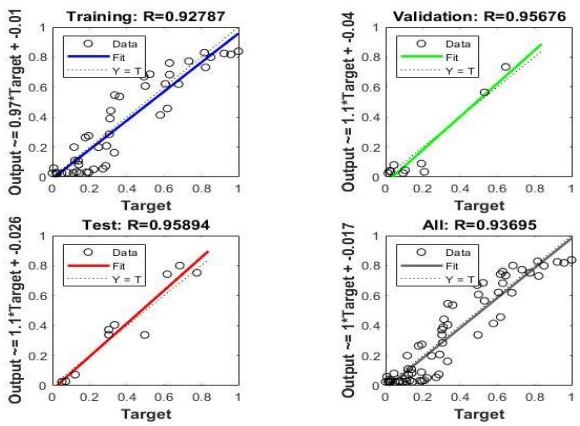	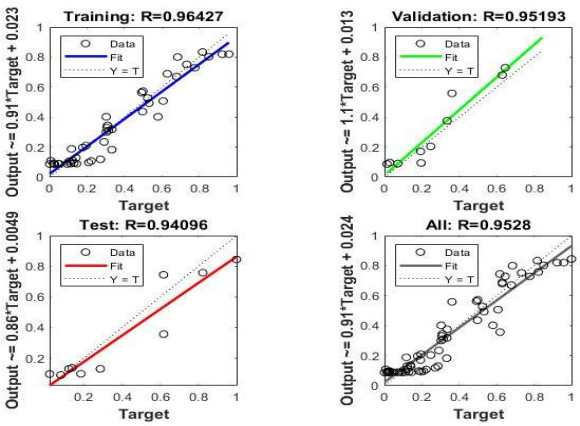

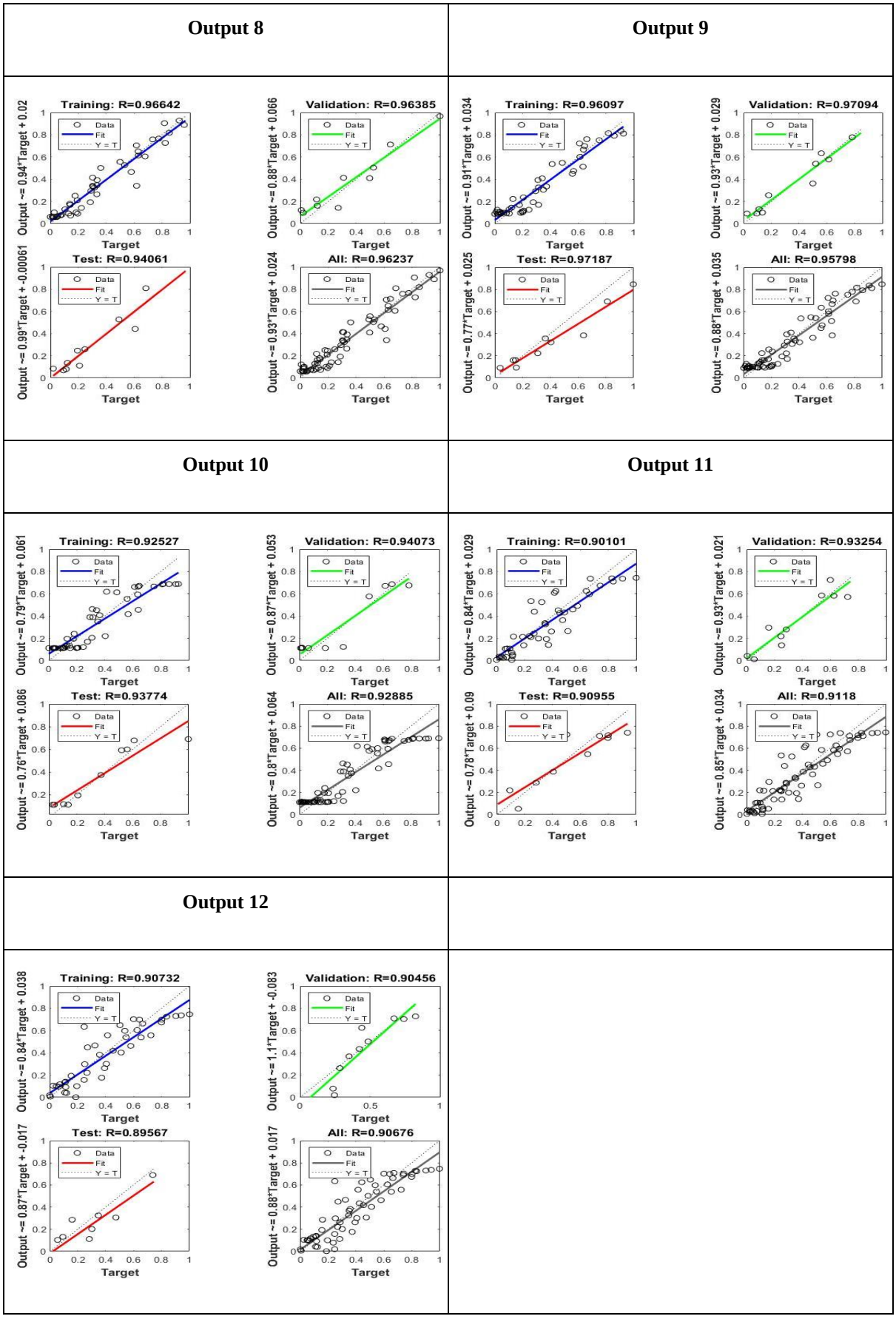

Figure A 6: The regression results of fitting porosity results at the different 12 positions across ribbon width except for position-5.

Table A 1: Experimental data used to build an artificial neural network.

Input conditions						Output- porosity %											
I	Yield strength	Roller force (kN)	Internal friction	Wall friction	(k)												
0	233	7.5	39.3	10.3	10.3	32.8	22	17.1	14.4	12.6	14	16.6	21.5	26.5	31.6	0	0
0	233	12.4	39.3	10.3	10.3	33	22.8	13.4	10.7	9.5	8.7	8.4	9.8	13.2	17.2	31.9	0
0	233	20.7	39.3	10.3	10.3	36.9	3	4	4.5	4.8	5.5	6.9	7.8	10.9	28.8	0	0
0	233	33.2	39.3	10.3	10.3	35.9	1.4	1.3	1.4	1.1	1	1.9	4.2	12.3	18	0	0
0	233	49.8	39.3	10.3	10.3	35.3	9.1	2.9	2.7	0.8	2.4	1.4	4.5	2.2	2.7	5.3	25.6
0	233	62.2	39.3	103	10.3	33	5.1	2.0	0.9	0.5	2.1	0.7	1.6	1.8	3.2	13.8	30.4
0	200	7.5	46.3	16.8	12.7	37.4	25.7	17.6	15.4	14.5	13.5	16	20.2	35.6	0	0	0
0	200	12.4	46.3	16.8	12.7	30	19.2	12.7	11.1	10.1	11.1	14.1	20	36	0	0	0
0	200	20.7	46.3	16.8	12.7	34.5	18.1	8.2	7	5.8	6.4	5.7	5.3	9.7	21	31.3	0
0	200	33.2	46.3	16.8	12.7	28	10	3.6	1.8	0.8	1.3	1.7	3	5	13.8	32.1	0
0	200	49.8	46.3	16.8	12.7	34.4	14.1	6.1	3.4	3.2	2.3	1.9	2.9	4.3	10.3	17.2	33.9
0	200	62.2	46.3	16.8	12.7	26.2	2.7	1.1	1.2	1.5	1.3	0.3	0.1	2.3	4.8	32.3	0
0	182	7.5	40.6	13.6	8.8	47.6	40.3	34.5	30.9	27.9	27	28.9	35.7	43.8	0	0	0
0	182	12.4	40.6	13.6	8.8	43.4	34.8	27.9	25.8	26.9	27.5	29	33.3	39.7	0	0	0
0	182	20.7	40.6	13.6	8.8	37.6	20.6	8.4	6.7	4.5	5.3	6.1	10.4	16.3	33.4	0	0
0	182	33.2	40.6	13.6	8.8	38	23.1	10.1	2.5	1.1	0.4	1.1	4.4	13.3	23.2	33.8	0
0	182	49.8	40.6	13.6	8.8	39.2	12.7	4.6	2.5	2.7	3.3	4	2.8	4.1	9.9	36.1	0
0	182	62.2	40.6	13.6	8.8	42	17.1	5.5	2.8	0.7	0.1	1.1	2.4	2.8	6.8	21.8	44.2

0	123	12.4	34.2	9.5	8.4	44.4	30.8	30.7	28.4	30.8	32.6	35.5	39.7	43.4	0	0	0
0	123	20.7	34.2	9.5	8.4	46.3	27.4	21.5	19.5	20.0	22.2	25.5	33.8	38.8	39.9	0	0
0	123	33.2	34.2	9.5	8.4	42.3	32.3	24.7	12.5	12	13	18.4	26	41.1	0	0	0
0	123	49.8	34.2	9.5	8.4	39.9	16.8	5.4	3	1.5	4.7	5.3	7.7	12.5	22.6	39.4	0
0	123	62.2	34.2	9.5	8.4	40.8	19.9	6.7	2.8	2.4	1	3.2	3.1	4	10.3	40.5	0
0	81	7.5	40.0	10.2	6.0	52.2	44.2	39.7	38.4	37.3	37.9	39.0	40	42.4	46.4	52.2	0
0	81	12.4	40.0	10.2	6.0	50.2	43.1	35.4	31.6	29	27.5	27.7	30	35.6	41.6	50.9	0
0	81	20.7	40.0	10.2	6.0	39.3	21.0	12.5	12.8	11.9	16.1	18.9	25.3	32.2	39.8	51.7	0
0	69	7.5	44.5	6.9	5.3	55.5	43.5	38.1	36.6	36.6	36.6	36.8	36.9	37.4	39.9	47.4	0
0	69	12.4	44.5	6.9	5.3	53.2	43.1	38	32.5	30.1	30.2	27.9	26.4	27.7	30.8	39.7	48.9
0	69	20.7	44.5	6.9	5.3	46	32.9	25.9	22.5	22.5	22.2	22.7	23.4	25.5	27	33.1	48.7
0	69	33.2	44.5	6.9	5.3	45.9	26.9	17.3	12.4	9.7	8.6	8.2	9	10.6	13	20.8	40.3
0	69	49.8	44.5	6.9	5.3	45.8	21.6	12	10.4	8.6	8.3	9.3	9.2	8.9	13.1	23.1	43.9
0	69	62.2	44.5	6.9	5.3	43.2	19.6	9.7	7.2	6.1	6.5	7.1	11.1	7.9	8.4	12.3	49.7
1	233	7.5	39.3	31.6	10.3	36.7	31.0	26.3	25.1	22.3	23.3	23.7	26.2	28.3	30.2	35.5	0
1	233	12.4	39.3	31.6	10.3	33.2	21.3	13.6	12.8	15.7	15	15.6	20.1	26.1	28.7	34.2	0
1	233	20.7	39.3	31.6	10.3	30.8	25.2	23.0	14.7	8.5	8.0	9.5	8.0	12.2	20.2	24.2	32.2
1	233	33.2	39.3	31.6	10.3	31.6	21.6	18.3	8.2	5.7	5.5	4.9	6.2	9.5	14.9	21.6	33.2
1	233	49.8	39.3	31.6	10.3	35.0	12.3	4.4	3.4	4	3.6	2.5	4.2	6	8.7	32.6	0.0
1	233	62.2	39.3	31.6	10.3	30.2	13.5	3.3	1.9	1.9	0.7	2.2	0.5	1	1.9	5.0	32.4
1	200	7.5	46.3	34.5	12.7	35.4	32.3	23.6	20.1	21.8	23.7	25.4	26	29.9	39.5	0	0
1	200	12.4	46.3	34.5	12.7	33.2	25.6	22	16.3	12.7	13.8	14.4	17.1	18.2	24.5	35.5	0
1	200	20.7	46.3	34.5	12.7	36.5	27.1	19.8	15.4	15.6	14.9	12.7	13.2	16.8	29.7	37.7	0
1	200	33.2	46.3	34.5	12.7	35.7	26.5	15	10.5	10.5	10	9.6	10.2	14	23.6	34.7	0

1	200	49.8	46.3	34.5	12.7	34.1	18.5	6.3	3.8	3.8	5.1	4.6	5.1	8.9	17.1	32.1	0
1	200	62.2	46.3	34.5	12.7	32.1	4.8	2.2	0.2	0.2	1.1	1.5	1.1	1	2.6	27.4	0
1	182	7.5	40.6	32.2	8.8	39.9	37.9	31.8	29.8	27.9	28	29	29.4	30.3	36.7	41.2	0
1	182	12.4	40.6	32.2	8.8	40.1	36.4	30	26.7	23.6	21.9	22.1	22.3	24.4	30.4	36.7	0
1	182	20.7	40.6	32.2	8.8	40.8	23.7	16	14.2	13	14.9	17	19	24.1	31.2	37.8	0
1	182	33.2	40.6	32.2	8.8	31.1	16.9	14.2	8.3	6.9	6.2	6.2	7.5	9	15.1	27.8	36.2
1	182	49.8	40.6	32.2	8.8	32.1	10.3	6.1	5.5	5.6	5.9	6.4	5.5	6	8	12.2	32.0
1	182	62.2	40.6	32.2	8.8	34.8	13.7	6.4	5.0	3.5	4.3	4.9	4.6	7.9	13.3	33.4	0.0
1	123	12.4	34.2	27.9	8.4	46.8	45.1	42.7	41.9	40.9	41.1	41.1	40.8	40.7	41.3	43.4	48.8
1	123	20.7	34.2	27.9	8.4	45.3	39.1	35.2	33.5	34.3	34.6	34.1	34.5	36.7	39.4	43.7	0
1	123	33.2	34.2	27.9	8.4	42.3	38.5	31.3	26.2	25.6	25.8	25.8	27.3	27.2	30.8	36.6	43.1
1	123	49.8	34.2	27.9	8.4	40.4	29.6	19.2	13.7	12.7	12.8	14.4	16.2	21.0	29.0	39.0	0
1	123	62.2	34.2	27.9	8.4	40	29.4	12.5	11.9	11	9.3	9.1	9.8	13.4	20.8	34.8	38.8
1	81	7.5	40.0	31.1	6.0	54.9	52.5	47.2	45.7	46.1	44.5	45.3	45.8	48.8	52.4	0	0
1	81	12.4	40.0	31.1	6.0	50.1	45.0	44.5	43.7	42.4	42.6	41.9	42.5	41.8	43.3	49	0
1	81	20.7	40.0	31.1	6.0	49.5	34.2	28.8	27.0	27.4	28.7	29.3	29.5	31.5	33.5	38.1	45.9
1	81	33.2	40.0	31.1	6.0	38.8	26.2	20.2	16.6	14.7	13.5	14.3	14.4	15.2	21.4	29.0	44.9
1	69	7.5	44.5	35.1	5.3	51.5	42.9	39.2	36.8	36.7	36.4	37.1	38.9	40.8	43.2	50.1	0
1	69	12.4	44.5	35.1	5.3	48.6	37.1	32.1	29.7	30.1	30.5	30.1	30	29.9	32.3	36.4	46.2
1	69	20.7	44.5	35.1	5.3	41.6	27.8	24.3	23.9	26.1	28.0	27.9	26.7	28.6	35.8	48.9	0
1	69	33.2	44.5	35.1	5.3	46.4	29.8	20.7	18.1	15.7	13.7	13.5	13.3	14.2	16.9	29.4	46.0
1	69	49.8	44.5	35.1	5.3	44.9	18.3	14.1	13.5	13.3	12.2	11.3	11.9	11.3	13.2	27.8	41.9
1	69	62.2	44.5	35.1	5.3	41.4	22.4	12.5	9.7	8.6	8.8	8.6	9.7	11.7	13.7	18.7	44.3

Table A 2: ANN predicted porosity distribution across ribbon width; rows were organised in the same order to that of table A-1.

output-ribbon porosity distribution											
35.2 ± 1.2	22.1 ± 2.5	18.25 ± 1.8	18.4 ± 2.3	14.2 ± 3.2	15.1 ± 0.9	18.8 ± 1.9	27.8 ± 2.0	27.1 ± 4.4	29.3 ± 2.6	0	0
34.7 ± 1.2	18.6 ± 2.5	13.5 ± 0.9	12.9 ± 1.9	9.8 ± 1.7	10.6 ± 0.6	13.0 ± 1.2	21.9 ± 2.3	21.5 ± 3.5	27.19 ± 2.5	30.0 ± 6.1	0
34.4 ± 1.0	14.4 ± 2.6	8.4 ± 1.6	6.7 ± 0.9	5.9 ± 1.1	6.6 ± 0.4	7.7 ± 0.7	12.9 ± 1.7	14.3 ± 4.0	23.5 ± 2.8	0	0
34.5 ± 1	11.5 ± 2.7	5.4 ± 1.9	3.7 ± 0.9	4.1 ± 1.2	4.6 ± 0.6	5.2 ± 0.4	6.9 ± 0.8	7.9 ± 3.2	17.3 ± 2	0	0
34.8 ± 1.3	10.3 ± 2.2	4.4 ± 1.93	3 ± 1	3.6 ± 1.3	3.9 ± 0.9	4.5 ± 0.9	5.3 ± 0.9	3.3 ± 2.4	10.6 ± 1.7	19.5 ± 7.7	26 ± 5.6
33.5 ± 1.8	10 ± 2.4	3.1 ± 2.2	3.6 ± 1	4.1 ± 1.3	4 ± 0.9	4.4 ± 1	5.3 ± 1	3.6 ± 2.7	8.5 ± 3.3	13.9 ± 3.5	27.6 ± 7.4
34.4 ± 1.3	24.8 ± 1.5	16.9 ± 3.3	15.6 ± 1.3	13.3 ± 4.5	13.7 ± 2.3	15.5 ± 1.7	27.6 ± 3.1	35.7 ± 3.3	0	0	0
33.8 ± 1.4	21.6 ± 1.6	13.5 ± 2.2	11.3 ± 1.3	9.8 ± 3.3	9.9 ± 1.7	10.9 ± 1.5	21.7 ± 3.3	29.2 ± 2.2	0	0	0
32.9 ± 1.7	16.9 ± 1.6	9.3 ± 1.5	6.8 ± 1.5	6.3 ± 2	6.5 ± 0.6	7 ± 0.8	12.8 ± 2.4	17.7 ± 1.9	19.4 ± 5.2	33.6 ± 4.7	0
32.1 ± 1.9	12.5 ± 1.6	6.0 ± 1.4	4.1 ± 0.9	4.3 ± 1.3	4.6 ± 0.6	5.1 ± 0.4	7 ± 0.8	7.8 ± 2.9	12.5 ± 2.9	29.7 ± 3.5	0
31.5 ± 2.6	10.5 ± 1.8	4.7 ± 1.5	3.2 ± 0.8	3.5 ± 1.4	3.9 ± 0.9	4.4 ± 0.9	5.3 ± 0.8	4.2 ± 2	8.2 ± 2	26.3 ± 3.5	20.4 ± 9
31.1 ± 3.4	10.1 ± 1.8	4.3 ± 1.5	3 ± 0.8	3.3 ± 1.5	3.8 ± 1	4.2 ± 1	5 ± 0.9	3.5 ± 1.7	7.2 ± 1.7	25.9 ± 4.2	16.6 ± 7.8
42.4 ± 2.7	35.1 ± 2.8	26.5 ± 4.2	25.6 ± 1.7	24.1 ± 4.3	22.1 ± 2	25.4 ± 2.2	31.6 ± 1.5	39.4 ± 4.5	0	0	0
41.7 ± 2.5	31.4 ± 2.7	21.1 ± 3	19.8 ± 1.3	17.6 ± 3.3	16.1 ± 1.6	19.1 ± 1.7	26.7 ± 1.5	33.6 ± 4.8	0	0	0
40.4 ± 2.3	24.9 ± 2.5	13.5 ± 1.7	11.1 ± 1.6	9.1 ± 1.8	9.2 ± 1.1	10.5 ± 1.2	16.7 ± 1.4	22.8 ± 5.7	28.5 ± 4	0	0
39 ± 2.1	17.4 ± 2.2	8.0 ± 1.3	5.2 ± 0.9	4.8 ± 1	5.3 ± 0.3	5.9 ± 0.4	8 ± 0.7	11.8 ± 3.8	19.1 ± 3.1	33.2 ± 3.9	0
38.4 ± 1.8	12.6 ± 1.9	5.7 ± 1.4	3.4 ± 0.8	3.8 ± 1.2	4 ± 0.8	4.6 ± 0.7	5.5 ± 0.8	5.1 ± 1.6	10.7 ± 1.2	27.5 ± 3	0
38 ± 1.8	11.2 ± 1.7	5 ± 1.5	3.1 ± 0.9	3.8 ± 1.4	3.9 ± 1	4.3 ± 1	5.1 ± 0.9	3.5 ± 1.6	8.7 ± 1.4	23.4 ± 2.5	39.3 ± 3.5
45.9 ± 0.9	33.5 ± 5.3	33.5 ± 2.2	30.7 ± 2.6	29.1 ± 2.2	33.5 ± 1.6	35.5 ± 1.2	38.5 ± 2.1	45.7 ± 3.1	0	0	0
44.4 ± 1.3	30.8 ± 4.1	27.6 ± 2.7	21.2 ± 2.9	20.5 ± 1.5	27 ±.2.7	29.1 ± 1.4	36.7 ± 2	42.3 ± 3	42.4 ± 3.5	0	0
43.1 ± 1	26.7 ± 2.3	18.6 ± 2.2	10.3 ± 2.1	9.4 ± 1.9	13.5 ± 3.3	14.1 ± 2.9	28.9 ± 3.7	33.7 ± 5.5	0	0	0

41.8 ± 1.6	21.1 ± 2.1	10.6 ± 2.5	5.4 ± 1.6	5 ± 1.6	5.7 ± 0.5	6.2 ± 0.8	11.8 ± 2.5	14.5 ± 3.3	21.5 ± 3.5	41.3 ± 4.5	0
41.1 ± 2.3	17.1 ± 2.5	7.9 ± 2.1	4.2 ± 1.5	4.5 ± 1.6	4.3 ± 0.7	4.9 ± 0.5	6.7 ± 0.7	6.3 ± 1.8	14.7 ± 2.5	42.2 ± 6.4	0
49 ± 2.2	39.8 ± 2.2	37.0 ± 2.3	36 ± 2.7	34.9 ± 2.5	34.9 ± 1.8	36.1 ± 1.1	37.9 ± 2	42.0 ± 2.8	43.7 ± 2.1	51 ± 4.4	0
48.2 ± 1.3	36.7 ± 2.4	33.3 ± 1.5	31.8 ± 2.3	31.7 ± 2	32 ± 1.2	33.4 ± 0.5	36.6 ± 1.8	39.2 ± 1.9	42.2 ± 1.7	49.6 ± 3.1	0
47.1 ± 1.3	31.8 ± 3.1	25.8 ± 1.2	22.6 ± 2.2	22.4 ± 2.8	24.2 ± 2	25.5 ± 1.1	32.0 ± 1.9	33.0± 2.8	37.3 ± 1.8	46.3 ± 2.5	0
50.2 ± 3.7	43 ± 3.2	35.8 ± 2.5	34.1 ± 2.4	35.2 ± 2.9	32.3 ± 1.3	33 ± 0.9	35.2 ± 1.8	35.8 ± 0.8	37 ± 1.9	44.5 ± 4.3	0
49.6 ± 2.9	40.8 ± 2.6	31.3 ± 1.8	29.6 ± 2.2	31.9 ± 2.6	28 ± 1.2	28.7 ± 1.6	32.1 ± 2	31.5 ± 1.9	33.4 ± 1.9	41.3 ± 2.6	46.6 ± 3.1
48.3 ± 1.8	36.2 ± 1.8	23.2 ± 1.9	20.8 ± 2.3	22.1 ± 4.2	18.5 ± 2.8	18.6 ± 1.8	23.5 ± 2.6	23.6 ± 4.1	25.7 ± 2.6	35.7 ± 2.2	45.6 ± 4.9
46.8 ± 1.5	28.8 ± 1.8	15.0 ± 1.9	10.8 ± 2.7	9.8 ± 4.7	8.6 ± 2	8.1 ± 1.3	10.8 ± 1.4	14.7 ± 6.2	17.2 ± 3.7	28.4 ± 3.6	44.8 ± 3.9
45.7 ± 1.2	20.9 ± 1.6	10.8 ± 1.7	6.7 ± 2.4	5.4 ± 2	4.7 ± 0.4	5 ± 0.5	5.9 ± 0.7	9.0 ± 3.6	12.5 ± 3.1	21 ± 2.8	46.6 ± 2.6
44.7 ± 1.8	17.1 ± 2.3	9.3 ± 1.5	5.5 ± 2.1	4.4 ± 1.3	4.1 ± 0.8	4.5 ± 0.8	5.2 ± 0.8	7.1 ± 2.1	11.1 ± 3.2	17.4 ± 4.4	47.5 ± 4.2
35.8 ± 1.1	29.9 ± 1.7	24.6 ± 1.9	23.3 ± 3.2	23.4 ± 2.5	23.6 ± 1.9	26 ± 1.8	27.7 ± 2.7	27.5 ± 3.1	28.7 ± 2.3	35.2 ± 4.5	0
35.1 ± 0.7	26.2 ± 2.1	21.3 ± 2.7	18.4 ± 2.9	17.8 ± 3.4	17.5 ± 1.1	19.5 ± 1	22 ± 3.3	23 ± 2.6	26.7 ± 2.2	33.6 ± 3.2	0
34.1 ± 0.4	21.3 ± 2.3	16.8 ± 4.2	11.5 ± 2.1	10.7 ± 3.7	9.8 ± 0.9	10.8 ± 1	13.1 ± 2.9	15.6 ± 2.6	23.3 ± 2.8	30.6 ± 2.3	33.5 ± 3
33.1 ± 1	16.8 ± 1.9	11.5 ± 3.9	6.3 ± 1.8	5.4 ± 2	5.5 ± 0.5	6 ± 0.4	7.0 ± 1.3	7.8 ± 3.2	17.5 ± 3.2	27.2 ± 2.8	32.9 ± 2.3
32.3 ± 1.6	13.8 ± 1.9	6.5 ± 1.6	4.1 ± 1.1	3.7 ± 1.5	4.1 ± 0.8	4.6 ± 0.7	5.3 ± 0.9	4.5 ± 2.4	9.9 ± 2.9	23.6 ± 4.6	0
32.1 ± 1.7	13 ± 2.7	5.1 ± 1.4	3.4 ± 0.7	3.5 ± 1.6	3.9 ± 1	4.4 ± 0.9	5 ± 0.9	3.7 ± 3.3	7.8 ± 2.6	19.4 ± 8.6	33.5 ± 3.1
35.9 ± 1.6	33.3 ± 1.7	24.0 ± 2.7	20.2 ± 3.3	21.5 ± 3.5	21.3 ± 2.4	22.0 ± 2.0	27.7 ± 1.3	28.5 ± 3.4	33.7 ± 2.2	0	0
35.3 ± 1.4	30.6 ± 1	21.6 ± 1.1	16.3 ± 2.9	18 ± 2.9	15.5 ± 2.5	15.7 ± 2.3	21.6 ± 1.6	23.8 ± 2.4	31.9 ± 2.2	37.5 ± 3.4	0
34.6 ± 1.3	26.0 ± 2.4	17.9 ± 1.3	11.4 ± 3.4	12.8 ± 3.4	9.1 ± 1.7	9.1 ± 1.8	12.6 ± 1.6	16.8 ± 2.4	27.9 ± 2.8	36 ± 3.1	0
33.8 ± 1.2	19.9 ± 4	13 ± 1.4	7.6 ± 2.5	7.1 ± 1.9	5.4 ± 0.5	5.7 ± 0.4	6.9 ± 0.8	10.4 ± 2.9	19.4 ± 2.8	34.2 ± 1.9	0
33.0 ± 1	14.3 ± 2.6	7.7 ± 1.6	4.9 ± 1.4	4.2 ± 1.5	4.1 ± 0.8	4.6 ± 0.7	5.3 ± 0.8	6.8 ± 1.9	10.6 ± 1.4	31 ± 1.7	0
32.6 ± 1.1	12.0 ± 2.3	6.2 ± 2.1	4 ± 1.1	3.7 ± 1.6	3.9 ± 1	4.3 ± 1	5 ± 0.9	4.7 ± 3	8.6 ± 1.8	27.1 ± 2.1	0
40.5 ± 1.8	35.5 ± 3.5	30.6 ± 2.2	30.3 ± 2.9	29.9 ± 2.9	29.5 ± 1.5	30.9 ± 1.2	31.4 ± 1.6	29.9 ± 2	34.4 ± 2.4	39.2 ± 4.1	0

39.1 ± 1.5	31.8 ± 2.7	27 ± 1.8	25.5 ± 2.2	24.1 ± 3.5	24.4 ± 1.4	25.8 ± 1.3	26.5 ± 2.2	25.7 ± 1.3	32.1 ± 2.1	37.9 ± 3.3	0
37.1 ± 0.9	25.4 ± 2	21.3 ± 2.2	17.5 ± 3	14.8 ± 4.3	14.6 ± 1.5	15.2 ± 0.9	16.7 ± 2.7	18.5 ± 2.3	27.6 ± 1.9	34.9 ± 3.7	0
35 ± 0.6	18.5 ± 2.3	14.5 ± 2.6	9.7 ± 3.5	7.4 ± 2.6	6.9 ± 0.7	7.1 ± 0.9	8.0 ± 1.5	10.7 ± 1.8	19 ± 2.1	29.6 ± 5.9	36.6 ± 1.7
33.6 ± 0.9	14.3 ± 2.2	8.6 ± 2.3	5.9 ± 1.9	4.5 ± 1.3	4.4 ± 0.7	4.9 ± 0.5	5.5 ± 0.9	6.9 ± 1.6	10.4 ± 1.6	24.4 ± 6.7	34.2± 3.8
33.1 ± 1.5	13.2 ± 2.6	6.7 ± 1.9	4.3 ± 0.9	4.1 ± 1.5	4 ± 0.9	4.4 ± 0.9	5.1 ± 0.9	5.6 ± 2.8	8.6 ± 1.5	23.4 ± 7.5	0
47.5 ± 1.8	43.3 ± 2.5	40.9 ± 3.9	40.2 ± 2.2	37.5 ± 2.8	36.8 ± 2.7	37.7 ± 2.1	38.5 ± 2	41.5 ± 3.5	42.6 ± 2.5	44.6 ± 5.5	48.1 ± 5.6
45.3 ± 1.3	40.9 ± 1.5	36.0 ± 3.2	34.8 ± 3.5	33.7 ± 3.2	32.9 ± 1.5	33.8 ± 1.4	36.7 ± 1.6	38 ± 3.4	40.4 ± 1.4	43.2 ± 5.1	0
42 ± 1.5	37.1 ± 1.5	26.5 ± 2.7	22 ± 4.2	22.5 ± 4.9	20.8 ± 2.7	20.2 ± 3.2	28.8 ± 3.1	28.9 ± 4.2	33.6 ± 3.5	41.0 ± 5.1	45.8± 4.8
39.1 ± 1.2	31.4 ± 2.3	15.8 ± 1.8	10.7 ± 3.4	10.0 ± 3.9	7.5 ± 1.3	7.6 ± 1.9	11.8 ± 2.8	17.5 ± 3.7	22.1 ± 4.1	37.7 ± 4.2	0
37.9 ± 1.9	27 ± 2.8	11.5 ± 2.4	7 ± 2.2	6.6 ± 2.1	4.9 ± 0.4	5.4 ± 0.4	6.7 ± 1.1	13 ± 2.2	15.5 ± 2.6	34.2 ± 3.9	40.1 ± 3.3
50.6 ± 2	44.2 ± 2.7	42 ± 3.6	41.3 ± 2.3	38.9 ± 3.3	37.6 ± 3.1	38.2 ± 2.1	37.9 ± 1.8	41.9 ± 4.1	45.3 ± 3.1	0	0
49.3 ± 1.5	42 ± 1..8	39.3 ± 2.6	38.8 ± 1.6	37.5 ± 2.8	36.0 ± 2.2	36.5 ± 1.4	36.4 ±1.5	38.8 ± 2.7	43.3 ± 2.3	43.9 ± 3.2	0
47.1 ± 1.2	37.3 ± 1.8	33.2 ± 2.1	32.6 ± 2.5	32.7 ± 1.9	31.2 ± 0.7	31.5 ± 0.4	32.1 ± 1.3	31.8 ± 1.3	37 ± 2.2	39.4 ± 2.9	47.9 ± 8
44.1 ± 1.9	29.9 ± 4	23.6 ± 2.8	20.5 ± 4.3	18.4 ± 3.2	17.9 ± 3	16.6 ± 2.1	18.6 ± 2.7	20.4 ± 2	26.5 ± 2.6	32.4 ± 4.3	47.1 ± 8
49.9 ± 2.5	41.9 ± 2	38.6 ± 2.2	38.5 ± 3.1	36.4 ± 2.3	36.2 ± 2.4	36.6 ± 1.3	35.4 ± 1.4	38.2 ± 3.8	41.2 ± 2.2	44.9 ± 3.3	0
48.8 ± 2.2	39.4 ± 2	35.2 ± 1.8	35.2 ± 2.8	34.2 ± 2.1	33.9 ± 1.5	34.2 ± 0.7	32.4 ± 1.1	33.4 ± 3	37.3 ± 1.7	43.1 ± 2.7	43.0 ± 3.3
47.1 ± 1.6	34.6 ± 2.8	28.9 ± 3	28.2 ± 3.5	28.7 ± 2.7	27.2 ± 1.9	27 ± 1.2	23.9 ± 1.6	25.1 ± 2.5	29.3 ± 2.5	39.3 ± 2.9	0
45 ± 1.5	27.1 ± 4.5	21 ± 3.6	17.6 ± 4.1	17.5 ± 2.6	13.7 ± 3.9	12.2 ± 1.9	10.9 ± 1.5	15.6 ± 1.3	19.4 ± 2.4	33.0 ± 3.2	44.5 ± 2.6
43.3 ± 1.4	20.0 ± 4.6	14.2 ± 2.6	10.5 ± 3	8.1 ± 3	5.9 ± 0.7	5.8 ± 0.5	5.9 ± 0.8	10.4 ± 1.6	13.6 ± 2.2	26.1 ± 3.3	43.9 ± 2.2
42.3 ± 1.3	16.8 ± 3.9	11.7 ± 3.8	8.0 ± 2.7	6 ± 2.7	4.4 ± 0.5	4.7 ± 0.6	5.2 ± 0.9	8.2 ± 3.6	12.4 ± 2.8	21.8 ± 3.9	41.7 ± 5.2